Triply periodic minimal surface-based structures for load-bearing bone tissue engineering applications

---

PhD Thesis

Tejas Mahesh Koushik

in October 2024

For the degree of Doctor of Philosophy

in the College of Science and Engineering

James Cook University

Townsville

Advisors: Dr Elsa Antunes, A/Prof Catherine Miller

DECLARATION

I declare that this thesis is my own work and has not been submitted to elsewhere in whole or in part to obtain other degree award. The content of this thesis is the result of author work, and the contribution of others has been acknowledged in the statement of contribution of others.

Tejas Mahesh Koushik

Tejas Mahesh Koushik

October, 2024

STATEMENT OF ACCESS TO THIS THESIS

I, the under-signed, the author of this research work, understand that James Cook University will make this thesis available for use within the University Library and via the Australian Digital Thesis Network, for use elsewhere.

I understand that an unpublished work, a thesis has significant protection under the Copyright Act. I do not wish to place any restriction on access to this thesis, but any use of its content must be acknowledged.

Tejas Mahesh Koushik

Tejas Mahesh Koushik

October, 2024

STATEMENT ON THE CONTRIBUTIONS OF OTHERS

Nature of assistance	Type of Contribution	Description of Contribution
Intellectual support	Editorial Assistance	I would like to thank my advisors (Dr Elsa Antunes and A/Prof Catherine Miller) for helping me with editing of my thesis and publications.
Financial Support	Research Costs Stipend	Graduate Research School, James Cook University
Data Collection	Research Assistance	

ACKNOWLEDGEMENTS

First and foremost, I would like to wholeheartedly thank Dr. Elsa Antunes and Dr. Kate Miller for their unwavering support throughout this journey. I would also like to acknowledge all the lab technicians who took the time to train and guide me.

Reflecting on the past four years, it's clear that the journey of a PhD is filled with both highs and lows. From the exhilarating moments of submitting my first research article and successfully presenting my thesis seminar, to the challenging times of addressing blunt comments from reviewer 2, each experience has been a crucial dot in the larger picture. At the time, it was hard to see how these moments would connect, but looking back, they form a coherent path that has shaped my growth. As Steve Jobs said, "The journey is the reward."

The true anchors through these wild ups and downs have been my friends and family. My journey has introduced me to friends from all around the world, and I am eternally grateful for their acceptance and the opportunity to learn from their experiences.

Last but not least, I would like to thank my dear parents and my sister for their support. Their mere presence in the background provided me with the confidence to push beyond what I thought I was capable of. I hope that when I look back on this thesis in the future, I will fully appreciate the hard work of everyone involved and my own ability to venture into the unknown.

ABSTRACT

Bone tissue engineering (BTE) has garnered significant interest over the past decade due to advancements in materials processing techniques and a deeper understanding of bone healing pathways, which have opened new avenues of research. BTE scaffolds are challenged with the dual responsibility of providing load-bearing capability while interacting with the local extracellular matrix (ECM) to promote bone healing, especially in synthetic scaffolds. This thesis examines the usage and processing of multi-materials and hierarchical structures designed to mimic the natural bone tissue, functioning as bioactive and load-bearing synthetic scaffolds.

The research work focuses on the use of 3% mol Y_2O_3 stabilized zirconia (3Y-TZP) along with Hydroxyapatite (HAp), common bioceramics in BTE scaffolds, to improve patient outcomes and accelerate healing times. However, significant differences in thermal expansion between these ceramics pose challenges to co-sintering them without compromising functionality and strength. A two-step sintering (TSS) process was employed to co-sinter composites using (1-x)3Y-TZP and xHAp, where x varies between 20 and 80 wt%. The optimal TSS conditions, with a peak temperature of 1300 ℃, a plateau temperature of 1175 ℃, and a heating rate of 10 ℃/min with a holding time of 600 minutes, produced specimens with grain sizes between 0.5 and 1.2 μm and compression strengths ranging from 88 to 176 MPa. The similarity in compression strength of these zirconia-hydroxyapatite composites with natural bone and the retention of HAp render them suitable for BTE applications in load-bearing areas.

Additionally, this thesis investigates the influence of porous scaffold architecture on osteointegration with host tissues, biofunctionality, and mechanical strength. Hydroxyapatite scaffolds were designed with three triply periodic minimal surface (TPMS) structures (gyroid, lidinoid, and split-P) at porosities ranging from 50% to 80%. The split-P architectures exhibited the highest compression strength between 15 and 25 MPa but provided the least surface area for bone apatite precipitation, whereas gyroid and lidinoid structures showed the highest quantity of bone apatite precipitation across all porosities. To combine these benefits and further improve compression strength, graded structures were designed with multiple TPMS structures arranged in a core and shell configuration. The structure featuring a solid core with a 70% porous gyroid shell

exhibited the highest compression strength of 120 MPa, with cell attachment equivalent to the porous core structure. The similarity in compression strength with cancellous bone and the ability of the 70% gyroid with a solid core structure to facilitate cell attachment and proliferation akin to highly porous structures make it an ideal candidate for load-bearing BTE applications.

Furthermore, the thesis explored a multi-ceramic approach using 3Y-TZP and HAp through 3D printing to create a bioactive external shell with an inert, high-strength core, comparing with a single ceramic approach. Co-sintering of the two ceramics resulted in finer sub-micron grain sizes within the 3Y-TZP core and grain sizes between 2 and 5 μm in the outer shell. The 3Y-TZP–HAp composite showed a compression strength of 56 ± 2 MPa along the longitudinal direction with pore sizes ranging from 800 to 2000 μm in the outer HAp ring, whereas pure 3Y-TZP scaffolds exhibited a compression strength of 226 MPa under similar conditions. The osteoblast cell proliferation on pure HAp and 3Y-TZP structures was similar to that of composite samples, with identical expression of osteogenic markers, indicating positive potential for tissue integration and new bone tissue formation. Therefore, this study suggests that 3Y-TZP based scaffolds with triply periodic minimal surface (TPMS) structures show the best potential for load-bearing BTE applications requiring multi-directional strength. Future research should look at overcoming the limitations of multi-ceramic processing in 3D printing to address the challenges associated with the current 3Y-TZP–HAp composite design.

1.2 TABLE OF CONTENTS

LIST OF TABLES

LIST OF FIGURES

LIST OF PUBLICATONS

Journal Publications

T. M. Koushik, C. M. Miller, and E. Antunes, "Bone Tissue Engineering Scaffolds: Function of Multi-Material Hierarchically Structured Scaffolds," *Advanced Healthcare Materials,* p. 2202766, 2023. doi: https://doi.org/10.1002/adhm.202202766.

T. Koushik and E. Antunes, "9 - Ceramic three-dimensional printing," in *Advanced Flexible Ceramics*, R. K. Gupta, A. Behera, S. Farhad, and T. A. Nguyen Eds.: Elsevier, 2023, pp. 193-214. doi: https://doi.org/10.1016/B978-0-323-98824-7.00009-9.

T. M. Koushik, C. M. Miller, and E. Antunes, "Optimisation of two-step sintering parameters to produce bioactive and dense zirconia-hydroxyapatite composite ceramics," *Journal of the European Ceramic Society,* vol. 43, no. 5, pp. 2222-2233, 2023, doi: https://doi.org/10.1016/j.jeurceramsoc.2022.12.021.

T. M. Koushik, C. M. Miller, and E. Antunes, "Graded hydroxyapatite triply periodic minimal surface structures for bone tissue engineering applications," *Advanced healthcare materials* (Under review).

T. M. Koushik, D. J Browne, C. M. Miller, and E. Antunes, "Multi-ceramic approach to bone tissue engineering scaffold design: Influence on mechanical and *in-vitro* performance", *Journal of the European Ceramic Society* (Under review).

1 INTRODUCTION

1.1 Problem statement

Bones play a critical role in supporting and providing a framework for all the soft tissues in the human body. The structure of bone tissues extends from nano-scale to macro-scale features, providing strength and functionality to bone tissues. Throughout the day, bones are under constant stress from a combination of static and dynamic loads. These loads, caused by exercise, injuries, and disease, can inflict damage on bone tissues. Damages during day-to-day activities are usually self-healed through a cascade of chemical signals that initiate and sustain the repair of bone tissue [1]. However, for damages beyond a critical size of 6 mm, the body cannot self-heal the damaged bone sections causing chronic pain and leading to permanent deformity in patients. For older adults and patients with underlying conditions this will have a direct impact on their quality of life. Furthermore the cost of bone fractures annually is estimated at $3.4 billion in Australia (2017) where 68% of the costs were associated with the fractures due to osteoporosis [2].

Conventional treatment options for repairing damaged bone tissues involve the use of allografts, autografts or inert metallic implants. Autografts are extracted from the patient's iliac crest, however, their limited supply and need for additional surgical intervention prevents them from being an ideal option in all cases [1]. Allografts extracted from donors are associated with risks of disease transmission, poor efficacy in enabling a bone healing response and therefore are not usually preferred [1]. In recent times, development of engineered bone substitutes has become a popular choice. The field of designing and developing engineered bone substitutes is known as BTE . Materials used for preparing bone substitutes include metals, ceramics, polymers and composites [2]. Functions of these bone substitutes, involve structural support to the damaged sections and ability to interact with the surrounding niche. While structural support is critical, interaction with the surrounding niche enables supply of nutrients to the cells responsible for healing damaged sections and the cascade of chemical signals required to maintain the healing response [3, 4]. Micro and nano scale pores present in the bone tissues enable this exchange of nutrients and interactions, therefore are a critical requirement in BTE

scaffolds. However, pores present in the scaffold structure compromise the strength of the scaffold, fulfilling these contradictory requirements is a major challenge. In addition to these challenges, damaged bone sections can be in multiple shapes and sizes, thus scaffolds must be customised to ensure a perfect fit. Conventional approaches as discussed previously fail to provide this flexibility, therefore engineered bone substitutes which can be tailored to individual requirements are better suited for functioning as scaffolds for bone tissues.

BTE scaffolds are 3D templates providing cells with a physical structure for support and function as well as a reservoir for the supply of nutrients. Materials such as Ti-6Al-4V or tantalum, popularly used in BTE, have the benefit of having high strength and being inert but cannot be degraded inside the body [5, 6]. Furthermore, large differences in Youngs moduli between these materials and natural bone tissue lead to stress shielding [7]. Stress shielding occurs when the load on the bone tissue is redistributed due to the presence of a stiffer structure, causing resorption of the tissue in the surrounding areas and resulting in loosening of the implant [7, 8]. To address their inert nature polymer or ceramic coatings and composites are often used for improving their interactions with the surrounding niche [9]. Polymers such as polycaprolactone and polylactic acid are increasingly being used to prepare scaffolds due to their ability to degrade allowing natural bone tissue to gradually replace the damaged sections [3, 10]. However, polymers tend to be weaker and are not suitable on load-bearing areas such as the hips and knees.

On the other hand, ceramics offer the benefit of being non-toxic and bioactive. For example, hydroxyapatite-based ceramics or bioglasses are actively involved in the healing process [3]. However, the brittle nature of ceramics is a common issue that prevents its use in load-bearing areas. R-curve behaviour or toughening observed in advanced ceramics such as ZrO_2 with 3 mol% of Y_2O_3 prevents immediate fracture observed in calcium phosphates but lacks any bioactivity to support bone healing. Therefore, a single material is often incapable of addressing these opposing requirements of being bioactive and having strength to bear load. A multi-material approach on the other hand can be used to combine the benefits offered by bioactive materials along with load-bearing ceramics, polymers or metals. Incorporation of these multi-materials can be achieved through strategies such as coating, blending, doping, layering or chemical adhesion. While the benefits of multi-material scaffolds are promising, processing these

scaffolds require specialised techniques. Thus, only multi-material approaches that improve efficacy of bone healing or patient outcomes should be selected. In addition to the material choices, scaffold structures play a significant role enabling vascularisation through pores and distribution of applied stresses.

The structure of the natural bone tissue has high strength in the direction of the applied load while also maintaining a low density, that is essential for providing support while also being light weight. Cellular internal structure enables nutrient transport and vascularisation of tissues. Since introduction of porosity within ceramic structures reduces damage tolerance due to the stress concentration, the porous network has to be carefully designed onto a structure to maintain mechanical strength [11, 12]. The wide-ranging pore sizes (300 μm – 1200 μm) and an interconnected network of pores are challenging to replicate using conventional manufacturing techniques. Development of additive manufacturing (AM) techniques for ceramic processing have opened the possibility of utilising lattice structures that mimic the architecture of natural bone tissues. Triply modified minimal surfaces (TPMS) have become a popular choice for application in BTE due to their similarity with natural bone and their ability to combine high strength and porosity [3, 13].

The range of TPMS structures combined with the flexibility of AM, create a large combination of structures for the purpose of load-bearing BTE scaffolds. Results from this thesis provide a framework to utilise TPMS structures in BTE scaffolds and highlight a multi-material approach to BTE scaffold design using AM techniques. The use of a combination of a multi-ceramic and TPMS in design of BTE scaffolds can enable their use in load-bearing areas while also allowing bone in-growth. This advancement will reduce the need for surgeries to remove the scaffold and allows osseointegration with native bone tissue. Lastly, the versatility offered by AM techniques unlocks patient-specific scaffold designs for BTE applications.

1.2 Research Objectives

This thesis aimed to develop ceramic scaffolds for load-bearing BTE using TPMS structures. Also, this thesis explored the potential of a multi-structural and multi-material design approach for ceramic BTE scaffolds. Outcomes of this thesis are contributing towards the development of personalised approaches to ceramic BTE scaffolds.

The specific objectives of this research were.

1. To assess the feasibility of co-sintering 3Y-TZP–HAp composites and identify the effect of sintering variables on phase composition and densification of the ceramic composite.

2. To investigate different TPMS structures and its mechanical properties and *in-vitro* response to osteoblast cells.

3. To investigate a combination of suitable TPMS structures for use in load-bearing BTE scaffolds.

4. To investigate the feasibility of a multi-ceramic approach to load-bearing BTE scaffold design by examining the impact of ceramic composite on the proliferation, attachment and differentiation of osteoblast cells.

1.3 Thesis organisation

Chapter 1: Introduction - Includes an overview about the field of BTE and the main motivation for this work.

Chapter 2: Literature review - This chapter looks into the hierarchical organisation of the bone tissue while also highlighting its functions during healing of bone fractures. A detailed comparison of different biomaterials and BTE approaches were discussed. The function of triply periodic minimal surfaces as BTE scaffold were discussed highlighting critical features required to function as BTE scaffolds. Emerging trends in BTE scaffolds development are discussed. Finally additive manufacturing techniques for processing

BTE scaffold are described and their benefits over conventional manufacturing techniques are also discussed.

This chapter was published as Tejas Koushik, Catherine Miller, Elsa Antunes. “Bone tissue engineering scaffold: Function of multi-material hierarchical structured scaffolds”. Advanced Healthcare Materials.

Chapter 3: Ceramic 3D printing - This book chapter investigates additive manufacturing techniques used for processing ceramics as BTE scaffolds. The available ceramic 3D printing techniques are reviewed, and their benefits and limitations are discussed.

This study has been published as Tejas Koushik, Elsa Antunes. Ceramic 3D printing. “Advanced Flexible materials”.

Chapter 4: Phase reactions during two-step sintering of 3Y-TZP-HAp composites – This chapter investigates the effect of two-step sintering parameters on the phase composition and mechanical performance. The relative importance of two-sintering parameters was determined using a Taguchi experimental design. Identified parameters; hold time and plateau temperatures were optimised using a factorial experiment design to maximise retention of HAp phase during sintering. Optimised two-step sintering conditions for 3Y-TZP–HAp composites that showed mechanical properties similar to human cancellous bone were identified through this chapter.

This study was published as Tejas Koushik, Catherine Miller, Elsa Antunes. “Optimisation of two-step sintering parameters to produce bioactive and dense zirconia-hydroxyapatite composite ceramics”. Journal of European Ceramics society.

Chapter 5: Graded hydroxyapatite triply periodic minimal surface structures for bone tissue engineering applications – This chapter investigates the effect of different TPMS structures (gyroid, split-P and lindinoid) at porosities ranging from 50 – 80% on their mechanical performance and calcium precipitation ability. Identified structures are further optimised to provide mechanical strength comparable to cancellous bone. Further, cellular proliferation and attachment within these structures were examined to determine

their functionality as load-bearing BTE scaffolds. Through this chapter, critical features responsible for interaction were identifed and TPMS structures with pore sizes greater than 700 µm were developed for load-bearing BTE applications. Lastly a strategy to tailor the compression strength by incorporation of solid core within a TPMS based BTE scaffold was discussed. It was shown to be an effective arrangement to enable maximum fluid intrusion while also providing the strength to function as a load-bearing BTE scaffold.

Chapter 6: 3D Printed 3Y-TZP-HAp scaffolds with triply periodic minimal surface structures for bone tissue engineering – This chapter describes a multi-ceramic approach to BTE scaffolds design using additive manufacturing. Core and shell arrangement of 3Y-TZP and HAp respectively were explored based on the capability of current ceramic stereolithography techniques. Based on the results from chapter 5, the architecture of the HAp shell was selected to maximise fluid intrusion and the solid 3Y-TZP core was chosen to enhance compression strength. The effect of this multi-ceramic design on load-bearing capacity and *in-vitro* performance was investigated in this chapter. Phase composition of the composite at the interface of the 3Y-TZP-HAp composite was analysed to identify formation of undesirable phases highlighted in chapter 4. Outcomes from this chapter provided a strategy to utilise high strength 3Y-TZP and bioactive HAp for load-bearing BTE applications. Furthermore, positive influence of ceramic composite on seeded osteoblast cells indicated that the core and shell strategy can be used to take advantage of the osteoinductive behaviour of HAp ceramics and R-curve behaviour of 3Y-TZP to improving toughness.

Chapter 7: Conclusions and recommendations – This chapter provides a topical conclusion of all the key ideas discussed in this thesis and suggests recommendations for further work.

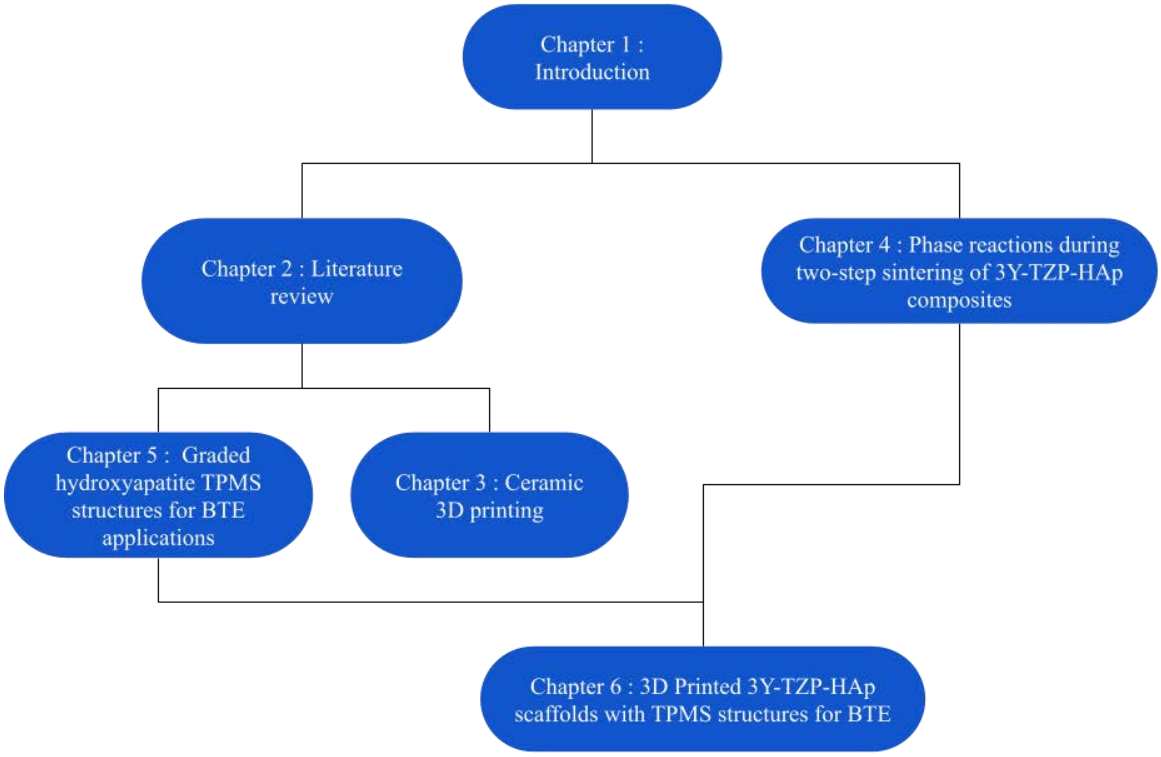

Figure 1: Thesis organisation structure and relationships between chapters.

2 LITERATURE REVIEW

Abstract

Bone tissue engineering has been a topic of interest for the last decade, and advances in materials, processing techniques, and the understanding of bone healing pathways have opened new avenues of research. The dual responsibility of BTE scaffolds in providing load-bearing capability and interaction with the local ECM to promote bone healing has been a challenge in synthetic scaffolds. This article describes the usage and processing of multi-materials and hierarchical structures to mimic the structure of natural bone tissues to function as bioactive and load-bearing synthetic scaffolds. The first part of this literature review describes the physiology of bone healing responses and the interactions at different stages of bone repair. The following section reviews the available literature on biomaterials used for BTE scaffolds followed by some multi-material approaches. The next section discusses the impact of the scaffold's structural features on bone healing and the necessity of a hierarchical distribution in the scaffold structure. Finally, the last section of this review highlights the emerging trends in BTE scaffold developments that can inspire new tissue engineering strategies and truly develop the next generation of synthetic scaffolds.

2.1 Introduction

Bone is a multifaceted tissue that provides structural support while simultaneously contributing to critical biological functions that keep us alive and functioning. It protects our soft tissues from the physical trauma endured while doing daily tasks. However, like any other human body tissue, defects or accidents can severely damage bone tissues beyond self-recovery. While the bone tissue has a self-healing ability, it is only capable of regenerating and remodelling small (<6 mm) defects/damages but remains insufficient for larger defects [14, 15].

The gold standard for the recovery of larger fractures involves using autologous grafts derived from human donors. The limited supply of autologous grafts has seen the development of studies focusing on developing novel BTE strategies for bone regeneration [16-18]. Scaffolds used for BTE applications must be designed, taking in consideration their structural capacity and interaction with the extracellular matrix (ECM). For example, the foreign body response is triggered due to the preferential adsorption of fibrin onto the implant's surface [19]. Neutrophils in the implant area attract monocytes to the fibrin-dominated implant surface, which subsequently differentiate into macrophages, releasing pro-inflammatory factors such as tumor necrosis factor-alpha (TNFα), interleukin-6 (IL-6), and interleukin-8 (IL-8). These macrophage populations at the injury site encapsulate the surface with fibrous tissue, preventing any further interaction with local ECM [19]. The inability to interact with the ECM prevents the transfer of ions and nutrients required for the damaged tissue to undergo osseointegration. Lack of osseointegration could eventually require additional surgeries for removal and, therefore, compromise recovery in the long term. The specificity in fibrin adsorption could be due to the scaffold's surface charge, wettability, and chemical composition [20].

Thus, materials that positively interact with the local cells and initiate a bone healing response must be chosen. Just like bone tissue, organic components present within their structure must interact with the cells around it while inorganic components enhance their structural strength. Similarly, BTE scaffolds must have a dual function of inducing positive healing processes while simultaneously supporting the damaged areas.

Osteoinductivity, osteoconductivity, and biocompatibility of the scaffold are the three critical requirements of BTE scaffolds. Osteoinduction refers to the ability of scaffolds to recruit the host mesenchymal stem cells (MSCs) from surrounding tissues and differentiate them into osteoblast cells, which are responsible for bone growth [21]. Osteoconduction is the ability of the material to facilitate the growth of cells on the scaffold [21]. Biocompatibility, as described in the previous section, refers to the scaffold's ability to not trigger the foreign body response when implanted. In addition to these material properties, the scaffold's architecture (macrostructure and microstructure) will dictate the extent of angiogenesis achievable. The extent of angiogenesis is known to directly impact the extent of cell spreading, transportation of nutrients (blood, biomolecules, or waste), and bone in-growth [22]. Further, the hierarchical nature of the bone structure has a wide range of porosities depending on the type, location, and function [23-25]. Therefore, the scaffolds will require a range of porosities (size, shape, and extent) to function as effective BTE scaffolds.

Previous reviews have described the effects of material chemistry or processing techniques on the bone healing response [26-28]; however, these reviews have discussed the effects of a single material, whereas as discussed in this review, most scaffolds are comprised of multiple materials. Although using additives such as signalling molecules, growth factors, stem cells and other functional materials has been a popular approach to

supplement the regenerative pathways during bone healing ,most recent review articles do not describe the regenerative pathways influenced by composite materials to improve bone healing ability [29]. Limitations of conventional techniques to manufacture next generation tissue engineering scaffolds (biofunctionality, patient specific and degradable) have been previously discussed [30, 31] as well as the role and capabilities of additive manufacturing (AM) in the future of regenerative medicine [32]. However, previous review articles discussing AM for BTE applications are focussed on the operational challenges and the strategies to overcome them [33, 34]. Therefore, this review aims to highlight the synergistic effects of multi-materials and scaffold architecture on the bone healing response. The function of materials in the bone healing pathways as well as structural features effecting bone healing and the need to introduce hierarchy to enhance the adaptability and efficacy of these scaffolds is discussed. Conventional methods to manufacture porous material have been previously discussed extensively; thus, this review will only focus on techniques capable of producing hierarchical porosities and the ability to process multiple materials.

2.2 Scaffold function in bone tissue engineering

2.2.1 Structure of Bone tissue

Bone is a living material that supports the musculoskeletal system, functions as a source of calcium and stores the bone marrow. It is organised in a complex hierarchical structure extending from a few nanometres to micrometres, as shown in Figure 2.1a. The various cell types present in the ECM of these bone tissues enable them to repair and remodel themselves constantly. Osteoblasts, osteoclasts, bone lining cells, and osteocytes present at the injured site have specific functions responsible for initiating or sustaining the bone healing response. Osteoblasts are responsible for forming bone tissue by producing bone

extracellular matrix components such as type I collagen, proteoglycans, non-collagenous proteins, and cell attachment proteins [35]. Matrix vesicles secreted by the osteoblasts and present in the ECM provide a nurturing environment for the nucleation of calcium phosphates. Mineralisation of these vesicles begins when crystalline calcium phosphates appear inside them, this step is governed by transporter membranes and enzymes [36, 37]. Osteoclasts are multi-nucleated cells derived from monocytes that are responsible for bone resorption in response to local stimuli [38]. The resorption process is critical in maintaining blood calcium levels [39]. Osteocytes are osteoblast cells surrounded by mineralised bone tissue [39]. The location and interconnectivity of these cells make them ideal for detecting and transducing mechanical stresses into a physiological response [39]. Osteogenic cells (bone lining cells) form a thin layer on bone tissues, functioning as a protective layer from further osteoclast activity. However, with suitable stimulation, they could form osteoblasts [39]. These osteogenic cell types are usually up to a few microns in size depending on their location and are the basic building blocks essential for the formation and maintenance of bone tissue.

Cell types (osteoblasts, osteoclasts, bone lining cells, and osteocytes) are responsible for maintenance and repair of the bone tissue. The supply of oxygen and nutrients for these cell types is critical to ensuring their survival. The diffusion limit for oxygen for tissues has been reported to be within the range of 100 - 200 μm i.e oxygen diffusion will only occur in the tissues within 200 μm of the oxygen source [40]. Blood distributes oxygen and nutrients to bone tissues through capillaries. The hypoxic state of the cells at the injured site (due to the inflammatory wound healing response triggered after the injury) triggers the release of vascular endothelial growth factor (VEGF) [41]. VEGF causes the differentiation of angioblasts into primitive blood vessels; this process is termed vasculogenesis and needs to occur prior to angiogenesis. Endothelial cells present within

the tissue bridge the gaps between these primitive blood vessels to form capillary buds and sprouts; this process is defined as angiogenesis [41].

The structural morphology of bone tissues can be divided into osteons, lamella, collagen fibres, and collagen fibrils, considering their relative sizes [42]. The collagen fibrils consist of several sub-nanometre type I collagen molecules that are discretely separated by plate-like hydroxyapatite crystals and other impurities such as HPO_4, Na, Mg and K [43]. The fibrils self-assemble into bundles and orient themselves in specific directions forming collagen fibres with a diameter between 3 - 7 μm [44]. Arrangement of these fibres concentrically forms osteons in the range of 10 – 500 μm [44, 45]. When these fibres are concentrically arranged around Haversian canals, they form Haversian systems, which are 150 – 300 μm thick, as shown in Figure 2.1b. Differences in the arrangement of these components within the bone produce two types called cortical and trabecular bone, as shown in Figure 2.1c-i. Cortical bone consisting of concentrically distributed osteons forms the dense exterior of bones, as shown in Figure 2.1c-iv. Trabecular bone shown in Figure 2.1d-ii consists of a more open network, where the empty spaces are occupied by blood vessels and bone marrow. This hierarchical organization of bone tissue extends from a few nanometres to micrometres, as shown in Figure 2.1c [44].

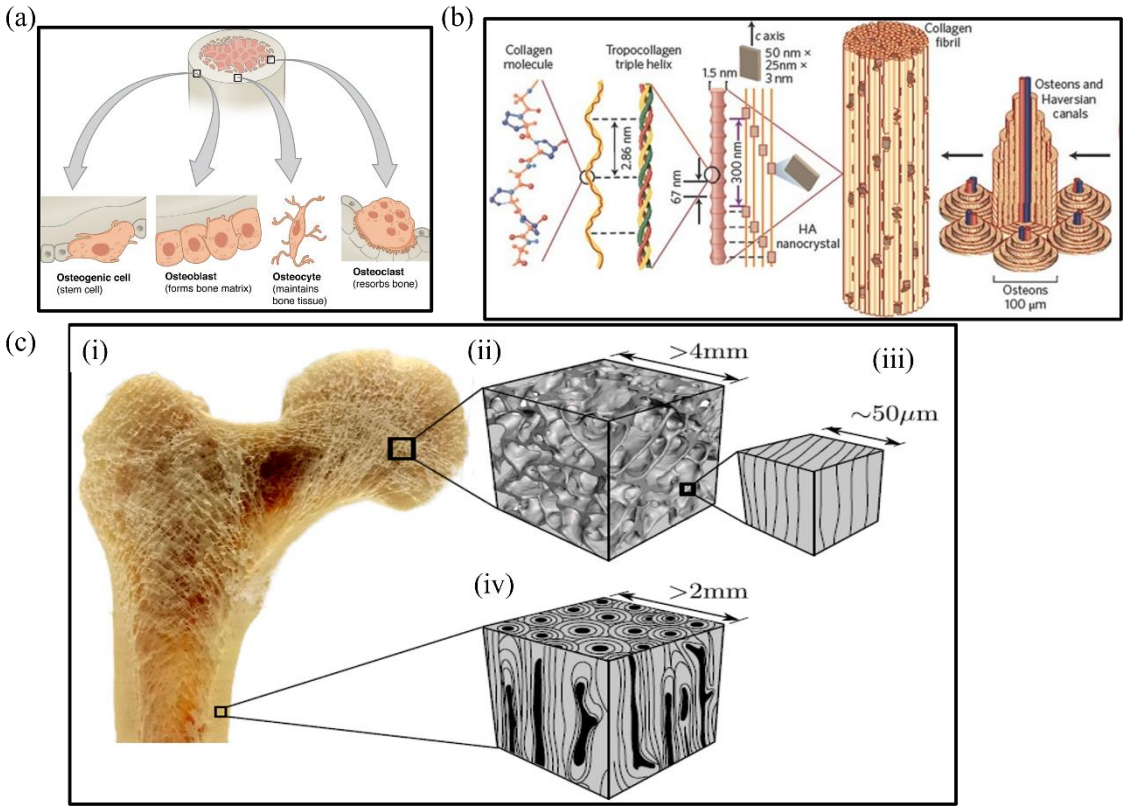

Figure 2.1: (a) Each bone tissue consists of four cell types: osteoblasts, osteoclasts, osteocytes and osteogenic cells (bone lining cells). (b) Type I collagen is an abundant protein consisting of polypeptide chains that fold into triple-helical tropocollagen molecules. Tropocollagen molecules self-assemble into microfibrils, which aggregate in longitudinal and horizontal directions to form collagen fibrils. The collagen fibrils' dimensions vary within the bone structure [42]. Osteoblasts precipitate calcium and phosphate through the action of alkaline phosphatase on the phosphate and calcium groups available. Stoichiometry of the precipitated calcium and phosphate is highly dynamic and often changes depending on the required osteoclast activity [23]. The multi-scale features at different organisational levels show bone as a complex arrangement of multi-scale tissues. (c) The morphological distinction between trabecular and cortical bone (i) representing the cross-section of the long bone (ii) internal morphology of trabecular bone structures (iii) arrangement of lamellae within the trabecular bone matrix (iv) arrangement of osteons in the cortical bone matrix [46].

Synthetic scaffolds used for BTE provide the template for tissue formation and stimulate bone tissue regeneration through interaction with ECM. Most importantly, scaffolds are meant to mimic the local niche of the tissue being regenerated. Mimicking the local niche requires a scaffold to facilitate angiogenesis for transporting critical nutrients, waste and

biomolecules to the synthetic scaffold [22]. Osteogenesis, coinciding with the above process, is augmented with the successful vascularisation of the synthetic scaffold. Physical attributes such as pore size, porosity, pore structure and interconnectivity of the scaffold are crucial factors in replicating the local microenvironments. Recent advances in the design of BTE scaffolds have enhanced in-vivo scaffold-tissue interactions Table A1 also shows that using multiple materials for fabricating these scaffolds is essential to simultaneously address both physical and chemical attributes necessary for an effective BTE scaffold.

2.3 Bone healing response

Bone healing is a complex regenerative process that relies on a cascade of events triggered by the body in response to the trauma. The cascade of events leading up to the formation of bone can be broadly divided into (1) an inflammatory phase, (2) a repair phase, and (3) a remodelling phase as described in Figure 2.2a [26]. Osteoblasts and osteoclasts formed as a response to this trauma are responsible for the propagation and termination of the bone healing response.

The inflammatory response is activated immediately after the trauma. It enables the recruitment of inflammatory cells and pro-inflammatory cytokines (Interleukin-1 (IL-1), Interleukin-6 (IL-6), Tumour necrosis factor Alpha (TNF-α), Chemokine ligand 2 (CCL2) and others) that assist in intercellular communication necessary for the initiation of bone healing [22, 47]. Previous studies have shown that, during this phase of bone healing, macrophages (M1 and M2) play a crucial role in recruiting inflammatory cells as well as upregulating the expression of bone markers such as Osteocalcin and Osteopontin in mesenchymal stem cells (MSCs) [48]. The MSCs differentiate into

osteoblasts, and osteocytes replace damaged tissue, as shown in Figure 2.2c. The pro-inflammatory M1 phenotype macrophages remain at the injured site for up to 4 days before transitioning into anti-inflammatory M2 phenotypes and reducing the inflammation at the injured site [49]. Simultaneously, osteoclasts in the vicinity of the fracture site resorb the bone fragments maintaining the net bone mass as shown in Figure 2.2b. Since the precise nature of the intercellular interactions between the macrophages and the osteoclasts are still unknown, it is unclear whether the macrophages directly or indirectly regulate this crucial step of bone resorption.

The repair or regeneration phase begins when the inflammation at the injured sites begins to reduce, indicating the increased presence of M2 phenotype macrophages. The M2 macrophages introduce growth factors such as IL-10, Transforming growth factor – beta (TGF-β) and Interleukin-1 receptor antagonist (IL-1Ra) to initiate a bone healing response (as shown in Figure 2.2b) [50]. Osteoblasts at this stage stimulate bone formation through intramembranous ossification and endochondral ossification [51]. Endochondral ossification involves the conversion of secreted collagen fibres into a soft woven callus. The soft callus gradually undergoes mineralisation through a process of hypertrophic differentiation, causing cartilage to bone transition [51].

On the other hand, intramembranous ossification causes the direct conversion of secreted collagen fibres into a hard callus. However, to complete the repair phase, the fractured ends must be integrated with the implanted scaffold (osseointegration). Any misalignment can lead to fracture non-unions and subsequently lead to re-fractures. Eventually, the osteoblasts are completely covered with a mineralised matrix as shown in Figure 2.2d and are termed as osteocytes [51, 52]. Presence of these osteocytes are critical

for long-term bone remodelling or functional adaptation of bone in response to specific mechanical stimuli [53].

The remodelling phase during the bone healing process represents the balance between osteoblastic and osteoclastic activity. The osteocytes described previously function as mechanical transducers that convert mechanical stimuli during the loading of the bone to initiate the remodelling processes [53]. Activation of the bone healing process allows the osteoclasts to migrate to a particular site and begin the process of bone resorption. This process usually lasts up to 2 – 4 weeks, after which the osteoclasts undergo apoptosis ceasing the process of bone resorption [51, 54]. Cavities formed because of resorption then function as sites of new bone formation. Osteoblasts, monocytes and pre-osteoblasts present in these cavities assist in forming the new bone matrix, similar to the process described in the repair phase [54, 55]. The remodelling process is also a physiological process that generally occurs with age as well as a response to metabolic activity. While the healing mechanism remains the same for both cortical and trabecular bone, differences lie in their respective bone balance (amount of bone formed minus amount of bone resorbed) [54]. Bone balance in cortical bones is slightly positive, whereas it is negative in trabecular bone. Therefore, progressive loss of trabecular type bone with age, metabolic activities and mechanical stimuli can lead to unique structural outcomes in different patients.

The above-mentioned processes (inflammatory response, repair and remodelling) can only occur due to the presence of the extracellular matrix (ECM). The ECM has a unique composition based on the tissue type, bone tissues generally consist of an ECM containing 40% of organic (type 1 collagen, non-collagenous proteins) and 60% of inorganic compounds (calcium deficient apatite and other trace elements), respectively [56].

However, this composition generally varies based on sex, gender and health conditions. In bone tissues the primary source of ECM is from osteoblast cells prior to mineralisation. Bone cells within this ECM use specific glycoproteins (osteonectin, thrombospondins, R-spondins, small integrin-binding ligand N-linked Glycoproteins (SIBLINGS), TGF-β to enable functions such as bone remodelling, differentiation (of MSCs) and maintaining bone mass [56]. The collagen present in the ECM provides a matrix for the osteoblast cells to be deposited, which on further deposition of cells form structured bone tissues [57]. Bone remodelling is also a crucial process in addition to bone formation, these functions are performed by osteoclasts present in the bone tissue. Changes in the stiffness of the ECM surrounding osteoclasts cells regulate the expression of dentin matrix protein-1 (DMP1), which affects osteoclast attachment allowing the commencement of remodelling [58]. Therefore, mechanical stimuli are sensed by the osteocytes through glycoproteins such as DMP1 present in the ECM.

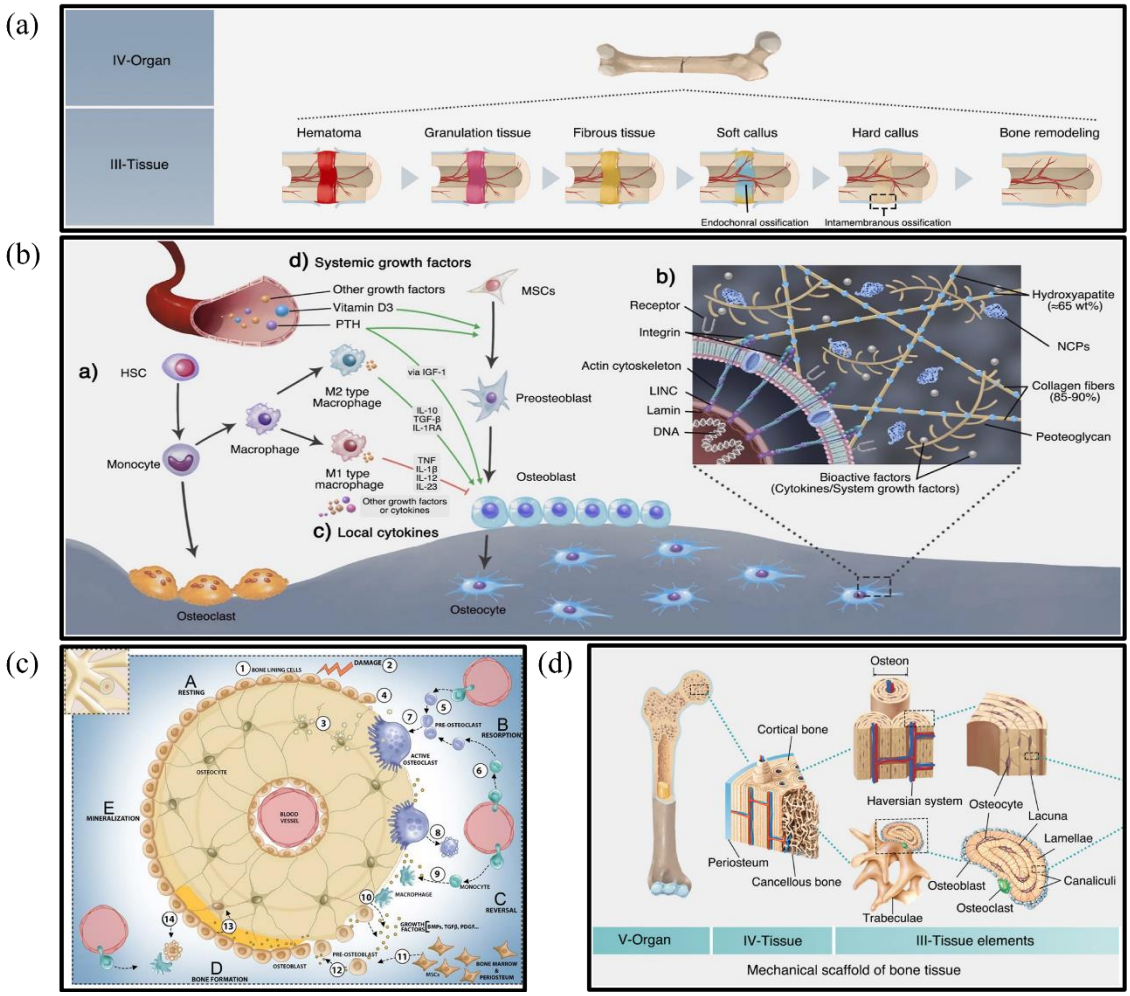

Figure 2.2: (a) Bone healing can be broadly divided into three processes; inflammation, repair and remodelling. The actual repair process can be broken down into 5 steps. These steps include hematoma formation, granular tissue formation, fibrous tissue formation, formation to soft callus and formation of hard callus. The formation of a hard callus at the fracture site marks the termination of the bone healing step and begins the remodelling process. (b) Cascade of cellular interaction between the monocytes and the MSCs through growth factors and cytokines lead to differentiation of MSCs responsible for the bone healing response. (c) As shown, the process of bone formation is described in several stages A, B, C, D and E. (A) In response to tissue damage, osteocytes undergo apoptosis, and bone lining cells detach from their surface and initiate resorption. (B) Active osteoclasts promote the mineralisation of bone tissue and the resorption of broken bone fragments. Once resorption is complete, the osteoclasts undergo apoptosis. (C) Macrophages differentiated from monocytes along with other growth factors ad cytokines initiate the differentiation of MSCs to osteoblasts. (D) Osteoblasts produce a non-mineralised matrix and transform into osteocytes after being full surrounded by mineralised bone tissue. (E) Matrix deposited by the osteoblasts undergoes mineralisation, and surface osteoblasts remain as bone lining cells [59] (d) location of multiple tissue elements of cancellous and cortical bone [51].

2.4 Biomaterials for bone tissue engineering

Metals, ceramics, and polymer classes of materials individually offer unique properties necessary for initiating and sustaining bone healing processes [27]. However, bone healing processes require materials that enable the adsorption of specific proteins, interact with local extracellular matrix (ECM) through the exchange of ions and attract specific biomolecules or growth factors. Based on the type of interaction, materials used for manufacturing scaffolds can be classified into three types, bioinert, bioactive and biomimetic, as shown in Figure 2.3a. Their differences in interactions from a material perspective can be narrowed down to surface chemistry, roughness, solubility, and crystallinity.

Interactions with ECM primarily occur after protein adsorption has occurred, and the nature of proteins adsorbed onto the material surface will determine the physiological response initiated by the body [20]. Positive interaction with the host tissue will enable the bone healing cascade to progress, as described previously in section 2.2. The release of the ions can initiate the release of growth factors VEGF and BMPs, as shown in Figure 2.3b. On the other side, unsuitable materials initiate a foreign body response where fibrin is preferentially adsorbed onto the implant's surface. This specificity in adsorption could be due to surface charge, wettability, chemical composition, and protein structure [20]. As previously mentioned, neutrophils present in the local area of the implant attract monocytes to the fibrin-dominated implant surface. The monocytes recruited undergo differentiation into macrophages (type M1), releasing pro-inflammatory factors such as TNFα, IL-6, and IL-8. These macrophage populations at the injury site encapsulate the surface with a fibrous tissue, as shown in Figure 2.3c [19].

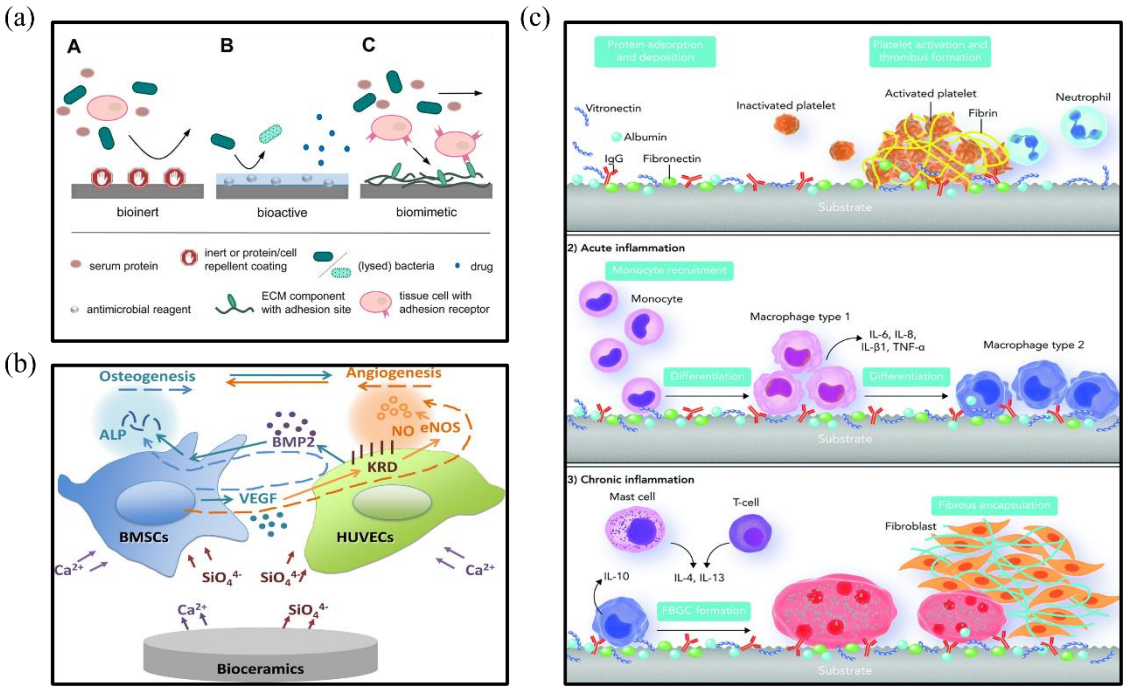

Figure 2.3: (a) Materials based on the nature of interaction can be classified into bioinert, bioactive and biomimetic. Bioinert materials repel or do not interact with ECM proteins. When implanted inside the body, bioactive materials can release biomolecules, enabling interaction with ECM through biomolecule uptake. Biomimetic surfaces can mimic naturally found tissues in the body, allowing cellular interactions through surface-bound ECM proteins [20]. (b) The exchange of ions at the interface of bioceramic – ECM initiates osteogenesis and angiogenesis at the implanted site. Mesenchymal stem cells present in the ECM undergo specific differentiation into osteoblasts and osteocytes in the presence of specific biomolecules. Osteoblasts initiate bone formation leading to an upregulation of alkaline phosphatase (ALP) activity. Osteoclasts regulate bone formation and assist in their constant remodelling.[60] (Reproduced with permission from Ref.[60]. Copyright 2022 Elsevier.) (c) Foreign body response to implanted material, as shown here, occurs in three stages involving (1) non-specific protein adsorption, (2) monocytes recruited at the local site induce inflammation and differentiate into type 2 macrophages, (3) Type 2 macrophages along with T cells and Mast cells increase the number of foreign body giant cells. Fibroblasts recruited by the FBGCs cause collagen deposition around the implant surface, forming a thick fibrous layer [19].

Some commonly used materials used in BTE scaffolds are shown in Table 2.1. This section will discuss the cellular interactions occurring while materials are in contact with the local ECM.

Table 2.1: Biomaterials commonly used for BTE applications.

Material type	Materials
Ceramics	Calcium phosphate ceramics (HAp, α-TCP, β-TCP and BCP), ZrO_2, black akermanite (Ca_2MgSiO_7)
Polymer	Polylactic acid (PLA), Polyurethanes, Polyethylene glycol (PEG), Polyglycolid (PGA) and Poly Caprolactone (PCL), Polyether ether ketone (PEEK), Collagen, Chitosan, Alginate, Hyaluronic acid
Metals	Stainless steel, Titanium alloy (Ti6Al4V), Tantalum, Magnesium, cobalt-chromium alloys
Bioglass	Acidic oxide bioglasses and Basic oxide bioglasses, 45S5 Bioglass, Borate based bioglasses (BBG)

2.4.1 Ceramics

Ceramics have been used in biomedical applications primarily due to their inertness, hardness, and abrasion resistance [61, 62]. For example, 3Y-ZrO_2 has been extensively used in dental crowns and bridges due to its inert nature, mechanical and tribological behaviour [63, 64]. Femoral heads of hip replacement joints, which were previously made from metals, are being replaced by ceramics (alumina, zirconia, zirconia toughened alumina or silicon nitride) due to their superior tribological properties and wear resistance [65]. These ceramics discussed here are, fully capable of satisfying the mechanical requirements of the above-described applications however their inert nature prevents any interaction with the body.

The only ceramics capable of interacting with the body include bioglasses and calcium phosphate-based ceramics. Bioglasses are synthetic vitreous materials chemically similar to natural bone mineral. They are known to undergo rapid degradation forming hydroxyapatite (HAp) on their surface, leading to biological fixation [66]. More recent studies have identified techniques to tailor these degradation rates to the growth of the tissue [67]. While they are superior to phosphate-based ceramics in their ability to interact with the body, they lack the mechanical properties to provide support, making them unsuitable to be used on their own [67]. Calcium phosphate ceramics (CPCs) used for BTE scaffolds are known to be osteoinductive and osteoconductive. The bone healing effect of the CPCs is strongly dependent on the Ca/P ratios, crystallinity, and composition. CPCs with a Ca/P ratio of 1.5 are highly soluble in aqueous environments causing the release of Ca^{2+} and PO_4^{3-} ions, so a carbonated apatite layer forms over the surface. CPCs such as hydroxyapatite possess a stoichiometric ratio of 1.67, making them more stable and, therefore, less soluble in the aqueous environment of the body [26]. Therefore, bioceramics enable protein adsorption and communication with the local ECM through a solution-driven and cell-mediated process. While the exact nature of this communication with the ECM is still unknown, the process is highly dependent on the type of proteins adsorbed onto the surface of the ceramic [19]. Therefore, to modify this property, CPCs are doped with cationic or anionic impurities to alter their dissolution rate and stability or improve biological functionality. Table 2.2 shows how functionality of certain CPCs has been improved by doping.

Table 2.2: Effects of cationic and anionic dopants in CPCs on their cellular interactions.

Calcium Phosphate ceramics	**Dopants**	**Biomedical properties**	**Ref.**
BCP	Cu	• Controlled release of Cu^{2+} ions • The release of Cu^{2+} ions introduced an anti-microbial effect • Cu^{2+} increased angiogenesis at the injured site by enhancing the hypoxia-like tissue reaction	[68, 69]
BCP	Mg	• Increased rate of apatite formation in the presence of Mg^{2+} ions • Mg^{2+} ions upregulate Fibroblast growth factor (FGF23) through elevation in Runx2, osteocalcin and osterix expression. • Higher integrin receptor affinity to Mg^{2+} ions improved cell adhesion to the doped microscaffold • Collagen secretion and ALP activity was absent	[70, 71]
β-TCP	Mn	• Increase in protein adsorption capacity • Increase in expression of ALP, Runx2, type 1 collagen and osteocalcin • Optimal concentration of Mn^{2+} ions must remain below 7.17 μg/L to observe improvement in mBMSC proliferation and promote early-stage differentiation	[72, 73]

		• Mn^{2+} and Mn^{3+} ions are responsible to limit the accumulation of ROS* species at inured site	
HAp	Sr	• Higher expression of Type 1 collagen and BMP compared to pure HAp • Could be toxic to cell at high concentrations • Increased formation of bone compared to HAp • Inhibited osteoclast activity thereby producing increased bone formation	[74]
HAp	CaF_2	• Enabled rapid formation of apatite layer when soaked in simulated body fluids • Showed good stability in the Ca/P ratio after immersion in SBF fluids • Micropore formation due to dissolution of F-HA coating enhanced osteogenesis and ion exchange • ALP activity showed a significant increase at early stages of soaking	[75]

*The role of reactive oxygen species (ROS) are still an active area of research and therefore future research will determine their necessity in bone healing pathway. Note: Biphasic calcium phosphates (BCP), tri-calcium phosphate (TCP), hydroxyapatite (HAP), Ostoegenic – related transcription factor (osterix).

The low mechanical strength and brittle nature of CPCs still make them unsuitable for use in load-bearing areas [76]. To enhance their structural strength, they are used in combination with polymers, metals and other ceramics which are termed multi-material scaffolds. Incorporation of more than one material can be achieved in several ways such

as homogenous mixtures, polymer matrix composites, coatings, ceramic matrix composites and in the form of layers.

2.4.2 Polymers

Polymers used for BTE can be further classified into natural or synthetic, based on their source. As shown in Table 2.3, alginate, chitosan and collagen are natural polymers that are used for BTE applications. Natural polymers tend to elicit a positive response during ECM interactions due to their ability to easily bind proteins to their surfaces and their similarity with tissues found naturally in the body [77]. For example, type 1 collagen is a constituent of bone, as described in previous section 2.2. However, its low structural strength, difficulties in processing samples, and the potential risk of disease transmission restrict its usage in BTE applications [78]. Synthetic polymers such as polylactic acid (PLA), polycaprolactone (PCL), polyglycolic acid (PGA) and polyurethane (PU) can address the above limitations of natural polymers as the hydrophobic nature of these polymers prevents protein adsorption and requires direct interactions with extra cellular matrix to induce a bone healing response [79]. Therefore, polymers are often functionalized with natural proteins or peptides such as RGD, YIGSR and IKVAV to enhance cell attachment and proliferation [17].

Polymers such as PLA, PGA and PCL undergo degradation through hydrolysis of the ester linkage, lasting anywhere between a few months to years depending on the polymer's crystallinity, composition, and hydrophilicity. Degradation times of 3 – 6 years, 1 – 2 years and 3 – 4 months are typically observed for PLA, PCL, and PGA, respectively [80]. Degradation of the polymer occurs when the scaffold is in contact with ECM causing physiological and mechanical changes to the implanted scaffold. For example, hydrolysis of PGA leads to increasing local pH slowing down the process of osteogenesis [81]. In

addition to hydrolysis of the polymer, proteins, biomolecules, growth factors and peptides bound to the polymer surface are critical to initiate a bone healing cascade [82]. Table 2.3 highlights the effects of using secondary phases/polymers to functionalise polymer scaffolds. Further, these bioactive polymers can be used as carriers of growth factors and biomolecules to aid bone healing [83]. Polymer scaffolds can be biologically effective as BTE scaffolds; however, the insufficient mechanical strength of polymers, along with increasing porosity, make them unsuitable for use in load-bearing areas [27].

Table 2.3: Function of secondary phases used along with polymer composite scaffold and its implications on their cellular interactions.

Primary polymer	**Secondary polymer/phase**	**Biomedical property**	**Ref.**
PCL	Bioglass and GelMA	• Enhanced hydrophilicity of PCL scaffold • Reduction of contact angle to less than 40° • Increased protein adsorption • The release of Na, Si, and Ca ions present in bioglasses assist in mineralization and initiating the bone healing cascade • Negative surface charges increased the rate of bone mineralization	[82]

Citric acid-based polymer	HAp	• Upregulation of ALP activity and Osterix gene expression • Citrate molecules assist in bridging mineral platelets improving bone crystallinity (improving bone strength)	[84, 85]
PLA	Polydopamine (PDA) and Type 1 collagen	• Up to 92% increase in type 1 collagen immobilization on the polymer surface • Increased cell proliferation after seven days of culture • The presence of PDA enhanced metabolic activity • 3D infiltration of ECM was achieved due to covalent immobilization of ECM proteins • Presence of PDA enables covalent immobilization of biomolecules such as BMP-2, VEGF and RunX2	[86, 87]
PCL	Gelatin, bacterial cellulose and HAp	• Increased proliferation and attachment due to the inclusion of natural polymers	[88]
Chitosan	AgNP	• Chelation with silver ions improved the degradation rate of chitosan • An antibacterial effect was observed due to the presence of silver nanoparticles	[89]

		• Upregulation of RunX2 and increased Alp activity	
PLGA	TiO_2	• Increased mechanical strength • Increased protein adsorption • TiO_2 nanoparticles aid in the precipitation of bone-like apatite • In-process formation of calcium titanate leads to high osteoblast adhesion • Increased attachment sites for binding bioactive receptors • The presence of TiO_2 leads to accelerated hydrolytic degradation	[90]
PVA and Chitosan	Carbonated Hap (CHAp)	• The occurrence of carbonated HAp nanoparticles was identical to that of natural bone • Reduced polymer crystallinity due to the presence of amorphous interfaces • The increase in mechanical strength was less than 30% • Reduced elongation due to accumulation of HAp nanoparticles on polymer fibre • The presence of CHAp increases the number of favourable sites for the protein adsorption • Interaction of Ca^{2+} and PO_4^{3-} ions leads to bone mineralization	[91]

PVDF	Graphene oxide	• Increased mechanical performance due to graphene oxide reinforcement • Increase in hydrophilicity due presence of hydroxyl functional groups • Electro-mechanical stimulation of scaffolds showed upregulation in ALP activity	[92]

2.4.3 Metals and alloys

Metals commonly used for BTE are bioinert, i.e., they do not initiate a foreign body response when implanted [27]. These metals and alloys include titanium alloys, tantalum alloys, magnesium alloys and zinc. The use of these metals and alloys for BTE application could be in the form of bulk materials, nanoparticles or both. Functionalities observed based on the distinction in their form are vastly different [27, 93]. However, the critical issue in the utilization of metal alloys in their bulk material form is the mismatch in mechanical properties with natural bone. The mismatch in load-bearing capacities can cause resorption of bone in the surrounding areas of the implant leading to loosening or complete failure in attachment [27, 52]. Further, the bioinert nature of some metals and alloys in bulk and nanoparticle form limits their ability to interact positively with the local ECM and initiate a bone healing response [93, 94].

Titanium alloys are commonly used for orthopaedic applications primarily due to their bioinert qualities [94]. To functionalize these metal alloys for BTE applications, alloying elements such as Zr, Nb, Al and V are added to improve the interaction with the local niche and improve corrosion behaviour [95, 96]. Previous studies utilising Nb and Zr

additions to Ti alloys have shown increased ALP activity and reduced cytotoxicity [96, 97].

Bioresorbable metals such as Zn, Fe and Mg are recently becoming more popular for BTE applications. Zn has recently been a popular material for usage in BTE applications because of its nominal degradation rate and the importance of Zn finger proteins (ZFPs) in the human body as DNA binding transcription factors responsible for the regulation of numerous cellular processes [98, 99]. Zn, when implanted, undergoes degradation due to galvanic coupling, releasing Zn ions which further interact with Ca^{2+} and PO_4^{3-} ions present in the simulated body fluids (SBF) [99]. However, the uptake of Zn ions within the body is limited to about 15 - 40 mg/day [99, 100]. Therefore, degradation of the scaffold needs to be adjusted to not exceed this physiological limit.

Magnesium, like Zn, is bioresorbable in nature and the major difference lies in the degradation rate. Degradation of Mg within the body occurs rapidly, leading to a release of hydrogen gas (H_2) [101]. The release of H_2 gas was shown to interrupt the bone healing cascade due to the increase in local pH of the surrounding area [102]. Even with these limitations, Mg is used as a prospective material for bone replacement due to the similarity of its mechanical strength to that of bone and the importance of Mg ions for physiological functions within the body [101].

Nanoparticles used along with other bioactive materials can impart osteogenic or other properties necessary to initiate and sustain the bone healing cascade [93]. The most commonly used nanoparticles include gold (AuNP), silver (AgNP), iron, aluminium, copper, zirconium and hydroxyapatite nanoparticles [93]. Low dosages of AuNP have been shown to function as synthetic replacements for bone morphogenic proteins (BMP),

that are directly responsible for regulating bone mass through Wnt/β-Catenin signalling pathways [103]. Silver nanoparticles are known for their bactericidal effects, being able to penetrate the bacterial cell wall and damage their DNA [93]. Titanium oxide nanoparticles are commonly used in BTE applications through addition into polymer scaffolds. The addition of these nanoparticles has been shown to improve the wettability and mechanical properties of the resultant polymer scaffold [90].

2.5. Multi-material scaffolds

Multi-material scaffolds involve using two or more materials in the form of homogenous mixtures, discrete structures, doping agents or surface coatings. Depending on the nature of the combination, the properties of the composite can be significantly different. For example, nano-HAp, when homogeneously mixed with zirconia-based scaffolds, can function firstly as a bioactive site and, secondly, improve mechanical strength by delaying crack propagation [104]. Scaffolds with nano-HAp coatings on Ti alloys enable interaction with the ECM to improve osseointegration but do not contribute to the strength of the material due to its weak surface adhesion [105]. Bioglasses (BG) as previously described, are highly bioactive and could assist in early osteointegration. As a result BG coatings are applied on stainless steel, Ti-6Al-7Nb, nitinol and other biocompatible alloys [106]. Multi-material scaffolds have more recently seen application as drug delivery devices, which has become possible with the combination of organic and inorganic biomaterials. Chitosan-HAp based scaffolds have been shown to function as therapeutic metal ion delivery vehicles of strontium and copper ions. The strontium-substituted HAp functioned as a source of Sr ions, which are known to enhancing bone formation and influencing gene expression of osteoclasts [107, 108]. The chitosan polysaccharide, being the carrier of copper ions, inhibited the replication of bacteria due to the initial burst

release of Cu ions [107, 109]. The inclusion of natural polymers in bioceramic scaffolds is still a challenge due to the high post-processing temperatures required to increase the mechanical strength of ceramic materials. The inclusion of starch-based natural polymers into HAp-polycaprolactone-based composites has been shown to improve the mechanical properties by functioning as a binder [110, 111]. Further, the presence of starch increased the degradation time of these scaffolds. Preventing increased surface degradation allows cellular growth and adhesion which are essential in BTE scaffolds [111]. Materials used on their own are more likely to be unsuitable for BTE applications due to their inherent limitations, thus, combining them to form composites can help overcome the limitation described above. Therefore, recent studies have explored multi-material scaffold for BTE applications [2, 112, 113].

Including a secondary phase in the form of nanoparticles, doping agents or uniform mixtures can influence the composite's chemical nature; the processing methods of composites are also known to have similar effects. For example, processing magnesium alloys containing nano-BG particles using the powder metallurgy technique has been shown to introduce intermetallic Mg_2Si and MgO phases that lead to rapid *in-vitro* degradation of the magnesium-based composite [114]. However, processing the same composite using spark plasma sintering (SPS) prevented the formation of intermetallic phases and the retention of nano-BG within the matrix of the magnesium alloy reduced *in-vitro* degradation and improved cell viability [115, 116]. Therefore, simultaneously processing these materials will pose challenges in creating multi-material scaffolds.

2.6. Scaffold structure

The porous architecture of BTE scaffolds is characterised by 4 factors: (1) porosity (%), (2) pore size, (3) surface area and (4) interconnectivity as shown in Figure 2.4. Porosity

refers to the volume percentage of free space present within the scaffold architecture. Pore sizes refer to the average dimensions of the pores present in the scaffold. Surface area of the scaffold is a function of pore sizes present on the surface and porosity of the scaffold. Interconnectivity of the scaffold is a function of the spatial location of the pores, their sizes and porosity and determines the extent of cell infiltration and nutrient transport achievable when the scaffold is implanted inside the body.

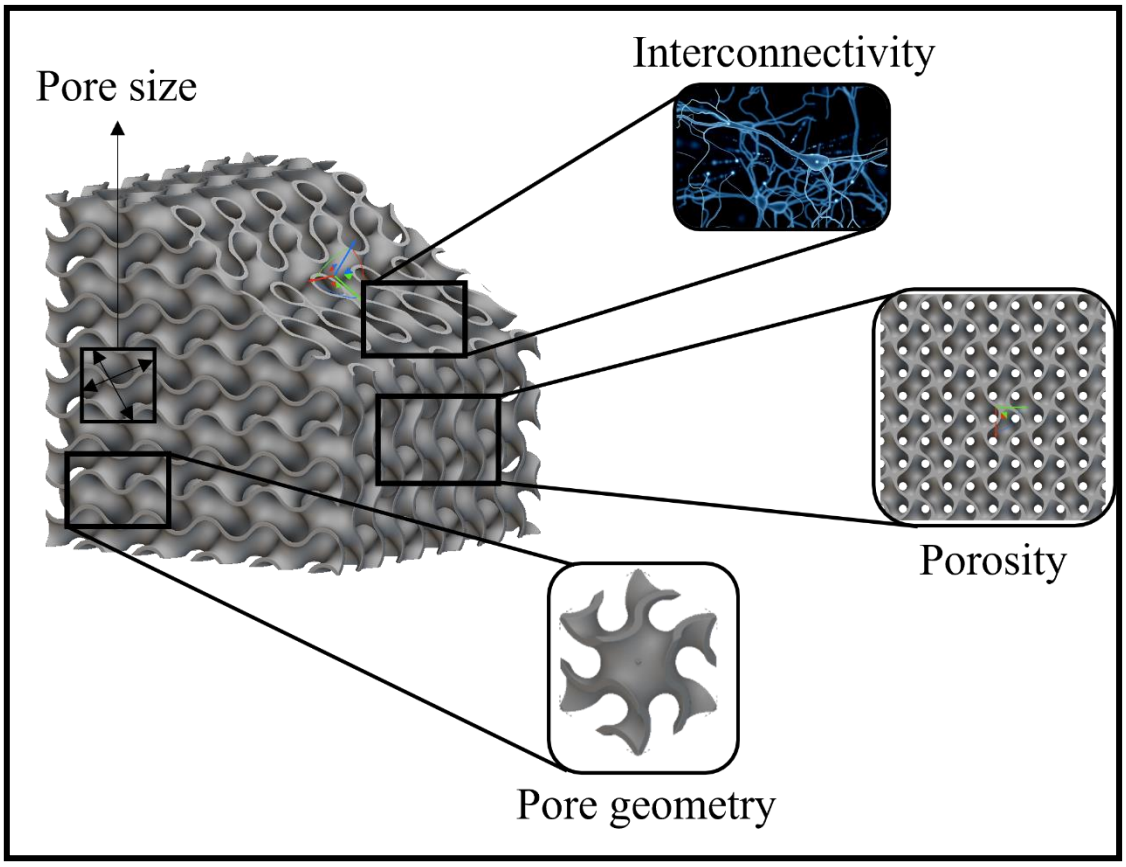

Figure 2.4: Description of the features of a porous scaffold used for BTE. Pore sizes refer to the diameter/dimension of the pore. Porosity of the scaffold refers to the ratio of the total pore volume to the volume of the scaffold. Pore geometry refers to arrangement of pores within the scaffold. Interconnectivity of the scaffold refers to the number of paths connecting the pores present in the scaffold.

2.6.1. Pore size

Pore size of the scaffold is a critical parameter that determines the extent of infiltration achievable and its mechanical strength. Figure 2.5a shows that an increasing pore size is inversely proportional to the compression strength of these porous scaffolds and, therefore, pore size must be carefully chosen to allow for fluid ingress and provide strength. Pore sizes commonly used in BTE scaffolds vary between 100 and 900 μm [117]. Osteoblast cells (10 – 50 μm in size) prefer pore sizes greater than 300 μm as this enables infiltration of biomolecules and transportation of nutrients and waste [2, 118]. Increasing pore sizes has also been shown to reduce the water contact angle, enabling higher fluid ingress when implanted within the body [119].

Bone in-growth within the scaffold during the healing process is critical to ensure load transmission and fixation of the scaffold to the natural bone. Smaller pore sizes (200 – 300 μm) and limited space for infiltration is known to induce chondrogenesis of the mesenchymal stem cells leading to the formation of cartilaginous tissues as opposed to bone tissue [120].

Optimal pore sizes for in-growth have been shown to be within the range of 250 – 500 μm [28, 121, 122]. The inclusion of large pores, while beneficial for functionalising the scaffold, can reduce the strength of the scaffold affecting their structural capacity [123]. However, smaller pores (≤ 100 μm) cause fibrous tissue formation around the scaffold, which physically prevents angiogenesis and any interaction with the scaffold surface [2]. Previous studies have shown that micropores (within 10 μm) increase the available surface area, promoting ion exchange and bone protein adsorption [124, 125]. These results indicate that different pore sizes impart unique physiological and structural

properties to BTE scaffolds. Thus, heterogeneity in pore sizes can simultaneously enable multiple features critical for bone healing [126].

2.6.2. Porosity

The porosity of the BTE scaffold is a function of pore size and geometry of the scaffold, when implanted the porous volume of the scaffold houses osteoblasts cells and functions as a site for cellular interaction. Scaffolds used for BTE application have porosities ranging from 50% to 80%, depending on the required mechanical performance. Higher porosities (greater than 65%) allow greater infiltration of ECM but reduce the structural capacity of the scaffold as shown in Figure 2.5 [4]. Higher scaffold porosities provide larger surface areas ensuring greater interaction with the ECM [127]. This promotes faster degradation or bone ingrowth and assists in vascularisation [120]. Further, continuous contact with ECM will lead to pore occlusion over time, therefore, larger porosities present in the scaffold will ensure sufficient permeability for the transport of nutrients and biomolecules. Porosities below 65% provide higher mechanical strength while reducing the ability to interact with the ECM. The reduced ECM interaction and lack of cell spreading reduces the ALP activity of the cells.

Permeability is a critical requirement, which is influenced by the porosity and interconnectivity of the porous scaffold. The required extent of permeability will depend on the size of the defect, larger defects require a greater supply of oxygen and nutrients for the process of bone healing to proceed [128]. For example, cell proliferation studies performed on a 3D printed stainless steel scaffold with a porosity of 58% showed higher cell proliferation and growth compared with scaffolds with 60% and 70% porosity. The higher cell proliferation and growth at the lower porosity was due to its ability to retain

the cell media for longer compared to scaffolds with 60% and 70% porosity [129]. Therefore, the nature of porosity can also influence the bone healing behaviour. A highly open porous scaffold, while good for promoting angiogenesis, can have reduced ability to promote cell growth and proliferation.

2.6.3. Scaffold geometry

Scaffold geometry refers to the arrangement of pores within the scaffold matrix. The scaffold geometry observed in BTE scaffolds can be classified into two types based on the orientation of their structure as randomised and regular. Randomised orientation refers to scaffolds which lack any repeating units. While these structures tend to mimic the natural bone morphology [130], their random orientations create inconsistencies in scaffold compression strength and are extremely difficult to replicate [131, 132]. Scaffolds with regular orientations include cubic, hexagonal, triply periodic minimum surfaces (TPMS), spherical and honeycomb arrangements. While these structures are not directly responsible for bone healing, their ability to ensure vascular growth, nutrient diffusion and load-bearing ability make them an ideal choice [133-135]. TPMS structures have recently become a popular choice for use in BTE scaffolds because of their ability to ensure the ideal combination of stiffness and permeability [136, 137]. Yanez et al. [138] showed that gyroid-based scaffolds used for bone defect reconstruction showed compression strengths within the range of human trabecular bone (1.5 – 45 MPa) at porosities of 75% and 90%. Further, the layer-by-layer collapse of the scaffolds and the elliptical strut shape oriented in the direction of load provided a high stiffness and strength to the scaffold. It also indicated the significant differences in plastic deformation at 45° loads when compared to axial loading [138]. Thus, load direction must also be considered when selecting scaffold geometry. Since the effect of pore geometry on bone healing

response is a function of porosity, pore sizes, interconnectivity and surface area, isolating the effects of pore geometry can be challenging. However, its influence on mechanical properties can be clearly isolated as shown in previous studies [139-141], hence the most common approach involves analysing bone healing behaviour based on scaffold features (pores size, porosity and interconnectivity) while the mechanical properties are explored via the influence of pore geometry.

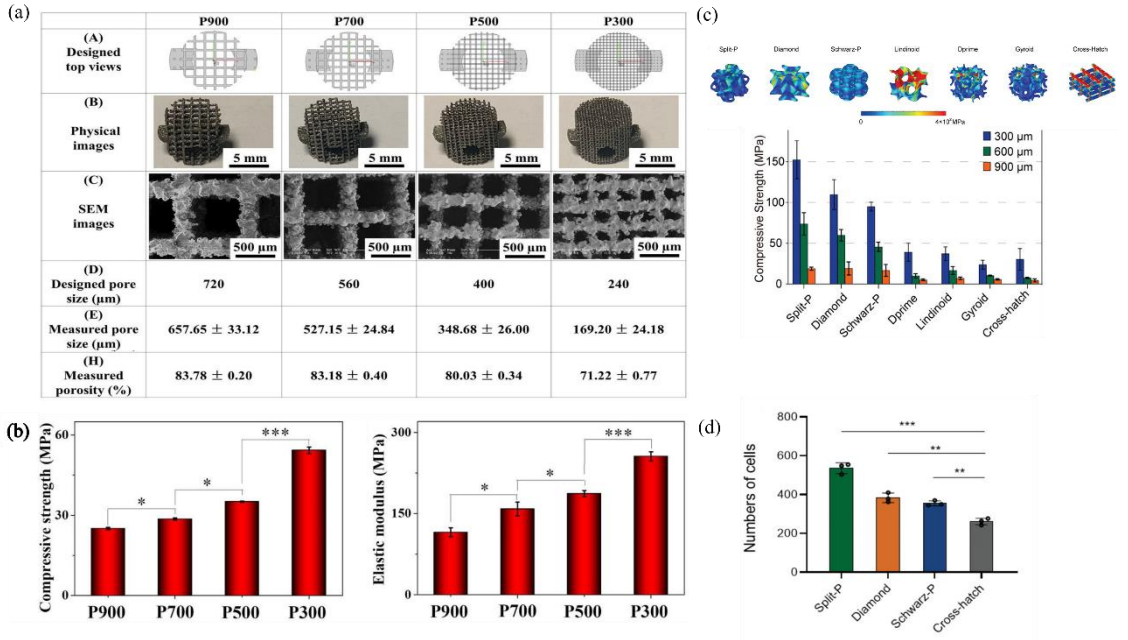

Figure 2.5: (a) Cylindrical Ti-6Al-4V scaffolds fabricated using selective laser melting (SLM) at 4 different pore sizes and struct thickness values [142]. (b) Increasing pore sizes from P300 to P500 shows a significant reduction in compression strength. Compression strength of P500, P700, and P900 scaffolds remained similar. There was a gradual decrease in elastic modulus with increasing pore sizes. (c) Pore geometries (gyroid, split-P, diamond, schwarz-p, lindinoid D-prime, cross-hatch) showed varying stress distributions when loaded. The split-P, diamond and schwarz-P structure showed low stress concentration while the lindinoid and cross-hatch structure showed high stress concentration on the scaffold surface. Split-P structure showed the highest compression across all pore size ranges (300 µm , 600 µm and 900 µm) while the cross-hatch and gyroid structure showed lowest compression strengths at all pore sizes [143]. (d) The interconnected nature of TPMS structures allowed for increased cell migration throughout the porous volume which is reflected in its higher cell density compared to the cross-hatch structure [143].

2.6.4. TPMS structures

Minimal surfaces can be defined as surfaces with a zero mean curvature and possessing the least surface area within the bound area. When these surfaces are periodically repeated along any three axes they are termed triply periodic minimal surfaces. The implicit functions of these structures can be defined using the trigonometric functions, unit cell length and type of unit cell [144]. Due to this they can be modified using the variables described in Table 2.4. The three basic types of TPMS structures include the primitive type (P-type), gyroid type (G-type) and diamond type (D-type).

Table 2.4: Mathematical equations describing triply periodic minimum surface structures where 'w' represents 2π/l, l represents the unit length of the unit cell and c represents the level-set function.

TPMS structure	**Equation**	**Ref.**
Gyroid	$\cos(wx) + \cos(wy) + \cos(wz) = c$	[144, 145]
Diamond	$\sin(wx)\sin(wy)\sin(wz) + \cos(wx)\sin(wy)\sin(wz) + \sin(wx)\cos(wy)\sin(wz) + \sin(wx)\sin(wy)\cos(wz) = c$	
Primitive	$\cos(wx) + \cos(wy) + \cos(wz) = c$	

Mechanical strength and energy absorption of TPMS structures have been shown to be more reliant on the type of structure rather than the material itself. P-type structures exhibited a fluctuation in stress at the plateau stage due to localised buckling of curved walls. Failure in these uniform P-type structures initially occurred perpendicular to the applied load which represents the first peak on the stress-strain curve while the remaining fluctuations arose from the gradual buckling of the P-type unit cell [146]. Thus, the stress-

strain response can be altered by changing the geometry and thickness of the P-type unit cell structure.

Gyroid-type structures, having an unconnected porous structure, prevent propagation of microcracks making them structurally stronger than the P-type TPMS structures [146, 147]. Diamond-based TPMS structures have been shown to provide the highest mechanical strength when compared to P-type and G-type structures. Stress-strain response of diamond-based structures showed a significant change in plateau stress when changing from a sheet-diamond to a skeletal diamond [148]. Skeletal-diamond structures undergo a single diagonal shear when applied stress exceeds peak stress, while a sheet-diamond requires the formation of a double shear band for failure to occur [149]. Allowing for greater energy absorption and, hence, higher toughness of the sheet-diamond structure [148, 149].

Interconnecting and non-penetrating architecture of TPMS structures are very common in biological systems due to its ability to fulfill unique requirements demanded by the cellular functions [144, 150]. The concave surfaces of TPMS structures promote osteogenic cell differentiation compared to scaffolds with flat or convex surfaces. For example, an HAp scaffold with a split-P architecture was showed to be more favourable in the formation of new bone compared to HAp scaffolds with the cross-hatch architecture when implanted into rabbit joints [143]. Bone growth was shown to begin at the outer surfaces of scaffold and continue inwards and the interconnected architecture of the split-P scaffold enabled the complete recovery of rabbit femur within 12 weeks [143]. The architecture of these structures (pore size, porosity and geometry) will influence the mechanical strength, permeability and cellular growth. Similar to natural bone structures, there is hierarchical distribution of structural features as shown previously. In order to

mimic this natural environment, scaffolds need to have an ordered arrangement of features that provide the ideal combination of mechanical strength, stiffness and permeability.

2.6.5. Hierarchical structures

Hierarchical structures involve the use of a combination of pore sizes, porosities, and pore geometries. As described previously in section 2.4, differences in these critical scaffold features can elicit vastly different responses during the bone healing process since bone healing involves a cascade of signalling pathways that are based on the scaffold – ECM interaction. The presence of multiple pore sizes and geometries thus become essential features for BTE scaffolds.

Xu et al. [151] showed that 3D printed bioceramic-silk composite scaffolds showed an increase in recruitment of BMSCs and expression of the osteogenic markers, OPN, BMP 2 and RUNX2. Cell attachment rates during the first 7 days were the highest in the prepared hierarchical scaffold. While larger pore sizes of greater than 100 μm enabled full infiltration of ECM, mesopores ranging between 50 – 100 μm at the silk fibroin prevented cell leakage from the larger pores during cell culture. In-vivo studies involving implantation of scaffolds in rabbit femur defects showed increased new bone formation [151].

Lei et al. [152] prepared hierarchical scaffolds having pore sizes ranging from 8 nm – 5 μm, using Hydroxyapatite-doped dendritic mesoporous silica nanoparticles (HAp-DMSN). The presence of these nanopores is known to be an interesting prospect for drug delivery systems involving in-situ delivery of growth factors to the implanted site. In-vivo bone regeneration on a rat cranial defect model using HAp-DMSN scaffolds showed

the largest bone formation after just 4 weeks of implantation. A primary reason for increased bone formation was an interconnected nano and microporous structure. The similarity in scaffold porosity to natural bone assisted in inducing specific functions for bone regeneration.

Lee and Kim [153] prepared a hierarchical nanofibrous collagen scaffold with varying strut thicknesses. The 3D printed structure consisted of macropores, micropores and nano-fibrous struts introducing a hierarchy in the scaffold architecture. *In-vitro* studies using MC3T3-E1 cells showed better protein adsorption (fibronectin, vitronectin, fibrinogen and laminin) due to the higher surface area available on the fibrous struts. Further, this nanofibrous structure allowed for unipolar extension of the cell cytoskeleton allowing for extension and contraction of the cell structure. Since the cell absorption was higher in the nano-fibrous scaffold and there was a lack of interconnectivity, proliferation of cells was hindered. However, the larger pores present in the collagen-based scaffold were able to provide a significantly larger area for the cell proliferation.

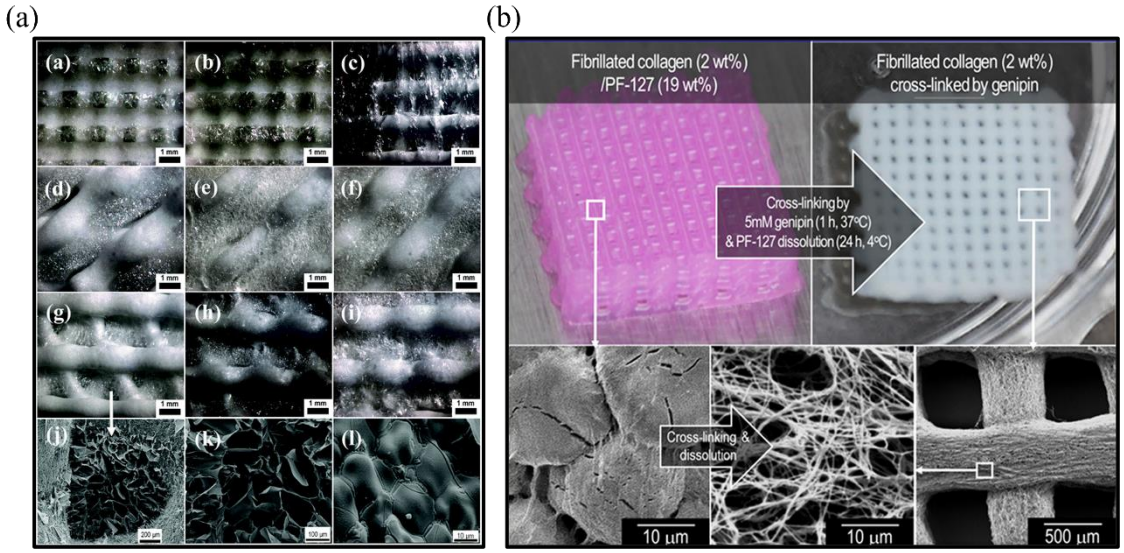

Figure 2.6: (a) Represents the range of pore shapes (square, parallelogram and triangles) explored for BTE application using bioceramic – silk scaffolds. Macropores (~1mm) were introduced using

3D printing and micropores (~ 50 – 100 µm) were produced by freeze drying of different concentration of silk (0.625% , 1.25% and 2.5%) [151]. (b) Fibrillated collagen scaffolds produced with combination of pore sizes that extend from a few mm to nanometres using bioprinting and the selective leaching of PF-127 solution [153].

2.7. Manufacturing hierarchical structures for bone tissue engineering

Manufacturing hierarchical porous structures requires control over the size and position of the pores introduced. Conventional manufacturing techniques for the production of porous materials are briefly described in Figure 2.7 and can be used to produce macro (d > 50 nm), meso (50 nm > d > 2 nm) and micro (d < 2 nm) porosities [154]. Only specific techniques under these pore forming methods can produce hierarchical porosities. These techniques include freeze casting, self-assembly, spin coating, hydration process, nano-stereolithography and additive manufacturing [155-157] .

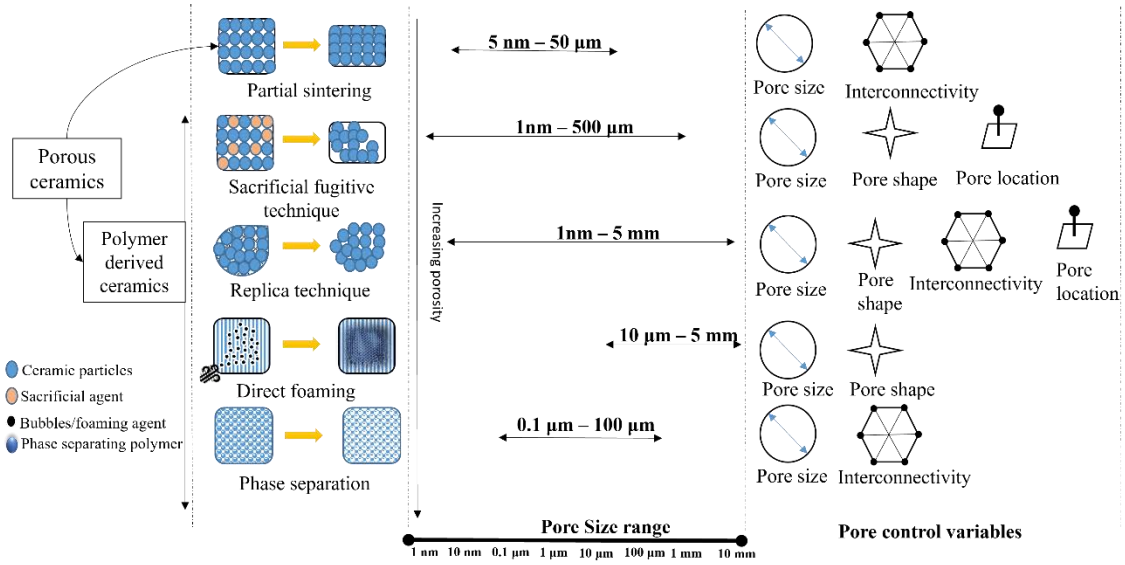

Figure 2.7: An overview of conventional manufacturing techniques to produce porous ceramics.

Freeze casting is a technique used to produce aligned porosities; this technique involves cooling liquid template-creating channels within the slurry in the direction of the thermal gradient. Dendrites formed during the cooling of the liquid template function as a link between the pore channels [154]. Process parameters of the freeze casting process include freezing rate, slurry formulation and the solvent used. While freeze casting can produce a range of pore sizes, pores generated are oriented in the direction of cooling. Also achieving different pore sizes within the same structure will require careful tuning of process parameters (freezing rate, slurry viscosity and concentration of suspension and preforming agent). Freeze casting has previously been used in the preparation of hydroxyapatite-gelatine scaffolds, producing a lamellar microstructure with pore sizes between 18 and 125 μm. The concentration of HAp and cooling rate showed a significant impact on the microstructure and morphology of the sample [158]. Lee et al. [159] produced graded porous hydroxyapatites using sequential freeze casting process. This was achieved by using different concentrations of HAp (10, 15, 20, 25, 40 and 50 vol%), producing a porosity between 25 % and 70 %. Pore sizes up to 160 μm were fabricated using this method depending on the HAp concentration, concentrations exceeding 45 vol% showed very low porosity and pore sizes due to the high viscosity of the slurry used for freeze casting [159]. However as described in Figure 2.7, this technique lacks control over spatial location of the pores and pore shape.

The principle of **replica technique** involves using open celled porous templates coated with ceramic slurry to form a defined internal pore network. This is followed by thermal heat treatment to eliminate the template through thermal decomposition [160]. Once the template is eliminated from the matrix, it is sintered to form the required porous ceramic. Porous ceramics generated using these methods have been used to prepare scaffolds for BTE [161-163] due to their highly reticulated nature and control over pore sizes. For

example, polyurethane (PU) foams used as templates while producing porous ceramic scaffolds need to have high porosity (>90%) with pore sizes larger than 100 μm [164, 165]. Commonly used PU foams having pore density values ranging from 5 to 80 ppi have been shown to produce well-defined pore structures undergoing complete burn off before 600 °C [16, 166-168].

Electrospinning is a technique to produce fine fibres by charging a polymer melt or solution under high voltages. The high voltage counteracts the surface tension of the fluid to form a thin fibre or filament that is deposited onto a spinneret. Arrangement of these fibres on the spinneret will dictate the porous volume of surface structure. Electrospinning can produce fibres at the nanometric level which can mimic the features present in natural bone. For example, Xu et al. [169] produced a 3D electro-spun scaffold with hierarchical porosities up to 300 μm. Huang et al. [170] showed that 3D printed scaffolds with electro-spun meshes produced dual scaffolds introducing a combination of macro and micro pores within the scaffold. *In-vitro* studies showed that activity of the scaffold was affected by fibre alignment and mesh density [171]. OCN expression showed an improvement irrespective of processing parameters used. The anisotropic nature of the electro-spun fibres showed a positive influence over cytoskeletal attachment. However, the major limitation of electrospinning is in the production of fibres in the submicron sizes. Further, the pore sizes produced form nanoscale pores that make it impossible for the infiltration of ECM and cell migration [172]. Electrospinning can be used to process metals and ceramics indirectly, this involves preparing polymer composites containing the metal or ceramic of interest followed by post-processing the obtained nanofibers [173].

2.8. Limitations of conventional manufacturing techniques

As discussed in sections 2.2 and 2.3 porous scaffolds used for BTE applications have specific requirements of pore sizes, shapes and materials depending on the intended role (structural strength or interaction with ECM). Conventional manufacturing processes, as described in Figure 2.7, lack the required spatial control of pores and the ability to simultaneously process multiple materials. To mitigate these shortcomings, some recent studies have explored combining different materials and conventional processes at specific stages of scaffold production. For example, hydroxyapatite scaffolds were prepared by combining them with polyesters (polyol and di-isocynate) as foaming agents. This produced a porous ceramic scaffold based on the polyurethane sponge and simultaneously obtained a cellular structure due to the carbon-dioxide bubbles generated in-situ. Pore sizes produced using this technique showed 4 major pore sizes distributed in different amounts. These major pore sizes are as follows; (1) > 1 μm (less than 0.5 cc/g); (2) 4 – 20 μm (0.5 cc/g); (3) 20 – 210 μm (3 cc/g) and (4) 150 – 1000 μm (less than 0.5 cc/g) [174]. This HAp-based scaffold with multi-scale porosities showed excellent biocompatibility. With pore formation occurring in-situ the lack of any spatial control over the porosity makes their mechanical strength unpredictable. Further, the inability to process multiple materials could impair their ability to address all the requirements of BTE scaffolds as described in section 2.2.

Freeze casting, as described in section 2.7 can produce porosities mimicking biological materials but only at single length scales and directions. Previous studies have shown that, while multi-scale porosities can be achieved by utilising different methods, establishing an interconnection between these multi-scales porosities is still a major challenge [126, 175-177]. Specifically, in the case of BTE scaffolds where pore interconnectivity is

critical for vascularisation of implanted cells responsible for the bone healing response. The design of internal and external complex features on BTE scaffolds can be a significant challenge for conventional techniques alone or even a combination. To overcome these challenges, additive manufacturing techniques have been used or incorporated into conventional techniques.

2.9. Additive manufacturing

Additive manufacturing (AM) can be defined as the process of building up objects or parts layer-by-layer [178]. There are several techniques (as described in Table 2.5) such as fused filament fabrication , stereolithography, selective laser sintering which have been previously used for scaffold manufacturing across different materials [179-182]. Additive manufacturing techniques offer resolutions from a few microns to millimetres depending on the technique used, further they can process polymers, ceramics, and metals [183]. The combination of AM with computer modelling enables free form fabrication of parts which can address the unique physiological and mechanical requirements of bone injuries or defects.

Table 2.5: Description of additive manufacturing techniques previously used to produce BTE scaffolds.

3D printing process and material	Description	Ref.
Extrusion-based 3D printing with CaP material	• Scaffolds possessed pore sizes ranging from 60 – 100 μm • Bone growth direction was determined by scaffold geometry • Instability of implanted scaffold could lead to foreign body response/formation of fibrous tissue. • Formation of thick fibrous tissue within the pores • Resorption of CaP was absent	[184]
Selective laser melting with Tantalum	• Porosity of 70 % and a pore size of 334 μm was used • Surface roughness of deposited layer was higher for Tantalum scaffold compared to the control • Higher cell proliferation on Tantalum based scaffold • Significant difference in osteogenic markers (ALP, OPN, OCN and Col-1) compared to the control at the 14 day mark • Tantalum scaffolds were able to maintain bone formation significantly longer than the control	[18]

Stereolithography with Biphasic CaPs	• Surface topographies on the scaffold had a mean heigh of 6.5 µm • Pore sizes on the biphasic CaP based scaffold were smaller compared to the HAp (control) • Up to 72 % of bone in-growth was observed after 3 months of implantation • No resorption of material was observed • Fibrous connective tissue and blood vessels were observed at the host bone and biomaterial interface	[185]
Electron beam melting with Ti-6Al-4V	• Surface defects created during the EBM process can cause a major health hazard when implanted • Nanotubes were observed on the scaffold structure after post-processing (etching and anodising) • Presence of smooth surface with post-process samples produced more bone at scaffold-host interface	[186]

In-vivo studies involving implantation of CaP 3D-printed scaffold into the patient's cleft showed increased bone growth when the gap between the host bone and the scaffold was minimal (shown in Figure 2.8a). Therefore, the patient-specific 3D printed implant contributed towards a faster healing response by accurately filling the gap between the fractured ends. Changing pore geometry from 30° to 60° showed a significantly different bone healing response and differentiation of mesenchymal stem cells [184, 187]. A tantalum-based scaffold 3D printed using SLM showed positive responses towards bone healing (shown in Figure 2.8c), where the bone in-growth was enabled through the

channels created during 3D printing [18]. The irregular surface created from the laser-powder interaction is known to positively influence bone healing ability and increase surface area for interaction [18, 188]. 3D printed biphasic calcium phosphates showed a significant increase in both in-growth (up to 72%) and presence of blood vessels at the scaffold – host bone interface [185]. Further, the irregular nature of the scaffold surface is a result of the low resolution offered by UV-based stereolithography. Hierarchical microstructure and pores created using a combination of EBM and post-processing were the primary cause for increased bone formation. Integration of the implanted tissue occurred directly with the natural bone without formation of any fibrous connective tissue, ensuring a strong fixation (shown in Figure 2.8b) [186].

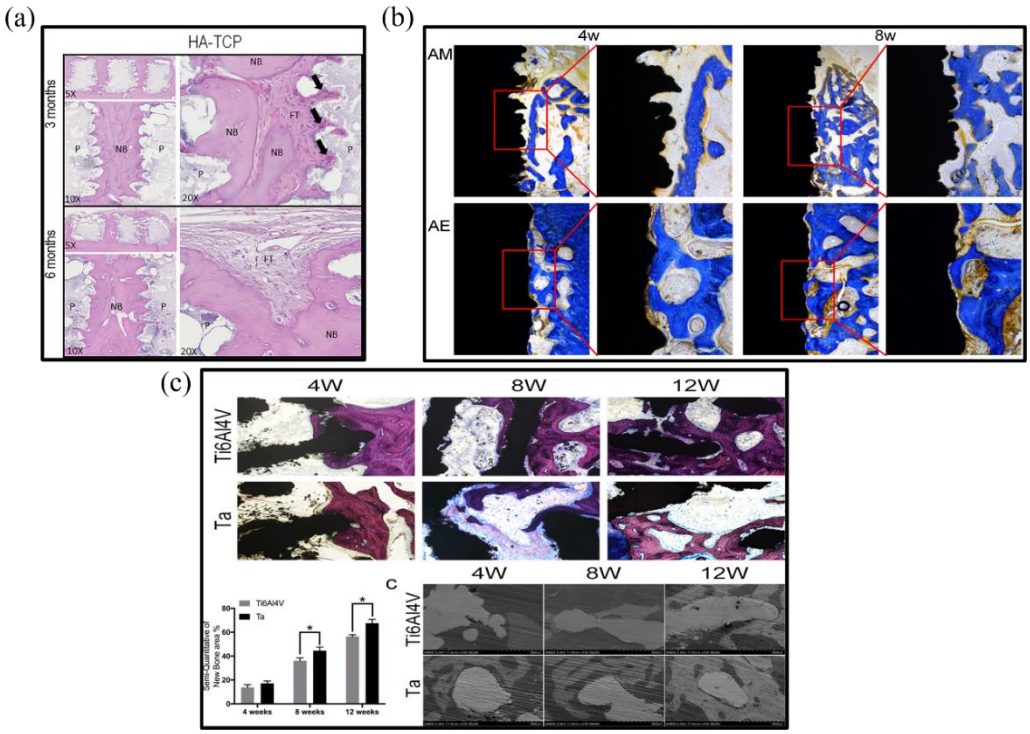

Figure 2.8: (a) HAp-TCP based scaffolds show positive interaction with local ECM forming new bone (NB) that is integrated with the existing bone. Presence of fibrous tissue at the interface of the new and existing bone indicate that an early foreign body response was initiated [185]. (b) Histological staining of a Ti-6Al-4V based scaffold prepared using electron beam melting showed the formation of new bone tissue within 4 weeks of implantation. Anodic oxidation of the surface

showed an improved bone healing performance [186]. (c) Histological analysis of the Ta based scaffold indicates higher new bone formation compared to Ti-6Al-4V. At the 4th week, appearance of bone lining cells at the implanted site indicates the superior osteoinduction capabilities of Ta-based scaffold. Further, at the 12th week, density of new bone formed appears to be higher on the Ta based scaffold when compared to the Ti-6Al-4V scaffold [18].

2.10. Conclusion

Discussions around the efficacy of BTE scaffolds indicate that these scaffolds require biomaterials that can positively interact with the local ECM and simultaneously provide structural support to the damaged areas. To fulfill these dual requirements, an in-depth understanding of the chemical and physical factors responsible for the initiation and continuation of the bone healing response is necessary. Since the bone healing pathway is an active area of research, designing better BTE scaffolds that can provide an ideal bone healing environment is still a challenge.

The multi-faceted requirement of BTE scaffolds make them a complex arrangement of porosities (shapes, sizes and interconnectivity) and biomaterials that mimic the natural structure of bone tissue. Changes in mechanical strength requirement across different types of bone (cancellous and trabecular) and their location in the body, alters this complex arrangement. Further damages/defects presented by individuals are often unique, therefore, a one-size-fits-all approach to the manufacturing of BTE scaffolds will be less effective in improving patient outcomes.

In-vitro assessments used to validate the efficacy of the scaffold utilize osteoblast cells which are infiltrated into the bulk of the 3D scaffold. Increasing the geometrical complexity to address strength and biofunctionality of the scaffold is a popular solution although visualizing the growth of the cells within the scaffold bulks (non-destructively)

to assess the efficacy of the scaffold can be difficult. Bone tissues and their surrounding ECM are highly dynamic in nature, therefore, developing scaffolds that respond to either chemical or physical stimuli can be challenging. Further, the precise mechanisms that trigger and sustain bone healing processes are still an area of active research, therefore, requirements of future BTE scaffolds might change based on results of new research. 4D printing technologies that can produce materials that respond to external stimuli could be utilized to introduce new functionalities in BTE scaffolds.

Conventional fabrication techniques are unable to capture these unique features to produce patient-specific scaffolds. Further, conventional fabrication techniques can produce hierarchical porosities that mimic natural bone structures, but they lack the ability to simultaneously process multiple materials. This increases the number of steps during the production of multi-material scaffolds that are a requirement to produce bio-functional scaffolds. In addition, they lack control over positioning the pores and features within the scaffold architecture. Since the structural capacity is closely linked with the presence of these pores, control over their spatial location can alter their structural capacity. The type of porous structure can also affect the infiltration of ECM into the scaffold, controlling the interaction of scaffold and, hence, its bone healing ability. Therefore, by using a combination of materials and structural features, unique scaffolds with specific bone healing and structural capacities can be designed.

Recent advances in 3DP technologies combined with imaging systems (Magnetic resonance image, computer tomography and synchrotron-based CT scanning) allow us to capture and translate the unique defects/damages into scaffold designs. Incorporating finite element analysis into this design loop could allow us to predict the structural capacity of these scaffolds before manufacturing them, thereby allowing professionals to

make informed decisions before implanting the scaffolds. While 3DP systems do provide significant design freedom, they are also associated with challenges in accurately replicating geometries due to poor resolutions and materials that can be 3D printed are required to be modified (converted into slurries, pastes, filaments, or powder). More knowledge is required to understand the impact of these modifications on bone healing ability or even their mechanical strength. When processing multiple materials using 3DP, interaction of dissimilar materials can create defects (cracks or residual stresses) further the adhesion between the materials will be a critical factor when determining the mechanical strength of the produced composite. These knowledge gaps will need to be addressed to truly produce the next generation of patient tailored BTE scaffolds.

3. Ceramic 3D printing

Ceramics have been one of the oldest materials used by mankind, starting from the tools used by early man to building blocks of megastructures. Their brittle nature and extremely hard surfaces make them very challenging to work with, and consequently, they have been replaced in several applications by metals and alloys that are considerably easier to form. Development in manufacturing technologies has introduced new processes such as injection molding, slip casting, tape casting, cold pressing, etc. While these methods did allow for easier processing of ceramics, they still have the limitation of being expensive and limited to relatively simple shapes. 3D printing (3DP) which was first developed in the 1980s primarily for polymers, has been recently applied to the manufacturing of ceramics [189, 190]. The freedom of design and quick turnaround times offered by these processes have led to new applications such as biomedical scaffolds, custom cutting tools and high-temperature impellers. This chapter describes and discusses the available technologies for ceramic 3DP. It also reviews the feedstock requirements and processing parameters for each 3DP. This will function as an effective guide for 3DP technology selection. 3DP processes can be described as additive manufacturing (AM) processes; involving the repeated addition of two-dimensional layers to form a three-dimensional object [178]. This layer-by-layer approach is the cornerstone of the 3DP process, breaking down complex structures into a series of simple layers or images. The slicing process is usually performed with the assistance of software, information from the software is extracted either as a sequence of machine positions or images depending on the 3DP technology used. The resolution achievable at every layer depends on the technology used hence making the choice of technology a very critical decision that needs to take into consideration the engineering requirements, cost, product size and infrastructure

available. Figure 3.1 illustrates the general workflow used for 3DP, from the understanding of the engineering requirements to the final part. Ceramic 3DP was first reported by Marcus et al. [189] and Sachs et al. [190] in the 1990s, when 3DP processes used for processing polymers were adapted to manufacturing ceramic components. While previously the only available technique was binder jetting, which showed considerable anisotropic shrinkage after post-processing [191]. Recent developments in pre-processing ceramics for 3DP has opened other techniques such as stereolithography (SLA), digital light processing (DLP), robocasting, and fused filament fabrication (FFF) [192]. Unlike metals and polymers where the final component produced by 3DP processes can be used with almost no post-processing, ceramics parts need to undergo sintering to obtain the desired strength.

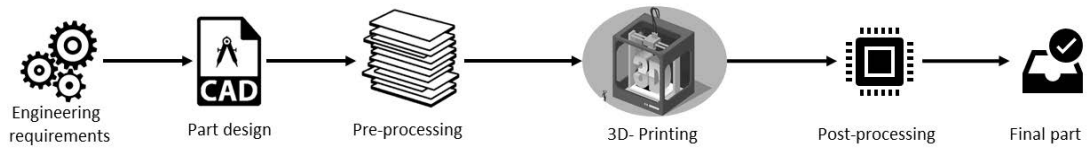

Figure 3.1: General workflow of three-dimensional printing process.

3.1. Classification of 3D-printing processes

Ceramic 3DP processes could be classified into three types based on the nature of feedstock: (1) slurry-based processes, (2) powder-based processes, and (3) bulk solid materials (Figure 3.2) [192].

3.1.1. Slurry based processes

Slurry-based processes involve the use of fine ceramic particles dispersed in a liquid medium containing suitable additives, to form inks or pastes depending on the required solid loading. The choices of these additives are based on the rheological requirements and nature of the 3DP process. The main steps of ceramic 3DP using slurry-based processes are shown in Figure 3.3. This section includes the requirements of the feedstock for slurry-based processes, processing parameters and their influence on ceramic parts fabrication, and *in-situ* and *ex-situ* quality control (QC) techniques as well as energy consumption of each technique.

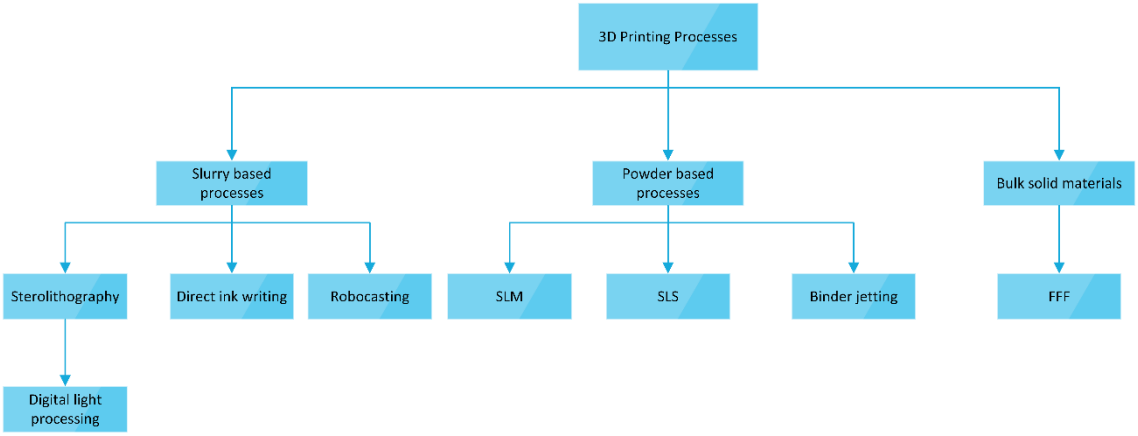

Figure 3.2: Classification of three-dimensional printing processes.

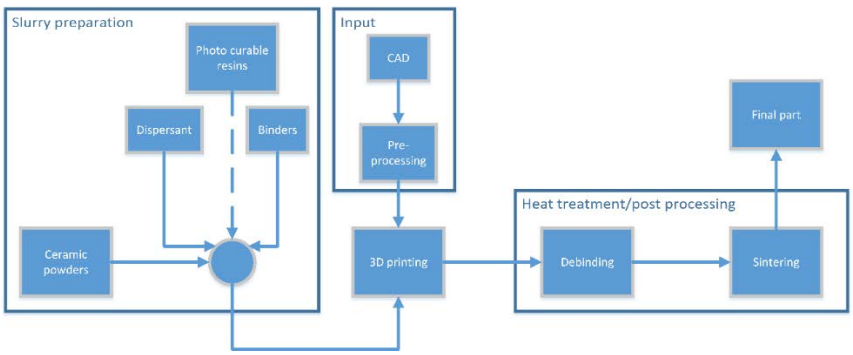

Figure 3.3: Workflow of slurry-based processes.

3.1.1.1. Process description

SLA requires the incorporation of ceramic particles within photocurable polymeric resins. The mixture is selectively exposed to a suitable light source using either a digital micromirror device or scanning galvanometers [193]. The light source used for SLA-based processes includes lasers or light projection-based systems. The major difference between these processes lies in the light source used, laser-based systems have small exposure areas and hence are slower while light projection-based systems are able to fully cover the build area.

While the process of curing the polymeric resin remains the same, it can be classified into two types based on the position of the light source as top-down and bottom-up approaches. Top-down approaches require the light source to be directly above the top surface of the printed object. During this printing process, the printed object moves down into the slurry tank, exposing a fresh layer of slurry for the subsequent reaction [194]. This approach allows for using larger build areas and eliminating the need for parts to be lifted off from the base to accommodate subsequent layers. However, printing defects can occur due to inconsistent layer formation on the top surface.

Bottom-up approach requires the light source to be below the top layer of the printed object. During the process, the printed object is lifted off from the platform to expose a new layer of ceramic slurry [194]. Further, additional systems are required to ensure an even layer of slurry is coated over the platform, making this a relatively slow process in comparison to top-down approaches. Specific to the bottom-up approach, slurries are required to be redistributed along the surface using an additional tool. Slurry viscosity has to be carefully optimized to ensure a uniform layer is coated. Commercially, the bottom-up approach has been widely explored considering some of the key benefits of

the top-down. This includes consistency in the slurry layer exposed to the source of irradiation, slurries with increased solid loading can be used to limit shrinkage during post-processing. Lastly, to produce final components, these ceramics are debinded to burn-off the binders followed by densification to obtain the desired strength.

Robocasting is a versatile tool for ceramic fabrication, with the ability to process multiple ceramics at different length scales. Further, with low binder contents during the slurry preparation process, high densities are achievable after post-processing. As the nozzle, which is connected to the feeding, traverses its defined path, slurry is carefully deposited along every layer. The simplicity of the setup enables the use of multiple ceramic slurries using multiple nozzles and feeding systems [195]. The rheology of the slurry must be optimized to ensure that does not undergo deformation due to the stacking of multiple layers. Near-net-shape manufactured green parts produced from robocasting require a sintering step that provides strength to the final part.

Direct-ink writing is an AM technique for processing ceramics that uses polymer- based ink containing ceramic particles. The delivery of the ink onto the building surface can be achieved using (1) a droplet-based writing system and (2) filament- based writing system [196]. Droplet-based writing systems use the principle of ink-jet printers to carefully deposit ceramic ink layer-by-layer. These can be further divided into drop-on-demand systems or continuous-jet methods. Drop-on-demand systems eject inks only when required, simplifying the design of the ink dispenser and preventing ink contamination [196]. A major limitation of this system is the high viscosity of ceramic inks, but recent advances in ink dispenser designs and understanding of printing parameters have enabled the printing of high-viscosity ceramic inks [197].

3.1.1.2. Feedstock requirements

Feedstock requirements for slurry-based AM are unique to each process. Some of these requirements include solid loading (vol%), binder quantity, dispersant quantity, rheology, and stability. The slurry rheology is affected by feedstock preparation, factors such as solid loading, particle size, binder quantity, dispersant quantity, and milling time are critical [198]. Further, these factors are correlated, thus making a list of specific individual requirements is challenging. However, ranges of rheological parameters or critical characteristics of ceramic slurry for different materials can be identified from the literature and are summarized in Table 3.1.

Solid loading represents the volume occupied by the ceramic particles in the ceramic slurry. Higher solid loading produces dense ceramic objects post sintering; however, increasing solid loading negatively impacts its performance during plastic forming which is essential for slurry-based AM processes. Therefore, the concept of critical powder volume concentration (CPVC) described in previous studies represents the volume limit of ceramic particles added to produce a paste or slurry that remains stable while being processed [199]. This CPVC value depends on the nature of the processing technique used, for example, robocasting and direct-ink writing processes require stiff ceramic pastes that are able to resist any residual stresses and minimize drying shrinkage [200, 201]. Although solid loading greater than 50 vol% is preferred to obtain fully dense structures, thus rheology and particle size requirements of the 3DP process need to be considered.

Table 3.1: Key rheological requirements of ceramic slurries used for different slurry based AM processes.

Additive manufacturing processes	Key requirements of slurry/raw material	Ref
Robocasting or Direct ink writing	• Viscoelastic property must be described by the Herschel-Bulkley model • Particle agglomerates must not exceed extrusion nozzle diameter • Reversible shear thinning behaviour is required at viscosities of 10-100 Pa s at high shear rates • Storage modulus(G') must be greater than 200 Pa • Organic additive quantity should be less than 3 vol% • Powder particles sizes should be within 1μm - 100 μm • Slurry must possess pseudoplastic behaviour	[196, 202]

Stereolithography	• Must show thixotropic behaviour • Viscosity of the slurry must be in the range of 0-10 Pa s • Curing thickness of the resin mixture must be 5-10 μm higher than the required layer thickness • Particle size needs to be carefully considered during slurry preparation • Solid loading greater than 55 vol% is required to achieve good densification post-sintering	[198]

Binders and dispersants are added to the slurry formulation to increase and decrease its viscosity respectively. Further they could also be added to introduce critical features required for chosen processing technique. An example of this is seen for the case of stereolithographic processes that require photocurable polymers to process the ceramic layers [203]. Some commonly used binders and dispersants have been described in Table 3.2, their addition will be dependent on the required rheology. These binders and dispersants used affect particle-particle interactions, inducing an attractive or repulsive force causing the formation of aggregated or well-dispersed slurries respectively. Dominant mechanisms that induce these responses are classified into three types (1) electrostatic, (2) steric and (3) combined electrosteric stabilisations [202].

Table 3.2: Some commonly used binders and dispersants to prepare ceramic slurries for additive manufacturing processes.

Binders	Dispersant	Additive manufacturing process	Ref
SP-RC700 (epoxy acrylates, acryloylmorpholines and trimethylolpropane triacrylate)	DISPERBYK-103, TEGO-685	Stereolithography	[204]
1,6-hexanediol diacrylate (HDDA) and acryalted polyetherpolyol	Solsperse 41000, Melpers 4350	Stereolithography	[205]
Carboxy-methylcellulose	Darvan C-N	Robocasting/Direct-ink writing	[206]
WB4101 (Aqueous acrylic-based binder) and PL008 (plasticiser)	DS001	Robocasting/Direct-ink writing	[207]
Polyvinylpyrrolidone (PVP) and nano-sized MgO particles		Direct-ink writing	[208]

Uniform dispersion of ceramic particles and polymer binders prevents particle segregation prior to sintering [192]. Zeta potential measurements can accurately determine the dispersion of ceramic particles in slurries but can be challenging in the case of highly solid-loaded slurries mixed in nonpolar resins due to weak electrostatic interaction [209]. Therefore, viscosity, thermogravimetric and Fourier-transform infrared spectroscopy measurements are usually required to fully understand the influence of

dispersants on ceramic slurries. Another relatively simple technique to assess the dispersion of the ceramic particle is using sedimentation tests, where dispersion can be compared by measuring the ratio of the height of clear solution (*HT*) post sedimentation to the initial height of the slurry (*Ho*).

The particle dispersion state can be understood with hydrostatic pressure measurements taken at the bottom of a cylinder containing the slurry. The decreasing slopes of the hydrostatic pressure vs time plots dictate the state of the slurry, smaller slopes indicate uniform dispersions [210]. Dispersion of ceramic particles is a function of particle size, solid loading, and quantity of additives, which determines its feasibility to be processed using slurry-based AM techniques.

Slurries used in SLA-based processes require the inclusion of photocurable polymers and their selection depends on the excitation source available in the 3DP system. Other optical characteristics such as diffraction and absorption must be also considered [211-213]. Specifically, in case of direct-ink writing, studies have shown a strong correlation between slurry rheology and printability. The dimensionless number introduced by M'Barki et al. captures the effects of capillary and gravitational forces acting on the printed layers, which is fundamental to designing ceramic inks or slurries that provide consistently dense materials [214].

3.1.1.3. Energy consumption

Energy consumption occurs in three different steps: (1) pre-processing step, (2) in-processing step, and (3) post-processing step. Pre-processing step includes energy consumed in preparing ceramic slurries but does not include ceramics powder production processes because these processes are significantly different for each type of ceramic.

Slurry preparations require uniformly mixing ceramic powders with suitable binders and dispersants. Energy consumed during these processes depends on the mixing time and quantity, larger quantities require higher-capacity mixers that consume more power. Lab scale high shear mixers used for preparing uniform dispersion are known to have an operating capacity of 1 mL−50 L with 750 W motors. Increasing the capacity of these mixers to 1−8000 gallons for industrial applications, increasing their power consumption up to 150 kW.

Energy consumption during the operation of a ceramic 3D printer is highly dependent on the type of ceramic AM technique utilized. Energy sources to cure ceramic slurries differ based on the energy source which could be either a laser or digital light projection system. In digital light projector systems, the wattage of the projector bulb determines its maximum energy consumption. Similarly, in laser-based systems energy consumption will depend on the wattage of the laser used. Curing of ceramic slurries requires a specific critical energy, which changes depending on processing parameters. Similarly, an ultraviolet-based system or a laser-based system will consume energy based on processing parameters as described in Table 3.3. Stereolithographic techniques require an additional recoating system to ensure a uniform layer of slurry is available during processing. However, the energy consumed by motor drivers is significantly lower than the energy consumed by the laser source.

Specifically, in robocasting processes, the lack of usage of any lasers limits the energy consumption (during the process) to the energy consumed by the slurry pump and motor drivers. Energy consumption of these pumps can range between 0.36 and 216 W depending on pump flow rates and pressure requirements at the nozzle end. Sintering and debinding are critical steps toward producing fully dense ceramics.

Table 3.3: Energy consumption during vat polymerisation processes.

Process type	Light used	Wavelength/pixels	Maximum electrical power consumption
STL	Ultraviolet	405 nm	2 kW
DLP	Ultraviolet	2560 x 1600 pixels	
DLP	LED	405 nm	
STL	Ultraviolet	35 – 5 nm	1. 9 kW
DLP	Ultraviolet	-	500 W

The sintering process is a thermally driven process that usually occurs at temperatures greater than 1200 °C. Sintering is carried out in high-temperature furnaces and energy consumption depends on peak temperature, hold time and heating rate. Both peak temperature and hold time depend on the extent of densification required and the type of ceramic material. The power consumption of lab-scale sintering furnaces usually lies between 5 and 20 kW.

3.1.2. Powder Based processes

Powder-based AM processes utilize the unique binding system to either bond or fuse ceramic particles together. Most commonly used are either a CO_2 or Nd:YAG laser; however, the power of these lasers depends on the binding mechanism required, which can be classified under selective laser melting (SLM) and selective laser sintering (SLS).

While the above-mentioned processes utilize heat as their primary mode of binding particles, binder jetting process utilizes a resin to selectively adhere ceramic particles [193]. The selection of the AM process will impact post-processing steps.

3.1.2.1. Process description

SLM requires a high-power laser to heat the ceramic particles to a temperature between $T_m/2$ and T_m (melting temperature), causing the ceramic particle to fuse. The laser source is selectively scanning across the powder bed to fuse ceramic particles on the powder layer. Once completed, the build plate is lowered to the height of the layer thickness and a fresh powder layer is deposited over it. The process is repeated for each subsequent layer to form the three-dimensional part. High melting temperatures of ceramics make them extremely hard to process, to minimize the heat required low temperature liquid phases are commonly used to favor the sintering process (liquid phase assisted sintering). The liquid phase mixed within the ceramic raw material melts prior and binds the ceramic particles forming a dense ceramic part [215]. Melting of ceramic powders might produce cracks and heterogeneous microstructure, therefore is not the preferred technique for ceramics processing [215].

SLS of ceramics can be performed directly or indirectly. The direct technique involves heating the ceramic powders and partially fusing them together [193, 215]. A combination of particle sizes is required to obtain a high packing density of powders. The indirect method uses low-temperature matrix phases such as polymers [193, 215]. The laser source causes these sacrificial polymers to bind, forming a green part that has to be sintered to obtain the final component with the desired strength.

Binder jetting is an AM process that utilizes a suitable binding agent to adhere ceramic particles forming a green body. The binding agent is selectively applied across the surface of the powders to produce a single layer, the build plate is then lowered to allow a new layer of the powder to be deposited. This process is repeated several times to produce the final three-dimensional component. This can be achieved in two ways: (1) binders are mixed with ceramic particles and the dispensed liquid triggers the reaction between the ceramic particles and binder and (2) ceramic particles are precoated with a solid binder, and liquid dispensed triggers the chemical reaction to bind the ceramic powders [191]. The produced green part is heated to temperatures close to 200 °C, causing the binder to undergo cross-linking and toughen the green ceramic body. Finally, the organics are completely removed through a debinding step and then sintered to obtain ceramic parts with the desired strength [191].

3.1.2.2. Feedstock requirements

Ceramic raw materials are required to be prepared prior to use. This preparation step is dependent on the process selected. SLM process require no preparation as powders are melted during the process, causing the particles to fuse. SLS process consist of a low temperature phase that require to be coated or mixed with the ceramic particles. Some commonly used low temperature phases or binders include $NH_4H_2PO_4$, B_2O_3, Aluminium, Epoxy resin and phenolic resins (shown in Table 3.4) [216]. The quantity of these binders included depends on the required green strength, low quantity additions are insufficient to create a stable bond between particles however excess additions of polymers will increase porosity during the debinding stage. Key factor that also need to be considered during the addition of polymers is its flowability to allows a unform layer of powder to be deposited across the build plate.

Technologies used for the preparation of ceramic powder include mechanical mixing and spray drying. Mechanical mixing involves agitating the mixture of ceramic particles and binders to produce a uniform mixture. While this technique can ensure a uniform distribution, it has no impact on the particle size distribution (PSD), therefore it is often combined with spray drying to produce ceramic powders. Spray drying involves the transformation of a fluid slurry containing the material of interest into dried powder. During the preparation of the slurry, suitable binders are required to be added to function as the low temperature phase for the SLS process. Choice of binder must be based on the nature of interaction during the debonding phase i.e., binders inducing changes in chemistry of the ceramic phase must not be selected. Quantity of ceramic phase added strongly influences the homogeneity and viscosity of the slurry. For example large viscous forces present in the slurry will require more energy to form small droplets, leading to larger particles sizes [217, 218].

Flowability of these powders as previously mentioned, is critical for all powder-based processes, a uniform bed created by these powders ensures consistency among layer features. Measurement of the powder flowability is a complex process, based on the measure of hausner ratio. The hausner ratio is defined as the tapped density divided by the apparent density [219]. The powders hausner ratio can be altered based on the flowability and packing requirements, as these two properties tend to contradict one another. Literature has shown that a balance can be achieved by carefully choosing powder particle size distribution and volumetric contents of each size [219, 220].

Shape of powder particles will have an effect on the flowability and packing of powder particles. Spherical powders reduce packaging density but with their ability to roll relative to one another, offering good flowability at high ceramic loading. Irregular particles on

the other hand, tend to agglomerate due to the increased friction between their surfaces, allowing for higher packaging densities and green strength but reduced flowability [191]. Therefore, a multimodal distribution of powders consisting of various shapes and sizes when used in powder-based process can produce fully dense ceramic products.

Wettability is a key factor specifically in case of the binder jetting process. Binder dispensed from the extruder will penetrate through microscopic pores between ceramic particles ensuring adhesion to its previous layer [191]. Wettability is influenced by multiple factors such as powder shape, size and viscosity of binder. It can be measured by analysing the contact angle created between the binder and particles, low contact angles signals high wettability while high contact angles signal low wettability [191]. Viscosity of the binder determines its ability to penetrate through the powder surface, low viscosities of the binder are more suitable. However, resolution of printing is closely tied to its viscosity, very low viscosities of the binder will cause it to spread uncontrollably leading to a loss in resolution [191].

Once the binder is in contact with the powder particle, reaction between the powder particles and binder solution ensures adhesion to its previous layer. Previous studies have shown that size distribution of voids have a greater impact as opposed to surface area of contact [191].

Table 3.4: Resins commonly used as a low temperature phases for powder processed using SLS.

Materials description	Quantity	Type of resin	Ref
Al_2O_3	4 - 6 wt%	Epoxy resin	[216]
SiC	3 wt%	Epoxy resin	[221]
Iron oxide doped Al_2O_3	2 wt%	Polyethylene glycol (PEG)	[219]

Absorption of laser energy is critical in processes such as SLM and SLS; energy from the laser needs to be effectively converted to heat for the ceramic particles to fuse. Studies have indicated oxide-based ceramics show poor absorptivity to near-infrared lasers [219, 222]. Addition of dopants such as carbon, iron oxide, graphite and boron carbide to name a few, have been known to increase the energy absorbance of near-infrared lasers, improving laser-powder interactions [219, 222-224].

3.1.2.3. Energy consumption

Energy consumption during a process could be a critical criterion when considering its limited availability. To analyse the energy consumed during the processing of the ceramic raw material to final product, here we are going to only consider energy consumed by the 3D printing machine, intermediate steps required in preparing the raw material and post processing steps. This approach to measuring energy consumption assumes ceramic powders prepared using various methods are of required quality, thereby allowing for a fair comparison between different processes.

Energy consumption during powder-based process such as SLM and SLS primarily arise from the laser source, difference in the energy consumption lies in the wattage of the lasers used in these processes (shown in Table 3.5). Further energy consumption also lies in the operation of auxiliary components such are motor drivers, hydraulics and powder dispensing systems. Energy consumption during these processes changes based on the scale of the machine and available build area. In Table 3.5 we provide ranges of total power consumption of these machines including small prototype machines to large machines with multiple work heads.

Table 3.5: Wattage of laser systems used in SLM and SLS based processes.

Powder based process	**Laser type**	**Laser Power**	**Total power consumption**
SLM	CO_2 laser or Nd:YAG laser	200 – 1000 W	1.7 – 50 kW
SLS	Ytterbium Fiber laser, Diode lasers and CO_2 laser	10 – 100 W	1.5 – 26 kW
Binder jetting	N/A	N/A	1.3 – 27 kW

Ceramics produced after processing them using 3D printing systems are termed as green components as they are not fully dense. Production of the fully dense components require additional post processing steps such as debinding and sintering. These post processing steps differ in each of the mentioned powder-based processes for ceramics. SLM does not require any post-processing and is able to produce fully dense parts. SLS and binder jetting systems require a debinding and sintering stage to produce fully dense parts.

Debinding performed for these green components, involves thermally treating them to temperatures within the range 200 – 700 °C [104, 225, 226]. Furnaces used for debinding ceramics have lower maximum operating temperatures of within 1200 °C, as the temperature requirements are considerably lower. Power consumption of these lab scale furnaces lie in the range of 16.5 – 27 kW, depending on the volume of the heating chamber.

Sintering process as previously mentioned is essential to produce fully dense parts and remains common to all ceramic based 3D printing technique. Energy consumed during this process has been previously described in Section 3.1.1.3.

3.1.3. Bulk solid materials

The bulk solid materials approach to additive manufacturing of ceramics uses a material extrusion process consisting of a solid feedstock in the form of a filament. These filaments consisting of over 45 vol% of ceramic powders are mixed-in with suitable binders to ensure they can be extruded into continuous filament. This process is very similar to ceramic injection molding and can produce wide range of part sizes [227].

3.1.3.1. Process description

Fused filament fabrication (FFF) for ceramics involves the extrusion of a highly viscous blend of polymers and ceramic particles through a heated nozzle. Polymers exposed to the heated nozzle transition from a brittle to a viscoelastic state allowing it to flow. This viscous solid material containing ceramic particles is selectively deposited according to the intended design, before printing the next layer. This process is repeated layer-by-layer until the complete green part is formed.

3.1.3.2. Feedstock requirements

Feedstock preparation for bulk solid based ceramic 3D printing as mentioned requires thermoplastic polymer binders that provide sufficient green strength to the formed component. In addition to this polymer binder must ensure feedstock remains a low viscosity while being extruded from the hot-end nozzle. Solid loads of 45 – 60 vol% are required to ensure minimum warpage after debinding and sintering phases.

Particle sizes of the ceramic powder used can play a critical role in the achievable resolution in FFF printing. Firstly, particles must be smaller than the extrusion nozzle to prevent blockage during the extrusion process. Resolution of structural features during FFF method is strongly dependent on the nozzle diameter [193], however when utilising filaments loaded with ceramics particles, resolution is also dependent on size of ceramic particles. Debinding stage will cause the polymers to be burnt off, leaving behind the loaded ceramics particles as shown in Figure 3.4. Where the white outline represents the required part resolution and the particles in red represent in the excessively large particles that contribute to the loss in part resolution. Therefore as a rule the particle size must be within 10% of the required resolution [227].

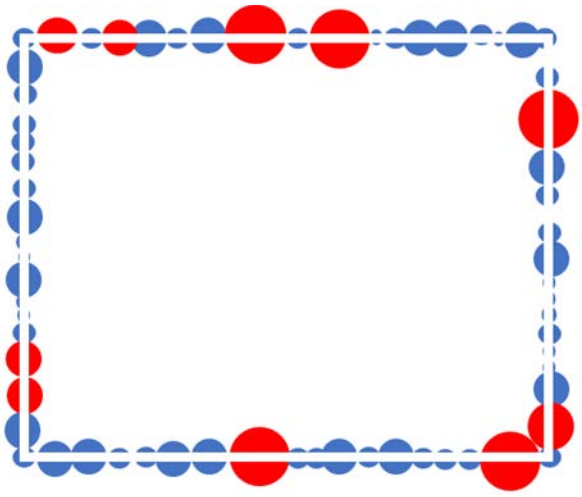

Figure 3.4: Influence of ceramics particle size on the achievable resolution in FFF.

Polymers commonly used as binders are poly-lactic acid (PLA), Acrylonitrile butadiene styrene (ABS) or Thermoplastic Polyurethane (TPU). These polymers must undergo a reduction in viscosity at the nozzle hot end allowing it to be extruded; the viscosity must be carefully controlled to ensure void-free parts.

3.1.3.3. Energy consumption

Energy consumption during FFF process arises during the pre-processing, processing and post-processing stages. While energy consumed during the post-processing stage is similar for all ceramic based AM processes, energy consumed during pre-processing and processing stages differ.

Pre-processing stage or during the preparation of solid filament, ceramic powders and polymer binders are first pelletised prior to being extruded. Energy consumed during the production of ceramic powder is not considered in this analysis. Ceramic powders are initially mixed in with polymer binders using a ball milling or mixing stage, energy consumed during this stage has been described in section 3.1.1.3. Uniformly distributed mixture is then feed into a pelletiser which converts the mixture into pellet of fixed sizes.

Energy consumed during this stage can run anywhere between 0.375 – 4 kW, depending on its processing capacity. Pellets are then extruded using a filament extruder, processing capability of these machines can vary from 1 kg/hr to 20 kg/hr. Power requirements for these machines also vary between 1.1 – 15 kW depending on the scale and its processing capability.

Energy consumption during the FFF process is dependent on size of the build volume and number of extruders. Larger build areas require more heating elements necessary to heat up the build plate, thereby consuming more energy. Multi-extruder printers used in FFF processing consume more energy only during the simultaneous operation of both extruders. Table 3.6 indicates how the power consumption increases with an increase in build volumes as well as the number of extruders.

Table 3.6: Energy consumption in FFF processes as a function of build volumes and extruders.

Build volumes (l)	**Number of extruders**	**Energy rating**
4.9 – 18.7	1	150 – 350 W
4.4 – 31.5	2	320 – 600 W

Energy consumption during post-processing stage is mainly from the debinding and sintering stages; energy consumption during this stage has been previously described in section 3.1.1.3.

3.2. Process parameters

Process parameters described here refers to the machine parameters influencing the green part produced by the 3D printer. Layer-by-layer processing being a common feature in all 3D printing processes, process parameters common to all the described processes will be discussed. These parameters include layer height, part orientation, nozzle diameter and laser spot size.

Slicing is a critical step during the preparation of parts prior to being additively manufactured, involving division of part into several 2D layers parallel to the build surface. Increasing the number of layers reduces the thickness of layers and vice-versa. Having an impact on the attainable resolution perpendicular to the build surface i.e. increasing the number of layers provides greater resolution of part features but at the same time significantly increases build time [193]. However, capabilities of each individual process must also be considered, for example FFF process have minimum layers heights within the range of 50 – 350 μm but whereas stereolithography techniques can produce layer thickness within the range of 25 – 100 μm.

Part orientation is position of the part with respect to the build plate of the 3D printer. It decides the necessary support structures required to ensure sufficient contact with the base plate. Process such as FFF, SLM and SLA process require supporting structures when overhangs are angled greater than 60° [193]. However, some SLS, BJ and direct writing technologies do not require support due nature of these processes. Selection of suitable part orientation will depend on available build area and number of parts to be produced in case of ceramic based 3D printing processes.

Resolution of produced in case of FFF and Powder based techniques are dependent on nozzle diameter and laser spot size respectively. Nozzle diameter can be easily changed in FFF process, and they usually range between 0.1 – 2 mm in diameter. Larger nozzle sizes can deposit higher quantity of material, thereby reducing build times but at the cost of resolution. Spot sizes in powder-based system work in a similar function, increasing spot sizes causes a loss in resolution in the XY direction but increases productivity.

The above described processing parameters remain similar for all additive manufacturing processes, but certain processes have special conditions that need to be met prior to deciding these processing parameters.

3.2.1. Slurry based processes

Stereolithography based AM techniques utilised to process ceramics relay on selective curing of the photosensitive polymer. The interaction between light and the slurry is chemical in nature governed by Beer-Lamberts law shown in equation (1). Incident light causes epoxy or acrylate resins to initiate a chemical reaction causing them to polymerise. Cure depth (C_d) shown in equation 1 indicates the depth of this reaction, D_p indicates the ability of the light to penetrate the slurry. Factors such as laser power (P_L) , scan speed (V_s), W_o (radius of laser beam) and E_c (critical exposure) are the processing parameters that can be adjusted for all slurry based 3D printing processes [193].

$$C_d = D_P \ln \sqrt{\frac{2\,P_L}{\pi W_o V_S E_C}} \tag{1}$$

Laser power (P_L) is only relevant in case of laser based systems, incident power of the beam must exceed the critical energy (E_c) value of the slurry to initiate the previously

described chemical reaction. Solid particles added cause scattering of the incident light, limiting the light involved in initiating chemical reactions [228]. Further they have also shown to behave as heat sinks, limiting the energy available for propagation of the chemical reaction. Scan speed (V_s) describes the speed at which the laser rasters across build surface, faster scan speeds result in higher build rates but can also reduce the energy received at a single point. A combination of these factors largely influences the cure depth formed, thereby affecting the final part produced [193].

Light projection-based system as previously described use light projector that causes photopolymerization reaction as opposed to using a laser. This simplifies the relationship of cure depth (C_d) and incident energy to equation 2 [193].

$$C_d = D_p e^{\frac{-H.T}{E_c}} \quad (2)$$

Where cure depth is only function of incident irradiance (H) and exposure time (T), limiting the processing variables compared to laser-based systems.

Layer thickness chosen while preparing the part, must be chosen according to the identified cure depth (C_d), as a rule of thumb the it must be within 60% of the achievable cure depth to ensure there is sufficient adhesion to previous layers [193].

Rate of deposition is a critical parameter in case of robocasting and direct ink writing process used for 3D printing ceramics. In case of direct ink writing uncontrolled increase in rate of deposition will lead to droplet formation or damaged nozzle tips. In case of robocasting the flow rate (Q) is limited by the maximum shear rate (γ_{max}) of the nozzle as given in equation 3 [202]. Deposition rates lying between 5 mm/s to 50 mm/s is known

to provide good shape tolerance [196], however individual slurry and nozzle properties must be considered in its choice. Further robocasting process has been known to uses larger nozzle sizes in the range 100 – 1000 μm to prevent clogging.

$$\Upsilon_{max} = \frac{4Q}{\pi r^3} \qquad (3)$$

3.3. Quality control technique

Quality control (QC) is an essential step to ensure printed parts meet the requirements of the design and ensure consistency during production. Shown in Figure 3.5 is the general steps performed during the development of the 3D-printing process. Development phase allows the user to identify critical parameters, optimisation techniques, process-effect interrelations and degree of compliance with user requirements. Once compliance has been met, process can be utilised for production activities.

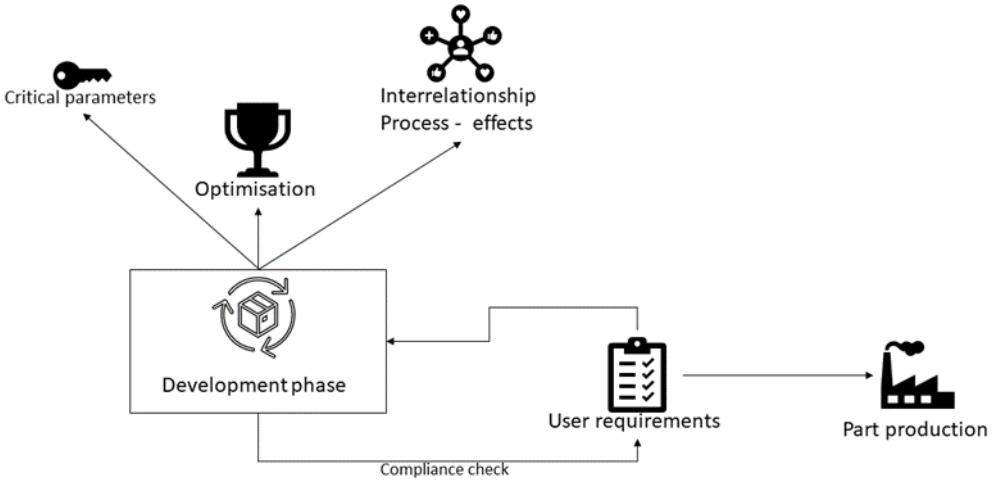

Figure 3.5: Description of tasks during development phase and their relationship to production.

QC during the production stage identifies dimensional accuracy, defects and features that do not comply with the specified requirements. Thereby, limiting rejection rates of parts further down the production line.

Dimensional accuracy of produced parts are checked using manual measurements and standard gauges fabricated to meet the specified user requirements. Complexity of 3D printed parts make conventional measurement techniques unsuitable, there automated systems such as co-ordinate measuring machines (CMM) are used for this purpose instead. Touch probes present on the CMM map out all the relevant dimensions and identifies deviation from specified drawings [229]. However, this process is extremely slow and cannot be used during in-line quality control procedures. Instead, standard gauges fabricated according to the specified requirement provide a quick but effective screening technique to separate defective parts [230, 231]. However multiple gauges might be required in case of complex 3D printed designs, thereby behaving as a bottleneck in the production process.

Porosity in ceramics parts having significant effect on their own mechanical performance, densification process is unable to eliminate large pore sizes. Therefore, QC process must ensure they remain within a specified limit after 3D printing ceramics. Ultrasonic non-destructive techniques are used to detect pores and their sizes, screening out defective parts produced [232]. However, this technique is slow and is requires to be measured after the sintering process. With the development of new technologies, high speed cameras or scanners mounted inside machine build chambers can detect and measure the porosity to high accuracies. Allowing the compliance check of the 3D printed part to specified requirements before parts move further down the production processes [233, 234].

Similar process can be used to estimate parameters such as surface roughness layer adhesion and density of 3D printed ceramic parts [235, 236].

Multi-material ceramics require switching nozzles or slurry vats, causing contamination of layers. Low volumes of this contamination prevent their detection, therefore they only way to is to eliminate this contamination. Studies have shown the effectiveness of automatic cleaning or solvent purging system being prior to processing the next material to prevent contamination in slurry-based processes [237, 238].

In-situ techniques on the other hand use computer vision coupled with artificial neural networks to modify processing parameters during the process, suitably to produce parts meeting the user requirements (as shown in Figure 3.6). This will assist in reducing defective parts [239], especially in cases where production quantities are large and stopping production is more expensive than the impact of defective products. However, the only challenge to this lies in fact that artificial neural networks require large quantities of historical data to make such decisions. While this is ideal for defects within specified limits of the artificial neural network, larger defects requiring redevelopment.

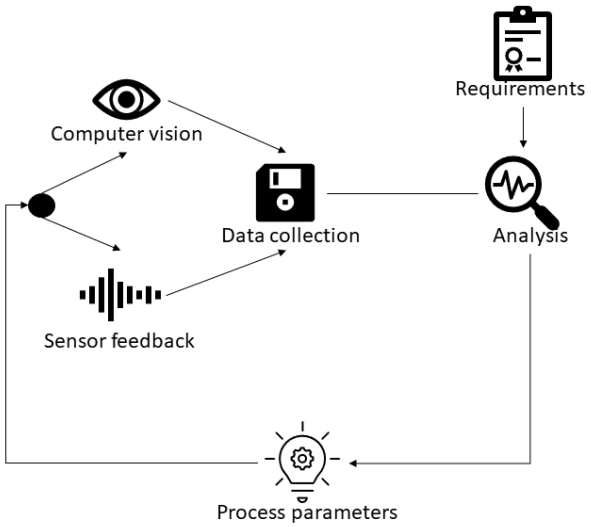

Figure 3.6: Closed loop feedback system for in-situ quality control during AM processes.

Development phase is typically a lengthy process, involving the use of long statistical experiment designs but with recent improvement in technology has enabled the faster development of optimum parameters. For example, predictive porosity models are able to utilise data from machine setting parameters and interpret into physical effects during the process, thereby increasing the efficiency of process optimisation [240]. Most ceramic 3D printing techniques require the use of low temperature polymer phases, polymerisation of these phases during 3D printing releases heat causing distortions in part dimensions. Studies have shown that multi-physics modelling tools currently available can co-relate specific machine parameters to part features observed prior to 3D printing, thereby speeding the development process [241].

3.4. Guidelines for technology selection

Each of the ceramic 3D printing techniques discussed in previous sections seems to have unique advantages and limitations, therefore selecting a technique for ceramic part production can be a multifaceted process. The pre-processing complexity, processing speed, build size and post-processing steps widely differ based on the 3D printing

technique selected. Understanding the features of each 3DP process and relating them to the design and production requirements of the ceramic parts is critical for technology selection. The map below classifies the relative complexity, significance and capability of all the ceramic 3D printing techniques discussed. In conclusion, this map can be used as a guide for technology selection to 3D printing ceramic materials.

3D printing process		Pre-processing		Processing							Post processing		
		Ceramic loading	Preparation complexity	Support Structures	Process speed	Build volume	Productivity	Defect generation	Energy consumption	cost	Debinding	Sintering	Other
Slurry based porcesses	Stereolithography	>55vol%	High	Yes	Very slow	Very small	Low	Less likely	High	High	Required	Required	None
	Vat-polymerisation	>50vol%	High	Yes	Slow	Very small	Low	Less likely	High	High	Required	Required	None
	Robocasting	>40vol%	Low	No	Very fast	Very large	High	Likely	Low	Low	Required	Required	Surface finishing
	Direct Ink writing	>50vol%	High	Yes	Fast	Very small	Low	Less likely	Very low	High	Required	Required	None
Powder based processes	Selective laser melting	100%	None	Yes	Slow	Medium	Medium	Highly likely	Very high	High	Not required	Not required	Surface finishing
	Selective laser sintering	>50vol%	low	No	Slow	Medium	Medium	Likely	High	Medium	Required	Required	Surface finishing
	Binder jetting	94wt%	High	No	Fast	Medium	High	Less likely	Low	Medium	Required	Required	Surface finishing
Bulk solid based processes	FFF	>45vol%	High	Yes	Very fast	Large	Very high	Likely	Low	Low	Required	Required	Surface finishing

Figure 3.7: Guide for additive manufacturing technology selection based on process requirements.

3.5. Applications of Ceramics

Ceramics are characterized by high mechanical strength and hardness, good thermal and chemical stability. These properties make ceramics ideal for a wide range of applications such as the chemical industry, catalyst support, electronics, aerospace, and biomedical engineering. Some of these applications require highly complex shapes, high dimension accuracy and lightweight ceramics that cannot be produced by conventional ceramic processing techniques [192]. Therefore, 3DP has become very attractive allowing the production of ceramics with complex shapes, porosity and multimaterials. Highly porous

ceramics characterized by low density and good mechanical properties can be used for many value-added applications such as filtration membranes, catalyst supports, lightweight materials and tissue-engineering scaffolds. 3DP is a suitable technique to produce customized shapes with hierarchical structures. The structure and type of pores (close or open pores) impact on mechanical and thermal properties of ceramic parts. Ceramic specimens with an open porosity of 83%–94% have shown a compressive strength between 3 and 16 MPa. Another study demonstrated the production of hierarchical scaffolds with a porosity between 4 nm and 400 μm [242]. 3DP has revolutionized the manufacturing industry and is suitable for the preparation of ceramics with hierarchical and honeycomb structures, but the control of porosity is still challenging [242].

Biomedical scaffolds have to be precisely designed to meet the requirements of the living host such as bioactivity, biocompatibility, biodegradability, mechanical properties, structure, and architecture. The size of the pores in the scaffold architecture is fundamental for all the cellular steps: cellular adhesion, migration, proliferation, differentiation and colonization of cells. However, the architectural design must also take into consideration the mechanical properties required for the specific anatomical site. 3DP has a great potential to tailor-made biomedical products to specific patients,then significantly reduce the adaption phase to the new product. With the need of customizing to the patient, 3DP is a suitable and cost-effective technique to produce biomedical ceramics compared with conventional manufacturing methods. 3DP technology is suitable for the production of complex and highly porous hierarchical structures required for biomedical scaffolds, but obtaining ceramics with high mechanical properties with simultaneously high bioactivity, biodegradability and biocompatibility is still under development [243].

3.6. Conclusions and Perspectives

3DP has been an area of great interest mainly due to its ability to process a wide range of material classes and provide the unrestricted designing ability. Utilizing this technology for the processing of ceramics has vastly increased their scope of usage in different applications such as biomedical scaffolds, chemical filtration and high-performance aerospace components. Even with significant achievements around 3DP technology, its adoption for processing ceramics is still very slow. This has arisen primarily due to the uncertainty in feedstock material requirements for each process and the influence of processing parameters on the final part. In this chapter, a summary of the feedstock requirements for each ceramic 3DP process has been provided and key processing parameters influencing these processes are briefly discussed. This was followed by a brief comparison of the energy consumption of each process which is a crucial consideration for commercial applications. Based on this information, a technology selection guide has been developed that can assist in understanding the demands of each process and their relative difficulty. This information is crucial to narrowing down suitable 3DP technologies for specific ceramic applications.

Technological advances in 3DP are making this technology more reliable and affordable for processing technical ceramics. While the challenge to scale-up build sizes in these cases still requires attention from the broader research community. More recently, sustainability becoming a driving factor in various industries, and energy consumption of these processes from raw materials to fully sintered parts must be studied to understand the full impact of 3DP adoption. Finally, optimization of material composition, 3DP processing parameters and sintering conditions are required to not only increase the available technical ceramics that can be processed using 3DP technology, but also to make the production of fully dense ceramics using 3DP more versatile and efficient.

4. Optimisation of two-step sintering parameters to produce bioactive and dense Zirconia-Hydroxyapatite composite ceramics

Abstract

3Y-TZP along with Hydroxyapatite (HAp) are common bioceramics used in BTE scaffolds to yield better patient outcomes and faster healing times. However, significant differences in thermal expansion of these ceramics result in challenges to co-sintering these materials without losing functionality and strength. In this work, a two-step sintering (TSS) process was utilised to co-sinter composites using (1-x)3Y-TZP and xHAp where x varies between 20 and 80 wt%. A peak temperature of 1300 ℃, a plateau temperature of 1175 ℃ and heating rate of 10 ℃/min were the optimum TSS conditions for all compositions, holding time of 600 min. The TSS process produced specimens with grain sizes between 0.5 and 1.2 μm and a compression strength between 88 and 176 MPa. The similarity in compression strength of these zirconia-hydroxyapatite composites with natural bone and the retention of HAp make them suitable for BTE applications in load-bearing areas.

4.1. Introduction

Zirconia (ZrO_2) is a commonly used biomedical ceramic due to its ability to withstand high stresses prior to failure and remain bioinert when implanted. Transformation toughening observed in partially stabilised ZrO_2 offers significant advantages in preventing crack propagation, thus enabling its usage in load-bearing applications [61, 245]. To introduce transformation toughening, the tetragonal Zirconia (t-ZrO_2) must be partially stabilised through the addition of dopants such as Yttria (Y_2O_3) or Ceria (CeO_2). Y_2O_3 is the most used dopant for stabilisation of t-ZrO_2, its addition ranges between 3 and 8 mol% depending on the extent of stabilisation required. Previous studies have shown that while partially stabilised ZrO_2 has sufficient mechanical strength, lack of bioactivity prevents any interaction with the host body [62, 246]. Osteoinduction and osteoconduction are essential mechanisms for bone healing and only occur when implanted scaffolds positively interact with the host body [21]. Thus, partially stabilised ZrO_2 being bioinert is unable to be used in BTE applications.

Hydroxyapatite (HAp) is a widely used ceramic for BTE applications due to its chemical similarity to natural bone tissue. HAp, being native to human bone tissue, is osteoconductive and osteoinductive when implanted inside the body, promoting interactions with the host body [247]. The compression strength of HAp lies between 10 and 40 MPa which decreases as porosity increases, natural bone on the other hand is known to possess compression strengths up to 200 MPa [248, 249]. Therefore, the low mechanical strength of HAp prevents its application in load-bearing areas. To address these shortcomings and take advantage of its functionality, composites containing HAp are often used in biomedical applications in the form of coatings and dispersions. For example, Mondal et al. [250] showed that fabricated polylactic acid (PLA) scaffolds, when coated with thin layers of HAp, showed significant improvements in cell attachment and

compression strength. However, low adhesion between the HAp coatings and the substrate prevented the application of these composites in load-bearing BTE applications [251].

Composites containing ZrO_2 particles are known to enhance yield strength by restricting crack propagation and minimising grain growth. For example, Zhang et al. [104] showed an improvement in tensile and bending modulus of the hydroxyapatite ceramics with up to 6 wt% of zirconia. The zirconia (ZrO_2) particles dispersed in the hydroxyapatite matrix functioned as pinning sites preventing grain boundary migration or growth during the sintering process, resulting in an improvement in mechanical performance. Ferreira et al. [252] showed that having up to 20 wt% of HAp in a zirconia-hydroxyapatite composite significantly improved the compression strength. Further, the implanted scaffold demonstrated an increase in bone mineral density and improvement in osseointegration when implanted in a rat model [252]. The implications of combining ZrO_2 with HAp look very promising, but there are challenges in incorporating more than 15 wt% of HAp in these composites due to HAp low phase stability at temperatures exceeding 1100 °C, causing phase transformations into α-tricalcium phosphate (α-TCP), β-tricalcium phosphate (β-TCP) or other spinel phases during the co-sintering process with ZrO_2 [252, 253]. In-situ phase reactions of HAp in presence of ZrO_2 are known to release H_2O which increase the porosity of the structure and consequently reduce their ability to bear load [254]. Mismatch in thermal expansions of ZrO_2 and HAp introduces residual stresses during the co-sintering process, these residual stresses can improve the strength of the composite or introduce defects depending on the orientation of these materials within the composite. Wang and Xiao [255] showed that electrophoretic deposition of yttria-stabilised zirconia/alumina coatings on Ferroalloys developed tensile stresses during the sintering process. The nature of these residual stresses was shown to change from compressive to tensile with increasing coating thickness, therefore, leading to coating failure [255]. On the other hand, zirconia and alumina ceramic blends developed compressive stresses during the sintering process (due to thermal mismatch) leading to an improvement in

fracture toughness [256]. With multiple processes occurring in addition to densification, single step conventional sintering processes are unable to simultaneously ensure densification and control phase reactions. Further, in conventional sintering processes, exposure times exceeding 300 min at the sintering temperature are required to achieve full densification leading to grain growth. Fracture strength of 3Y-TZP ceramics can be improved up to a critical grain size of 2 μm due to enhanced transformability of the tetragonal phase; however, further increase in grain sizes will lead to a reduction in fracture strength [257].

Two-step sintering (TSS) introduced by Chen and Wang can produce fully dense ceramics with minimal grain growth [258]. Sintering parameters in the TSS process include: (1) Peak temperature (T_{peak}); (2) Plateau temperature ($T_{plateau}$); (3) heating rate (H_r) (°C/min); and (4) Holding time (T_H) (min). Kinetics of the sintering process indicate that pre-firing ceramic at a higher T_{peak} enables the formation of triple point junctions due to the energy available to overcome the activation energy of the ceramic [259]. The immediate decrease in sintering temperature to $T_{plateau}$ locks the triple point junctions in place restricting grain boundary or junction mobility and hence preventing grain growth during densification [260]. The ability of TSS to control grain size has been previously demonstrated in the case of 3Y-TZP [64]. However, in the case of ceramic composites, interaction between crystalline phases can influence the densification process. For example, zirconium diboride (ZrB_2) containing 4 wt% of boron carbides (B_4C) could undergo full densification when sintered at 1850 ℃ for 60 min. Reactions between the B_4C and ZrB_2 ceramics during the sintering process eliminated oxide impurities presented in ZrB_2 particles and enhanced densification [261]. Formation of these grain boundary phases during phase reactions can affect mechanical, electrical, or thermal properties of ceramic composites. Therefore, controlling the extent of phase reactions between 3Y-TZP-HAp ceramics at specific sintering conditions is critical to avoid the formation of unwanted crystalline phases during the co-sintering process. Therefore, the two knowledge gaps identified from the current literature include: (1) the impact of the addition

of more than 15 wt% of HAp in 3Y-TZP-HAp composites have not been explored; (2) usage of TSS process to co-sinter 3Y-TZP-HAp ceramics to retain sufficient strength and functionality for usage in BTE applications has not been investigated in previous studies.

In this study, HAp content was varied between 20 and 80 wt% in the 3Y-TZP-HAp composite. Critical TSS parameters influencing the formation of new crystalline phases, and the densification process were identified by carrying out a 5-factors 4-levels Taguchi experiment, which were then optimised using a factorial experiment. Further, quantification of crystalline phases, grain size and compression strength of the 3Y-TZP-HAp ceramic pellets sintered at optimised conditions was carried out.

4.2. Methods and Materials

Commercially available 3 mol% Yttria stabilised zirconia powder (Tosoh, Japan) and nano-structured hydroxyapatite powders (Fluidinova, Portugal) were used to prepare the composite mixtures, properties of these raw materials are shown in Table A2. 3Y-TZP and HAp powders were weighed out according to the mass ratios specified in Table 4.1 ethanol was then added to the mixture to disperse the powder particles and form a slurry. The slurry was blended in a Silversons L5M-A laboratory mixer for 60 min, to produce a uniform slurry that was subsequently dried in a laboratory oven at 60 °C. The dried composite powder was pressed into pellets using a die of diameter 20 mm and applying a pressure of 125 MPa. The pressed pellets were then sintered according to conditions specified in the Taguchi based experiment design as shown in Table 4.1.

Table 4.1: Factors and parameters of the two-step sintering process considered in the experiment design using both Taguchi (preliminary experiment) and factorial (optimisation experiment) methods.

Stage 1 - Taguchi Design		**Two-step sintering parameters**			
Factors	Composition (3Y-TZP wt%: HAp wt.%)	Peak temperature (°C)	Plateau temperature (°C)	Holding time (min)	Heating rate (°C/min)
	90:10	1400	1350	1200	20
	70:30	1350	1300	900	15
	50:50	1300	1250	600	10
	30:70	1250	1150	300	5
Stage 2 - Factorial Design					
	70:30		1150	600	
	50:50	1300	1175	900	10
	30:70		1200	1200	

This study was performed using a two-staged approach illustrated in Figure 4.1. The 1st stage consisted of identifying critical parameters of the TSS process to produce 3Y-TZP-HAp composite pellets with relative densities greater than 98% and retain key crystalline phases (t-ZrO2 and HAp).

The range of TSS conditions for 3Y-TZP-HAp composites were identified for designing the 5-factors 4-levels Taguchi experiment using previous literature. Analysis of the Taguchi experiment results of samples ZH1 – ZH16 (shown in Table 4.1) showed that the plateau temperature ($T_{plateau}$) and holding time (T_H) had a large influence on the crystalline phase composition and density of the co-sintered composites. To optimise the co-sintering conditions, a factorial experiment was then designed to optimise the plateau temperature and holding time for three compositions ZH18, ZH17 and ZH19 (70 wt% 3Y-TZ : 30 wt% HAp , 50 wt% 3Y-TZP : 50 wt% HAp and , 30 wt% 3Y-TZP: 70 wt% HAp) using a peak temperature of 1300 °C and heating rate of 10 °C/min. The parameters considered for the optimisation of the TSS process (factorial design) are shown in Table 4.1.

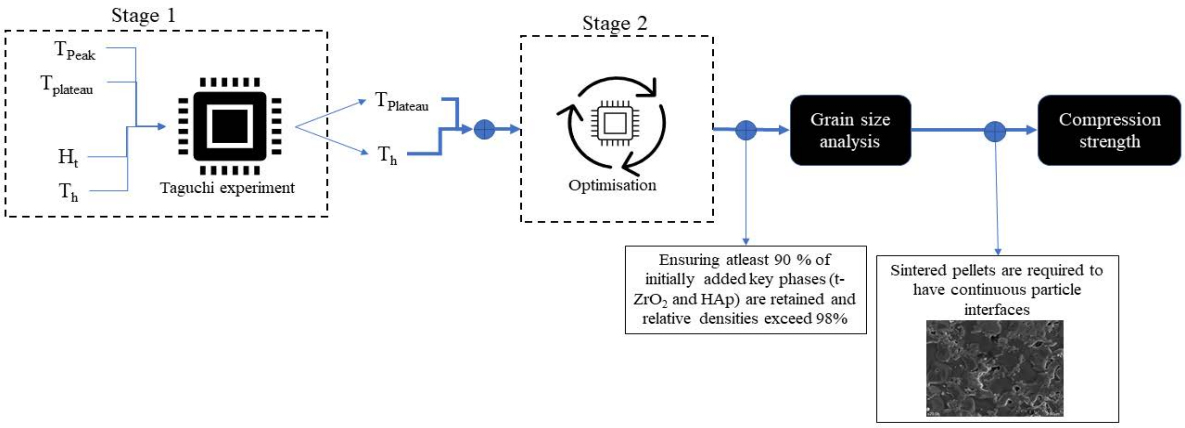

Figure 4.1: Overview of the two-staged approach used to optimise TSS conditions for the 3Y-TZP-HAp composites to ensure maximum functionality, density and strength.

Table 4.2: Phase composition and density of samples analysed for the Taguchi experiment.

	Sintering conditions					**Phase composition**					**Density measurement**		
Sample	Composition (3Y-TZP wt%: HAp wt%)	T_{peak} °C	$T_{plateau}$ °C	$T_{holding}$ min	Heating rate °C/min	Y-TZP-tetragonal wt%	ZrO2-Ca cubic wt%	HAp wt%	α-TCP wt%	β-TCP wt%	Theoretical density g/cc	Experimental density %	g/cc
ZH1	90:10	1250	1150	1200	5	83.4	5.9	5.2	4.4	1.2	5.73	94.56	5.42
ZH2	70:30	1300	1250	300	15	34.2	33.4	2.6	29.7	0.1	4.91	96.92	4.76
ZH3	70:30	1400	1150	1200	10	52.9	21.8	3.4	23.3	0	5.22	87.23	4.56
ZH4	30:70	1300	1150	1200	20	16.5	12.1	70.6	0.7	0	3.96	93.72	3.72
ZH5	90:10	1300	1250	900	10	68.4	15.4	0.9	15.2	0	5.49	96.92	5.33
ZH6	30:70	1350	1250	600	10	27.0	5.0	65.0	1.8	1.0	4.07	89.31	3.64
ZH7	50:50	1350	1300	1200	15	12.4	30.4	0.7	56.5	0	4.12	94.11	3.88
ZH8	50:50	1300	1150	600	10	40.7	15.0	10.2	33.6	0.5	4.63	86.40	4.00

ZH9	30:70	1250	1150	900	15	16.1	9.5	59.0	15.4	0	3.83	100	3.83
ZH10	90:10	1400	1350	600	15	54.5	24.5	0.8	19.7	0.7	5.31	94.65	5.03
ZH11	30:70	1400	1300	300	5	12.0	2.3	15.1	70.2	0.2	3.36	100	3.36
ZH12	50:50	1400	1250	900	20	41.7	1.4	0.6	55.8	0.5	4.24	93.66	3.97
ZH13	70:30	1250	1150	600	20	63.7	16.8	5.4	13.6	0.5	5.40	85.33	4.61
ZH14	90:10	1350	1150	300	20	75.9	7.7	4.2	12.2	0	5.53	95.41	5.27
ZH15	70:30	1350	1250	900	5	46.3	24.3	2.7	26.5	0.3	5.04	90.94	4.59
ZH16	50:50	1250	1150	300	10	51.6	4.84	42.6	0.6	0.3	4.79	87.18	4.18

4.2.1. Characterisation of sintered pellets

The crystalline phases of sintered composite pellets were characterised using X-ray diffraction (XRD, Bruker D2 PHASER). The XRD scan was set between 10˚ and 80˚ with a step size of 0.02° for a dwell time of 1 sec/step. The XRD profiles were then analysed using Profex to perform Rietveld refinement and determine the phase composition of the sintered pellets [262]. The statistical parameter (χ^2) determined during the Rietveld refinement indicated the quality of the fit (shown in Table A3). The density of the samples was measured according to the procedure described in ISO 18754 and compared to the theoretical densities calculated by using the quantity of crystalline phases identified from Rietveld refinement of the XRD [263].

Scanning electron microscopy (SEM, Hitachi SU5000) was used to characterise surface morphology and energy dispersive spectrometry (EDS) was used to identify elemental composition of the sintered pellets. Pellets for SEM-EDS were mounted in clear epoxy resin and then ground using a diamond disc until a plane surface was obtained, followed by fine grinding using 9 μm and 3 μm diamond particle suspension for up to 10 min each. Samples were then polished using OP-S solution until the surface of the pellet had a mirror-like finish. Polished samples were removed from the epoxy resin and thermally etched at a temperature 100 ℃ lower than the corresponding $T_{plateau}$. Only ceramic pellets with fired densities greater than 98% were further analysed for grain size quantification according to the procedure described in the ASTM E112-13 [264].

While retention of bioactive phases is critical for producing bone healing responses, achieving densification greater than 98% and retention of more than 90% of the initial t-ZrO_2 phase content in 3Y-TZP-HAp composites is fundamental for applications in load-bearing areas of the body [265]. However, the presence of multiple crystalline phases in the ceramic composite pellets initiate the formation of spinel phases or phase transformation in addition to densification [266,

267]. The extent of these interactive effects and their relationship with TSS parameters are explored in the later sections (4.3.1, 4.3.2 and 4.3.3).

4.2.2. Compression test of ceramic pellets

Ceramic pellets with relative densities greater than or close to 95% or having the ability to retain 90% of their initial key crystalline phases (t-ZrO_2 and HAp) were used for compression strength characterisation. SEM images of the selected samples were analysed to ensure interfaces between grains are uniform, since improper transmission of cracks occurs in regions with discontinuous interfaces, therefore, affecting the compression strength [268]. The selected ceramic pellets were compressed (using the setup shown in Figure 4.2) at a crosshead speed of 0.1 mm/min to determine the compression strength and an average value was calculated from three tests.

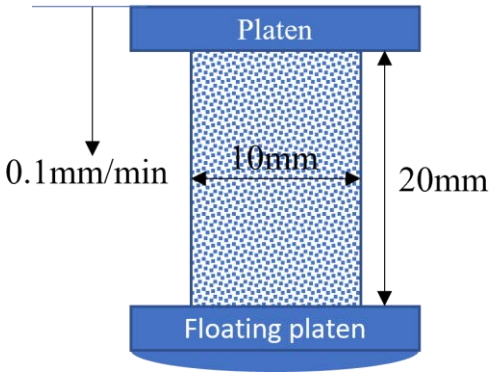

Figure 4.2: Setup describing compression tests carried out on 3Y-TZP-HAp composite pellets.

4.3. Results and discussions

4.3.1. Criticality of TSS parameters on crystalline structure and density

Results from the 1st experimental study (Table 4.1) indicated a strong influence of $T_{plateau}$ and T_H on crystalline phase retention and densification. At a $T_{plateau}$ of 1300 °C, less than 10% of the initial HAp was retained at all holding times while the remaining content was replaced by the alpha-

tricalcium phosphate (α-TCP) across all composites. Therefore, $T_{plateau}$ values equal or greater than 1300 °C were unsuitable for the co-sintering of these two materials (3Y-TZP and HAp). Similar results were found in other studies as the lack of stability of HAp at temperatures beyond 1100 °C causes dehydration leading to the transformation into hydroxyoxyapatite ($Ca_{10}(PO_4)_6\ O_x\ (OH)_{2(1-x)}$) as shown in equation (3) where x represents the quantity of water [269, 270]. Longer exposure to temperatures greater than 1000 ℃ causes the breakdown of hydroxyoxyapatite into α-TCP or β-TCP as shown in equation (4); the decrease in HAp content results in the formation of calcium oxide (CaO).

$$Ca_{10}(PO_4)_6(OH)_2 \rightarrow Ca_{10}(PO_4)_6\ O_x\ (OH)_{2(1-x)} + \uparrow x\ H_2O \quad (3)$$

$$Ca_{10}(PO_4)_6\ O_x\ (OH)_{2(1-x)} \rightarrow 3(\alpha,\beta)\ TCP + CaO + (1-x)\ H_2O \quad (4)$$

For all holding times and a $T_{plateau}$ of 1300 ℃ only 50% of the initial t-ZrO_2 phase was retained across all composites. Diffusion of the CaO, formed in the previous step, leads to the transformation of t-ZrO_2 to calcium stabilised ZrO_2 (Ca-c-ZrO_2) or calcium zirconate ($CaZrO_3$) as shown in equation (5) [254]. The extent of diffusion appears to increase with an increase in holding time as shown in Table 4.1.

$$ZrO_2 + CaO \leftrightarrow CaZrO_3 \quad (5)$$

At a $T_{plateau}$ of 1250 ℃, close to 90% of the initial t-ZrO_2 was retained irrespective of the holding time and produced composite pellets with fired densities between 90 and 96%. Formation of Ca-c-ZrO_2 observed at a $T_{plateau}$ of 1250 °C depended only on the chemical ratio of ZrO_2 and HAp

phases. For example, compositions containing more than 70 wt% 3Y-TZP (ZH15, ZH2 and ZH5) resulted in the formation of up to 40 wt% of Ca-c-ZrO_2 phase while compositions containing 50 wt% or less of 3Y-TZP (ZH6 and ZH12) showed less than 5 wt% of Ca-c-ZrO_2 after sintering. This indicates that the diffusion reaction shown in equation (5) is not only dependent on temperature but depends also on the amount of 3Y-TZP and HAp present in the sample. 3Y-TZP-HAp composites initially containing 30 wt% or more of 3Y-TZP and sintered at $T_{plateau}$ of 1250 °C exacerbated the dehydration reaction shown in equations (3) and (4), losing up to 95% of the available HAp content. Simultaneously, the α-TCP content increased to more than 90% of the initial HAp content in all ceramic composites containing 30 wt% or more of 3Y-TZP, which is similar to the results obtained at a $T_{plateau}$ of 1300 °C. Compositions (ZH11, ZH7 and ZH10) sintered at $T_{plateau}$ close to the eutectic temperature of the α-TCP phase (1287 °C) showed a significant reduction in ZrO_2 content. Gremillard et al. [271] showed that in Al_2O_3 – HAp composites, the α-TCP liquid phase formed at sintering temperatures greater than 1287 °C migrates to the surface masking the ZrO_2 composition. XRD analysis performed on ZH11 before and after polishing the top surface as shown in Figure A1a show a loss in α-TCP phases. SEM-EDS shown in Figure A1b and c of the cross-section revealed Ca rich regions at the surface of the pellet as compared to the bulk. Therefore, $T_{plateau}$ values equal or greater than 1250 °C is unsuitable for the retention of HAp and t-ZrO_2.

At a $T_{plateau}$ of 1150 °C more than 50% of the initial t-ZrO_2 phase is retained without conversion into Ca-c-ZrO_2. Retention of HAp in most sintering conditions (ZH1, ZH3, ZH13, ZH14), is less than 10 wt%; however, in compositions initially containing 70 wt% of HAp retention is greater. Only ZH14, ZH4 and ZH1 showed densification greater than 90%. Among them only ZH4 retained more than 50 wt% of the initial HAp composition. Reduced sintering driving force at this $T_{plateau}$ temperatures has limited the extent of densification to less than 90% in most compositions.

Increasing holding time from 300 min to 900 min at all $T_{plateau}$ values, increased the formation of Ca-c-ZrO_2 as well as α-TCP. Long exposure times allowed for the completion of chemical reactions shown in equations (3), (4) and (5), leading to the increase in Ca-c-ZrO_2 and α-TCP. For example, ZH3 (70 wt% 3Y-TZP: 30 wt% HAp) composition with a holding time of 1200 min demonstrated a 20 wt% loss in t-ZrO_2. In contrast, ZH13 (70 wt% 3Y-TZP: 30 wt% HAp) with a holding time of 600 min only lost 10 wt% in t-ZrO_2 phase while exposed to the same $T_{plateau}$ temperature (1150 ℃). Further, increasing holding times led to an increase in the formation of α-TCP and Ca-c-ZrO_2 with corresponding losses in HAp and t-ZrO_2, respectively. However, compositions initially containing 30 wt% or more of 3Y-TZP and sintered at $T_{plateau}$ values less than 1250 ℃ showed a higher retention of HAp when T_H was increased to 1200 min. Previous studies have indicated the possibility of rehydration of α-TCP and tetracalcium phosphate (TTCP) back into HAp at temperatures less than 1290 ℃ [272, 273]. Therefore, longer holding times at $T_{plateau}$ less than 1250 ℃ can reverse the dehydration process to reform HAp.

Fired densities of samples sintered at a $T_{plateau}$ of 1150 ℃ remained between 85% and 95%. Therefore, $T_{plateau}$ and T_H can be further optimised to maximise the retention of key crystalline phases (t-ZrO_2 and HAp) and increase the fired densities. Based on the preliminary results $T_{plateau}$ values of 1200 °C, 1175 °C and 1150 °C were selected for further optimisation. Similarly, holding times of 600, 900 and 1200 min were selected for the optimisation study (stage 2).

Heating rates explored in this study did not have major impacts on phase reactions but showed a minor influence on the extent of densification (shown in Table 4.1). An increase in heating rates from 5 °C/min to 10 °C/min resulted in a decrease in the retention of t-ZrO_2 and HAp. For example, compositions containing 70 wt% of 3Y-TZP (ZH15 and ZH2) that were exposed to the same $T_{plateau}$ temperature showed an increased loss in t-ZrO_2 phase when heating rate was increased from 5 ℃/min to 15 ℃/min. While this trend was observed across most samples, Ji, et al. [274] reported

the difficulty in isolating the effect of heating rate from sintering temperature and holding time at sintering temperatures close to 1300 ℃. For example, ZH13 (70 wt% 3Y-TZP: 30 wt% HAp) sintered at $T_{plateau}$ of 1150 ℃ retained 64 wt% of the initial t-ZrO_2 phase when heated at 20℃/min. However, ZH3, while having a similar composition and sintered at the same $T_{plateau}$, retained only 53 wt% of t-ZrO_2 when heated at 10℃/min. The heating rates of these two compositions differed by 10℃/min, also their holding times for the compositions differed by 600 min (ZH3 > ZH13). Therefore, it is unclear if it was the larger holding time of ZH3 composition or the higher heating rate of ZH13 that was responsible for loss of t-ZrO_2. This observation clearly highlights the limitation of the Taguchi method which is only able to capture major effects leaving out any minor effects. Thus, this trend cannot only be related to the heating rates but also the differences in holding times of ZH13 and ZH3. Therefore, a heating rate of 10 °C/min was chosen, as it produced specimens with fired density exceeding 90% across all compositions while ensuring retention of large quantities of key crystalline phases (t-ZrO_2 and HAp).

Peak temperatures below 1300 ℃ showed only a minor influence on the crystalline phases post sintering. For example, in compositions containing 70 wt% of 3Y-TZP (ZH3 and ZH13) a 150 °C increase in T_{peak} amounted for less than 10 wt% change in both t-ZrO_2 and HAp phase content. Short exposure times less than 5 min at all T_{peak} values are insufficient to sustain phase changes, but rather only initiate the densification process and phase changes. Further, increasing T_{peak} values greater than 1300 ℃ resulted in an accelerated degradation of HAp and t-ZrO_2 phases, causing a loss in bioactivity and strength. Therefore, a T_{peak} of 1300 °C was selected for the optimisation study (stage 2 – section 3.2) because there was a retention of 50 - 90 wt% of the initial t-ZrO_2 and HAp crytsalline phase compositions after sintering, while also producing fired densities greater than 90%.

4.3.2. Stage 2 - Optimisation of plateau temperature

To optimise the plateau temperature a factorial experimental design was used, three compositions containing different quantities of 3Y-TZP and HAp (ZH17, ZH18 and ZH19), T_{peak} of 1300 ℃ and heating rate of 10 ℃/min were selected. The study indicated that the optimal plateau temperature lies between 1150 ℃ and 1200 ℃.

Crystalline phase composition of ZH19 (30 wt% 3Y-TZP: 70 wt% HAp) shown in Figure 4.3a indicates that changes in the phase composition only occurred at specific $T_{plateau}$ values irrespective of holding times. Plateau temperature of 1150 °C retained up to 50 wt% of the initial HAp with the remaining undergoing dehydration to form α-TCP as shown in equation (1), this behaviour was observed for all holding times [275]. Figure 4.3a (plots 1, 2 and 3) showed a gradual increase in the extent of the dehydration process with an increase of the $T_{plateau}$ and holding times. As a consequence of the dehydration reaction (shown in equation 1), the newly produced CaO diffuses into ZrO_2, replacing Zr^{4+} ions to form a solid solution of either $CaZrO_3$ or Ca-c-ZrO_2 as shown in equation (3) [268, 276, 277]. However, the quantity of Ca-c-ZrO_2 phase is less than 5% for $T_{plateau}$ values lower than 1200 ℃. While the presence of Yttria in 3Y-TZP is known to increase the diffusion coefficient of CaO into t-ZrO_2 forming Ca-c-ZrO_2 [269], this diffusion process appears to occur only at $T_{plateau}$ greater than 1200 ℃. Kumar et al. [277] showed that the CaO produced during the sintering process could also diffuse into ZrO_2 forming $CaZrO_3$ at sintering temperatures greater than 1000 ℃. Formation of these phases could influence the mechanical and biological properties of the sintered ceramic composite.

Fired density of the sintered samples shown in Figure 4.3a (plots 4, 5, and 6) is within the range of 92% - 98%. $T_{plateau}$ of 1150 °C seems to be insufficient to produce high density composites irrespective of the holding time. At a $T_{plateau}$ of 1200 ℃ there was a small reduction in the extent of densification across all holding times. This primarily arises from the high activation energy oP

ceramics requiring a higher temperature for densification to proceed [278]. A parabolic trend of relative density as a function of $T_{plateau}$ was observed for all conditions with a maximum densification observed at $T_{plateau}$ of 1175 ℃. Therefore, a plateau temperature of 1175 °C appears to provide the optimum conditions to maximise the bioactive phase retention and densification for composition ZH19 (30 wt% 3Y-TZP: 70 wt% HAp).

Crystalline phase compositions of ZH17 (50 wt% 3Y-TZP: 50wt% HAp) are shown in Figure 4.3b (plots 1, 2 and 3) indicating a strong impact of plateau temperature as well as holding time on crystalline phase transformation and densification. Initial crystalline phases (t-ZrO_2 and HAp) undergo transformation at a $T_{plateau}$ equal or greater than 1175 °C across holding times less than 1200 min. Higher quantities of t-ZrO_2 in the ZH17 composition caused rapid dehydration of HAp forming α-TCP. The low quantities of Ca-c-ZrO_2 phases showed that CaO produced during this dehydration process did not diffuse into the t-ZrO_2 phase to form Ca-c-ZrO_2 as previously shown in the ZH19 composition. This could indicate that the CaO available after the dehydration reaction could be forming small amounts of spinel compounds or $CaZrO_3$ that were not detected by XRD due to their low concentrations [269]. $T_{plateau}$ of 1150 °C showed no transformation of t-ZrO_2 and HAp phases at holding times equal or lower than 900 min. However, when T_H is increased to 1200 min there was a 15 wt% and 25 wt% decrease in t-ZrO_2 and HAp phases respectively, and simultaneously an equal increase in α-TCP and Ca-c-ZrO_2 phases was observed. Specifically, at $T_{plateau}$ of 1175 °C and holding time of 900 min there was a 40 wt% decrease in HAp composition from its initial composition while simultaneously there was an equal increase in α-TCP phase, which is consistent with the reactions shown in equations (1) and (2). At $T_{plateau}$ of 1175 °C and holding time of 1200 min, a similar response is observed. $T_{plateau}$ of 1200 °C and holding times greater than 600 min showed a decrease in the retention of t-ZrO_2 and a corresponding increase in Ca-c-ZrO_2 phase composition as shown in Figure 4.3b (plots 2 and 3). Increasing $T_{plateau}$ to

1200 °C enabled the complete consumption of HAp phase and forming a combination of α-TCP (major) and β-TCP (minor).

$T_{plateau}$ of 1150 °C retained the HAp and t-ZrO_2 crystalline phases, but the extent of densification is lower than 95% across all holding times. A $T_{plateau}$ of 1175 °C promoted good densification resulting in densities greater than 95%. The graph of density vs $T_{plateau}$ shows a parabolic trend where the maximum densification was achieved at 1175 °C for holding times less than 1200 min. The optimal temperature for the retention of t-ZrO2 and HAp and achieving densities greater than 95% is at $T_{plateau}$ of 1175 °C for a holding time of 600 min. Increasing holding time by 300 or 600 min at this same plateau temperature increases slightly the extent of densification but leads to 30 wt% drop in HAp content making it biologically less suitable. The depletion of the initial HAp and t-ZrO_2 phases at $T_{plateau}$ of 1200 °C and the formation of lower density phases such as α-TCP, β-TCP and Ca-c-ZrO_2 can potentially impact on the mechanical strength of the composites.

Crystalline phase compositions for the ZH18 (70 wt% 3Y-TZP : 30 wt% HAp) as shown in Figure 4.3c , indicate a dependence on both plateau temperature and holding time, similar to the ZH17 composition. High quantities of 3Y-TZP presented in the composite mixtures further exacerbate the dehydration process of HAp shown in equations (2) and (3). The retention of HAp phase at all sintering conditions was below 30 wt%. Also, the presence of Ca-c-ZrO_2 can be observed across all holding times and plateau temperatures, indicating CaO diffusion into ZrO_2 can occur at all $T_{plateau}$ values (1150 °C, 1175 °C and 1200 °C) for composites containing 70 wt% or more of 3Y-TZP. All $T_{plateau}$ values seems to reduce the quantity of t-ZrO_2 phase present in the sample to less than half of its initial amount, having a potential impact on the mechanical performance. When samples are sintered at plateau temperatures of 1175 °C for 600 min, there is almost a complete conversion of HAp into α-TCP. Correspondingly, at this $T_{plateau}$ temperature of 1175 °C, formation of Ca-c-ZrO_2 seems to be absent, indicating the potential formation of an intermediate phase

hydroxyoxyapatite as shown in equation (2). The formation of the intermediate phase hydroxyoxyapatite is indicated by the high goodness-of-fit ($\chi^2 = 2.17$) values reported during the Rietveld refinement of compositions ZH18_4 in Table A3. Further analysis will be required to better understand the specific influence of this intermediate phase and quantify its amount. Increasing holding time to 900 min or 1200 min at 1175 °C showed a similar trend regarding the loss of HAp, leading to a reduction in fired density of the reported samples. While the higher quantities of 3Y-TZP in ZH18 composition drive the reactions shown in equations (1) and (2), shorter holding times might have prevented the complete transformation of HAp to α-TCP or β-TCP and the production of CaO. When $T_{plateau}$ value is increased to 1200 °C, HAp phase was completely transformed into α-TCP phases across all holding times. This caused a reduction in achievable density of the composite mixture as shown in Figure 4.3c (plots 4 – 6). Fired densities of the pellets showed a low dependence on holding time, remaining between 88 and 95% across all holding times. A plateau temperature of 1175 °C appears to be the optimal temperature considering phase retention of both t-ZrO_2 and HAp along with the highest achieved density for the ZH18 composition. Therefore, the optimum $T_{plateau}$ temperature for sintering the ZH18 composition and simultaneously retaining the highest quantities of t-ZrO_2 and HAp, while achieving densities close to 95% was at 1175 °C.

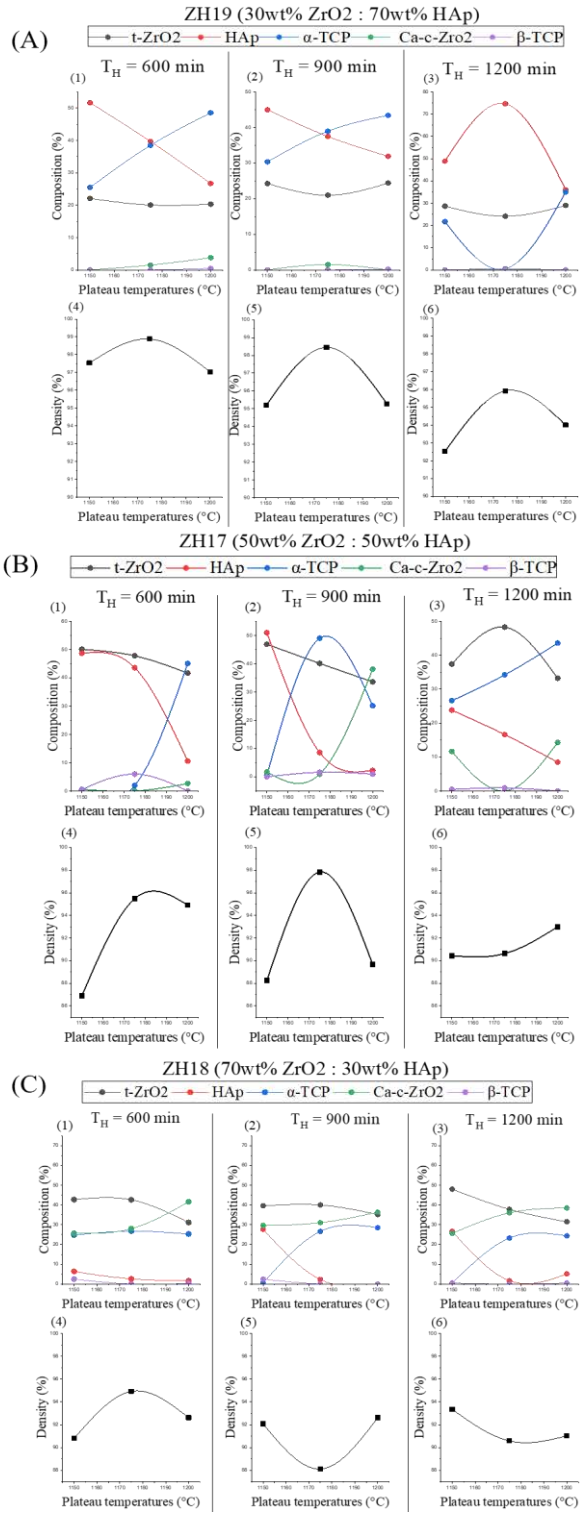

Figure 4.3: Phase composition and density obtained after sintering for the 3 compositions (a) ZH19 (30 wt% 3Y-TZP:70 wt% HAp); (b) ZH17 (50 wt% 3Y-TZP:50 wt% HAp) and (c) ZH18 (70 wt% 3Y-TZP:30 wt% HAp) as function of plateau temperatures at various holding times (1 and 4) 600 min, (2 and 5) 900 min, and (3 and 6) 1200 min.

Impact of plateau temperature appears to change depending on the initial ratio of zirconia to hydroxyapatite. Our results showed that the optimal $T_{plateau}$ is around 1175 °C when considering retention of key crystalline phases (HAp and t-ZrO_2) and densification. However, for compositions with 50 wt% and 70 wt% of 3Y-TZP, the optimal $T_{plateau}$ for phase retention appears to be 1150 °C. Holding times at these plateau temperatures (1150 ℃ and 1175 ℃) influence the phase reaction process, which has been a key factor during densification. Therefore, in the coming section, trends in phase retention and fired densities as a function of holding time are examined.

4.3.3. Optimisation of holding time

To optimise the plateau temperature a factorial experimental design was used, three compositions containing different quantities of 3Y-TZP and HAp (ZH17, ZH18 and ZH19), T_{peak} of 1300 ℃ and heating rate of 10 ℃/min were selected. The study indicated that the optimal holding time lies between 600 min and 1200 min.

Figure 4.4a shows the crystalline phase composition of ZH19 (30 wt% 3Y-TZP: 70 wt% HAp) sintered at different $T_{plateau}$ ranging from 1150 °C to 1200 °C with holding times ranging from 600 to 1200 min. Retention of HAp and t-ZrO_2 crystalline phases are observed to be a function of both $T_{plateau}$ and T_H. At a $T_{plateau}$ of 1150 ℃, increasing T_H values from 600 to 1200 min showed similar composition of t-ZrO_2, HAp, α-TCP and Ca-c-ZrO_2 phases indicating that phase change at this $T_{plateau}$ is independent of the holding time. A $T_{plateau}$ of 1175 ℃ showed similar composition at a T_H of 600 and 900 min; however, at a T_H of 1200 min there is full retention of HAp phase. The densification achieved at 600 and 900 min appears to greater than the densification achieved at 1200 min. This is unusual as stability of α-TCP phases at temperatures beyond 1100 ℃ is the major reason for driving the transformation of HAp to α-TCP [279]. This lack of formation of Ca-c-ZrO_2 at $T_{plateau}$ of 1175 ℃ at 1200 min, indicates the potential formation of an intermediate phase hydroxyoxyapatite as shown in equation (4). This is also reflected by the relatively higher χ^2 value

obtained during the Rietveld refinement (shown in Table A4) for composition ZH19_9. The presence of 3Y-TZP increases the rate of dehydration of HAp as discussed in previous sections. However, formation of Ca-c-ZrO_2, according to equation (5), was only less than 5 wt% at all $T_{plateau}$ values and holding times. Therefore, low concentration of 3Y-TZP (30 wt%) in the ZH19 composition was sufficient to drive the dehydration of HAp but there was minimal diffusion of CaO into the 3Y-TZP to form Ca-c-ZrO_2.

Previously in section 3.2, a $T_{plateau}$ of 1175 °C produced optimal results for both phases (t-ZrO_2 and HAp) retention and sintered densities for ZH19 composition. As shown in Figure 4.4a, a $T_{plateau}$ of 1175 °C with a holding time of 600 min offers the highest relative density of 98.45% while retaining key phases (35 wt% and 20 wt% of HAp and t-ZrO_2, respectively). Further, the presence of 35 wt% of α-TCP phase observed for this composition at this optimum TSS condition can improve osteointegration since it is more readily resorbable, however, it could also destabilise the scaffold structure for the same reason [280]. Therefore, the usage of ZH19 composition is ideal for rapid interaction with extracellular matrix as required by the exterior surface of BTE scaffolds [281].

Crystalline phase composition of ZH17 (50 wt% 3Y-TZP: 50 wt% HAp), as shown in Figure 4.4b, demonstrates that final phase composition depends on the holding time as well as $T_{plateau}$. Densification of this composition increased with increasing holding time for $T_{plateau}$ of 1150 °C. At $T_{plateau}$ of 1150 °C, phase composition was similar for holding times of 600 min and 900 min, but a further increase in holding time to 1200 min enabled the formation of α-TCP and Ca-c-ZrO_2 at the expense of HAp and t-ZrO_2 phases, respectively. At a $T_{plateau}$ of 1175 °C and holding times greater than 600 min, an increase in the formation of α-TCP was observed, the obtained fired densities were greater than 90%. Relative densities of the pellet sintered at $T_{plateau}$ of 1175 °C for 900 min are above 95%, the densification of the ZH17 composition increased as a function of

holding time from 88% at 600 min to 97% at 900 min. At a $T_{plateau}$ of 1200 ℃ relative densities greater than 90% was only observed at holding times of 600 and 1200 min while. While the formation of high quantities of Ca-c-ZrO_2 and α-TCP when sintering at 1200 ℃ for 900 min reduced the achievable density of the composite. Therefore, holding times equal or greater than 900 min produced high densities. Thus, the identified optimum $T_{plateau}$ of 1175 °C from section 3.2 produces high retention of key phases (t-ZrO_2 and HAp) and densities greater than 95% at a hold time of 600 min.

Crystalline phase composition of the ZH18 (70 wt% 3Y-TZP: 30 wt% HAp) shown in Figure 4.4c reveals that phase transformations depend on both holding time and plateau temperature. High concentration of 70 wt% of 3Y-TZP presented in the ZH18 composition, is primarily responsible for the rapid dehydration of HAp phases for most of the sintering conditions as shown in Figure 4.4c. At 1150 ℃ increasing the holding time from 600 to 900 min showed a reduction of HAp and t-ZrO_2 phases. At $T_{plateau}$ values of 1175 °C and 1200 ℃ the HAp content was less than 10 wt% across all holding times. The longer holding times at $T_{plateau}$ of 1175 and 1200 ℃ allowed for the complete consumption of HAp content and the formation of Ca-c-ZrO_2. This is reflected in Figure 4.4c where the quantity of Ca-c-ZrO_2 gradually increases with holding. Time. ZH18 samples sintered at a $T_{plateau}$ of 1200 °C for 600 min showed an increased transformation of t-ZrO_2 to Ca-c-ZrO_2 phases compared to 900 and 1200 min. The quantity of Ca-c-ZrO_2 at 900 and 1200 min were similar, indicating that this further dehydration of HAp will cease to occur beyond 900 min at a $T_{plateau}$ of 1200 °C. Previous studies exploring the co-sintering 3Y-TZP – HAp composites have only explored limited holding times of up to 3 hrs [269, 270, 282] and, therefore, further studies are required to understand the reasons for the dehydration reaction to cease beyond 900 min.

Densification of the samples lies between 90 and 95%. Increasing diffusion of calcium in ZrO_2 during diffusion reduces the overall molecular weight and, hence, reduces the density of Ca-c-ZrO_2 [283]. As mentioned previously, low densities of α-TCP (2.86 g/cc) compared to HAp reduce the theoretical densities of these co-sintered ZrO_2 – HAP composites [284]. Since the formation of Ca-c-ZrO_2 and α-TCP phases cannot be eliminated during the co-sintering of the ZH18 composition, sintering conditions that limit its formation must be selected to ensure sufficient functionality and mechanical strength [285]. Therefore, the previously identified optimum $T_{plateau}$ value of 1175 °C and a holding time of 600 min retained the highest quantity of t-ZrO_2 while only less than 5 wt% of HAp. Even though densification at this holding time was about 95% it offered higher retention of critical phase (t-ZrO_2). Therefore, holding time of 600 min at a plateau temperature of 1175 °C appears to be optimum for the ZH18 composition. Therefore, with high quantities of t-ZrO_2 phases, this composition can function as the structural component of a BTE scaffold. The optimum TSS conditions identified for the 3Y-TZP-HAp compositions are as shown in Table 4.3.

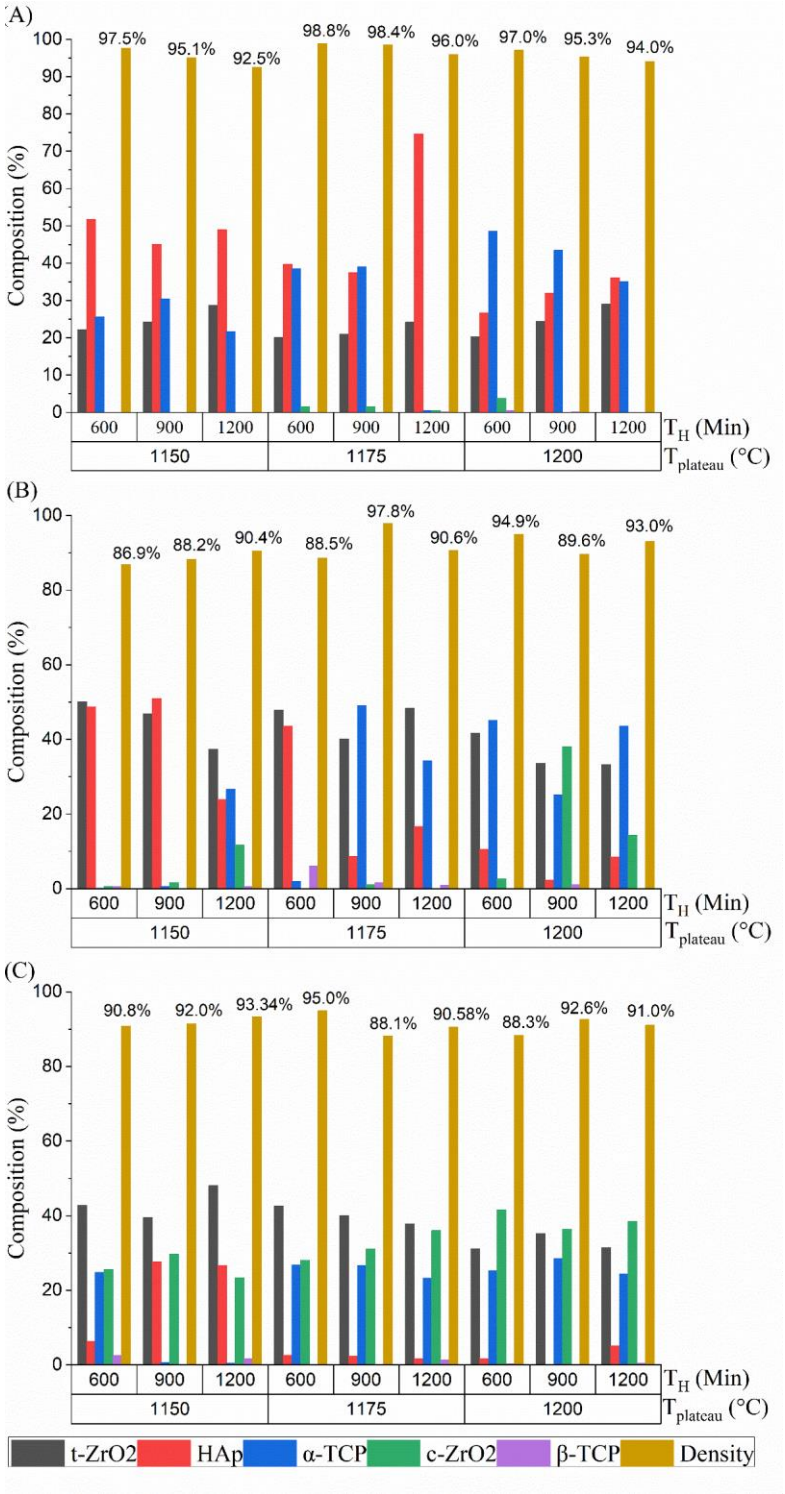

Figure 4.4: Phase composition of sintered composites (a) ZH19 (30 wt% 3Y-TZP: 70 wt% HAp); (b) ZH17 (50 wt% 3Y-TZP: 50 wt% HAp) and (c) ZH18 (70 wt% 3Y-TZP: 30 wt% HAp) as a function of holding times 600 min, 900 min and 1200 min at plateau temperature of 1150 ℃, 1175 ℃ and 1200 ℃, respectively. T_H represents holding time (min) and $T_{Plateau}$ represents plateau temperature (°C).

Table 4.3: Identified optimum TSS conditions to produce dense ceramics and retain significant quantities of bioactive phases.

	Composition* (initial)	**Composition*** (post-sintering)	**T_{peak}** (°C)	**$T_{plateau}$** (°C)	**T_H** (min)	**Heating rate** (°C/min)	**Fired Density** (g/cm^3)**
ZH19	30:70	20:40	1300	1175	600	10	3.67 (98.5%)
ZH17	50:50	39:8.5	1300	1175	600	10	4.17 (95.4%)
ZH18	70:30	46:18	1300	1175	600	10	4.77 (94.5%)

* 3Y-TZP wt%: HAp wt.% and ** extent of densification is specified within brackets.

4.3.4. Effect on grain size

Grain growth during sintering is a function of grain boundary migration, which is a thermodynamically driven process. The classical equation for grain growth in equation (6) shows a direct relationship between the increase in grain size, temperature (T), activation energy (Q) and time (t) [286].

$$R^n - R_o^n = k_o \exp(-Q/RT)\, t \qquad (6)$$

Where R, R_o and k_o represent the final grain size, initial grain size and diffusion parameter, respectively. The parameter 'n' is an empirical exponent that describes the type of grain growth phenomenon. While grain growth occurs simultaneously along with densification, these processes

are driven by grain boundary diffusion and grain boundary migration. While both processes are driven by the thermal energy available during sintering, surface diffusion or grain boundary migration is also driven by the difference in particle sizes [287]. Two-step sintering, introduced by Chen and Wang, promotes densification without significant grain growth by exploiting the differences in the kinetics of grain boundary diffusion and grain boundary migration [258]. 3Y-TZP ceramics processed using conventional sintering produced mean linear intercepts (i.e. a measure of grain diameter) of 0.25 μm and 0.39 μm while sintering for 2 hrs at temperatures of 1400 ℃ and 1500 ℃ respectively [288]. While conventionally sintered HAp produced grain sizes of 2.03 μm and 12.26 μm at sintering temperatures of 1200 ℃ and 1400 ℃ for 2hrs respectively [289]. This clearly indicates the differences in grain growth activation energies for 3Y-TZP and HAp, which are around 352 kJ/mol and 197 kJ/mol, respectively [278, 289].

The ZH18 composition initially containing 70 wt% of 3Y-TZP and sintered at temperatures between 1175 ℃ and 1200 ℃ showed average grain size and linear intercept values of 0.48 μm and 0.44 μm respectively (shown in Figure 4.5). Increasing sintering temperature from 1175 ℃ to 1200 ℃ accounted for less than 5% change in average grain size. Further increasing the holding time from 600 min to 1200 min at 1200 ℃ showed no effect on the grain size. The reasons for the lack of grain growth can be attributed to the high activation energies of 3Y-TZP ceramics, therefore, the low sintering temperatures ranging from 1150 – 1200 ℃ were insufficient to drive the grain growth process [288]. Further, the flat grain boundaries present in the ZH18 composition, shown in Figure 4.5a, are known to reduce the diffusion parameter k_0 in equation (4), thereby limiting grain growth during the TSS process [290].

The ZH17 composition initially containing 50 wt% of 3Y-TZP showed an average grain size of 0.82 μm which is larger than the grain sizes reported for other compositions in this study. Higher quantities of HAp phases in the initial composition that have a lower activation energy undergo

grain growth at sintering temperatures between 1175 ℃ and 1200 ℃ [289]. However, with the increased presence of 3Y-TZP in the initial composition it was expected to pin the grain boundaries and hence prevent grain growth [278]. Grain sizes reported for ZH17_5 and ZH17_9 are smaller than the average grain size (1.68 μm) across the ZH17 composition while ZH17_8 composition has a grain size greater than the average value. This could be due to the agglomeration of HAp phases within the 3Y-TZP-HAp mixture, leading to larger grain sizes within these agglomerates and hence a larger average grain size across the sintered pellet. The ZH19 composition as shown in Table 4.4 contained the highest initial quantity of HAp (70 wt%) and produced an average grain size of 0.63 μm. Since the lower activation of energy of HAp compared to 3Y-TZP can produce larger grains, 20 wt% of t-ZrO_2 present in the sintered composite is known to pin grains boundaries limiting grain growth even with increasing $T_{plateau}$ or T_H values [269]. These results also indicate that the HAp and 3Y-TZP phases are well distributed and do not form agglomerates as observed previously in Figure A3.

Table 4.4: Grain size distribution of sintered samples as a function of plateau temperature and holding time.

Sample	Composition (3Y-TZP wt%: HAp wt%)	$T_{plateau}$ (°C)	Holding time (Min)	Average grain size (µm)	Standard deviation (µm)
ZH19_8	30 : 70	1175	900	0.63	0.24
ZH17_5	50 : 50	1200	600	0.69	0.19
ZH17_8	50 : 50	1175	900	1.19	0.25
ZH17_9	50 : 50	1175	1200	0.60	0.39
ZH18_4	70 : 30	1175	600	0.48	0.13
ZH18_7	70 : 30	1200	1200	0.49	0.01

Grain sizes appear to have a large standard deviation across the various samples as shown in Table 4.4. Differences in initial particle sizes and shrinkage rates of HAp and 3Y-TZP make it nearly impossible to have a consistent grain size across the sample microstructure [266, 287]. However, the EDX results shown in Figure A3 show a uniform distribution of HAp and 3Y-TZP compounds across all compositions.

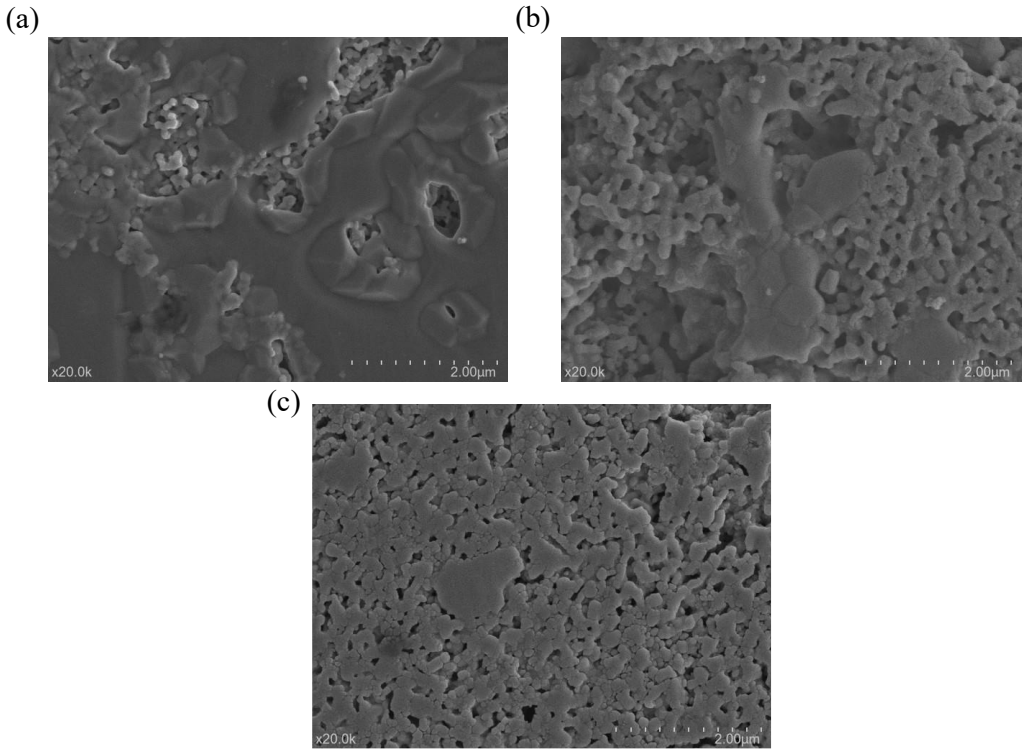

Figure 4.5: Microstructure of 3Y-TZP-HAp composite pellets (a) ZH18_4 (70 wt% 3Y-TZP : 30 wt% HAp) sintered at $T_{plateau}$ = 1200 °C for 900 min; (b) ZH17_8 (50 wt% 3Y-TZP : 50 wt% HAp) sintered at $T_{plateau}$ = 1175 °C for 900 min and (c) ZH19_8 (30 wt% 3Y-TZP : 70 wt% HAp) sintered at $T_{plateau}$ = 1175 °C for 600 min.

4.3.5. Compression strength

The compression strength of the sintered pellets ranged between 88 and 176 MPa (Table 4.5) depending on the fractions of zirconia, hydroxyapatite and other crystalline phases presented in the pellets. Further, differences observed in the compression strength between each composition were due to the variation in crystalline phase composition, density, presence of residual stresses and grain sizes. Specific impacts of these factors will be discussed in following sections. Composition ZH18_4 with up to 43% of t-ZrO_2 post-sintering showed a compression strength of 174 MPa, which is 10 times smaller than the compression strength achieved by pure 3Y-TZP as shown in Table 4.5. A lower sintering temperature optimised for the retention of the HAp phase, is insufficient to fully sinter the composite and therefore impacts on the achievable compression

strength. Inclusion of the HAp phase that is characterised by low mechanical strength (Table 4.5) in the ceramic composite can lead to early failure. Further, compositions ZH17_8 and ZH19_8 containing 40 wt% and 20 wt% of t-ZrO_2 phases along with 9 wt% and 40 wt% of HAp phases possess compression strengths of 88 MPa and 149 MPa, respectively. Specifically, composition ZH19_8 exhibited compression strength greater than results reported in literature for zirconia-hydroxyapatite composites [253, 291].

The variation in crystalline phase composition between the ZH17, ZH18 and ZH19 samples are the primary cause for the differences in the observed compression strengths. The presence of different phases in the above-mentioned compositions could result in crack pinning effects. Also, the introduction of residual stresses and transformation toughening could also contribute towards a higher compression strength. For example, the ZH18_4 sintered pellets containing up to 43 wt% of t-ZrO_2 along with 17 wt% of HAp shown in Figure 4.5a can deflect propagating crack fronts at the boundary between the two phases. This causes the crack front to propagate along a tortuous pathway, thereby increasing compression strength of the composite [292]. Further, phase transformation of the t-ZrO_2 phase to its respective monoclinic phase causes a volumetric expansion that bridges crack fronts and improves compression strength of the composite [293]. These effects of crack deflection and phase transformation toughening have been previously observed in 3Y-TZP composites containing less than 20 vol% of alumina particles. The dominance of these effects is a function of factors such as grain size and composition [292].

The ZH17_8 composite had the lowest compression strength of 87 MPa when compared to ZH18_4 and ZH19_8. While the ZH17_8 composition contained 39 wt% of t-ZrO_2 post-sintering, the presence of up to 49 wt% of α-TCP is unable to prevent crack propagation as observed previously in the ZH18_4 composition leading to early failure of the ZH17 composite [280]. Monolithic α-TCP when exposed to continuous compression load has been shown to undergo

failure primarily through a trans-granular fracture [44] indicating that the α-TCP crystals offer low resistance to crack propagation, making it a vulnerable phase in load-bearing BTE applications. However, t-ZrO_2 present in the ZH17_8 composition provide resistance to crack propagation and hence increase the strength. Further, the porous structure of the ZH17_8 composite shown in Figure 4.5b allows for crack deflection when exposed to continuous load. Miao et al. [294] previously showed that α-TCP composites consisting of secondary phases of HAp have showed more than a 300% increase in compression strength due to its porous nature. Although the structurally weak α-TCP phase is dominant in ZH17_8 composition, the compression strength of the final composite is much higher. Pure α-TCP and the presence of α-TCP are known to boost bone healing ability through rapid resorption inside the body and increased alkaline phosphatase activity [280]. Thus, its presence within the ceramic composite can add additional value apart from just mechanical strength to the scaffolds.

The ZH19_8 pellets, containing up to 40 wt% of HAp along with 20 wt% of t-ZrO_2 produced an average compression strength of 149 MPa. While cracks propagate through the HAp matrix, dispersed ZrO_2 particles in the mixture can pin cracks and therefore, improve compression strength. Pure HAp, as reported in previous studies, can achieve a compression strength of only 40 MPa, therefore, multiple strengthening mechanisms have been explored such as crack deflection and pinning by addition of secondary phases to improve its compression strength [295-297] .Curran et al. [298] showed that the presence of up to 5 wt% of nano sized ZrO_2 particles can completely pin grain boundaries preventing crack propagation as well as grain growth. Similarly, the presence of 20 wt% of t-ZrO_2 in the ZH19_8 composite prevents crack propagation and ensures small grain sizes that also contribute to increasing compression strength. Previous studies have reported a compression strength of 35 MPa when sintering HAp with 5 wt% of ZrO_2 [298-300], whereas in our study 20 wt% of t-ZrO_2 phases post-sintering in ZH19_8 produced a compression strength of 149 MPa. Thus, with a 15 wt% increase of t-ZrO_2 the compression strength was more

than three times the compression strength with just 5 wt% addition. This could also be due to additional factors such as presence of microporosities or residual stresses during the co-sintering process.

Grain size also has a significant effect on the mechanical strength of 3Y-TZP – HAp composites pellets. Sub-micron grain sizes achieved for compositions ZH18_4 and ZH19_8 (Table 4.4) revealed higher compression strengths of 176 MPa and 149 MPa, respectively. The ZH17_8 composition, with up to 1.19 μm average grain size, produced the least compression strength of 88 MPa. Smaller grain sizes observed in ZH18_4 and ZH19_8 increased the number of grain boundaries preventing their dislocation and improved fracture strength [301]. In addition to grain size, pore sizes also play a major role in compression strength. As previously mentioned, the presence of pores in the microstructure assist in crack deflection, but can also function as crack initiation sites and reduce cross-sectional area of the ceramics composites [302]. The microstructure of the composite pellets ZH18_4, ZH17_8 and ZH19_8 (Figure 4.5) shows that pore sizes range from sub-microns to a few microns. However, the actual contribution of different pore sizes to the compression strength requires further investigation.

Table 4.5: Compression strength of sintered 3Y-TZP-HAp ceramics with relative density greater than 98% and comparison with results reported in literature.

Sample	Composition	Grain size (µm)	Compression strength (MPa)	Ref
3Y-TZP	100 wt% 3Y-TZP	0.38	1968 ± 128	[303]
ZH18_4	70 wt% 3Y-TZP: 30wt% HAp	0.48	176.44 ± 22	This study
ZH17_8	50 wt% 3Y-TZP: 50wt% HAp	1.19	87.75 ± 22	This study
ZH19_8 (theoretical)	30 wt% 3Y-TZP: 70wt% HAp	N/A	433.83	
ZH19_8	30 wt% 3Y-TZP: 70wt% HAp	0.62	149.37 ± 65	This study
HAp	100 wt% HAp	0.19 – 1.7	40 - 125	[304-306]
α – TCP	100 wt% α-TCP	-	200 ±10.6	
β – TCP	100 wt% β-TCP	-	419 ± 28	[307]

Mechanism of failure during compression loading appears to occur in different stages as shown in Figure 4.7. In this study, all compositions have the matrix and reinforcement phases to be ZrO_2 (this includes Ca-c-ZrO_2 and 3Y-TZP) and calcium phosphates (this includes HAp and α-TCP), respectively as shown in Figure 4.6. Specifically, in composition ZH19_8, the HAp pining particles are further apart from one another, therefore, the cracks require more energy to propagate through the stronger ZrO_2 matrix. In composition ZH18_4 shorter distances between the HAp particles could have allowed cracks to easily propagate as they are weaker than 3Y-TZP ceramics. Therefore, the presence of these strengthening mechanisms in the ceramic composites improves the strength of the composite. The ZH19_8 composite with a compression strength of 149 ± 65 MPa is well within the compression strength of natural bone [308]. Therefore, ZH19_8 composition is a potential candidate for BTE since it has both bioactive and strengthening

crystalline phases that will initiate a bone healing response while providing structural support at the implanted site. In addition to this all compositions showed up to 14% deformation prior to failure. Compositions ZH18_4 and ZH17_8 showed a maximum strain of 10% before failure, while composition ZH19_8 showed a comparatively higher strain of 14%. The higher strain values prevented instant failure or major cracking prior to failure.

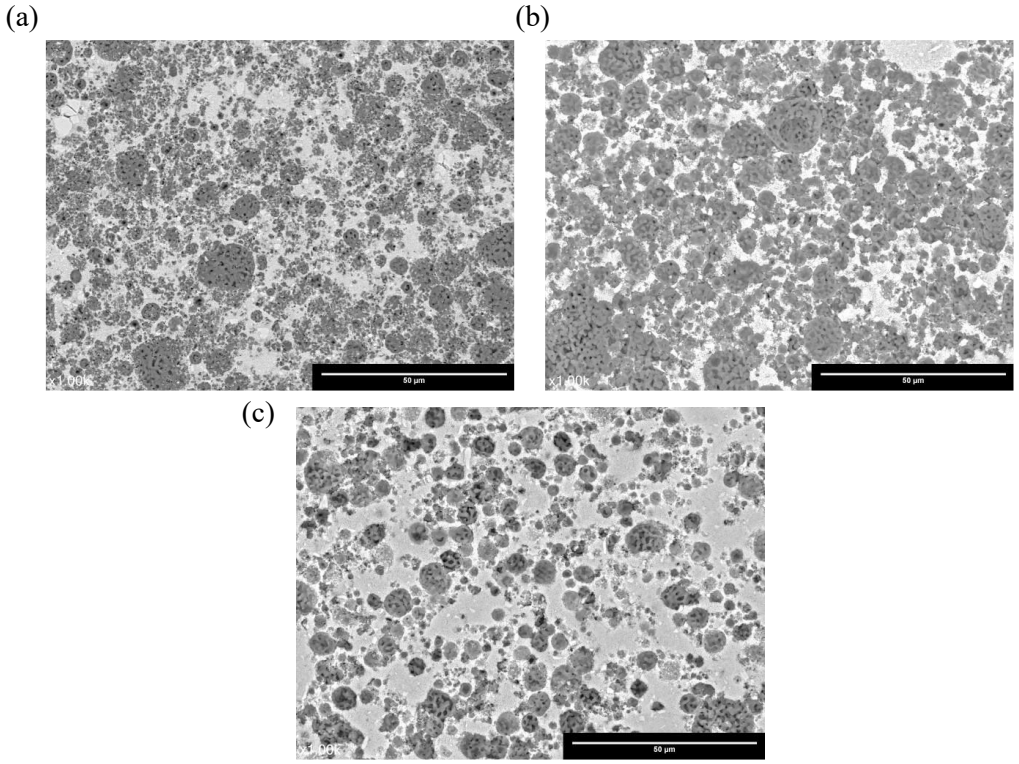

Figure 4.6: Back-scatter image of 3Y-TZP – HAp composites showing the distribution of ZrO_2 and HAp phases. (a) ZH18_4 (70 wt% 3Y-TZP: 30 wt% HAp) sintered at $T_{plateau}$ = 1200 °C for 900 min; (b) ZH17_8 (50 wt% 3Y-TZP: 50 wt% HAp) sintered at $T_{plateau}$ = 1175 °C for 600 min and (c) ZH19_8 (30 wt% 3Y-TZP: 70 wt% HAp) sintered at $T_{plateau}$ = 1175 °C for 600 min. The light-coloured region represents the ZrO_2 matrix (this includes Ca-c-ZrO_2 and 3Y-TZP) and dark-coloured region represents calcium phosphate reinforcement phases (this includes HAp and α-TCP).

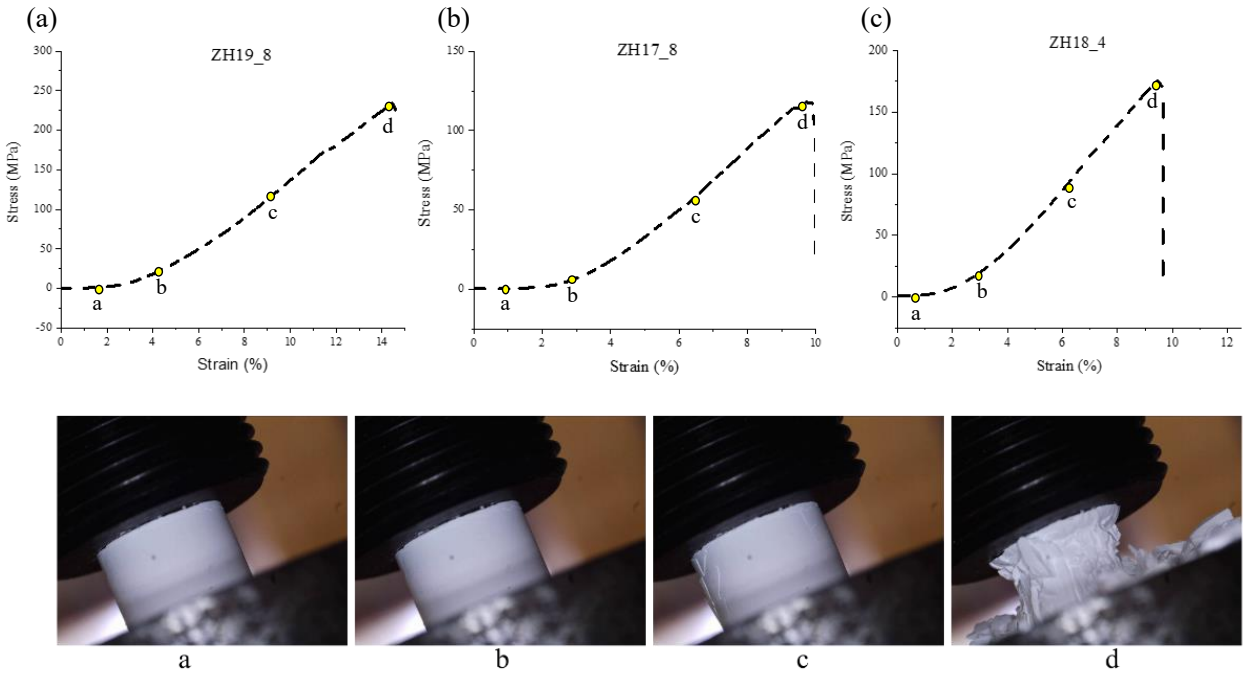

Figure 4.7: Stress vs strain curve for sintered samples (a) ZH19_8 (30 wt% 3Y-TZP : 70 wt% HAp), (b) ZH17_8 (50 wt% 3Y-TZP : 50 wt% HAp) and (c) ZH18_4 (30 wt% 3Y-TZP : 70 wt% HAp) and examples of strain response at points a, b, c and d shown on the stress-strain plot.

4.4. Conclusions

Zirconia-hydroxyapatite composites prepared using TSS showed better control over phase retention during sintering. Mechanical performance of the produced ceramics was found to be similar to that of natural bone tissue. Holding time and plateau temperature had a significant effect on both phase retention and densification. Optimised sintering conditions led to the retention of key phases (HAp and t-ZrO_2) ensuring the ceramic composite has sufficient bioactivity and structural performance for use in load-bearing BTE applications. Large quantities of brittle α-TCP and Ca-c-ZrO_2 phases observed in the 50/50 composite (ZH17) reduced the compression strength. This study demonstrated that TSS process is a practical approach to co-sintering 3Y-TZP-HAp ceramics while retaining key crystalline phases (t-ZrO_2 and HAp) and ensuring densification greater than 95%.

5. Graded hydroxyapatite triply periodic minimal surface structures for bone tissue engineering applications

Abstract

Porous scaffolds in BTE play a crucial role in facilitating osteointegration with host tissues and providing nutrients to cells involved in bone healing. The architecture of these scaffolds significantly impacts osteointegration, biofunctionality, and mechanical strength. Therefore, understanding the relationship between scaffold architecture and its performance as a BTE scaffold is essential. In this study, hydroxyapatite scaffolds were 3D printed with three types of triply periodic minimal surface (TPMS) structures: gyroid, lidinoid, and split-P, at porosities ranging from 50% to 80%. The split-P architecture exhibited the highest compression strength, between 15 and 25 MPa, but provided the least surface area for bone apatite precipitation. Conversely, gyroid and lidinoid structures demonstrated the highest levels of bone apatite precipitation across all porosities when immersed in simulated body fluid. To combine these advantages and enhance compression strength, graded structures were designed with multiple TPMS structures arranged in a core-shell configuration. A structure featuring a solid core and a 70% gyroid shell achieved the highest compression strength of 120 MPa, while also supporting cell attachment and differentiation comparable to that of a fully porous structure. This combination of compression strength similar to cancellous bone and ability for positive interaction with osteoblast cells makes it an ideal candidate for load-bearing applications in BTE.

5.1. Introduction

Bone tissue engineering involves the design and manufacturing of interconnected porous scaffolds providing a suitable microenvironment for the growth of bone tissues and mechanical support. Permeability of the BTE scaffolds enables vascularisation of bone tissues, to achieve high levels of permeability previous studies have recommended porosities greater than 60% [309, 310]. However, increasing scaffold porosity leads to a reduction in compression strength, limiting their load-bearing ability. This rigid dichotomy of BTE scaffold requirements makes it extremely challenging to develop a scaffold that encourages osseointegration while still having the necessary mechanical strength suitable for the application [310, 311]. Zhang et al. [312] showed that a hierarchically structured poly caprolactone surrounded with a hydrogel matrix (containing deferoxamine nanoparticles and MnCO nanosheets) can produce a positive effect in bone healing and produce compression strengths of 50 - 56 MPa. Jia et al. [313] showed that magnesium-based scaffolds with better interconnectivity and high porosities (greater than 70%) showed very low compression strength (less than 3 MPa) but showed greater cell migration through the scaffold. These observations further confirm the challenge of satisfying the rigid dichotomy of BTE scaffolds.

Hydroxyapatite (HAp) is a commonly used bone replacement material due to its biocompatibility and chemical similarity to the mineral phase of natural bone tissue. Although these materials are resorbable, resorption is an extremely slow process [314]. Other calcium-based compounds such as tricalcium phosphates (TCP) and biphasic calcium phosphate (BCP) have been shown to undergo faster resorption. While the faster resorption can be beneficial, it could also result in a local pH change which is shown to negatively impact cell activity during the bone healing response [315-317]. Resorption of these calcium-based compounds (HAp, TCP and BCP) has been shown to occur through two pathways; osteoclastic resorption during bone remodelling and chemical or

physical delamination [318]. This process will only occur when the full surface of the scaffold is vascularised and in contact with the surrounding medium. Surface area available for the resorption to occur on the BTE scaffolds will depend on their permeability and porosity. Resorption of calcium-based compounds (HAp, TCP and BCP) over time will lead to a reduction in mechanical strength, making them unable to provide long-term mechanical support to a recovering patient.

High strength BTE scaffolds are commonly made from Ti6Al4V, yttria partially stabilised zirconia, or other materials having mechanical strength greater than 100 MPa, however these are bioinert in nature. This lack of interaction makes them unsuitable to increase the efficacy of synthetic BTE scaffolds. Ceramic composites in the past decade (bioceramics) are increasingly being used as synthetic bone replacements. Pierantozzi et al. [319] showed that HAp or strontium-substituted HAp (Sr-HAp) used along with poly caprolactone (PCL) stimulated higher levels of alkaline phosphatase (ALP) activity when compared to the PCL polymer. While the ALP activity generally declines with the formation of calcium deposits, the Sr-HAp PCL scaffold was able to retain ALP activity until the 14-day mark indicating a delay in osteogenesis. Mancuso et al. [320] showed that up to 10 wt% inclusion of barium titanate ($BaTiO_3$) in PCL composite scaffolds showed an increase in mechanical strength and supported cell growth and viability when cultured with human osteoblast cells. Further the inclusion of ceramic particles (HAp and $BaTiO_3$) in the scaffold showed the retention of the osteoblastic phenotype and deposition of bone-like extracellular matrix onto the scaffold surface. This bone apatite formation *in-vitro* has been a crucial consideration in the choice of biomaterials for BTE applications as they provide an indication of the bone healing ability of scaffolds within a short time frame [321]. Simulated body fluid (SBF) tests have commonly been used for the measurement of bone apatite formation, and, while the conditions differ significantly from in-vivo experiments, they can be used to predict performance of HAp ceramics [321, 322]. Ca-P phases in aqueous solutions that have precipitated during the SBF test have been known to include dicalcium phosphate [$CaHPO_4.2H_2O$] (DCPD),

octacalcium phosphate [$Ca_8(HPO_4)_2(PO_4)_4.5H_2O$] (OCP) and hydroxyapatite [$Ca_{10}(OH)_2(PO_4)_6$] (HAp). OCP and the DCPD are the precursors of HAp during the SBF test, but HAp is thermodynamically favourable to exist in the SBF solution [323]. During the course of immersion, there are multiple association and dissociation reactions that help drive the precipitation of Ca-P phases on the scaffold surface; previous studies [323-326] have only considered the chemical properties of the SBF fluid and substrate. However, the nucleation rate of the Ca-P on the surface of a scaffold will also depend on the extent of SBF intrusion. In this study, we intend to assess the effect of scaffold geometry and porosity on the Ca-P phase precipitation.

Periodic lattice structures have been popularly used in tissue engineering applications due to their ability to be engineered based on the required porosity, structure and load-bearing capacity [3]. Examples of these lattices used specifically for BTE application include voronoi, cubes, octets and honeycomb lattices [327]. Triply periodic minimal surfaces (TPMS) have recently become a popular choice for use in BTE applications, due to their ability to mimic the internal geometry of natural bone tissues along with an optimal combination of strength and porosity [310]. Gyroids have been a popular choice for use in BTE applications due to the unique combination of permeability and strength offered by the structure [310]. Germain et al. [328] showed that gyroid-based scaffolds exhibited an isotropic stress response under compression and also showed high structural retention (up to 64 weeks) during aging in suitable physiological conditions. This was attributed to the greater contact area between layers and interconnectivity compared to strut-based lattice structures. Zhang et al. [329] showed that non gyroid-based structures such as split-P, diamond and schwarz structures offered high compressive strength across all pore sizes when compared to gyroids. The split-P structure showed the highest energy absorption across all pore sizes (300 – 900 μm) and concave surfaces of the split-P structure promoted osteogenic cell differentiation compared to the flat surfaces of a cross-hatch lattice. Lidinoid structures tended to show higher porosity compared to other TPMS structures for the same pore sizes (300 – 900 μm)

[329]. Feng et al. [330] showed that by combining IWP and P surface, a 30 – 55% improvement in stiffness could be achieved. Mechanical strength and permeability which are critical features of BTE scaffolds depend on scaffold architecture and porosity. While each of these TPMS structures have their unique advantages and disadvantages, a hierarchical arrangement of these multiple structures with varying porosities can be used to optimise the scaffold design for any requirement. However, there are limited studies exploring the effect of porosity and geometry on the mechanical strength and bone apatite formation in TPMS structures.

In this study vat polymerisation-based ceramic 3D printing was used to explore the effect of scaffold porosity and geometry of TPMS structures on their performance as BTE scaffolds. Mechanical strength of these different scaffold geometries (split-P, gyroid and lidinoid) at different porosities (50 – 80%) was explored. *In-vitro* testing was performed to assess bone apatite precipitation of the TPMS scaffold as a function of scaffold structure and porosity. This study demonstrates the functionality of different TPMS structure for BTE applications, providing a framework for creating hierarchical or composite structures for BTE scaffolds. Lastly, we have explored two different strategies for graded composite TPMS structures and examined their effect on cell proliferation and compression strength.

5.2. Methodology

5.2.1. TPMS structures

Surfaces of the gyroid (GY), split-P (SP) and lidinoid (LI) TPMS structures used in this study can be defined using the equations in Table 5.1.

Table 5.1: Surface functions of different (gyroid, split-P and lidinoid) TPMS structures.

TPMS structure	Equation	Ref
Gyroid	$Cos\ (wx)Sin(wy) + Cos(wy)Sin(wz) + Cos(wz)Sin(wx) - t$	
Split - P	$-0.2\left(Cos(wx)Cos(wy) + Cos(wx)Cos(wz) + Cos(wy)Cos(wz)\right) - 0.4\ (Cos(wx) + Cos(wy) + Cos(wz)) + 1.1\ (Sin(x)Sin(wy)\cos(z) + Sin(wx)Cos(y)Sin(z) + Cos(x)Sin(y)Sin(wz)$	[331]
Lidinoid	$Sin(x)Sin(wy)Cos(z) + Sin(wx)Cos(y)Sin(z) + Cos(x)Sin(y)Sin(wz) - Cos(wx)Cos(wy) - Cos(wx)Cos(2z) - Cos(wy)Cos(wz) + t$	

TPMS structures derived from the equations in Table 5.1 were mapped onto a cylindrical volume using nTopology. To produce different volume porosities (50 – 80%) within the cylindrical volume the wall thickness and mid-surface offset (shown in Figure 5.1) of each TPMS lattice type was modified using the values in Table 5.2. Wall thicknesses of lidinoid and split-P TPMS structures at porosities of 80% were less than 0.20 mm (recommended minimum thickness) and thus were excluded from the experimental analysis.

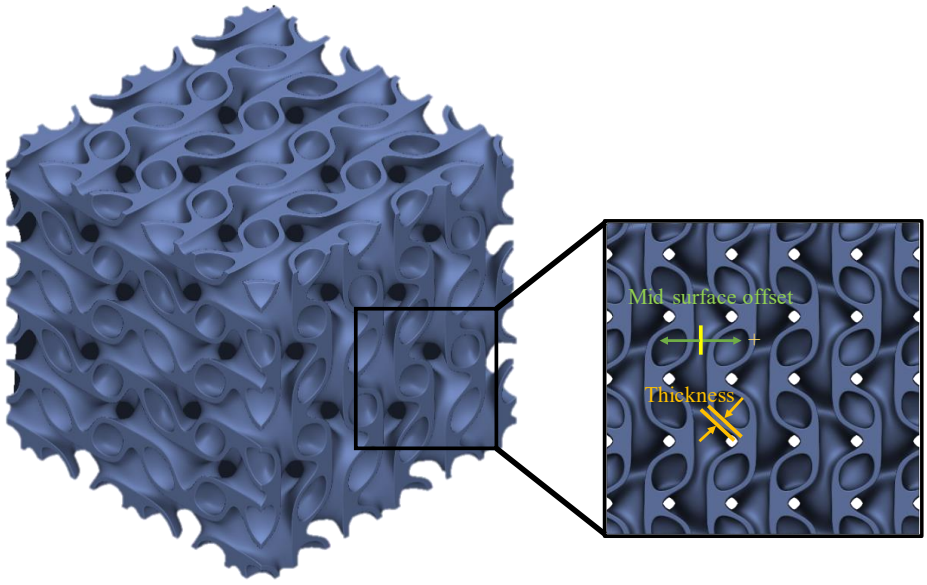

Figure 5.1: An example of a TPMS mapped onto a rectangular volume on nToplogy. Input variables such as mid-surface offset and thickness shown in the figure were modified to achieve the required volume porosity. Thickening the TPMS surface involves moving the surface by fixed distance. Mid-surface offset involves the movement of the mid-surface of the wall (shown in yellow) inwards (+ve) or outwards (-ve).

Table 5.2: TPMS lattice parameters used to obtain different porosity values in the mapped cylinder volume.

Unit cell type *	**Porosity (Vol %)**	**Mid-surface offset (mm)**	**Wall thickness (mm)**
GY	50	0.1	0.98
GY	60	0.2	0.78
GY	70	0.2	0.58
GY	80	0.25	0.38
LI	50	0.4	0.73
LI	60	0.41	0.6
LI	70	0.4	0.45
SP	50	0.19	0.79
SP	60	0.22	0.63
SP	70	0.2	0.62

*Note gyroid (GY), lidinoid (LI) and split-P (SP)

5.2.2. 3D printing of scaffolds

All parts were 3D printed through stereolithography of ceramic slurries on the C100 EasyFab (3DCeram, France) [332]. The parts were manufactured using photocurable HAp ceramic slurry supplied by 3DCeram. Processing parameters provided by the manufacturer were used for 3D printing the parts using the HAp feedstock. Green parts produced were debinded using the manufacturers recommendations. Further the debinded samples were sintered at 1280 ℃ with dwell of 60 min and a heating rate of 3 ℃/min. The sintered samples were cooled to room temperature at 3 ℃/min. In addition to the TPMS scaffolds described in Table 5.1, solid cylinders (diameter = 10 mm and height = 3 mm) were fabricated for further characterisation of the sintered HAp.

5.2.3. Characterisation of Sintered parts

Scanning electron microscopy (SEM, Hitachi SU5000) was used to characterise surface morphology and grain sizes. Discs for SEM were prepared using a series of grinding papers (180 grit, 320 grit, 600 grit, 800 grit, 1200 grit and 2500 grit) followed by polishing using a 1 μm diamond suspension and OP-S solution for up to 10 min each. The polished samples were thermally etched at 1180ºC for 60 min. Crystalline phases of the sintered HAp pellet were characterised using X-ray diffraction (XRD, Bruker D2 Phaser). The XRD scan was set between 10º to 80º with a step size of 0.02º and dwell of 1 sec/step. The density of the sintered samples was measured according to the procedure described in ISO 18754 and compared with the theoretical density of HAp.

5.2.4. Finite element modelling

ANSYS workbench 2023 was used to perform finite element analysis and determine the stress-strain response of the HAp scaffolds under uniaxial compression. The Youngs modulus and the Poisson's ratio of the HAp material was defined to be 10 GPa and 0.3, respectively [329]. A deformation of 0.01 mm (compressive) was applied to the cylinder keeping the bottom face fixed similar to a compression test. The stress, strain, and deformation along principal axis was recorded.

5.2.5. Compression test

Compression test samples had a cylindrical shape with a height of 7 mm and diameter of 7 mm. Ceramic parts were compressed at a crosshead speed of 0.1 mm/min to determine the compression strength and an average value was calculated from three tests.

5.2.6. Simulated body fluid

HAp parts of cylindrical shape with a height and diameter of 5 mm were fabricated as described in section 5.2.2. The structures detailed in Table 5.3 were soaked in a simulated body fluid (SBF) for a period of 5 weeks, change in concentration of Ca^{2+}, PO_4^{2-} along with Mg^{2+} was measured every week using ICP-MS. A detailed process of SBF preparation has been shown in Oyane et al. [333]. To ensure that the ion concentration was similar to the values reported in literature, ICP-MS and pH electrode analysis was used to determine the ion concentrations of the prepared SBF solution.

The minimum volume of SBF fluid required for soaking the samples is shown to be equal to half the surface area of the sample [325]. An additional 10 mL of SBF was added to account for the loss in volume during sampling done every week for 5 weeks. At the end of 5 weeks the TPMS

scaffolds were weighed to determine the change in mass and the presence of the precipitates was investigated using SEM-EDS.

Table 5.3: Volume of SBF fluid required for immersion of all TPMS scaffold structures.

Unit cell type	**Porosity (Vol %)**	**Surface area (mm^2)**	**Volume of SBF fluid (ml)**
GY	50	623.15	112
GY	60	621	112
GY	70	617.25	112
GY	80	611	112
LI	50	1065.37	160
LI	60	1079	160
LI	70	1104.40	160
SP	50	789.92	130
SP	60	796.45	130
SP	70	889.3	170

5.2.7. Proliferation assay

Hydroxyapatite scaffolds of diameter 5 mm and height 3 mm were prepared using the 3D printing technique described in section 5.2.2 for the proliferation assay. Based on the results from the compression testing and simulated body fluid tests, four structures were identified to create graded structures. The outer diameter of the scaffold is the section that is in direct contact with the surrounding tissue, therefore structures that showed maximum interaction with SBF were chosen (G70, L70 and G80). However, these structures showed the least compression strength compared to the other TPMS structures that were tested. S50 was chosen, therefore, to form the internal core with a diameter of up to 50% of the outer diameter (2.5 mm), as it showed the highest compression strength compared to all TPMS structures analysed (shown in section 5.3.2). To compare the performance of these graded structures, the chosen external geometries (G70, L70 and G80) were placed with a solid core of 50% diameter to the outer cylinder.

Seven structures shown in Table 5.4 were 3D printed to determine extent of cell attachment and proliferation of human osteoblast cells (hOB; CRL-3602 ATCC, Manassas, VA, USA). Cells were expanded in culture flasks with complete media (CM) consisting of Dulbecco's modified Eagle medium (DMEM), supplemented with 10% fetal bovine serum (FBS) and 1% penicillin–streptomycin solution (Sigma-Aldrich, Castle Hill, NSW, Australia) incubated at 37 ^{o}C, 5% CO_2, and 90% humidity. Media was refreshed every 3 days, and the cells were passaged at 95% confluence as confirmed using conventional microscopy (Nikon Eclipse TS100, Nikon Instruments, Tokyo, Japan). For experiments assessing cellular response, cells were lifted with trypsin (Sigma-Aldrich, Darmstadt, Germany) and seeded onto the structures. Cells were used between passages 5 and 6.

The hydroxyapatite scaffolds were placed in wells of a 48-well plate and 0.2 ml (containing 3.5 x 10^5 cells) of the cell suspension was added to each well to completely immerse the scaffolds.

Further, 0.2 ml of the cell suspension was added in triplicate to wells without a scaffold to assess the effect of the scaffold material on cell attachment and proliferation. The well plates were then incubated at 37 °C at 5% CO_2 for 10 days.

Osteoblast cell proliferation is critically dependant on its environmental, mechanical and chemical changes therefore providing an insight on the effects of scaffold geometry on the survival of the cells. Proliferation of the cells were assessed on days 1, 3 and 10 by measuring the reduction of resazurin to resofurin. Prior to measurement, scaffolds were incubated with resazurin for 5 hrs following which media from each of the specimens was transferred to a 96-well plate (in triplicate: 3 wells of 100 µl each). Absorbance of resorufin (reduction product of resazurin) at 570 nm and 600 nm wavelengths was recorded using a microplate absorbance reader (iMark™ Microplate Absorbance Reader, BioRad Laboratories, Hercules, CA, USA). The percentage of resorufin was calculated using the values obtained for stock solution (without cells). Measuring the reduction of resazurin to resofurin provides a direct and more sensitive measurement of cell viability compared to conventionally used MTT assay. Low toxicity and stability of the redox changes to the resazurin dye enables its use in long term cell viability studies [334, 335]. Due to the permeability of the scaffold structures and low surface tension, seeded cells do not have sufficient time to undergo attachment. Hence to ensure that proliferation of only the cells attached to the scaffold surface are measured, the structures were transferred into new wells 24 hrs after they were seeded with osteoblast cells.

Table 5.4: Hierarchical TPMS structures for cellular assay and compression testing.

Hierarchical structure	**Internal geometry**	**External geometry**
S50 - G70	S50	G70
S50 – L70	S50	L70
S50 – G80	S50	G80
Solid – G70	Solid	G70
Solid – L70	Solid	L70
Solid – G80	Solid	G80

Microscopy of the osteoblast cells present on the scaffold surface was carried to observe the extent of cell penetration and attachment on days 1, 3 and 10. The cell medium was drawn out and washed with PBS 2-3 times. The cells were then fixed using 3% paraformaldehyde (PFA) solution and set aside for 20 min at room temperature. The working solution for Abcam ifluor 594 was prepared using the manufacturer's protocol. The wells were then washed with PBS to remove any remaining PFA. Following which 100 µl of the previously prepared working solution along with 10 µl of DAPi were added and covered to prevent light exposure for 90 min. The cells were then imaged using an Olympus IX53 microscope with blue, green and red fluorescence channels with a 10X objective.

5.2.8. Alkaline phosphatase assay

Alkaline phosphatase (ALP) activity of the osteoblast cells cultured on the structures described in Table 5.4 were measured using an ALP kit (ABCAM, Cambridge, United Kingdom). The

structures were placed in a 24-well plate and seeded with osteoblast cells maintaining a cell density of 7 x 10^4 and incubated for 10 days. After day 10, cell lysates were collected according to the protocol specified by the manufacturer. Collected cell lysates were stored at -80 ℃ prior to measurement of ALP activity using a microplate absorbance reader (FLUOStar Omega, BMG Labtech (Offenburg, Germany)) at 405 nm.

5.3. Results and Discussions

5.3.1. Characterisation of sintered parts

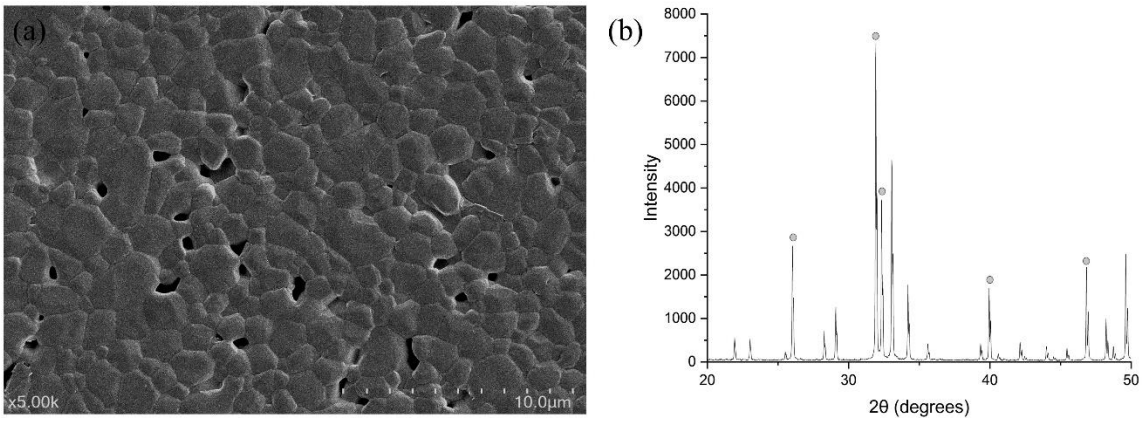

Figure 5.2: (a) Microstructure of the sintered HAp parts shows the presence of pores less than 2 µm (b) Major XRD peaks observed at 25.9º, 31.8º, 32.2º 39.6º and 46.6°that are indicated typical with HAp.

Average grain size of the sample was determined using the procedure highlighted in ASTM E112 -13 and was found to be 1.16 µm with a standard deviation of 0.03 µm. Density of the sintered samples was measured using the procedure highlighted in ISO 18754 and samples were found to have a solid density of 94% ± 2% compared to the theoretical density of the HAp. The lack of full densification can be observed in the SEM image shown in Figure 5.2a, with an average pore size less than 2 µm. XRD results shown in Figure 5.2b showed peaks at 25.9º, 31.8º, 32.2º 39.6º and 46.6º that are typically of HAp.

The stiffness matrix of each TPMS structure at different porosities (50 – 80 %) were analysed using nTopology and their distribution along the principal axis is shown in Figure 5.3. At 50% porosity, differences between the highest and lowest stiffness values across all structures is less than 15% of the peak value, therefore stiffness distribution can be assumed to be close to uniform. This indicates lower chances of stress concentration during loading and hence higher compression strength across all TPMS structures at 50% porosity. The distribution of stiffness values becomes more anisotropic when increasing porosities from 50 to 80% i.e. the difference between the lowest and the highest stiffness values increases up to 50% of peak value. Further, the maximum stiffness values lie along the principal directions leading to stress concentration and crack formation which can cause early failure in brittle materials such as HAp. Feng et al. [330] showed that material density distribution played a direct role in improving stiffness of a given TPMS surface. TPMS structures fabricated in section 5.2.2, show a reducing lattice wall thickness as the porosity increases, leading to a reduction in material distribution density. Thus, making their responses more anisotropic when porosities increase from 50% to 80%. Khaleghi et al. [336] showed that this stiffness anisotropy could be minimised by appropriate selection of multiple TPMS structures in different ratios.

Split-P structures tended to have the highest stiffness value [2 – 0.7 GPa] across all porosities indicating higher compression strengths, which is similar to results reported in previous studies [329]. Gyroid and lidinoid structures showed similar stiffness values at porosities 50 – 70%. At 80% porosity, stiffness offered by lidinoid is lower and anisotropic compared to the gyroid structure. Zhang et al. [329] showed that compression strengths of the gyroid and lidinoid structure were similar with increasing pore size from 300 µm to 900 µm.

Compression stresses are the primary forces experienced by BTE scaffolds, the above mentioned TPMS structures behave differently under compressive load. In Finite element analysis of the

different structures shown in Figure A8a, gyroid structures undergo a combination of bend and stretch dominated failure at different regions of the same structure. As the deflections along x and y axis increase with applied compression forces, indicative of stretching along the X-Y plane. Some regions of the lattice undergo deflection along either x or y axis which is indicative of bending. In Figure A8b and d with lidinoid and split-p structures respectively, only undergo bend dominated failure. The bending or stretching of the lattice sections creates tensile forces leading to failure due to the brittle nature of HAp ceramics. Therefore, reduction of stiffness with increasing porosities leads to excessive bending or stretching of the lattices during compression causing it to undergo early failure.

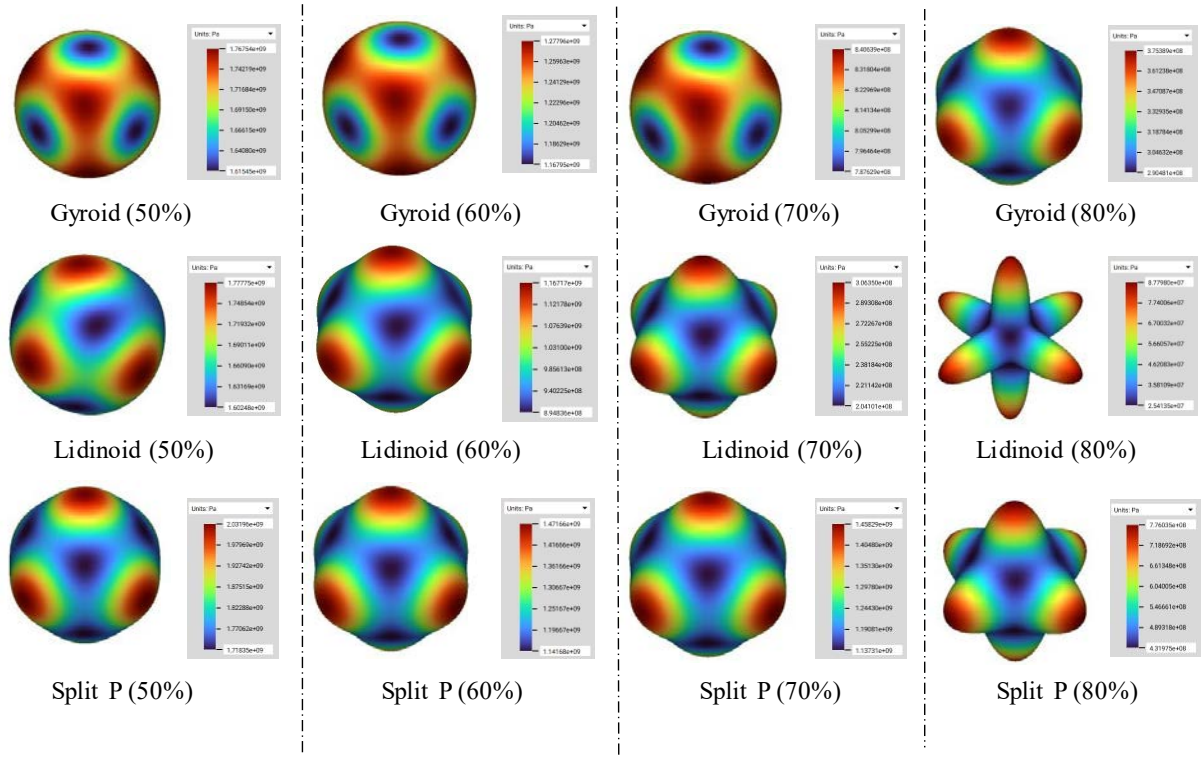

Figure 5.3: Effective Youngs modulus of gyroid, lidinoid and split-P TPMS structures as a function of porosity.

5.3.2. Compression strength of TPMS structures

Bone tissue can be classified into two types, the trabecular and cortical bones. The cortical bone segments are known to contribute more towards bone strength [337]. While the low strength of trabecular bone (2 - 12 MPa) helps in dissipating fracture energy during load transfer and the remaining spaces are filled with bone marrow/ECM [338]. Compression strength of the TPMS structures (gyroid, lidinoid and split-P) shown in Figure 5.4d is within a range of 2.5 – 25 MPa across all structures and porosities. This is within the range expected for trabecular bone but is insufficient to mimic cortical bone structures. Zhang et al. [329] showed that TPMS structures with porosities between 30 – 80 % were able to achieve compression strength of 30 – 150 MPa through stereolithography of ceramic slurry. However, these compression strengths were achieved when the average pore size was less than or equal to 0.6 mm. In this study pore sizes of all structures were greater than 1 mm reducing the achievable compression strength due to reduction in stiffness as discussed in the previous section. The presence of pores and defects in the ceramic matrix, is known to initiate crack formation and assist in crack propagation thereby reducing their compression strengths [339]. Therefore, these structures would require reinforcement prior to use in load-bearing areas.

To understand the effect of compression forces on TPMS structures it was simulated on the individual unit cells and their deformation response was observed in the principal directions. Gyroid structures predominately underwent stretch dominated failure with some amount of bending, causing the X and Y deflections to simultaneously increase with the applied load. Structures undergoing stretch dominated failures have high strength and stiffness but low energy absorption behaviour [340], explaining why gyroid structures performed similarly to the split-P structures. Split-P and lidinoid structures shown in Figure A8 show a bend dominated failure, where the struts buckle when compressed. Under compressive loading, split-P structures exhibit

demonstrably enhanced compressive strength due to the alignment of their constituent struts with the loading axis. Contrasting to this, lidinoid structures undergo premature failure in compression. This susceptibility can be attributed to the misalignment of their struts, which promotes catastrophic buckling events and the subsequent propagation of cracks through pre-existing porosity (shown in Figure A8b), leading to structural collapse.

Gyroid structures (shown in Figure 5.4a) showed similar compression strength at porosities 50 – 70% due to the uniformly distributed stresses within the gyroid structures. Ceramics are generally brittle in nature therefore a plane stress condition can be assumed during compression, Figure 5.4a shows the accumulation of stresses at the struts in the gyroid structures. Therefore, localised bending of the unit cell at the bottom of the structures becomes the first point of fracture, which is shown to propagate along the strut leading to final failure. Further the formation of X type double shear bands can be observed during the compression of these structures. Compression strength of gyroid structures was observed to be between 13 – 15 MPa.

Lidinoid structures (shown in Figure 5.4b) showed a decreasing trend in compression strength with increasing porosities. Wall thickness of lidinoid structures were progressively reduced from 0.8 mm to 0.5 mm to achieve higher porosities (60 and 70%), and further the stiffness matrix shown in Figure 5.3 began to indicate stress concentration in the principal directions at 60 and 70% porosities. Zhang et al. [329] showed that lidinoid structures undergo large deformation at the surface in contact with the applied load. The large deformation combined with thin-walled structure in lidinoids lead to failure. Therefore compression strength of lidinoid structures remained between 3 – 11 MPa.

Lidinoid and gyroid structures at 50 and 60 % porosity were comparable but a 70% porous gyroid structures showed higher compression strength than its similar lidinoid structure. As previously

shown in Figure 5.3, anisotropy in lidinoid structures is the highest at 70% porosity, making them weak in the direction normal to the applied load. Therefore, any in-plane forces acting on the lattice can cause damage which leads to failure. Further, Downing et al. [341] showed that during uniaxial compression of gyroid structures, helical substructures are responsible for transmitting load along the principal axis accounting for a higher compression strength. In case of the lidinoid structure, stresses are locally concentrated on the thin walls of the structure as shown in Figure 5.4c, leading to damage and hence failure. Further the mid-surface offset required for achieving porosities between 50 – 70% are twice that of split-P and gyroid structures, which reduces the effective thickness and material density distribution, leading to lower compression strength.

Split-P structures at 50 % porosity showed the highest compression strength (22.7 ± 4.9 MPa), while structures at 60 and 70% showed similar values of 11.0 ± 1.2 MPa and 11.5 ± 3 MPa respectively. Distribution of maximum principal stresses (shown in Figure 5.4b) appears to be a combination of helical pattern observed in gyroid structures and also locally distributed within the structure, making them capable of handling higher compressive forces. Pore sizes in these structures were between 0.1 – 0.15 mm in both structures and further their predicted stiffness matrix showed a similar response for both these structures (shown in Figure 5.3). Rezapourian et al. [342] showed that failure in split-P structures begin at the highest layers (top/bottom) and experience stretching and shearing during compression load, but extent of the stretching is a function of the relative density of the lattice. Therefore, increasing porosity, reduces the strength of these structures, allowing for easier stretching and bending of the lattice. However, in case of brittle materials such as HAp, small amounts of bending or stretching introduces defects within the lattice leading to early failure.

Orientation of the lattice struts in split-P and gyroid structures in the direction of an applied compressive load enables it to have higher compression strength as previously mentioned.

Whereas to function as an effective BTE scaffold, compression strength of the scaffold must be coupled with its ability to interact with its surroundings. Interaction with the local niche enables a bone healing cascade, triggering cells to repair damaged tissue and integrate the implanted scaffold. The simulated body fluid test described in the next sections provides an indication of potential osteoconductivty of the scaffold material. This test as described in previous studies [343] only measures the ability of the scaffold to promote the deposition of bone-like apatite on its surface, which is indicative of its potential to support bone regeneration in-vivo.

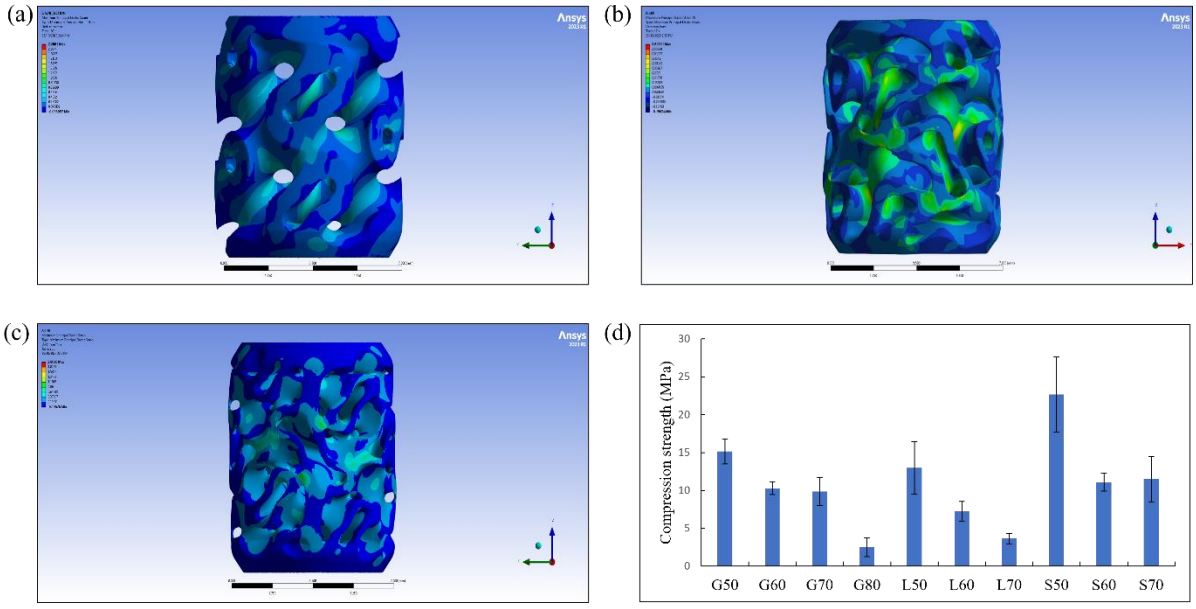

Figure 5.4: Maximum principal stress distribution observed in (a) G60 (b) L60 and (c) S60. (d) Compression strengths observed across all TPMS structures and porosities.

5.3.3. Simulated body fluid test

The simulated body fluid (SBF) solution used during this study, is known to simulate the ionic conditions of human blood plasma. The supersaturated solution consisting of calcium and phosphates undergoes precipitation as a function of changes in physiological conditions such as nucleation time, solution pH and interfacial energy [323]. Figure 5.5 shows the effect of scaffold geometry and porosity on the concentration of calcium (Ca) and Phosphorous (P) ions in the

solution. The calcium in the SBF solution is present in the form $CaCl_2$ and the phosphorus is mainly present in the form of phosphates from K_2PO_4. Therefore, the concentration of P and Ca of the solution were closely measured using ICP-MS, finally after 5 weeks of immersion surface of the structures were analysed using SEM-EDS.

One of the indicators that determines the quantity of HAp precipitated on the scaffold surface is the calcium and phosphate ions present in the solution containing the immersed TPMS structures. Kim et al. [326] showed that after initial soaking of HAp surfaces, the scaffold surface interacted with the surrounding Ca^{2+} ions in the SBF solution. Negative surface charges of the HAp scaffolds attract the Ca^{2+} ions forming the Ca-rich amorphous calcium phosphate (ACP). The formation of the ACP enables the scaffold to interact with the negatively charged phosphate ions (PO_4^{2-}) in SBF. Low stability of the amorphous phase in aqueous solution causes the transformation to an apatite crystal phase. After the formation of the apatite, the calcium, phosphate, magnesium and sodium ions present in the SBF lead to the growth of apatite crystal [324, 326].

The ICP-MS results showed that there is decline in Ca^{2+} ion concentration in the 1st week of immersion across all TPMS structures and porosities (as shown in Figure 5.5b). The Ca^{2+} concentration in the 1st week decreased with increasing porosity across all TPMS structures. Previous studies using hydroxyapatite – 316 stainless steel composites showed an increase in Ca^{2+} concentration due to dissolution of the surface hydroxyapatite layer [324, 326]. When immersion time was increased to 2 weeks, there was a gradual increase in Ca^{2+} ion concentration compared to the reference value taken prior to the start of the test. A similar increase in PO_4^{2-} ion content is observed between weeks 1 and 2 across all TPMS structures (shown in Figure 5.5a). This increase can be attributed towards the dissolution of calcium phosphates into the SBF solution in the form of Ca^{2+} and PO_4^{-} ions. As mentioned previously, rate of dissolution of HAp is higher than the rate of precipitation at the initial stages leading to an increase in ion concentration in the measured

solution. Increases in Ca^{2+} concentration observed in gyroid and lidinoid structures were proportional to the porosity of the structure. However, the split-P structure showed almost no change with increasing porosity. Lidinoid structures shown in Figure 5.6a have the highest surface area followed by split-P and gyroid structures, but this does not have a direct impact on the dissolution of Ca^{2+} and PO_4^{2-} ions into the SBF solution in week 2.

In weeks 3 and 4, the concentration of Ca^{2+} is shown to plateau across all structures but are still higher than the reference concentration of 90.9 ppm (as shown in Figure A4). The dissolution of surface HAp layer and the precipitation of HAp is a dynamic process that continues to occur until equilibrium is reached. Initially, as shown, the dissolution of the surface HAp layer outpaces the precipitation of HAp on the scaffold surface. When the reaction approaches equilibrium, the dissolution of Ca^{2+} ions decreases and therefore plateaus which is observed across all porosities and geometries between week 2 and week 4. The gyroid and split-P structures showed a small increase (5 – 10 ppm) and reached their highest values in week 3 before undergoing a gradual decrease from week 4. In week 5, there was a decrease in Ca^{2+} concentration in the SBF solution across all structures and porosities, due to the calcium apatite precipitation on the surface of these scaffolds (this is discussed further in section 5.3.4). As described previously, with the formation of the apatite crystals from the ACP there is a spontaneous increase in the consumption of Ca^{2+} ions, this is further extended to Mg^{2+} ions that undergo a gradual decrease in concentration in the SBF solution from week 2 onwards across all TPMS structures and porosities (shown in Figure A6).

Phosphorus content of the SBF solution shown in Figure 5.5a showed an initial reduction in week 1 across all TPMS structures and porosities. Week 2 shows a slight increase (less than 5 ppm) in P content, this could be attributed to the dissolution of the hydroxyapatite into the SBF solution. A similar increase was observed in Ca^{2+} ions during the same time interval. Xin et al. [324] showed

that the dissolution and precipitation of apatite on the surface of the scaffold is a dynamic process, which involves the dissolution of the surface layer increasing the Ca^{2+} ion concentration and the pH of the solution (due to OH^- ions). Spontaneous apatite precipitation begins to occur when the pH is over 7.4, leading to the consumption of Ca^{2+} and PO_4^- ions from the SBF solution to form apatite precipitates [326]. This study shows a similar trend where the P ion content reduction began from week 2 and reached a constant value by week 3 indicating that a significant amount of apatite precipitation occurred during this stage of the process. The next section describes the influence of scaffold geometry on bone apatite precipitation during SBF immersion.

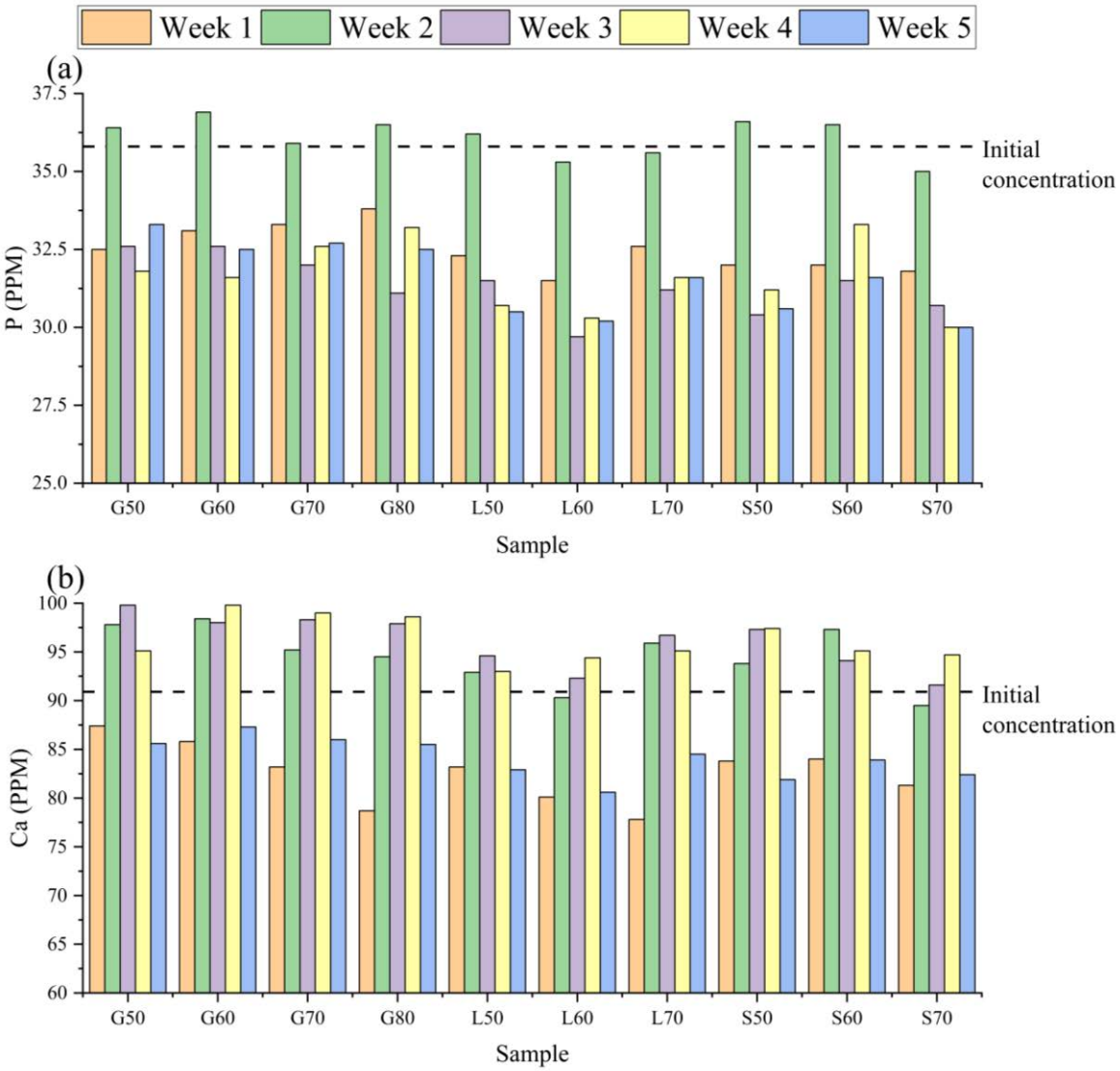

Figure 5.5: Measured concentration of (a) P & (b) Ca^{2+} ions in the SBF solution over 5 weeks as function of the TPMS structure porosity. The initial concentration of P and Ca^{2+} ions in the SBF solution has been indicated to be at 35.8 ppm and 90.0 ppm, respectively.

5.3.4. Effect of TPMS geometry on apatite precipitation

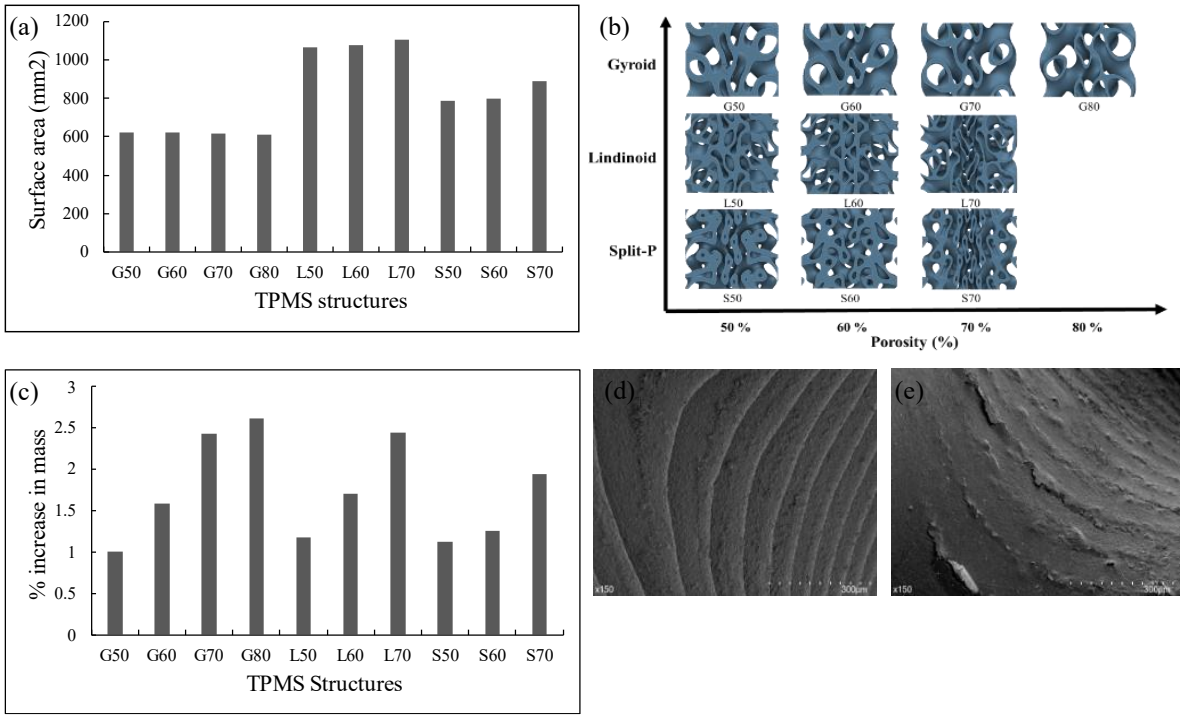

Figure 5.6: (a) Theoretical surface area calculated for the TPMS structures; (b) Internal architecture of the TPMS structures; (c) Increase in mass of the TPMS scaffolds after 5 weeks of immersion in SBF. Surface morphology of the (d) unsoaked TPMS structure (e) soaked TPMS structure observed after 5 weeks of immersion in SBF.

Surface area of the TPMS lattice structure is a function of scaffold porosity and pore sizes. Figure 5.6a describes the variation in the theoretical surface area (SA) of the TPMS structures (extracted from nToplogy software). Variation of the SA within each TPMS structure (gyroid, lidinoid and split-P) are less than 2%. However, variation across TPMS structures at the same porosities are between 40% - 80%. The internal architecture of the TPMS structures shown in Figure 5.6b, shows a reduction in closed porosity as the overall porosity increases from 50% to 70%. Gyroid and lidinoid structures of porosities 60% and 70% showed the highest increase (up to 2.5 %) in mass after 5 weeks of immersion in the SBF fluid whereas split-P structures showed the lowest quantity of apatite precipitation.

Presence of closed porosities at the core of split-P structures shown in Figure 5.6b reduces its interaction with SBF, hence reducing quantity of apatite precipitation observed. For example, in Figure 5.6b, the access to interior channels present in the split-P structure appear to be fewer in comparison to gyroid and lidinoid structures at 60% porosity. Therefore, ease intrusion into the TPMS structure is a critical criterion for the selection of lattice architecture for BTE scaffolds. Split-P structure showed low apatite precipitation even though available surface area was higher than the gyroid structures. Primary reason for this is due to the presence of closed porosities in the split-P structures (as shown in Figure 5.6b) preventing interaction with the surrounding fluid for precipitation to occur. Similarly, the same effect can be observed in the lidinoid structures where the percentage mass increase (shown in Figure 5.6c) is identical to that of the gyroid structure while its surface area is significantly higher. This indicates that interconnectivity of the scaffold structure and presence of open porosities are a better indicator of apatite precipitation as opposed to total surface area. Further, only surfaces fully exposed to the SBF fluid underwent changes in surface morphology (as shown in Figure 5.6e) indicating that interconnectivity which enables higher contact area with the SBF fluid can provide a better surface for precipitation to occur.

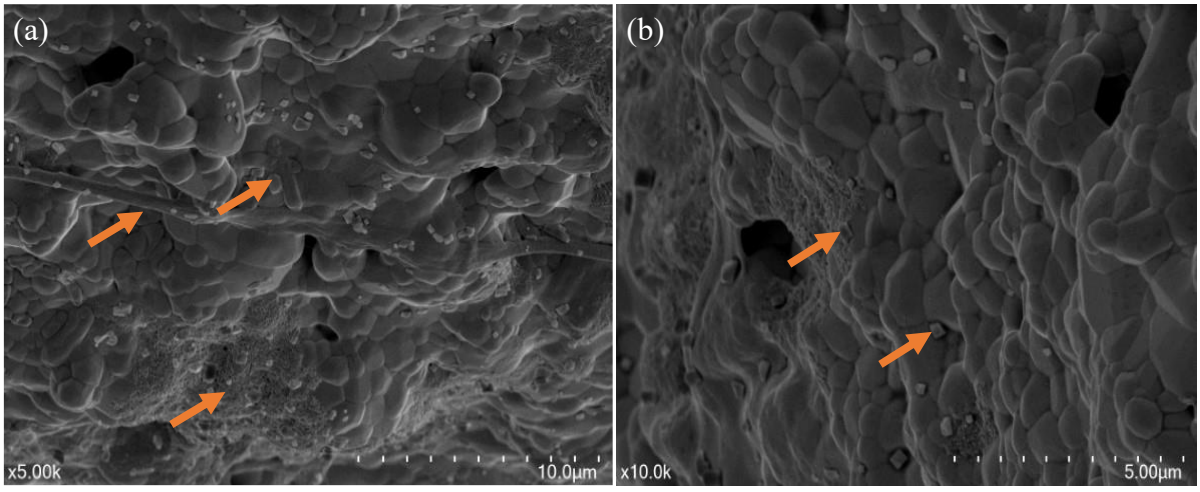

Figure 5.7: (a) Apatite precipitation observed in the form of spherules, fibres, and aggregated masses after 5 weeks of immersion. (b) Nucleation sites for further apatite precipitation.

Figure 5.7a showed that precipitates along the surface of the HAp appear in form of spherulites, aggregated masses, and fibres. Ofkeli et al. [344] showed that porous chitosan/gelatin composite cryogels when immersed in a SBF solution for 7 days, produced a mineralised hydroxyapatite coating in the form of spherules. These spherules are petal-like structures that are known to aggregate over the surface. These spherules are observed in Figure 5.7 however they appear to be distributed and not as individual masses as shown by Ofkeli et al [344]. Hydroxyapatite/collagen coated titanium scaffolds showed a uniform deposition of HAp on the surface of the immersed structure. The rough surface of the coated titanium scaffolds tended to have higher quantity of apatite precipitation [345]. A similar outcome was observed in our study where the apatite precipitation was preferentially deposited on the curved and rough edges as opposed to the flat surfaces on the TPMS structure (as shown in Figure 5.8). Vargas-Becerril et al. [346] showed that initial precipitation of apatite in the form of plate or sheet like morphology. These initial plates or sheet-like structures functioned as nucleation sites producing thicker layers of apatite precipitation with increasing immersion time. Similarly, the TPMS structures show formation of small plate-like structures as shown in Figure 5.7b, which eventually form homogenous distribution of apatite precipitate or fibres. Precipitation was primarily observed along the curved surfaces of the TPMS scaffold while flat surfaces of the scaffold show little to no precipitation as shown in Figure 5.8. Surface texture of the curved surfaces provide higher surface area to interact with the surrounding medium, thus allowing for higher precipitation. Furthermore, rough surfaces are known to promote the precipitation of HAp during SBF immersion which is indicated in Figure 5.8 [347].

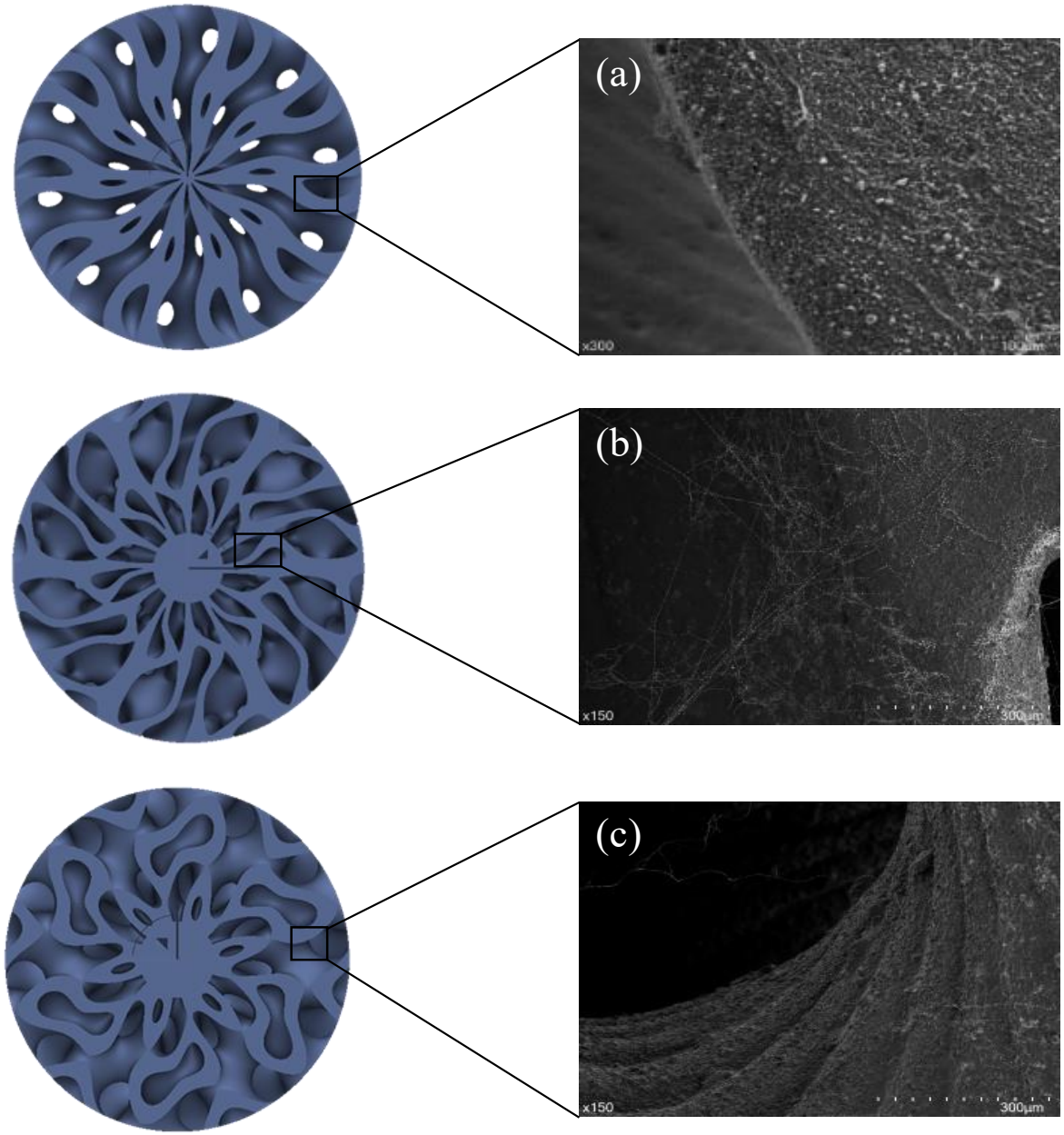

Figure 5.8: Precipitation of bone apatite on the surface of (a) gyroid (b) lidinoid and (c) split-P architectures. Apatite precipitation observed in all structures show a tendency towards undergoing precipitation along the curved faces of the TPMS structures.

Different types of precipitates on the surface of TPMS structures after 5 weeks of immersion in SBF are shown in Figure 5.9. Formation of these precipitates are driven by the reactions described previously; EDS was used to confirm the chemical nature of these precipitates. Ca/P ratio at the surface of the unsoaked sample (as shown in Figure 5.9a) was 1.49 ± 0.02 which is the typical

value reported for HAp with trace amounts of cationic impurities such as Mg [348]. Marques et al. [348] showed that localised pH of the solution has a major impact on the mineralisation of HAp. EDS spectrum collected at different precipitates showed that Ca/P ratio of the precipitates were different depending on the local conditions. For example, EDS spectrum measured and shown in Figure 5.9c and d showed an average Ca/P ratio of 1.4 ± 0.02 (measured at 6 different spots), which is similar to the Ca/P ratio reports for octacalciumphosphate ($Ca_8(H_2(PO_4)_6.5H_2O$). Further, formation of calcium deficient phosphates can be observed in different areas of the surfaces. EDS mapping of the precipitates showed a reduction in the intensity of Ca, indicating the precipitation of octacalciumphosphates. Whereas string like precipitates observed in Figure 5.9b showed a higher Ca/P ratio of 1.63 ± 0.06, which is higher than the reported value for the unsoaked HAp sample. Marques et al. [348] showed that a higher Ca/P ratio of 1.6 was observed during the formation of calcium deficient carbonate apatite. Substitution of PO_4^{2-} ions by CO_3^{2-} ions reduces the amount of atomic phosphorus leading to a higher Ca/P ratio. Therefore, nature of the chemical nature of the precipitate is function of the localised pH of the SBF fluid. There was no conclusive link between the scaffold architecture and the chemistry of the precipitate as the local conditions of each precipitation site would be unique.

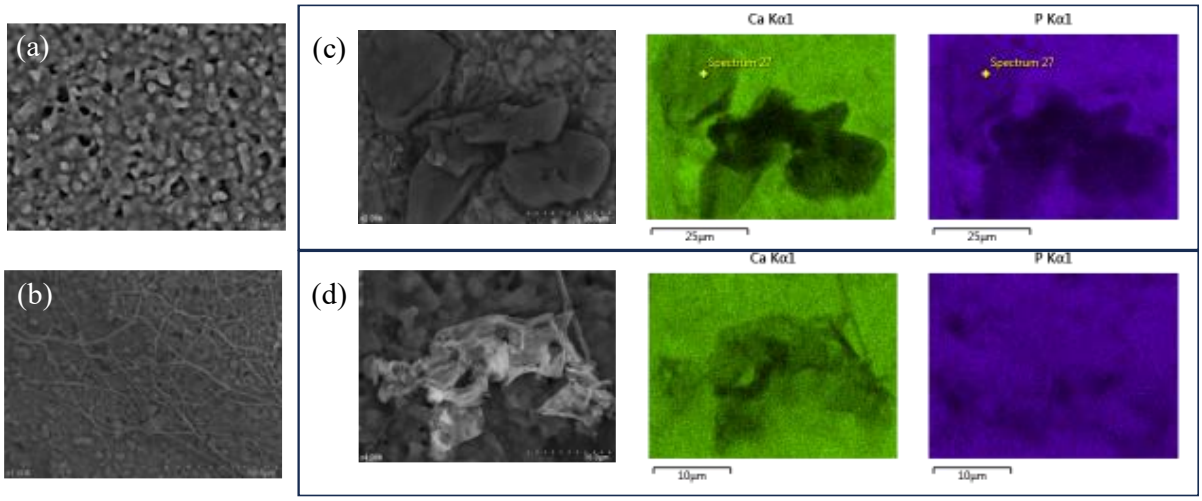

Figure 5.9: (a) SEM image of the unsoaked sample. (b) SEM image of soaked samples with string like precipitates. EDS mapping of the solid precipitates observed across the surface of the sample (c) and (d).

5.3.5. Graded TPMS structures

Graded TPMS structures provide significant advantage compared to single architectures due to their multi-functionality. Load-bearing BTE applications require a compression strength of at least 100 MPa while also providing sufficient porosity for the infiltration of the extracellular matrix and bone in-growth [310, 349]. Split-P structures at 50% porosity appeared to have the highest mechanical strengths (22.7 ± 4.9) while G70, L70 and G80 structures showed the highest apatite precipitation on the scaffold surface. Therefore, the core of the scaffold was designed using the structure with the highest compression strength while the outer shell was designed with TPMS structures that provided the highest apatite precipitation ability. Their compression strength and cellular proliferation were compared with structures having a solid core of diameter 3.5 mm while having an outer shell with G70, G80 and L70 architectures.

5.3.6. Compression strength

The graded composite structures with porous cores (S50) show a compression strength less than 10 MPa, which is significantly lower than the previously analysed TPMS structures (section 3.2).

Whereas structures with solid cores show compression strengths in the range of 50 - 120 MPa, which is close to the mechanical strength required for load-bearing application in BTE [329]. In this study the G70 structure with a solid core showed the highest compression strength of 122 MPa. Further the pore sizes of the outer shell were in the range of 0.9 – 1.2 mm and had a porosity of 70% allowing for cell penetration and bone in-growth during implantation [349]. Zhang et al. [329] showed a mechanical strength of 150 MPa using the split-P structure but at an average pore size of 0.3 mm and a porosity of 50%. Arabnejad et al. [349] achieved a compression strength of up to 120 MPa at a pore size of 0.5 mm and porosity of 70% using tetrahedrons made from Ti6Al4V alloy. Furthermore, pore sizes of 0.77 mm in the octet trusses reduced its compression strength to 31 MPa. In this study, the G80 structures with pore sizes between 0.9 – 1.8 mm produced a compression strength of 73.8 ± 3.8 MPa. TPMS structures with solid cores are more suitable for load-bearing BTE applications.

Porous cored structures shown in Figure 5.10a and 10b, were created by blending a core with the split-P architecture with an outer shell having lidinoid and gyroid architectures, respectively. Weak contact observed between the two structures as seen in Figure 5.10a and 10b indicates the relative ease in crack formation compared to the structures with the solid core. The structures with solid cores, show higher compression strength and offers higher contact area with the outer shell. Thus, G70 structures with a solid core having a compression strength of 122 MPa appears to the ideal configuration for load-bearing BTE applications. In the next section we will examine their effect of the solid and porous core in proliferation of osteoblast cells.

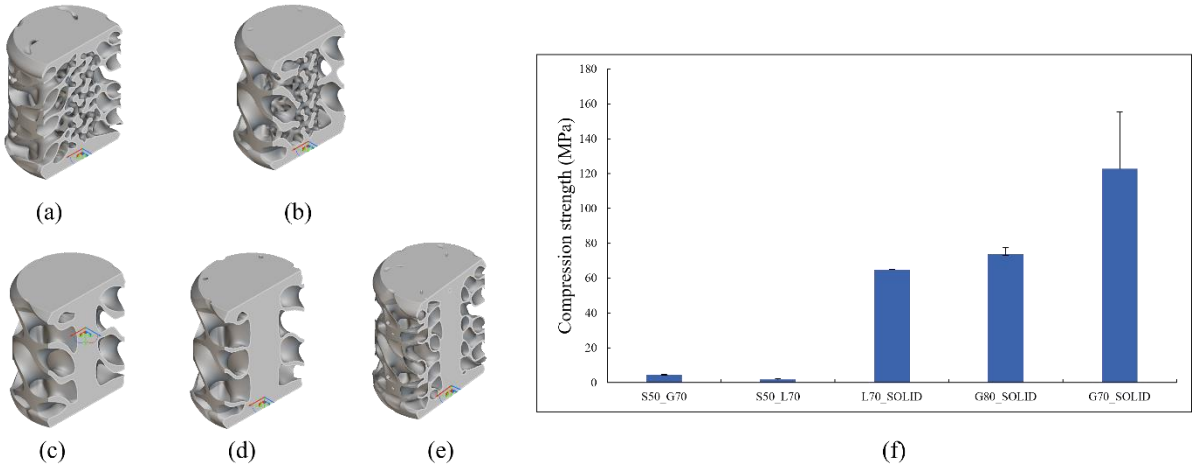

Figure 5.10: Graded TPMS structure having an inner core of S50 with a diameter of 3.5 mm and an outer shell made from structures (a) L70 and (b) G70. TPMS structure with a solid core of diameter 3.5 mm and an outer shell made from structures (c) G70, (d) G80 and (e) L70. (f) Measured compression strength of the solid cored TPMS and graded TPMS structures.

5.3.7. Proliferation Assay

Proliferation of human osteoblasts on the TPMS structures was determined by measuring the reduction of resazurin to resofurin. The absorbance was measured against wells only with cells at intervals of 1, 3 and 10 days (shown in Figure 5.11a). All scaffolds on day 1 showed similar cell viability compared to the cell only reference well. Day 3 showed the highest increase in cell activity across all structures and reference wells. The osteoblast cells appeared to have infiltrated the inner core of the structures as shown in Figure 5.11c, whereas structures with solid cores only showed attachment at the edge of the solid core and other areas as shown in Figure 5.11d. This could be due to ease of nutrient availability at the outer diameters of the porous sample [350], while the core structures do not receive sufficient nutrients resulting in a minor drop in cell proliferation after day 3. A student t- test was used to compare the observed reduction values in porous and solid core samples, the obtained p-value (0.3853) was significantly larger than 0.05, indicating that cells show a similar viability irrespective of the cores being porous or solid. Similarly, when the percentage reduction in solid core samples were compared with cell only

reference values using a student t-test the obtained p-value (0.4815) was greater than 0.05, indicating that there is no statistical difference in the viability of osteoblast cells.

ALP activity of the cells measured at day 10 during culture in an osteogenic medium is shown in Figure 5.11b. Structures show similar levels of ALP activity with minor variations within the range of their standard deviation. Observation of ALP activity in the cultured osteoblast cells mark the different stages of osteoblast maturation and help mediate deposition of hydroxyapatite [351, 352]. While there are other multiple regulatory factors that are responsible for bone forming, expression of ALP has been a common factor primarily because glycoproteins such as ALP help separate inorganic phosphates which then combine with the available Ca^{2+} ions to form hydroxyapatite, thereby integrating the scaffold structures to the damaged bone tissue [353, 354]. Although ALP activity cannot confirm bone in-growth, its presence alongside the scaffold structures indicates that there is no barrier to the cells forming bone tissues. Graded and solid core samples placed in a differentiation medium after 10 days showed similar ALP activity irrespective of their core design. Therefore, signals OF the osteogenic potential of these TPMS lattice structures are not affected by the core design.

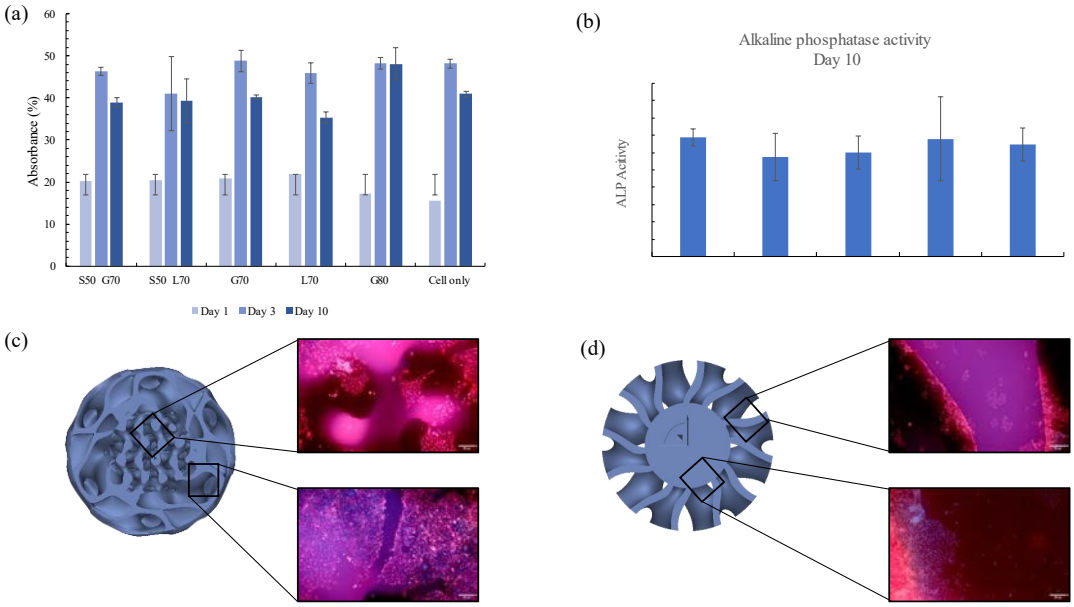

Figure 5.11: (a) Cell proliferation of the composite TPMS structures compared to a cell only reference. (b) ALP activity of osteoblast cells measured on day 10 cultured on the solid cored and porous cored scaffolds. Osteoblast cells attachment at the outer shell and the inner sections of the scaffold for (c) S50-L70 structure and (d) Solid core with G70 structure.

Structures G70 and G80 with the solid core provide similar performance when compared to the structures with a porous core. Further the G70 solid core structure provides a compression strength over 100 MPa making it an ideal choice for load-bearing BTE applications.

5.4. Conclusion

This study shows the performance of TPMS structures (gyroid, lidinoid, split-P) during apatite precipitation and determined their mechanical properties at porosities (50, 60 and 70%) and pore sizes (0.9 – 1.8 mm). Large pore sizes and high interconnectivity of G70, G80 and L70 structures, showed the highest increase in mass after 5 weeks of immersion in the SBF fluid. Further their ability to interact or undergo apatite precipitation was due to a combination of high porosity and interconnectivity, enabling ions transfer between the fluid and the scaffold surface.

Mechanical performance of these TPMS structures were lower than 30 MPa across all porosities and pore sizes, making them unsuitable to be used for load-bearing BTE applications, rather only offering mechanical performance similar to trabecular bone. Solid-cored TPMS structures, designed to leverage their apatite precipitation capability and enhance compressive strength, demonstrated mechanical performance (122 MPa) suitable for load-bearing applications in BTE at high porosities (70%) and large pore sizes (0.9 – 1.5 mm). Furthermore, cellular assays showed that cytoxicity and ALP activity of solid core samples (G70, L70 and G80) remained identical to their porous cored alternatives. While cellular penetration in porous cores structures remained marginally better as shown from the microscopic images captured, their poor compression strength makes them unsuitable for use in load-bearing BTE applications. The poor compression strength (less than 20 MPa) of porous cored structures is due to insufficient contact area between the core and shell. Since the porous cored structures can provide further bone in-growth and mechanical interlocking to provide long term structural support for the damaged bone tissue. Further work is required to identify suitable blending strategies between the TPMS structures to improve mechanical performance. These blending strategies could be applied to the solid core samples, reducing the diameter of solid core and increase the number of pores available for bone in-growth. Lastly, scaffolds used in load-bearing application are often subject to multi-directional loading, therefore ability to prevent fracture of the TPMS structures under loading could be a better indicator of the mechanical performance as opposed to only compression strength. These improvements will significantly contribute towards building a truly multi-functional scaffold for load-bearing application in BTE.

6. Multi-ceramic approach to bone tissue engineering scaffold design: Influence on mechanical strength and *in-vitro* performance

Abstract

Bone tissue engineering is a multidisciplinary field aimed at developing functional bone substitutes to treat skeletal defects caused by trauma, disease, or congenital anomalies. This approach combines principles from biology, engineering, and material science to create scaffolds that support cell attachment, proliferation, and differentiation, ultimately leading to new bone formation. However, challenges around vascularisation, mechanical stability and integration of the BTE scaffold with host tissue remain. In this study we explored a multi-ceramic (using 3% yttria stabilised zirconia (3Y-TZP) and hydroxyapatite (HAp)) based approach using 3D printing to have a bioactive external shell with an inert high strength core and compared it with a single ceramic approach. Co-sintering of the two ceramics produced finer sub-micron grain sizes within the 3Y-TZP core while having grain sizes in the range 2 – 5 μm in the outer shell. Compression strength of the 3Y-TZP – HAp composite along the longitudinal direction was 56 ± 2MPa at an average pore size of 800 – 2000 μm along the outer HAp ring. However, when loaded along the transverse direction, the composite structure underwent failure at 30 N of force. In comparison pure 3Y-TZP scaffolds showed a compression strength of 226 MPa at the same pore size in the longitudinal direction and underwent failure at a transverse load of 1000 N. Osteoblast cell proliferation on pure HAP and 3Y-TZP structures was identical to that of composite samples. Similarly, their expression of osteogenic markers was identical to that of HAp and TCP bioceramics indicating positive potential for tissue integration and formation of new bone tissue. Therefore, this study

showed that 3Y-TZP based scaffolds with triply periodic minimal surface (TPMS) structures showed the best potential for load-bearing BTE application requiring multi-directional strength. Future research to overcome the limitations of multi-ceramic processing in 3D printing has the potential to address the challenges with the current 3Y-TZP – HAp composite design.

6.1. Introduction

Biomechanics of the human body involves the application of Newtonian mechanics to muscular and skeletal systems. The bone tissues function as levers for the muscle fibres to pull against, generating a reaction force on the bone tissue during locomotion. High strength of the bone tissue dissipates the reaction force generated during locomotion and any physical impact. The hierarchical nature of bone tissue also allows the dissipation of reaction forces through microcracking, crack deflection and fibre bridging. Furthermore, the presence of the collagen network that is bound to the apatite crystals enhances the toughness by functioning as a matrix which can deform under load [355]. Bone tissues can heal small damages through a cascade of chemical signals triggered at the time of the facture however, large impacts can lead to major damage of the tissues which cannot be dissipated through the above-mentioned mechanisms. [3]. In the case of large fractures or defects, scaffolds are necessary to support the damaged tissues while also promoting bone healing. This requires a porous yet high strength structure that is bioactive [356]. Previous studies aimed at improving these properties have only focussed on compression strength in the longitudinal direction when considering the strength of the scaffolds [329, 342, 357, 358]. However, during most fracture events, impact forces act in multiple directions causing damage to bone tissue. For example, Cohen et al. [359] showed the importance of impact direction on the length and number of fractures. Wedel and Galloway [360] showed that oblique fractures during axial loading occurred due to a combination of axial compression, torsion and bending. With multiple forces acting on the bone tissues, designing scaffolds simply for high compression strength in the longitudinal direction is insufficient, their strength in other directions need to be considered.

Cellular structures offer a unique combination of low density and high strength, ideal for BTE applications where the porous structure allows for cell infiltration and strength to support the

damaged tissues [23, 361]. Triply periodic minimal surfaces (TPMS) such as gyroids, lidinoids, split-P and schwarz structures are known to have high stiffness while also being porous. With zero mean curvature at every point, there is a lack of stress concentration during loading, improving the material toughness [362]. Conway et al. [363] showed that the undulating surface of the gyroid structure increased the distance traversed by the propagating crack. Further, for the crack path to follow the surface of the gyroid, it involved multiple changes in direction leading to crack deflection and hence improvement in toughness. While gyroid structures have been a popular choice in BTE applications, there are limited studies exploring the use of other TPMS structures such as split-P, schwarz and lidinoid. The use of TPMS structures can certainly benefit the structural response of the material in BTE applications, however, the bioactivity of the material also plays a key role [3, 364]. For example, Feng et al. [365] assessed the application of PEEK/β-TCP composites, where the β-TCP provided the required bio-functionality and degradability while the continuous PEEK phase provided the necessary mechanical strength. Xu et al. [366] showed that a copper (6 wt%) modified Ti-6Al-4V alloy showed improved anti-inflammatory gene expression compared to the unmodified material and also upregulated the expression of vascular endothelial growth factor (VEGF), which plays an essential role in angiogenesis. While there have been multiple studies reporting the use of polymer, polymer-alloy, polymer-ceramic, metal-metal and metal-ceramic composites [3, 364, 367, 368], there have been very limited studies exploring the use of ceramic-ceramic composites.

In this study ceramic-ceramic composites were prepared using a combination of ceramic stereolithography and conventional manufacturing techniques. Phase composition and surface morphology of the ceramic composites were identified using Raman spectroscopy and scanning electron microscopy (SEM), respectively. Further, compression strength and resistance to transverse loading were assessed for the graded composite TPMS structures and compared with structures prepared with the single materials, HAp and 3Y-TZP. Fracture pattern of the structures

during compression and transverse loading were captured using a high-speed camera to understand the failure mechanisms. These results show the feasibility of a multi-ceramic-based approach to designing BTE scaffolds. Finally, osseointegration potential, proliferation, and alkaline phosphatase activity of cells on the composite structures were compared with activity of cells on similar HAp and 3Y-TZP structures.

6.2. Methodology

6.2.1. Fabrication of composite scaffolds

A CAD workflow was designed using nTopology to blend a solid core to the 70% gyroid structure that was identified from our previous work. All parts were 3D printed on the C100 Easy fab (3DCeram, Limoges, France) using photocurable resins of HAp and ZrO_2 supplied by 3DCeram.The slurries were processed using the manufacturers recommendation to produce green parts.

The composite structures were fabricated in a stepwise manner since HAp and 3Y-TZP slurries cannot be simultaneously processed in the 3D printer. Interaction of BTE scaffolds with the surrounding niche requires a bioactive material, hence the outer shell of the scaffolds was fabricated with a hollow inner core. Considering that the current configuration of the 3D printer does not allow the simultaneous processing of two different ceramic slurries, the hollow core was completely filled with uncured 3Y-TZP slurry using a pipette. In our previous work we showed that sintering 3Y-TZP-HAp composites at temperatures exceeding 1300 ℃ can introduce undesirable phase changes [369]. Therefore, the green parts produced were initially debinded and then sintered at 1280 ℃ for 60 min at 3 ℃/min as recommended by the manufacturer for the HAp slurry. Lower sintering temperature reduces the formation of cubic zirconia and β-TCP.

Performance of these composite structures was compared with similar structures fabricated using pure HAp and 3Y-TZP.

6.2.2. Characterisation of sintered parts

To characterise the grain size and porosity of the composite parts, solid cylinders (diameter = 10 mm and height = 5 mm) with a hollow core were fabricated using HAp and were subsequently filled with 3Y-TZP slurries as described in section 6.2.1. The sintered parts were prepared for SEM using a series of grinding papers (180 grit, 320 grit, 600 grit, 800 grit, 1200 grit and 2500 grit) followed by polishing using a 1 μm diamond suspension and OP-S solution for up to 10 min. The polished samples were thermally etched at 1180ºC for 60 min. Scanning electron microscopy (SEM, Hitachi SU5000) was used to characterise surface grain sizes and composition of the parts.

To analyse the phase composition of the composite, confocal laser Raman spectrometer (Witec, Germany) was used with a green laser (532nm). Measurements were taken using a 40X lens in static analysis from wave numbers 100 cm^{-1} to 3600 cm^{-1}. Readings were taken at multiple spots (as indicated in Figure 6.1) along the sample to map out the different phases present in the composite.

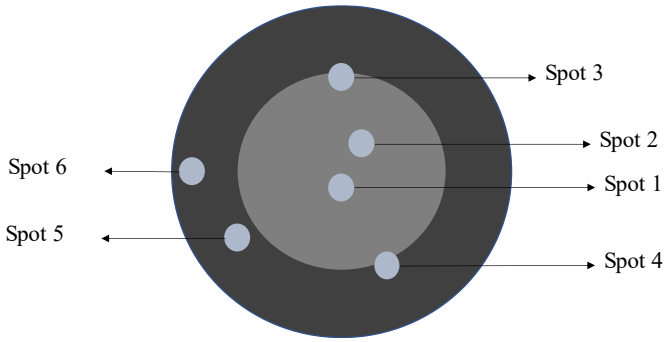

Figure 6.1: The 3Y-TZP core and HAp outer ring are represented by a dark and light grey, respectively. Locations where the Raman spectra were collected for the 3Y-TZP-HAp composite sample are indicated with spots.

6.2.3. Mechanical performance of 3D printed scaffolds

6.2.3.1. Compression testing

The compression strength of the composite scaffolds of diameter 10 mm and height 10 mm was measured by compressing the scaffolds at a crosshead speed 0.1 mm/sec. An average value was calculated from three repeats.

6.2.3.2. Indirect tensile test

Adhesion between the HAp outer shell and inner core is critical for load-bearing BTE applications. To measure the adhesion strength, the scaffolds were diametrically loaded similar to an indirect tensile test at the rate of 0.2 mm/sec. The process of material rupture was captured using high speed photography at 12500 frames per second.

6.2.4. *In-vitro* testing

6.2.4.1. In-vitro Osteoblast Culture

Human osteoblast hOB CRL-3602 ATCC cells (Manassas, USA) were expanded in complete media (CM) consisting of Dulbecco's modified Eagle medium (DMEM), supplemented with 10% foetal bovine serum (FBS), 2mm L-glutamine, and 1% penicillin–streptomycin solution (Sigma-Aldrich) incubated at 37ºC, 5% CO_2, and 90% humidity. For passage, adhered cells were lifted using 0.025% trypsin (Sigma-Aldrich) and resuspended in CM every 2 days as cells reached 95% confluence confirmed using a TS100 bright-field microscope (Nikon). Cells were cultured on scaffold structures following passage 5.

6.2.4.2. Culture on Scaffolds

Discs having a diameter and height of 10 mm and 3 mm respectively were placed in wells of a 24 – well plate and 0.40 ml (containing 7 x 10^4 cells) of the cell suspension was added to each well completely immersing the scaffolds. The plates were then incubated at 37 °C at 5% CO_2 for 10 days. All cell cultures were performed in triplicate.

Materials analysed in the following assays include HAp, 3Y-TZP-HAp composite and two types of 3Y-TZP. The two types of 3Y-TZP arise from the differences in sintering conditions, where type 1 3Y-TZP has been sintered at the sintering cycle recommended by the manufacturer, while type 2 3Y-TZP has been sintered at 1280 ℃ for dwell of 60 min at a heating rate of 3 ˚C/min to mimic the 3Y-TZP produced in the composite. The composite consisting of the 3Y-TZP core was sintered at 1280 ℃ as our previous work indicated that at temperatures greater than 1300 ℃ HAp begins to undergo dehydration to form α-TCP [369].

6.2.4.3. Proliferation Assay

Proliferation of the cells were assessed on days 1, 3, and 10 by measuring the reduction of resazurin to resofurin, as previously described [334, 335]. Briefly, 10% resazurin (Sigma Aldrich) was added to each osteoblast and scaffold culture which were incubated at 37 ^{0}C and 5% CO_2 for 5 hrs. Medium only plus 10% resazurin was used as a control. Triplicate replicate 100 µl media from each specimen was transferred to a 96-well plate, and the absorbance of resorufin at 570 nm and 600 nm wavelengths was recorded using an iMark™ Microplate Absorbance Reader (BioRad). The percentage of resorufin was calculated relative to the medium only control. To isolate the activity of cells on the test samples, the cells were transferred to new wells 24 hours before initiating the assay, thereby ensuring that only the activity on the scaffold materials was measured.

Further, HAp as a known bioceramic, was used as a relative control to compare proliferation across different scaffold materials.

6.2.4.4. Fluorescence microscopy

Microscopy of osteoblast cells adhered to the scaffold surface were conducted on days 1, 3, and 10 on technical replicates of the scaffold structures used in the proliferation assay. The remaining CM was removed, and scaffolds were washed twice with 1x PBS. The cells were fixed with a 20 min room temperature incubation in 3% paraformaldehyde (PFA) solution, followed by further washing with 1x PBS. Intracellular actin filaments were stained with a 1:1000 diluted working solution for Abcam ifluor 594 (Abcam, Cambridge, UK) prepared using the manufacturer's protocol and 150 µl of the solution was added per well, while cell nuclei were stained with 20 µl of 4′,6-diamidino-2-phenylindole (DAPi) (Biolegend, San Diego, USA) following incubation in the dark for 90 min. The cells were then imaged using an IX53 inverted-microscope (Olympus) with blue, green and red fluorescence channels and U-HGLGPS fluorescence light source using a 10 X objective.

6.2.4.5. Alkaline phosphatase assay

Alkaline phosphatase (ALP) activity of the cells attached to the scaffolds was analysed with an ALP kit (ABCAM, Cambridge, United Kingdom) using scaffolds of diameter 10 mm and thickness 3 mm which were technical replicates of the scaffold used previously. The structures were placed in a 24-well plate and seeded with osteoblast cells to maintain a cell density of 7×10^4 and incubated for 10 days. At day 10 cell lysates were collected according to the protocol described by the manufacturer and stored at -80 ˚C until the assay was performed. ALP activity in each sample was measured by adding pNPP as a substrate and incubating at 25 ˚C in the dark for 25 min as per the manufacturer's instructions. The absorbance at 405 nm was read using a FLUOStar

Omega microplate absorbance reader (BMG Labtech, Germany). The quantity of pNPP hydrolysed to pNP was determined from a standard curve using the absorbance values. The standard curve dilution was prepared by mixing the pNPP and ALP enzymes supplied by the manufacturer in different proportions. Therefore, ALP activity was measured as a function of the quantity of pNP solution in μmol/min/mL or U/mL.

6.2.4.6. Bone-specific gene expression analysis

The relative mRNA expression of *RunX2* (NM_001015051), *Osteocalcin* (*OCN*, NM_199173) and *Osteopontin* (*OPN*, NM_001251830) were measured using quantitative reverse transcription polymerase chain reaction (RT-qPCR). RT-qPCR was performed as previously described [370, 371]. Briefly, RNA was isolated from osteoblasts using a MagMAX™ mirVana™ Total RNA Isolation Kit (Applied Biosystems) with cells harvested at day 10 post-seed in 100 μL of MagMAX™ lysis buffer (Applied Biosystems) and homogenised with pipetting. The lysate was stored at -80 °C until extraction. RNA eluent was converted to cDNA using the SuperScript™ IV First-Strand Synthesis System (Invitrogen) in 10 μL total volume reactions with random hexamers and SuperScript™ reverse transcriptase at (10 $U/\mu L_{RNA}$), [371]. qPCR was performed using ssoAdvanced SYBR® SuperMix (BioRad) following the manufacturer's recommendations (hot start 2 min at 95 °C, followed by 40 cycles of 15 sec at 95 °C and 30 sec at 60 °C) [370]. Technical triplicate reactions were run at 5 μL total volume amplifying 1 μL sample, alongside a no template negative control containing Ultra-Pure H_2O (Invitrogen), as previously described [370, 371]. Reactions were measured by QuantStudio 5 Real-Time PCR Machine running QuantStudio Design and Analysis Software version 1.4.3, (Applied Biosystems). Cycle threshold values (Ct) were determined with the threshold set in exponential phase amplification at ΔRn 0.008. All reactions were followed by a melt curve analysis ensuring primer specificity and contained desalt-grade PrimerBank™ [372] primers (Sigma-Aldrich) run at 500 nM. Reaction efficiency was

calculated as previously described by Bustin et al. [373]. mRNA expression was calculated with the standard delta-delta cycle threshold ($2^{-\Delta\Delta Ct}$) method relative to *Succinate dehydrogenase complex, subunit A* (*SDHA*, NM_004168) expression, as previously described [374], using HAp-seeded cells as the control group.

6.2.4.7. Statistical Analysis

Group means were compared by unpaired *t*-tests, or one-way ANOVA, followed by Tukey corrected multiple comparisons testing. Analysis was carried out using GraphPad Prism version 7.0 (GraphPad). In all cases, $P < 0.05$ were considered significant.

6.3. Results and discussion

6.3.1. Characterisation of sintered part

The microstructure of the composite scaffolds is shown in Figure 6.2a, the transition zone indicates a gradual increase in grain sizes from the inner core to the outer shell. The internal 3Y-TZP core shown in Figure 6.2b shows very fine grain sizes (less than 1 μm). Grain sizes in the transition zone are a combination of large faceted and sub-micron grains as shown in Figure 6.2c. These faceted grains have an average size of 1.42 ± 0.48 μm while the finer grain sizes around these faceted grains are less than 1 μm. Moving along the transition zone, the grain sizes gradually increase as shown in Figure 6.2d, where the average grain sizes are within the range of 2 – 5 μm.

To measure the composition along the transition zone, a 250 μm line was drawn and the composition across the line was measured using EDS (as shown in Figure 6.2f). The inner zone shows a strong signal of zirconium (Zr) which reduces gradually moving from left to right. The calcium (Ca) content appears at the interface of the two materials and increases as we move from

left to right. Therefore, the EDS indicates intermixing of the Zr and Ca within 100 µm from the transition zone.

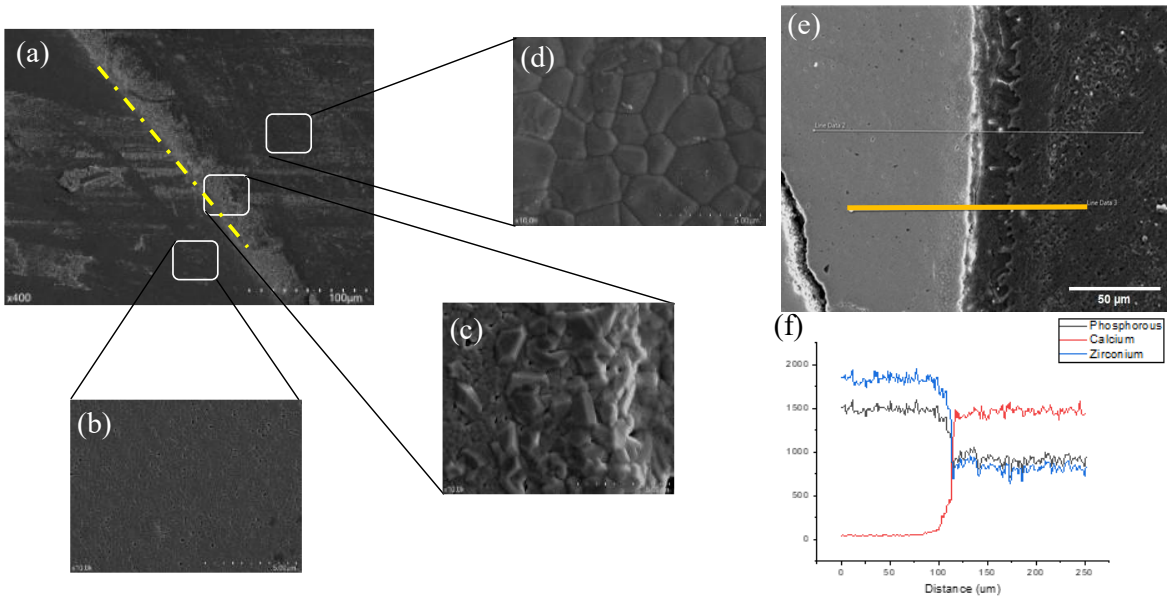

Figure 6.2: (a) Grain structures of the 3Y-TZP – HAp composite observed at magnification of 400x. The boundary between the outer shell and inner core is represent by a dashed line. (b) Inner 3Y-TZP core observed at 10000x magnification. (c) The Transition zone between the 3Y-TZP and HAp sections shows faceted grains along with sub-micron grains around it. (d) Microstructure of the HAp outer section, showing slightly larger grain sizes compared to the transition zone and significantly larger than the submicron grains observed in the 3Y-TZP core. (e) Back scatter image of the transition zone between the 3Y-TZP and HAp. (f) EDS spectrum captured along the 250 µm line drawn across the transition zone.

Figure 6.3 shows the Raman spectra acquired at different spots along the 3Y-TZP-HAp composite. Interior spots such as points 1, 2 and 3 show major bands located at 140, 257, 316, 461 and 639 cm^{-1}. While most of these major peaks correspond to tetragonal ZrO_2, twin peaks observed at wave number 178 - 189 cm^{-1} in spots 1 and 3 corresponded to monoclinic ZrO_2 [375, 376]. The small intensity of these peaks indicated that the quantity of monoclinic phases is relatively low and present only due to the transformation of tetragonal phase during the cooling process. Furthermore, in the case of spot 3, located at the transition of 3Y-TZP and HAp, minor peaks between wavenumbers 300 and 400 cm^{-1} and 500 and 600 cm^{-1} indicate the presence of blended monoclinic

and tetragonal phases [376]. Their intensities are significantly lower than the remaining tetragonal phases, therefore, the quantity of blended monoclinic and tetragonal phases is relatively small (as shown in Figure A9 and Figure A10). This also explains the minor overlap observed in the compositions of Zr and Ca from the EDS results shown in Figure 6.2f. In spots 5 and 6, located at the outer HAp shell, the peaks that appeared previously for 3Y-TZP and monoclinic zirconia have completely vanished. This sharp drop off confirms that the intermixing of HAp and 3Y-TZP occurs along a small region of their interface. We observed 5 major peaks in spots 5 and 6 at wavenumbers 420, 567, 938, 1017 and 3580 cm^{-1} that confirm the presence of HAp [377]. The peak observed at 938 cm^{-1} corresponds to the symmetric stretching of the P-O bond whereas the peak at 1017 cm^{-1} is from asymmetric stretching of the P-O bond arising due to triply degenerate T2 vibration mode. Peaks at 420 cm^{-1} occur due to the bending modes of O-P-O bonds whereas the peak at 567 cm^{-1} occurs from the asymmetric bending modes induced by the doubly degenerate T2 O-P-O bending mode. Furthermore, a peak observed at 3580 cm^{-1} is due to the stretching mode of the O-H bond [377]. Spot 4 has identical peaks to those seen in spots 5 and 6 but also has minor peaks visible at wavenumbers 1350 and 1600 cm^{-1} which do not correspond to HAp (as shown in Figure A10). These peaks could be due to microstructural defects, impurities or residual stresses on the surface since Raman spectra is known to be sensitive to such features [378]. Further analysis will be required to confirm this.

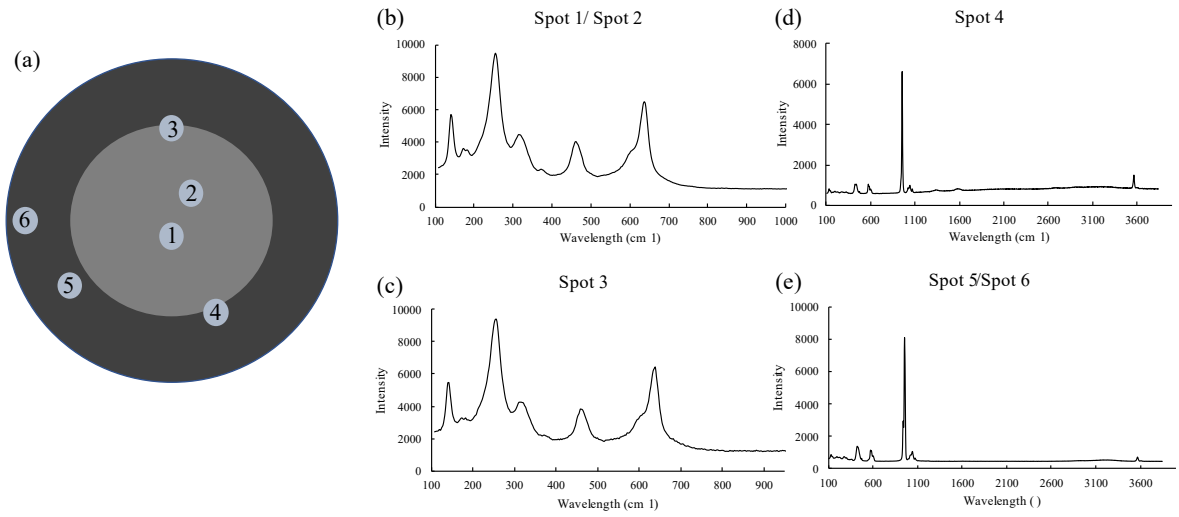

Figure 6.3: (a) Location of the spots analysed on the 3Y-TZP and HAp composite. Raman spectra obtained at (b) Spot 1 or Spot 2 (c) Spot 3 (d) Spot 4 and (e) Spot 5 or Spot 6 from wavenumbers 100 to 4000 cm^{-1}.

6.3.2. Mechanical performance of graded composite

Mechanical performance of the composite was compared with similar structures made of only HAp and 3Y-TZP. Failure of the samples was captured using a digital camera and analysed to identify the different mode of failure during compression. Similarly, a high-speed camera captured the failure modes during transverse loading on the different materials.

6.3.2.1. Compression strength

Load-bearing application in BTE requires a minimum compression strength of 100 MPa, which is similar to the compression strength of cancellous bone. Trabecular bone on the other hand, being marginally weaker at 2 - 12 MPa, plays a key role in dissipating fracture energy and improving load-bearing capacity. While the core and shell structures shown in our previous study demonstrated a compression strength of over 100 MPa, the effect of the inclusion of a 3Y-TZP core was still unknown. In this study, the composite structure showed a compression strength of 56 ± 2 MPa, which is slightly greater than the HAp sample (41.3 ± 4.76 MPa) as shown in Figure 6.4a. These compression strength values for a gyroid structure at 70% porosity and a pore size

between 800 – 2000 μm are significantly larger compared to values reported in literature. For example, Deng et al. [379] achieved a compression strength of 4.45 MPa in a HAp – Akermanite-based functionally graded gyroid structures with a total porosity of 60% by volume. Further Bouakaz et al. [380] showed a compression strength of 4.49 MPa in a HAp-based gyroid structure with 65% porosity. Zhang et al. [329] reported a compression strength of 150 MPa for a HAp-based split-P structure but this was achieved at a pore size of 300 μm whereas structures at porosities of 900 μm showed a compression strength less than 20 MPa. Although the reported compression strength in this study is higher than other reports, it remains insufficient for load-bearing BTE applications. 3Y-TZP structures at the same porosity and pore sizes achieved a compression strength of 226 MPa (as shown in Figure 6.4a) making them ideal for load-bearing applications. The R-curve behaviour of partially stabilised zirconia (3Y-TZP) as described in previous studies allows them to perform significantly better than HAp and the composite [381, 382].

The mechanism during failure as captured from the digital camera appeared to be similar across all samples, therefore, only the failure of the 3Y-TZP is shown in Figure 6.4. Gyroid structures are known to undergo bending-dominated failure during compression, where the localised bending of the struts leads to stress concentration and hence cracking as seen in Figure 6.4c and 6.4d [383]. Formation of these cracks at the bottom and top could be due to the proximity to the support or the presence of a pre-existing defects. Maskery et al. [383] showed that prior to cracking there was some extent of successive collapse of the layers in the case of Al-Si10-Mg double gyroid lattices. However, plastic deformation is not visible in our study as ceramics are brittle in nature. Furthermore, as shown in Figure 6.4e and 6.4h, application of load leads to the formation of diagonal shear bands which are approximately 45° to the applied load. This process continues until the shell is completely sheared off leaving behind a solid core as shown in Figure 6.4i. The retention of the solid core in these BTE scaffolds indicates that damaged tissues will still be

supported in a situation where the structure of the outer shell is compromised but also highlights the weakness of the interconnection between the outer ring and the inner rings.

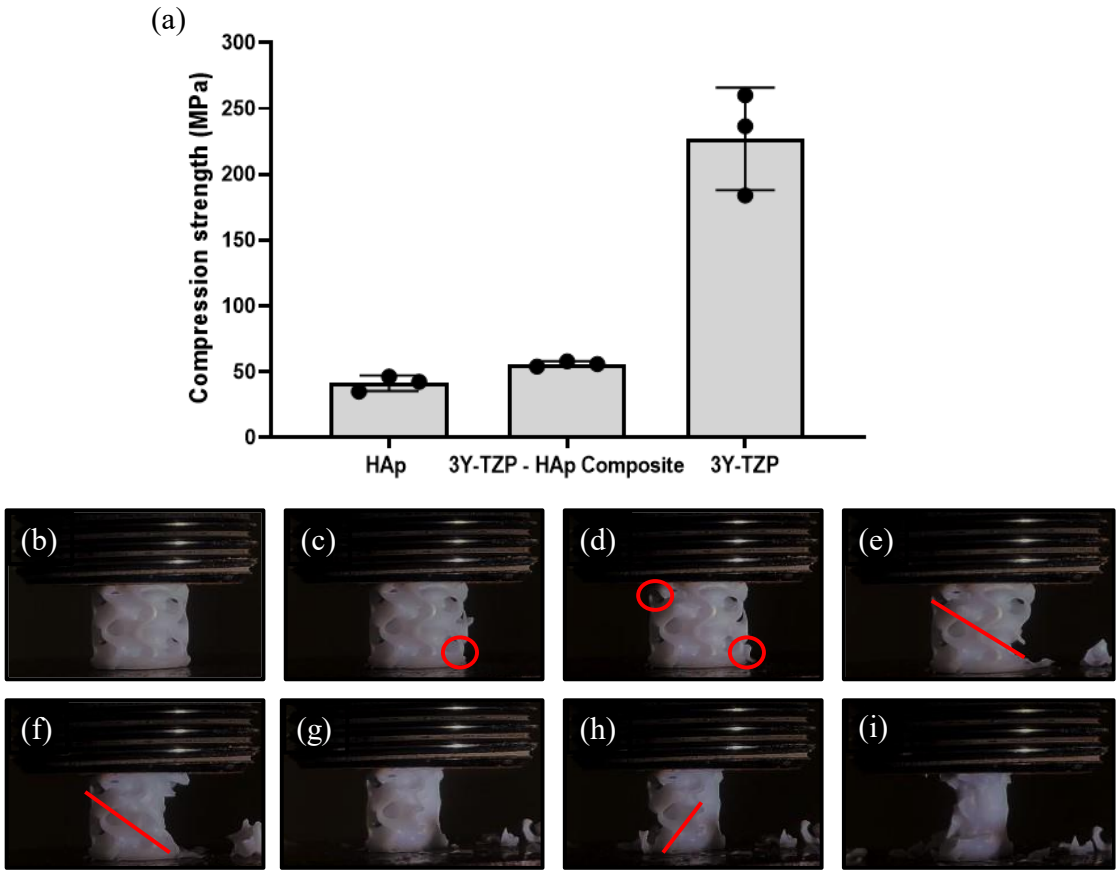

Figure 6.4: (a) Compression strength of HAp, 3Y-TZP-HAp composite and 3Y-TZP structures. (b) Initial setup of the structure prior to the application of load. (c) and (d) Formation of cracks due to local stress concentration. (e), (f), (g) and (h) Formation of shear bands approximately 45° to the applied load. (i) The complete shearing of the outer shell with the inner solid core still intact.

6.3.2.2. Effect of transverse loading on the composite structure

BTE scaffolds implanted in load-bearing areas often experience loading in multiple directions due to the biomechanics of our body. For example, the major forces acting on hips during exercise are the contact forces acting along the axis of the femoral head, a bending moment along the femoral neck and lastly the torsion acting around the femur axis. Keyak et al. [384] showed that, for a given magnitude of force, the risk towards hip fracture depends on the force direction. Therefore, in this

section we discuss the effect of transverse loading on the structure and show fracture propagation during loading.

Force-displacement curves shown in Figure 6.5a indicate that HAp undergoes failure at 80 N of force in the transverse direction. While the failure was not instantaneous, accumulation of micro-cracks and crack growth appeared to be the main causes. This can be observed in Figure 6.5b where the initial crack first appears on the periphery and propagates along the outer shell of the structure. As the compressive force is increased, the tension perpendicular to the loading direction causes further crack growth (as shown in Figure 6.5b). Miranda et al. [385] showed that when robocasted HAp structures were subjected to transverse loading, unsupported sections experiencing tensile load underwent failure causing the entire structure to fail. Similarly, during transverse load, cracks initially appear at the region where tensile stresses are maximum and subsequently propagate along the outer shell. Finally, the crack reaches the outer shell and causes complete failure. We observed that the crack/defects do not propagate close to the solid core, this could be due to the discontinuities present between the inner core and outer shell. Therefore, having a gradual transition from the outer shell to the inner core could help in load distribution. In the case of 3Y-TZP (shown in Figure 6.5c), the structure undergoes failure at 1000 N. As the applied load increases cracks are initiated at the surface and propagate inwards as shown in Figure 6.5d. The crack here tends to penetrate through the inner core unlike that of the HAp sample. The load displacement curve also shows that there are no micro-cracks, instead there is a rapid decline in the applied load (as shown in Figure 6.5c) indicating that the attachment of the outer shell and the inner core is stronger compared to the HAp sample. The R-curve behaviour predicted for partially stabilised zirconia could be the reason for its ability to withstand large forces prior to failure [386, 387].

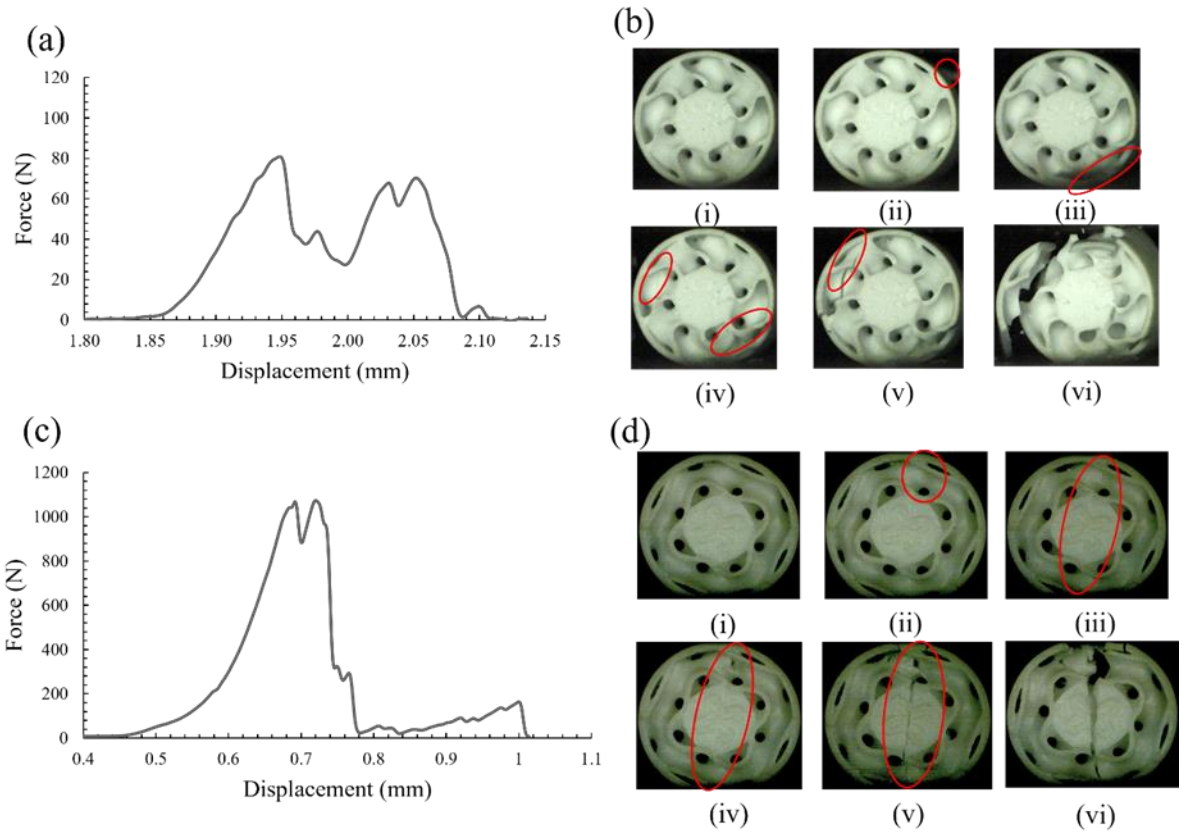

Figure 6.5: Force-displacement curve during transverse loading of (a) HAp and (c) 3Y-TZP structures. Digital images showing the stages of failure when the (b) HAp and (d) 3Y-TZP structures are subjected to a transverse load.

Force-displacement curves in Figure 6.6a indicate that the 3Y-TZP-HAp composite undergoes failure at 30 N of force in the transverse direction. This is significantly lower than the values observed for HAp and 3Y-TZP alone. Figure 6.6b shows the formation of cracks initially at the surface of the shell structure and propagating diagonally across that subsequently lead to failure as the applied force is increased. Unlike the force-displacement plots for the HAp and 3Y-TZP there are plateau sections observed for the 3Y-TZP-HAp composite sample. The first plateau is observed between a displacement of 0.10 – 0.15 mm. Micro-cracking within the shell structure might have caused a reduction in height of the sample causing the sensor to record a plateau. Energy absorption through cracking within the shell of the structure could also appear as a plateau in the force-displacement curve. Sarvestani et al. [388] showed that architectured ceramics panels

absorbed energy even after the first puncture and, as the applied load increased, the damaged area increased as opposed to an increase in the number of cracks. Similarly, in Figure 6.6b we observed the damaged area of the cracks was progressively increasing with applied force. The plateau observed at displacements between 0.2 – 0.3 mm, was due to the force being transmitted to the solid 3Y-TZP core, explaining the appearance of a peak even after several cracks had appeared. However, the HAp shell structure, already damaged, underwent complete failure before the cracks appeared within the 3Y-TZP core. The 3Y-TZP core remained intact after failure indicating a weak contact between the core and HAp shell. Weak contacts between the core and outer ring creates sites for cracks to appear as seen in Figure 6.6b; however, these cracks consume the energy from the main propagation thereby improving toughness. Severe crack deflection and bridging prevented instantaneous failure and allowed the structure to undergo some deformation. Further differences in volume shrinkage of the 3Y-TZP and HAP slurries contributed to the weakness of the structure, notably at the interface of the outer shell and solid core. This led to the complete separation of the inner core once the crack had propagated through the contact between the materials. Therefore, a gradual transition between the two materials could have been more effective as it would prevent the delamination of the core and shell. The diameter of the core could also be adjusted to suit different BTE applications, allowing some degree of personalisation.

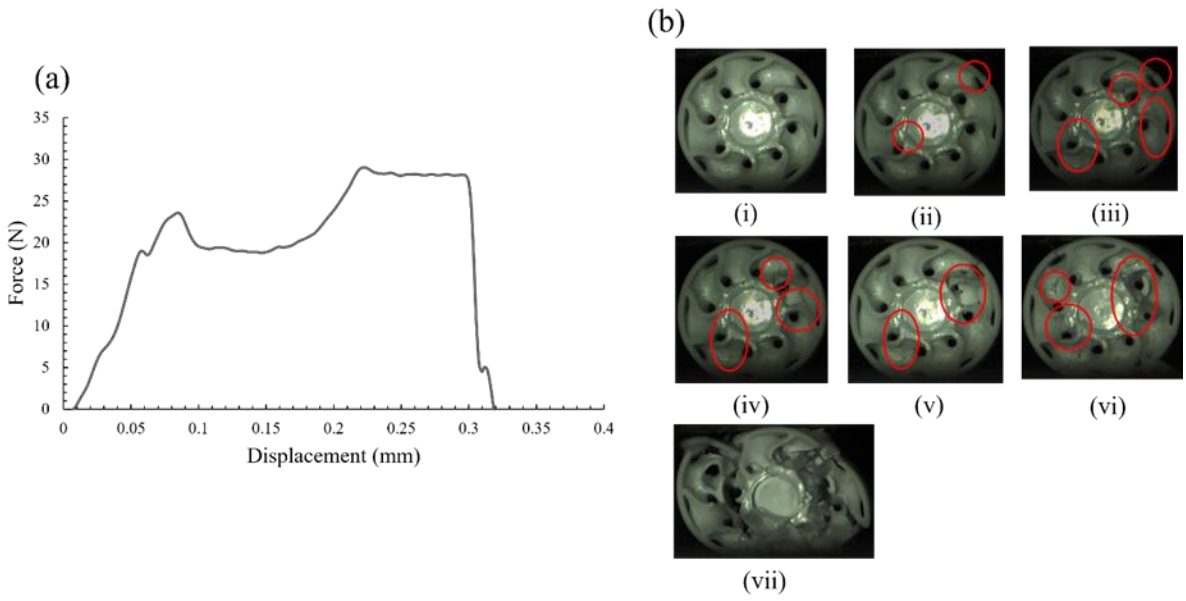

Figure 6.6: (a) Force displacement curve during transverse loading of the 3Y-TZP – HAp composite structure. (b) Digital images showing the stage of failure.

6.3.3. *In-vitro* performance

The percentage reduction of resazurin on the scaffold materials (shown in Figure 6.7) did not show significant differences between the scaffold material and the HAp control on day 1 ($P = 0.8862$), day 3 ($P = 0.5283$) and day 10 ($P = 0.0763$) as determined by one-way ANOVA indicating that the osteoblast cell proliferation was unaffected by the ceramic used.

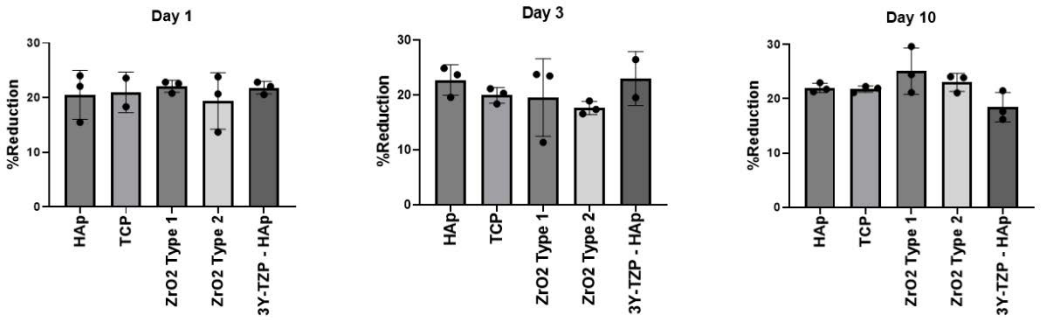

Figure 6.7: Osteoblast proliferation measured as percentage reduction of resazurin to resorufin was evaluated on days 1, 3, and 10 on five different material substrates: HAp, TCP, ZrO_2 Type 1, ZrO_2 Type 2, and 3Y-TZP – HAp composite scaffolds. Proliferation is represented as a percentage reduction of resazurin and measured across technical replicates (n=3) of each material substrate. Biological mean ± SD are shown.

Osteoblast cell attachment at the inner core and outer shell has remained abundant across the 10 days of incubation as shown in Figure 6.8. Cell attachment on the composite sample is concentrated at the inner core and outer shell. *In-vitro* cell attachment occurs in three phases (1) initial attachment (2) flattening and cell spreading and (3) focal adhesion [389]. Initial attachment is driven by integrin receptors binding with suitable ligands present on the surface of the scaffold. Post initial attachment, bidirectional signalling and mechanical linkage allows cells to undergo flattening or spreading. Cells undergo full spreading and structural organisation leading to focal adhesion [390]. Elevation inconsistencies between the inner core 3Y-TZP core and HAp outer shell due to the differences in shrinkage during the sintering process may have prevented osteoblast cell attachment (as previously mentioned in section 6.2.1). Flat or patterned surfaces (less than 50 µm) are known to enhance cell adhesion due to the availability of a large surface area for interaction with the integrins [391]. Greater elevation differences on the surface leads to loss of surface area and poor mechanical anchorage, leading to cell detachment. In pure material structures such as HAp and 3Y-TZP (type 1 and type 2) these effects were not observed, the nearly flat surface has cells attached along the entire surface as shown Figure A11. Therefore, minimising

elevation differences between the inner core and outer shell post sintering may allow cells to cover the entire surface of the scaffold.

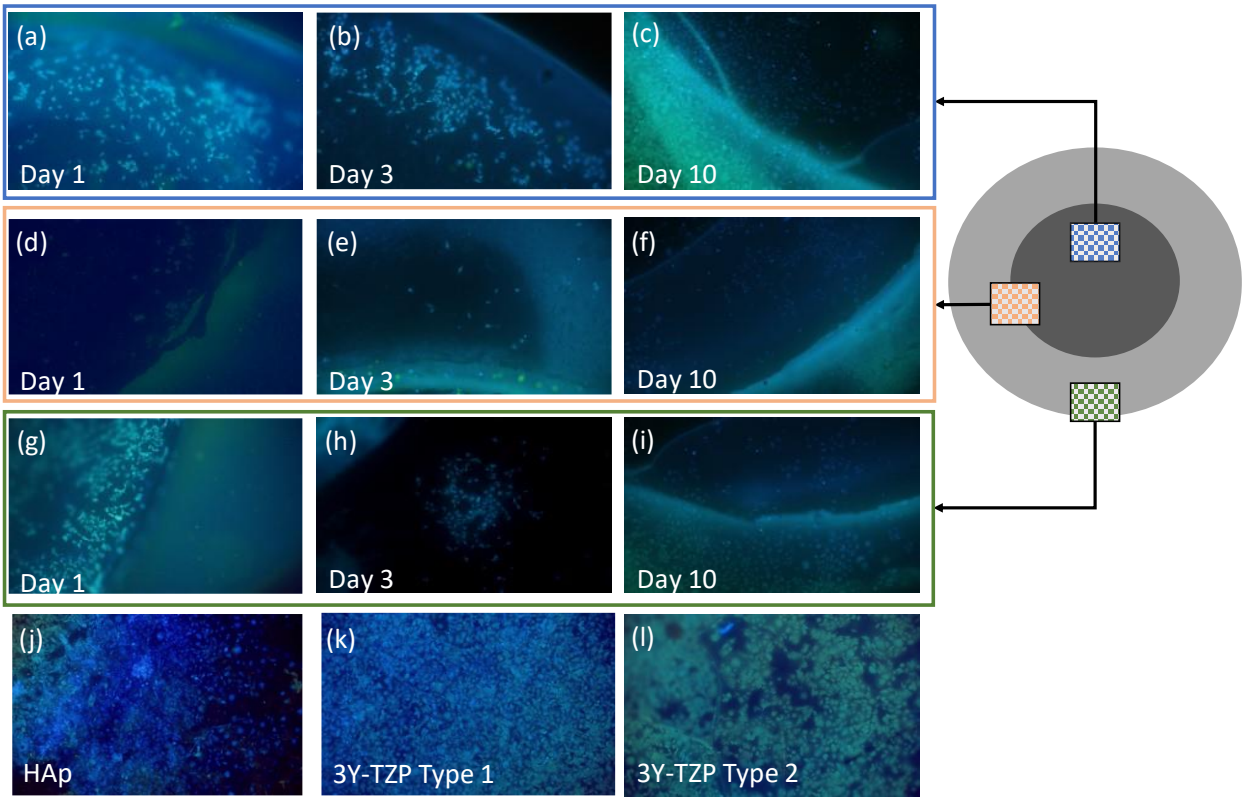

Figure 6.8: Fluorescence microscopy of osteoblast cells present on the 3Y-TZP-HAp composite substrate. Images (a), (b) and (c) were captured at the edge of the substrate which is made of HAp. Images (d), (e) and (f) were captured at the interface of the outer shell (HAp) and inner core (3Y-TZP). Images (g), (h) and (i) were captured at the inner core of the substrate which is made of 3Y-TZP. The blue fluorescence observed in the figures corresponds to DAPI-stained cell nuclei. All images were captured at a magnification of 10X using a blue fluorescence channel. Images (j), (k) and (l) were captured on the HAp, 3Y-TZP type 1 and 3Y-TZP type 2 respectively on Day 10.

Alkaline phosphatase (ALP) activity is essential for the mineralisation of bone ECM, through the release of inorganic phosphates. Accumulation of inorganic phosphates and calcium followed by crystal growth leads to stimulation of bone tissue formation [392]. Therefore, presence of ALP activity indicates potential for bone mineralisation. After 10 days incubation in the differentiation medium, observed ALP activity remained similar irrespective of scaffold material as shown in

Figure 6.9a, as the one-way ANOVA test did not indicate a significant difference between the scaffold materials and HAp (P = 0.6857; Figure 6.9). Previous studies exploring the effects of surface texture on ALP activity have shown similar responses [393], indicating that choice of material and surface texture do not affect the process of bone mineralisation. While accumulation of inorganic phosphates and calcium is essential for the formation of bone tissues, this process occurs at the early stages of bone healing [3]. However, a cascade of chemical signals is required to initiate and sustain the process of bone healing.

Previous studies have demonstrated the efficacy of HAp in promoting expression of genes essential for osteogenesis, and therefore, it was used as the control group in this study [394]. The tested gene markers were *RunX2*, *OCN* and *OPN*. Expression of *OCN* and *RunX2* shown in Figure 6.9b remained the same across all materials as found with a one-way ANOVA test (P = 0.088 and P= 0.3976 respectively). Scaffold materials influenced *OPN* expression, found with a one-way ANOVA (P = 0.02; Figure 6.9b). Multiple comparisons tests identified there were significant differences between expression of *OPN* in ZrO_2 compared with the HAp control (P = 0.0221 and P = 0.0470; Figure 6.9b). Downregulation of OPN expression was observed in the ZrO_2 scaffolds (type 1 and type 2) whereas TCP and composite scaffolds showed no difference in gene expression compared to the HAp scaffold.

Osteogenic differentiation is a multi-step process that is modulated by a cascade of gene expressions which occur in three stages (i) proliferation (ii) extracellular matrix deposition and maturation and (iii) mineralisation of bone ECM. *RunX2* has been shown to have an osteoinductive nature driving the accumulation of ALP and causing elevated calcium deposition[395]. ALP is a marker of early differentiation, signalling the end of cell proliferation and leading to maturation of the ECM. *OPN* and *OCN* are markers of late stage ECM mineralisation leading to the formation of bone tissue [396, 397]. *Osterix* (*OSX*) is an essential factor for the differentiation of osteoblast

cells and previous studies have shown that activation of *OSX* is necessary for the expression of *RunX2* and *OCN* [398]. Therefore, the composite, TCP and HAp show identical responses towards cells differentiation and expression of key osteogenic factors responsible for initiating bone healing. Similarly, ZrO_2 scaffolds also show positive response to support cell differentiation, however, their expression of *OPN* which is a marker for late-stage ECM mineralisation or bone tissue formation is down regulated. This could indicate that the rate of formation of bone tissues on ZrO_2 scaffolds could be slower compared to the other scaffold materials tested, however, further in-vivo studies are required to confirm this.

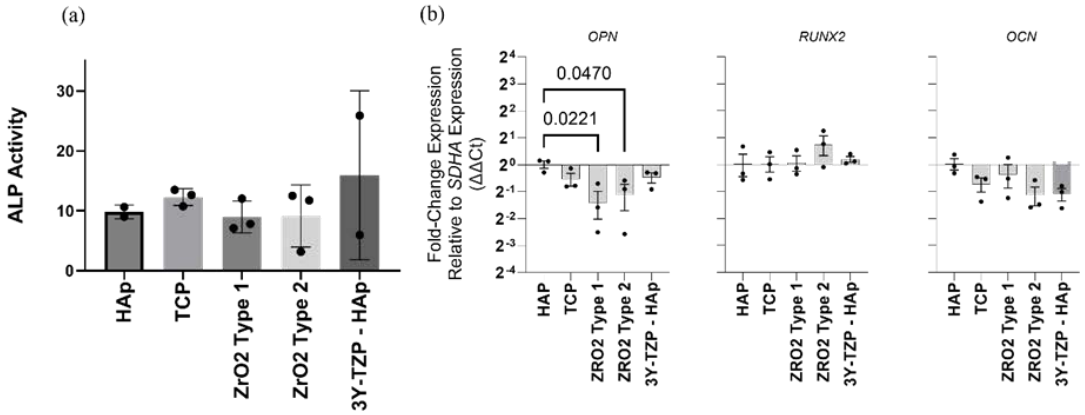

Figure 6.9: (a) Extent of ALP activity measured across technical replicates (n=3) ± SD are shown (b) Data were analysed using a one-way ANOVA with post-hoc Bonferroni's multiple-comparisons test (*P ≤ 0.05; **P ≤ 0.01; ***P ≤ 0.001; ****P ≤ 0.0001). Biological replicate (n = 3), single RNA extractions with single reverse transcription reactions per extraction were performed. Sample mean calculated from the mean of the technical triplicate qPCR reactions. Biological mean ± biological SEM are shown. Results with p<0.05 were significant and error bars shown correspond to the standard deviation.

6.4. Conclusion

This study discusses a core and shell arrangement to incorporate a multi-ceramic approach to scaffold manufacturing using stereolithography based 3D printing. Compression strength of the

3Y-TZP – HAp composite was comparable to the pure HAp sample at 56 ± 2 MPa while pure 3Y-TZP at similar pore sizes between 800 – 2000 μm produced a compression strength of 226 MPa, exceeding the required strength of 100 MPa for load-bearing BTE applications. Indirect tensile tests carried out on the HAp and 3Y-TZP samples showed that they are able to withstand a transverse load of 80 N and 1000 N prior to failure respectively while the 3Y-TZP-HAp composite underwent failure at a transverse load of 30 N. However, failure mode in the transverse direction was less catastrophic compared to the HAp and 3Y-TZP individually. Cell proliferation and differentiation potential of the composite scaffold remained similar to that of the pure HAp and 3Y-TZP samples indicating that the presence of 3Y-TZP core and HAp outer shell did not hinder its ability to support bone formation.

Failure modes of the composite during longitudinal and transverse compression loads showed that the limiting factor was the weak contact between the inner and outer shell. Further, differential grain sizes achieved after the sintering process showed the build-up of internal stresses. Considering the differences in the co-efficient of HAp and 3Y-TZP and initial grain sizes this was to be expected. However, the limiting factor in its performance is driven by the blended region between the core and shell, weak adhesion led to crack formation and finally delamination of the layers. In addition, the *in-vitro* studies discussed in this study show that the performance of the composite and 3Y-TZP scaffold is similar to that of typical bioceramics like HAp and TCP. Therefore, introducing new blending strategies at the interface of the HAp and 3Y-TZP layer can be used to offset limitation of the current 3Y-TZP-HAp composite. Furthermore, carrying out in-vivo studies on these scaffold structures can provide a complete picture of their ability to assist in bone healing.

7. CONCLUSION AND RECOMMENDATIONS

This chapter reports the overall conclusions of this thesis. Conclusions are presented according to the various key topics discussed throughout this thesis. The implications of this research are then presented. Finally, recommendations for future work are outlined.

7.1. Co-sintering of 3Y-TZP-HAp composites using two-step sintering

Sintering is a critical step in the production of ceramics, driving factors for sintering include energy, particle sizes and diffusion coefficient. While energy and particle sizes can be controlled, diffusion coefficients are dependent on the materials chosen. Specifically, in the case of the 3Y-TZP-HAp composites, dehydration of HAp causes phase transformation of HAp to α-TCP or β-TCP. In addition to this, diffusion of CaO during the process into the ZrO_2 stabilises it to form the respective cubic phase which is known to be brittle in nature. Controlling these phase reactions becomes critical while co-sintering these composites.

Variables within these sintering processes critically affect phase formation or retention. Conventional sintering cycles involve heating the sample to a peak temperature at a set heating rate and cooling back to room temperature. To improve densities, peak temperatures were increased thereby increasing the input energy into the process. While this produced high densities it also increased grain size. Two-step sintering (TSS) involves initially heating the sample to a peak temperature followed by cooling and holding it at a lower temperature before cooling it back to room temperature. Lower plateau temperature reduces the driving force available for grain growth during the sintering process, therefore allowing for densification without grain growth. Several parameters such as heating rate, peak temperature, plateau temperature and holding time are responsible for the final composition of the sintered composite. Using a Taguchi study, we

were able to identify that the plateau temperature (1150 – 1200 °C) and holding time (600 – 1200 min) were critically influencing the composition of the co-sintered composite.

Holding time and plateau temperature played a role by controlling the diffusion of CaO from HAp to 3Y-TZP, preventing the formation of α-TCP. Further, the extent of control was dependant on the initial composition, where the three different compositions studied showed widely different responses in phase composition and relative density. Apart from sintering variables, the weight percentages of ZrO_2 within the mixture played a critical role in determining the minimum temperature for the dehydration of HAp. Therefore, this study showed that along with TSS variables, composition of the mixture influences properties of 3Y-TZP-HAp composites. Reduction of plateau temperatures ensured smaller grain sizes (< 2 μm) which was observed across all sintering conditions in the factorial study. Mechanical strength produced by the 3Y-TZP-HAp composites were within the range of human cortical bone (80 – 100 MPa), however, the instantaneous failure of the composites at the ultimate stress indicated that more work is still required. Overall, this study showed a relationship between the variables of TSS along with composition on the phase reactions and densification of 3Y-TZP-HAp composites. Further, it also showed that by carefully controlling sintering variables, a composite of 3Y-TZP-HAp is feasible. Mechanical properties of the composites could be tuned using TSS variables. Lastly, mechanical strengths of the produced 3Y-TZP-HAp composites closely mimic that of natural bone tissue.

7.2. TPMS structures for load-bearing BTE applications

Natural bone tissues have a multi-scale hierarchical structure that provides strength to the structure while having their porous network vascularise the damaged tissue. The porous network serves a dual purpose, enabling dissipation of fracture energy through microcracking when mechanically loaded. The large pores of the network enable cellular interaction, allowing the cells to heal

damaged sections of the bone tissue. Replicating this natural bone architecture in BTE scaffolds can provide similar functionality and strength when implanted at the damaged site. TPMS structures have become a popular choice for usage in BTE applications due to their similarity to the porous architecture of bone tissue. In this work we looked at aspects that make TPMS structures suitable for usage in BTE scaffolds. To limit the size of the study, three TPMS structures (gyroid, lidinoid and split-P) that possessed critical features required for BTE applications were selected. The cubic symmetry of gyroid lattices made them less anisotropic and more damage tolerant in multiple directions. Lidinoid structures were selected due to their high surface areas available for interaction with the surrounding niche and split-P structures were chosen due to the high compression strengths reported in literature.

Simulated body fluid tests showed up to a 2.5% increase in mass of the structures after immersion in a simulated body fluid. Furthermore, the ICP- MS results taken at intervals of 7 days showed positive interaction with the fluid leading to the deposition of spherulites and deposits on the surfaces of the TPMS structures. The mass of apatite precipitated was directly proportional to the porosity of the scaffold, however, the organisation of the pores altered the extent of interaction. For example, 70% gyroid structures showed similar apatite precipitation to that of 70% lidinoid structures despite having twice the surface area. Cross sectional images of the TPMS structures indicated that, while the porosity of the structure is similar, the extent of SBF fluid intrusion is different. Extent of intrusion is a function of the porosity, pore sizes and interconnectivity of the structure and therefore, is a better indicator of interaction with surrounding niche compared with the available surface area.

Compression strength of the TPMS structures increased with reducing porosity and the highest compression strength of 25 MPa was achieved for the 50% split-P structure. During compression gyroid structures underwent a combination of stretch and bend dominated failures. The lack of

plasticity of the ceramics led to stress concentration at the zones of stretching and buckling which finally led to failure of the lattice. In the case of the split-P structures struts aligned in the direction of the load increased the load-bearing capacity prior to failure. In the case of lidinoid structures progressive reduction of the strut thickness and stress concentration caused early failure. Further, all the analysed TPMS structures had average pore sizes exceeding 700 µm, but the compression strengths offered were insufficient for use in load-bearing BTE applications. Therefore, while TPMS structures at pore sizes greater than 700 µm can provide better surface interactions with their surroundings, their mechanical performance is insufficient to be used as a BTE scaffold.

To meet the dual requirements of BTE scaffolds, we designed a scaffold with two zones. The inner core provided structural support, while the outer shell interacted with the surrounding environment. To identify the optimum combination, a solid core with a 70% gyroid, 80% gyroid and 60% lidinoid structure was chosen, which offered the highest apatite precipitation from the SBF tests. Since the solid core prevents bone in-growth a porous cored structure with 70% lidinoid and 70% gyroid (i.e S50_L70 and S50_G70 respectively) was designed to compare their performance. Interaction with osteoblast cells showed that cells primarily clustered along the curved sections of the scaffold structure, this was evident in the solid-cored and porous-cored scaffolds. Further, osteoblast cell proliferation was almost identical across all the structures, confirming that cell interaction was not affected by inclusion of a solid core. Compression strength of the solid cored structures was in the range of 80 – 122 MPa which is well within the requirements of cortical bone for load-bearing applications. However, structures S50_L70 and S50_G70 (these structures feature a split-P core with 50% porosity, combined with an outer shell exhibiting 70% porosity in lidinoid and gyroid configurations) produced a compression strength less than 20 MPa. The primary reason for this failure was due to the lack of a gradual transition from the porous core to outer shell. Structures underwent early failure at this intersection of the outer shell and inner core causing the entire scaffold structure to fail.

Overall, this study showed that the extent of fluid intrusion into the structure (combination of pore size and porosity) is critical while comparing cellular interactions with its surroundings. While TPMS structures at pore sizes greater than 700 µm on their own were insufficient for load-bearing BTE applications, graded TPMS structures with a solid core showed similar *in-vitro* performance to that of the porous cored structure. Simultaneously these structures possessed compression strengths in the range of 80 – 122 MPa, making them an ideal choice for load-bearing BTE applications.

7.3. Multi-material approach to ceramic load-bearing BTE scaffolds

Graded scaffold design with a solid core and 70% gyroid structure showed the highest compression strength as well as a positive interaction with osteoblast cells. Bones, in addition to providing strength to our soft tissues, also provide the necessary toughness which is critical to absorb stresses during physical activities. Lack of ductility in ceramic scaffolds, leads to failure when the applied load exceeds the ultimate tensile stress. Further, defects present within scaffold architecture exacerbate the rate of failure. Porous TPMS structures, as shown through this work, undergo microcracking to dissipate fracture energy due to the applied load, preventing instantaneous failure.

To enhance the toughness of these scaffolds a 3Y-TZP solid core was introduced. R-curve behaviour of 3Y-TZP ceramics enables higher compression strength and toughness. Compression strength measured in the longitudinal direction was at 56 MPa at an average pore size exceeding 1 mm which was marginally greater than the pure HAp scaffold. When the applied load was in the transverse direction the composite structure underwent a small amount of microcracking and finally led to delamination of the inner core. Due to the separation of the core from the outer shell the structures underwent complete failure at 30 N. Mismatch in shrinkages of HAp core and 3Y-TZP outer shell introduced a weak patch at the interface of the two materials. Hence a material

gradient at the interface between 3Y-TZP and HAp will provide a strong contact area enabling a distributed load transfer. Although there was diffusion of Ca at the interface of the HAp and 3Y-TZP leading to reduction of the monoclinic phases, but it did not have any effect on the interaction with osteoblast cells. *In-vitro* studies showed that proliferation and differentiation of osteoblast cells on the composite structures were similar to that of pure HAp and TCP biomaterials. Furthermore, expression of specific gene markers (early and late stage) such as OCN, OPN and RunX2 indicates positive potential for promoting bone healing and formation. Overall, the usage of 3Y-TZP-HAp ceramic composites showed a slight improvement in compression strength and toughness. Interactions with osteoblast cells did not show a significant difference compared to the bioactive materials, TCP and HAp, thereby establishing the feasibility of using a multi-ceramic approach for BTE scaffold design.

7.4. Recommendations

While phase composition is a critical aspect in 3Y-TZP-HAp composites, they also have a difference in the coefficient of linear expansion. During sintering these differences in thermal expansions introduce lattice defects and residual stresses. Nature and direction of these residual stresses can influence material response, for example, presence of compressive residual stresses can enhance the compression strength while residual tensile stresses can lead to early failure. The surface residual stresses can be identified using X-ray diffraction while the internal stresses cannot be identified due to low penetration depth of X-rays. High penetration depth of neutron diffraction can provide information on the residual stresses within the bulk of the sample allowing better interpretation of the mechanical performance of 3Y-TZP-HAp composites. Further in-situ neutron diffraction techniques can be used to observe phase changes during compression tests.

Particle size can affect grain growth and hence must be carefully controlled. Blending HAp and 3Y-TZP powders in a ball mill to achieve similar particle sizes can improve the homogeneity of the composite within the blend. With the same initial particle sizes, grain growth can be controlled accurately in both 3Y-TZP and HAp materials simultaneously.

Gradual transitions or intermediate sections between two dissimilar TPMS geometries could prevent stress concentration at the interface. Approaches to design these transition zones include utilising variable densities or connecting TPMS lattices. Structural performance of these variable lattices can be simulated using FEA tools available in nToplogy and correlated with physical mechanical testing. The effect of using different transition geometries or variable densities and their effect on cell interaction requires further study before porous cored ceramic scaffolds can be used for load-bearing BTE applications.

Multi-material scaffolds, as mentioned in this study, require gradual transitions at the interface of the two materials. Introduction of multiple slurry dispensing nozzles which are carefully controlled using the 3D printer will allow the processing of multiple materials simultaneously. Laser parameters suitable for processing each slurry will need to be optimised to ensure inter-layer fusion. Further developing blended 3Y-TZP-HAp slurries in different ratios could also be used to provide better control over the compositions at the material transition zone.

In-vitro tests carried out on the scaffold design provided an indication of its performance as a BTE scaffold; however, *in-vitro* tests are unable to mimic the chemical and physical conditions in the body. Bone in-growth is crucial for scaffold osteointegration with bone tissue. Understanding and optimising design parameters, such as scaffold porosity and pore structure, will achieve the ideal combination of strength and function for load-bearing BTE applications. Hence *in-vivo* studies

with large animal models will be needed to provide a further confirmation and move closer to producing patient specific load-bearing BTE scaffolds.

REFERENCES

1. Griffin, K.S., et al., *Evolution of bone grafting: Bone grafts and tissue engineering strategies for vascularized bone regeneration.* Clinical reviews in bone and mineral metabolism, 2015. **13**(4): p. 232-244.

2. Collins, M.N., et al., *Scaffold fabrication technologies and structure/function properties in bone tissue engineering.* Advanced functional materials, 2021. **31**(21): p. 2010609.

3. Koushik, T.M., C.M. Miller, and E. Antunes, *Bone tissue engineering scaffolds: Function of multi-material hierarchically structured scaffolds.* Advanced healthcare materials, 2023: p. 2202766.

4. Bose, S., M. Roy, and A. Bandyopadhyay, *Recent advances in bone tissue engineering scaffolds.* Trends in biotechnology, 2012. **30**(10): p. 546-554.

5. Qian, H., et al., *Current advances and applications of tantalum element in infected bone defects.* ACS Biomaterials science & engineering, 2023. **9**(1): p. 1-19.

6. Koju, N., S. Niraula, and B. Fotovvati *Additively manufactured porous Ti6Al4V for bone implants: A review*. Metals, 2022. **12**, DOI: 10.3390/met12040687.

7. Chmielewska, A. and D. Dean, *The role of stiffness-matching in avoiding stress shielding-induced bone loss and stress concentration-induced skeletal reconstruction device failure.* Acta biomaterialia, 2024. **173**: p. 51-65.

8. Yao, Z., et al., *Chapter 12 - Host response to orthopedic implants (Metals and Plastics)*, in *host response to biomaterials*, S.F. Badylak, Editor. 2015, Academic Press: Oxford. p. 315-373.

9. Mohammadi Zerankeshi, M., R. Bakhshi, and R. Alizadeh, *Polymer/metal composite 3D porous bone tissue engineering scaffolds fabricated by additive manufacturing techniques: A review.* Bioprinting, 2022. **25**: p. e00191.

10. Prasad, A., *State of art review on bioabsorbable polymeric scaffolds for bone tissue engineering.* Materials today: Proceedings, 2021. **44**: p. 1391-1400.

11. Wang, C.-a., et al., *Biomimetic structure design — a possible approach to change the brittleness of ceramics in nature.* Materials science and engineering: C, 2000. **11**(1): p. 9-12.

12. Wang, Y., S.E. Naleway, and B. Wang, *Biological and bioinspired materials: Structure leading to functional and mechanical performance.* Bioactive materials, 2020. **5**(4): p. 745-757.

13. Pugliese, R. and S. Graziosi, *Biomimetic scaffolds using triply periodic minimal surface-based porous structures for biomedical applications.* SLAS Technology, 2023. **28**(3): p. 165-182.

14. Claes, L., et al., *Influence of size and stability of the osteotomy gap on the success of fracture healing.* Journal of orthopaedic research, 1997. **15**(4): p. 577-584.

15. Verrier, S., et al., *Tissue engineering and regenerative approaches to improving the healing of large bone defects.* Eur Cell Mater, 2016. **32**: p. 87-110.

16. Balasubramanian, P., et al., *Ion release, Hydroxyapatite conversion, and Cytotoxicity of Boron-containing bioactive glass scaffolds.* International Journal of Applied Glass Science, 2016. **7**(2): p. 206-215.

17. Dwivedi, R., et al., *Polycaprolactone as biomaterial for bone scaffolds: Review of literature.* Journal of oral biology and craniofacial research, 2020. **10**(1): p. 381-388.

18. Guo, Y., et al., *In Vitro and in Vivo study of 3D-printed porous tantalum scaffolds for repairing bone defects.* ACS biomaterials science & engineering, 2019. **5**(2): p. 1123-1133.

19. Rahmati, M., et al., *Biological responses to physicochemical properties of biomaterial surface.* Chemical society reviews, 2020. **49**(15): p. 5178-5224.

20. Spiller, S., et al., *Improvement of wound healing by the development of ECM-inspired biomaterial coatings and controlled protein release.* Biological chemistry, 2021. **402**(11): p. 1271-1288.

21. Albrektsson, T. and C. Johansson, *Osteoinduction, osteoconduction and osseointegration.* European spine journal, 2001. **10**(2): p. S96-S101.

22. Ha, Y., et al., *Bone microenvironment-mimetic scaffolds with hierarchical microstructure for enhanced vascularization and bone regeneration.* Advanced functional materials, 2022. **32**(20): p. 2200011.

23. Liu, Y., D. Luo, and T. Wang, *Hierarchical structures of bone and bioinspired bone tissue engineering.* Small, 2016. **12**(34): p. 4611-4632.

24. Florencio-Silva, R., et al., *Biology of bone tissue: structure, function, and factors that influence bone cells.* BioMed research international, 2015. **2015**.

25. Follet, H., et al., *The degree of mineralization is a determinant of bone strength: a study on human calcanei.* Bone, 2004. **34**(5): p. 783-789.

26. Samavedi, S., A.R. Whittington, and A.S. Goldstein, *Calcium phosphate ceramics in bone tissue engineering: a review of properties and their influence on cell behavior.* Acta biomaterialia, 2013. **9**(9): p. 8037-8045.

27. Ma, H., et al., *3D-printed bioceramic scaffolds: From bone tissue engineering to tumor therapy.* Acta Biomaterialia, 2018. **79**: p. 37-59.

28. Jodati, H., B. Yılmaz, and Z. Evis, *A review of bioceramic porous scaffolds for hard tissue applications: Effects of structural features.* Ceramics International, 2020. **46**(10, Part B): p. 15725-15739.

29. Qu, H., et al., *Biomaterials for bone tissue engineering scaffolds: a review.* RSC Advances, 2019. **9**(45): p. 26252-26262.

30. Zhang, S., et al., *A review on the use of computational methods to characterize, design, and optimize tissue engineering scaffolds, with a potential in 3D printing fabrication.* Journal of Biomedical materials research part B: Applied biomaterials, 2019. **107**(5): p. 1329-1351.

31. Wubneh, A., et al., *Current state of fabrication technologies and materials for bone tissue engineering.* Acta Biomaterialia, 2018. **80**: p. 1-30.

32. Su, X., T. Wang, and S. Guo, *Applications of 3D printed bone tissue engineering scaffolds in the stem cell field.* Regenerative therapy, 2021. **16**: p. 63-72.

33. Moreno Madrid, A.P., et al., *Advances in additive manufacturing for bone tissue engineering scaffolds.* Materials science and engineering: C, 2019. **100**: p. 631-644.

34. Zhou, X., et al., *Recent advances in additive manufacturing technology for bone tissue engineering scaffolds.* The International Journal of Advanced manufacturing Technology, 2020. **108**(11): p. 3591-3606.

35. Anderson, H.C., *Vesicles associated with calcification in the matrix of epiphyseal cartilage.* The Journal of cell biology, 1969. **41**(1): p. 59-72.

36. Hasegawa, T., et al., *Ultrastructural and biochemical aspects of matrix vesicle-mediated mineralization.* Japanese dental science review, 2017. **53**(2): p. 34-45.

37. Anderson, H.C. and J.J. Reynolds, *Pyrophosphate stimulation of calcium uptake into cultured embryonic bones. Fine structure of matrix vesicles and their role in calcification.* Developmental biology, 1973. **34**(2): p. 211-227.

38. Walker, D.G., *Osteopetrosis cured by temporary parabiosis.* Science, 1973. **180**(4088): p. 875-875.

39. Mohamed, A.M., *An overview of bone cells and their regulating factors of differentiation.* Malays J Med Sci, 2008. **15**(1): p. 4-12.

40. Rouwkema, J., N.C. Rivron, and C.A. van Blitterswijk, *Vascularization in tissue engineering.* Trends in Biotechnology, 2008. **26**(8): p. 434-441.

41. Risau, W., *Mechanisms of angiogenesis.* Nature, 1997. **386**(6626): p. 671-674.

42. Wegst, U.G.K., et al., *Bioinspired structural materials.* Nature Materials, 2015. **14**(1): p. 23-36.

43. Ramchand, S.K. and E. Seeman, *The influence of cortical porosity on the strength of bone during growth and advancing age.* Current osteoporosis reports, 2018. **16**(5): p. 561-572.

44. Rho, J.-Y., L. Kuhn-Spearing, and P. Zioupos, *Mechanical properties and the hierarchical structure of bone.* Medical engineering & physics, 1998. **20**(2): p. 92-102.

45. Micheletti, C., et al., *Bone mineral organization at the mesoscale: A Review of mineral ellipsoids in bone and at bone interfaces.* Acta Biomaterialia, 2022.

46. Pahr, D.H. and A.G. Reisinger, *A review on recent advances in the constitutive modeling of bone tissue.* Current osteoporosis reports, 2020. **18**(6): p. 696-704.

47. Maruyama, M., et al., *Modulation of the inflammatory response and bone healing.* Frontiers in endocrinology, 2020. **11**: p. 386.

48. Nassiri, S., P. Graney, and K.L. Spiller, *Manipulation of macrophages to enhance bone repair and regeneration*, in *A Tissue regeneration approach to bone and cartilage repair*. 2015, Springer. p. 65-84.

49. Lee, J., et al., *Current advances in immunomodulatory biomaterials for bone regeneration.* Advanced healthcare materials, 2019. **8**(4): p. 1801106.

50. Shekaran, A. and A.J. García, *Extracellular matrix-mimetic adhesive biomaterials for bone repair.* Journal of biomedical materials research Part A, 2011. **96**(1): p. 261-272.

51. Zhu, G., et al., *Bone physiological microenvironment and healing mechanism: Basis for future bone-tissue engineering scaffolds.* Bioactive materials, 2021. **6**(11): p. 4110-4140.

52. Langdahl, B., S. Ferrari, and D.W. Dempster, *Bone modeling and remodeling: potential as therapeutic targets for the treatment of osteoporosis.* Therapeutic advances in musculoskeletal disease, 2016. **8**(6): p. 225-235.

53. Ansari, M., *Bone tissue regeneration: biology, strategies and interface studies.* Progress in biomaterials, 2019. **8**(4): p. 223-237.

54. Katsimbri, P., *The biology of normal bone remodelling.* European journal of cancer care, 2017. **26**(6): p. e12740.

55. Kim, J.-M., et al., *Osteoblast-osteoclast communication and bone homeostasis.* Cells, 2020. **9**(9): p. 2073.

56. Lin, X., et al., *The bone extracellular matrix in bone formation and regeneration.* Frontiers in pharmacology, 2020. **11**.

57. Kerschnitzki, M., et al., *The organization of the osteocyte network mirrors the extracellular matrix orientation in bone.* Journal of structural biology, 2011. **173**(2): p. 303-311.

58. Gluhak-Heinrich, J., et al., *Mechanical loading stimulates dentin matrix protein 1 (DMP1) expression in osteocytes in vivo.* Journal of bone and mineral research, 2003. **18**(5): p. 807-817.

59. Matsumoto, M., et al., *Bone tissue healing dynamics: From damage to reconstruction.* Journal of molecular signaling updates, 2016. **1**: p. 33-40.

60. Zhou, Y., C. Wu, and J. Chang, *Bioceramics to regulate stem cells and their microenvironment for tissue regeneration.* Materials today, 2019. **24**: p. 41-56.

61. Grech, J. and E. Antunes, *Zirconia in dental prosthetics: A literature review.* Journal of materials research and technology, 2019. **8**(5): p. 4956-4964.

62. Munro, T., et al., *Interactions of osteoprogenitor cells with a novel zirconia implant surface.* Journal of functional biomaterials, 2020. **11**(3): p. 50.

63. Zhang, C., et al., *Effect of graphene oxide on the mechanical, tribological, and biological properties of sintered 3Y–ZrO2/GO composite ceramics for dental implants.* Ceramics international, 2021. **47**(5): p. 6940-6946.

64. Grech, J. and E. Antunes, *Optimization of two-step sintering conditions of zirconia blanks for dental restorations.* Ceramics international, 2020. **46**(16): p. 24792-24798.

65. Merola, M. and S. Affatato, *Materials for Hip Prostheses: A Review of wear and loading considerations.* Materials, 2019. **12**(3): p. 495.

66. Erasmus, E.P., et al., *In vitro evaluation of porous borosilicate, borophosphate and phosphate bioactive glasses scaffolds fabricated using foaming agent for bone regeneration.* Scientific reports, 2018. **8**(1): p. 3699.

67. Ribas, R.G., et al., *Current advances in bone tissue engineering concerning ceramic and bioglass scaffolds: A review.* Ceramics international, 2019. **45**(17, Part A): p. 21051-21061.

68. Gomes, S., et al., *Cu-doping of calcium phosphate bioceramics: From mechanism to the control of cytotoxicity.* Acta biomaterialia, 2018. **65**: p. 462-474.

69. Wu, C., et al., *Copper-containing mesoporous bioactive glass scaffolds with multifunctional properties of angiogenesis capacity, osteostimulation and antibacterial activity.* Biomaterials, 2013. **34**(2): p. 422-433.

70. Ballouze, R., et al., *Biocompatible magnesium-doped biphasic calcium phosphate for bone regeneration.* Journal of biomedical materials research part B: Applied biomaterials, 2021. **109**(10): p. 1426-1435.

71. Qi, T., et al., *Insights into the role of magnesium ions in affecting osteogenic differentiation of mesenchymal stem cells.* Biological trace element research, 2021. **199**(2): p. 559-567.

72. Wu, T., et al., *Improving osteogenesis of calcium phosphate bone cement by incorporating with manganese doped β-tricalcium phosphate.* Materials science and engineering: C, 2020. **109**: p. 110481.

73. Sule, K., J. Umbsaar, and E.J. Prenner, *Mechanisms of Co, Ni, and Mn toxicity: From exposure and homeostasis to their interactions with and impact on lipids and biomembranes.* Biochimica et Biophysica acta (BBA) - Biomembranes, 2020. **1862**(8): p. 183250.

74. Hulsart-Billström, G., et al., *Osteogenic potential of Sr-doped calcium phosphate hollow spheres in vitro and in vivo.* Journal of biomedical materials research part A, 2013. **101A**(8): p. 2322-2331.

75. Cao, J., et al., *In vitro degradation assessment of calcium fluoride-doped hydroxyapatite coating prepared by pulsed laser deposition.* Surface and coatings technology, 2021. **416**: p. 127177.

76. Lu, J., H. Yu, and C. Chen, *Biological properties of calcium phosphate biomaterials for bone repair: A review.* RSC advances, 2018. **8**(4): p. 2015-2033.

77. Guo, L., et al., *The role of natural polymers in bone tissue engineering.* Journal of controlled release, 2021. **338**: p. 571-582.

78. Li, Y., et al., *Collagen-based biomaterials for bone tissue engineering.* Materials & Design, 2021. **210**: p. 110049.

79. Sharma, S., et al., *Critical review of biodegradable and bioactive polymer composites for bone tisue engineering and drug delivery applications.* Polymers, 2021. **13**(16): p. 2623.

80. Zhang, F. and M.W. King, *Biodegradable polymers as the pivotal player in the design of tissue engineering scaffolds.* Advanced healthcare materials, 2020. **9**(13): p. 1901358.

81. Benatti, A.C.B., et al., *Chapter 4 - Bioreabsorbable polymers for tissue engineering: PLA, PGA, and their copolymers*, in *Materials for biomedical engineering*, A.-M. Holban and A.M. Grumezescu, Editors. 2019, Elsevier. p. 83-116.

82. Ghorbani, F., et al., *Surface functionalization of three dimensional-printed polycaprolactone-bioactive glass scaffolds by grafting gelMA under UV irradiation.* Frontiers in materials, 2020. **7**.

83. Vo, T.N., F.K. Kasper, and A.G. Mikos, *Strategies for controlled delivery of growth factors and cells for bone regeneration.* Advanced drug delivery reviews, 2012. **64**(12): p. 1292-1309.

84. Sun, D., et al., *Citric acid-based hydroxyapatite composite scaffolds enhance calvarial regeneration.* Scientific reports, 2014. **4**(1): p. 6912.

85. Davies, E., et al., *Citrate bridges between mineral platelets in bone.* Proceedings of the national academy of sciences, 2014. **111**(14): p. E1354-E1363.

86. Teixeira, B.N., et al., *Evaluation of bone marrow stem cell response to PLA scaffolds manufactured by 3D printing and coated with polydopamine and type I collagen.* Journal of biomedical materials Research part B: Applied biomaterials, 2019. **107**(1): p. 37-49.

87. Cho, H.-j., et al., *Effective immobilization of BMP-2 mediated by polydopamine coating on biodegradable nanofibers for enhanced in vivo bone formation.* ACS applied materials & interfaces, 2014. **6**(14): p. 11225-11235.

88. Cakmak, A.M., et al. *3D printed polycaprolactone/gelatin/bacterial cellulose/hydroxyapatite composite scaffold for bone tissue engineering*. Polymers, 2020. **12**, DOI: 10.3390/polym12091962.

89. Vaidhyanathan, B., et al., *Fabrication and investigation of the suitability of chitosan-silver composite scaffolds for bone tissue engineering applications.* Process biochemistry, 2021. **100**: p. 178-187.

90. Rasoulianboroujeni, M., et al., *Development of 3D-printed PLGA/TiO2 nanocomposite scaffolds for bone tissue engineering applications.* Materials science and engineering: C, 2019. **96**: p. 105-113.

91. Januariyasa, I.K., I.D. Ana, and Y. Yusuf, *Nanofibrous poly(vinyl alcohol)/chitosan contained carbonated hydroxyapatite nanoparticles scaffold for bone tissue engineering.* Materials science and engineering: C, 2020. **107**: p. 110347.

92. Shuai, C., et al., *Graphene oxide assists polyvinylidene fluoride scaffold to reconstruct electrical microenvironment of bone tissue.* Materials & design, 2020. **190**: p. 108564.

93. Eivazzadeh-Keihan, R., et al., *Metal-based nanoparticles for bone tissue engineering.* Journal of tissue engineering and regenerative medicine, 2020. **14**(12): p. 1687-1714.

94. Geetha, M., et al., *Ti based biomaterials, the ultimate choice for orthopaedic implants – A review.* Progress in materials science, 2009. **54**(3): p. 397-425.

95. Wang, S., et al., *Pore functionally graded Ti6Al4V scaffolds for bone tissue engineering application.* Materials & design, 2019. **168**: p. 107643.

96. Xu, W., et al., *Novel porous Ti35Zr28Nb scaffolds fabricated by powder metallurgy with excellent osteointegration ability for bone-tissue engineering applications.* Materials science and engineering: C, 2019. **105**: p. 110015.

97. Xu, W., et al., *Fabrication and properties of newly developed Ti35Zr28Nb scaffolds fabricated by powder metallurgy for bone-tissue engineering.* Journal of materials research and technology, 2019. **8**(5): p. 3696-3704.

98. Cassandri, M., et al., *Zinc-finger proteins in health and disease.* Cell death discovery, 2017. **3**(1): p. 17071.

99. Su, Y., et al., *Zinc-based biomaterials for regeneration and therapy.* Trends in biotechnology, 2019. **37**(4): p. 428-441.

100. Cockerill, I., et al., *Porous zinc scaffolds for bone tissue engineering applications: A novel additive manufacturing and casting approach.* Materials science and engineering: C, 2020. **110**: p. 110738.

101. Kamrani, S. and C. Fleck, *Biodegradable magnesium alloys as temporary orthopaedic implants: a review.* BioMetals, 2019. **32**(2): p. 185-193.

102. Dayaghi, E., et al., *Magnesium-zinc scaffold loaded with tetracycline for tissue engineering application: In vitro cell biology and antibacterial activity assessment.* Materials science and engineering: C, 2019. **102**: p. 53-65.

103. Heo, D.N., et al., *Enhanced bone regeneration with a gold nanoparticle–hydrogel complex.* Journal of materials chemistry B, 2014. **2**(11): p. 1584-1593.

104. Zhang, J., et al., *Zirconia toughened hydroxyapatite biocomposite formed by a DLP 3D printing process for potential bone tissue engineering.* Materials science and engineering: C, 2019. **105**: p. 110054.

105. Arcos, D. and M. Vallet-Regí, *Substituted hydroxyapatite coatings of bone implants.* Journal of materials chemistry B, 2020. **8**(9): p. 1781-1800.

106. Rizwan, M., M. Hamdi, and W.J. Basirun, *Bioglass® 45S5-based composites for bone tissue engineering and functional applications.* Journal of biomedical materials research part A, 2017. **105**(11): p. 3197-3223.

107. Gritsch, L., et al., *Chitosan/hydroxyapatite composite bone tissue engineering scaffolds with dual and decoupled therapeutic ion delivery: copper and strontium.* Journal of materials chemistry B, 2019. **7**(40): p. 6109-6124.

108. Marie, P.J., et al., *Mechanisms of action and therapeutic potential of strontium in Bone.* Calcified tissue international, 2001. **69**(3): p. 121-129.

109. Grass, G., C. Rensing, and M. Solioz, *Metallic copper as an antimicrobial surface.* Applied and environmental microbiology, 2011. **77**(5): p. 1541-1547.

110. Lam, C.X.F., et al., *Scaffold development using 3D printing with a starch-based polymer.* Materials science and engineering: C, 2002. **20**(1): p. 49-56.

111. Koski, C., et al., *Starch-hydroxyapatite composite bone scaffold fabrication utilizing a slurry extrusion-based solid freeform fabricator.* Additive manufacturing, 2018. **24**: p. 47-59.

112. Betancourt, N. and X. Chen, *Review of extrusion-based multi-material bioprinting processes.* Bioprinting, 2022. **25**: p. e00189.

113. Ravanbakhsh, H., et al., *Emerging technologies in multi-material bioprinting.* Advanced materials, 2021. **33**(49): p. 2104730.

114. Dutta, S., et al., *In vitro corrosion and cytocompatibility studies of hot press sintered magnesium-bioactive glass composite.* Materialia, 2019. **5**: p. 100245.

115. Wan, Y., et al., *Mechanical and biological properties of bioglass/magnesium composites prepared via microwave sintering route.* Materials & design, 2016. **99**: p. 521-527.

116. Khodaei, M., et al., *The effect of the nano- bioglass reinforcement on magnesium based composite.* Journal of the mechanical behavior of biomedical materials, 2019. **100**: p. 103396.

117. Iviglia, G., S. Kargozar, and F. Baino, *Biomaterials, current strategies, and novel nano-technological approaches for periodontal regeneration.* Journal of functional biomaterials, 2019. **10**(1): p. 3.

118. Sugawara, Y., et al., *Three-dimensional reconstruction of chick calvarial osteocytes and their cell processes using confocal microscopy.* Bone, 2005. **36**(5): p. 877-883.

119. Velioglu, Z.B., et al., *3D-printed poly(lactic acid) scaffolds for trabecular bone repair and regeneration: scaffold and native bone characterization.* Connective tissue research, 2019. **60**(3): p. 274-282.

120. Gupte, M.J., et al., *Pore size directs bone marrow stromal cell fate and tissue regeneration in nanofibrous macroporous scaffolds by mediating vascularization.* Acta biomaterialia, 2018. **82**: p. 1-11.

121. Haugen, H.J., et al., *Bone grafts: which is the ideal biomaterial?* Journal of clinical periodontology, 2019. **46**: p. 92-102.

122. Ghayor, C. and F.E. Weber, *Osteoconductive microarchitecture of bone substitutes for bone regeneration revisited.* Frontiers in physiology, 2018. **9**.

123. Zhao, H., et al., *Effect of porous structure and pore size on mechanical strength of 3D-printed comby scaffolds.* Materials letters, 2018. **223**: p. 21-24.

124. Morejón, L., et al., *Development, characterization and In vitro biological properties of scaffolds fabricated From calcium phosphate nanoparticles.* International Journal of molecular sciences, 2019. **20**(7): p. 1790.

125. Diaz-Rodriguez, P., M. Sánchez, and M. Landin, *Drug-loaded biomimetic ceramics for tissue engineering.* Pharmaceutics, 2018. **10**(4): p. 272.

126. Jung, J.-Y., et al., *3D printed templating of extrinsic freeze-casting for macro–microporous biomaterials.* ACS Biomaterials science & engineering, 2019. **5**(5): p. 2122-2133.

127. Murphy, C.M., M.G. Haugh, and F.J. O'Brien, *The effect of mean pore size on cell attachment, proliferation and migration in collagen–glycosaminoglycan scaffolds for bone tissue engineering.* Biomaterials, 2010. **31**(3): p. 461-466.

128. Abbasi, N., et al., *Porous scaffolds for bone regeneration.* Journal of Science: Advanced materials and devices, 2020. **5**(1): p. 1-9.

129. Kanwar, S., O. Al-Ketan, and S. Vijayavenkataraman, *A novel method to design biomimetic, 3D printable stochastic scaffolds with controlled porosity for bone tissue engineering.* Materials & design, 2022. **220**: p. 110857.

130. Bicho, D., et al., *Porous aligned ZnSr-doped β-TCP/silk fibroin scaffolds using ice-templating method for bone tissue engineering applications.* Journal of biomaterials science, Polymer Edition, 2021. **32**(15): p. 1966-1982.

131. Gao, C., et al., *Bone biomaterials and interactions with stem cells.* Bone research, 2017. **5**(1): p. 17059.

132. Arora, A., A. Kothari, and D.S. Katti, *Pore orientation mediated control of mechanical behavior of scaffolds and its application in cartilage-mimetic scaffold design.* Journal of the mechanical behavior of biomedical materials, 2015. **51**: p. 169-183.

133. Sanz-Herrera, J.A., J.M. García-Aznar, and M. Doblaré, *On scaffold designing for bone regeneration: A computational multiscale approach.* Acta biomaterialia, 2009. **5**(1): p. 219-229.

134. O'Brien, F.J., et al., *The effect of pore size on permeability and cell attachment in collagen scaffolds for tissue engineering.* Technology and health Care, 2007. **15**: p. 3-17.

135. Dias, M.R., et al., *Permeability analysis of scaffolds for bone tissue engineering.* Journal of biomechanics, 2012. **45**(6): p. 938-944.

136. Castro, A.P.G., et al., *Micromechanical behavior of TPMS scaffolds for bone tissue engineering.* macromolecular materials and engineering, 2020. **305**(12): p. 2000487.

137. Castro, A.P.G., et al., *Permeability versus Design in TPMS Scaffolds.* Materials, 2019. **12**(8): p. 1313.

138. Yánez, A., et al., *Gyroid porous titanium structures: A versatile solution to be used as scaffolds in bone defect reconstruction.* Materials & design, 2018. **140**: p. 21-29.

139. Ataee, A., et al., *Ultrahigh-strength titanium gyroid scaffolds manufactured by selective laser melting (SLM) for bone implant applications.* Acta materialia, 2018. **158**: p. 354-368.

140. Alizadeh-Osgouei, M., et al., *High strength porous PLA gyroid scaffolds manufactured via fused deposition modeling for tissue-engineering applications.* Smart materials in medicine, 2021. **2**: p. 15-25.

141. Kelly, C.N., et al., *Fatigue behavior of As-built selective laser melted titanium scaffolds with sheet-based gyroid microarchitecture for bone tissue engineering.* Acta biomaterialia, 2019. **94**: p. 610-626.

142. Zheng, Y., et al., *Promotion of tendon growth into implant through pore-size design of a Ti-6Al-4 V porous scaffold prepared by 3D printing.* Materials & design, 2021. **197**: p. 109219.

143. Zhang, Q., et al., *High-Strength hydroxyapatite scaffolds with minimal surface macrostructures for load-bearing bone regeneration.* Advanced functional materials, 2022. **n/a**(n/a): p. 2204182.

144. Rajagopalan, S. and R.A. Robb, *Schwarz meets Schwann: Design and fabrication of biomorphic and durataxic tissue engineering scaffolds.* Medical image analysis, 2006. **10**(5): p. 693-712.

145. Zhang, L., et al., *Energy absorption characteristics of metallic triply periodic minimal surface sheet structures under compressive loading.* Additive manufacturing, 2018. **23**: p. 505-515.

146. Yu, S., J. Sun, and J. Bai, *Investigation of functionally graded TPMS structures fabricated by additive manufacturing.* Materials & design, 2019. **182**: p. 108021.

147. Yuan, L., S. Ding, and C. Wen, *Additive manufacturing technology for porous metal implant applications and triple minimal surface structures: A review.* Bioactive materials, 2019. **4**: p. 56-70.

148. Novak, N., et al., *Development of novel hybrid TPMS cellular lattices and their mechanical characterisation.* Journal of materials research and technology, 2021. **15**: p. 1318-1329.

149. Al-Ketan, O., R. Rowshan, and R.K. Abu Al-Rub, *Topology-mechanical property relationship of 3D printed strut, skeletal, and sheet based periodic metallic cellular materials.* Additive manufacturing, 2018. **19**: p. 167-183.

150. Han, L. and S. Che, *An Overview of materials with triply periodic minimal surfaces and related geometry: From biological structures to self-Assembled systems.* Advanced materials, 2018. **30**(17): p. 1705708.

151. Xu, M., et al., *Hierarchically porous nagelschmidtite bioceramic–silk scaffolds for bone tissue engineering.* Journal of materials chemistry B, 2015. **3**(18): p. 3799-3809.

152. Lei, C., et al., *Hierarchical dual-porous hydroxyapatite doped dendritic mesoporous silica nanoparticles based scaffolds promote osteogenesis in vitro and in vivo.* Nano research, 2021. **14**(3): p. 770-777.

153. Lee, J. and G. Kim, *Three-Dimensional hierarchical nanofibrous collagen scaffold fabricated using fibrillated collagen and pluronic F-127 for regenerating bone Ttssue.* ACS applied materials & interfaces, 2018. **10**(42): p. 35801-35811.

154. Ohji, T. and M. Fukushima, *Macro-porous ceramics: processing and properties.* International Materials reviews, 2012. **57**(2): p. 115-131.

155. Thompson, B.R., et al., *Hierarchically structured composites and porous materials from soft templates: fabrication and applications.* Journal of materials chemistry A, 2019. **7**(14): p. 8030-8049.

156. Tetik, H., et al., *Additive manufacturing of 3D aerogels and porous scaffolds: A Review.* Advanced functional materials, 2021. **31**(45): p. 2103410.

157. Chen, Y., et al., *Recent developments of biomaterials for additive manufacturing of bone scaffolds.* Advanced healthcare materials, 2020. **9**(23): p. 2000724.

158. Ghorbani, F., H. Nojehdehian, and A. Zamanian, *Physicochemical and mechanical properties of freeze cast hydroxyapatite-gelatin scaffolds with dexamethasone loaded PLGA microspheres for hard tissue engineering applications.* Materials science and engineering: C, 2016. **69**: p. 208-220.

159. Lee, H., et al., *The production of porous hydroxyapatite scaffolds with graded porosity by sequential freeze-casting.* Materials, 2017. **10**(4): p. 367.

160. Himoto, I., S. Yamashita, and H. Kita, *Heat press molding of open-celled porous Si-SiC ceramics consisting of skeletal strut via gelcasting with flexible and thermosetting polyurethane resin.* Advanced powder technology, 2016. **27**(3): p. 948-958.

161. Desimone, D., et al., *Biosilicate®–gelatine bone scaffolds by the foam replica technique: development and characterization.* Science and technology of advanced materials, 2013. **14**(4): p. 045008.

162. Bodišová, K., et al., *Porous silicon nitride ceramics designed for bone substitute applications.* Ceramics international, 2013. **39**(7): p. 8355-8362.

163. Sung, J.-H., et al., *Production of porous calcium phosphate (CaP) ceramics with highly elongated pores using carbon-coated polymeric templates.* Ceramics international, 2012. **38**(1): p. 93-97.

164. Karageorgiou, V. and D. Kaplan, *Porosity of 3D biomaterial scaffolds and osteogenesis.* Biomaterials, 2005. **26**(27): p. 5474-5491.

165. Kim, M., R.A. Franco, and B.-T. Lee, *Synthesis of functional gradient BCP/ZrO2 bone substitutes using ZrO2 and BCP nanopowders.* Journal of the European ceramic society, 2011. **31**(9): p. 1541-1548.

166. Goudouri, O.M., et al., *Development of highly porous scaffolds based on bioactive silicates for dental tissue engineering.* Materials research bulletin, 2014. **49**: p. 399-404.

167. Sun, Z., et al., *Preparation of reticulated MAX-phase support with morphology-controllable nanostructured ceria coating for gas exhaust catalyst devices.* Journal of the american ceramic Society, 2010. **93**(9): p. 2591-2597.

168. Loca, D., I. Narkevica, and J. Ozolins, *The effect of TiO2 nanopowder coating on in vitro bioactivity of porous TiO2 scaffolds.* Materials letters, 2015. **159**: p. 309-312.

169. Xu, T., et al., *Electrospun polycaprolactone 3D nanofibrous scaffold with interconnected and hierarchically structured pores for bone tissue engineering.* Advanced healthcare materials, 2015. **4**(15): p. 2238-2246.

170. Huang, B., et al., *Engineered dual-scale poly (ε-caprolactone) scaffolds using 3D printing and rotational electrospinning for bone tissue regeneration.* Additive manufacturing, 2020. **36**: p. 101452.

171. Sankar, S., et al., *Electrospun nanofibres to mimic natural hierarchical structure of tissues: application in musculoskeletal regeneration.* Journal of tissue engineering and regenerative medicine, 2018. **12**(1): p. e604-e619.

172. Yu, Y., et al., *Fabrication and characterization of electrospinning/3D printing bone tissue engineering scaffold.* RSC advances, 2016. **6**(112): p. 110557-110565.

173. Sigmund, W., et al., *Processing and structure relationships in electrospinning of ceramic fiber systems.* Journal of the American ceramic society, 2006. **89**(2): p. 395-407.

174. Novotna, L., et al., *Biphasic calcium phosphate scaffolds with controlled pore size distribution prepared by in-situ foaming.* Materials science and engineering: C, 2019. **95**: p. 363-370.

175. Bai, H., et al., *Biomimetic gradient scaffold from ice-templating for self-seeding of cells with capillary effect.* Acta biomaterialia, 2015. **20**: p. 113-119.

176. Jung, H.-D., et al., *Fabrication of titanium scaffolds with porosity and pore size gradients by sequential freeze casting.* Materials letters, 2009. **63**(17): p. 1545-1547.

177. Li, W., et al., *Sintering of bi-porous titanium dioxide scaffolds: Experimentation, modeling and simulation.* Materials science and engineering: A, 2015. **636**: p. 148-156.

178. McFarland, M. and E. Antunes, *Small-scale static fire tests of 3D printing hybrid rocket fuel grains produced from different materials.* Aerospace, 2019. **6**(7): p. 81.

179. Wang, Z., et al., *Pharmaceutical electrospinning and 3D printing scaffold design for bone regeneration.* Advanced drug delivery reviews, 2021. **174**: p. 504-534.

180. Zhang, L., et al., *Three-dimensional (3D) printed scaffold and material selection for bone repair.* Acta biomaterialia, 2019. **84**: p. 16-33.

181. Hu, X., et al., *Recent progress in 3D printing degradable polylactic acid-based bone repair scaffold for the application of cancellous bone defect.* MedComm – Biomaterials and Applications, 2022. **1**(1): p. e14.

182. Koyyada, A. and P. Orsu, *Recent advancements and associated challenges of scaffold fabrication techniques in tissue engineering applications.* Regenerative engineering and translational medicine, 2021. **7**(2): p. 147-159.

183. Liu, G., et al., *Additive manufacturing of structural materials.* Materials science and engineering: R: Reports, 2021. **145**: p. 100596.

184. Korn, P., et al., *3D printing of bone grafts for cleft alveolar osteoplasty–in vivo evaluation in a preclinical model.* Frontiers in bioengineering and biotechnology, 2020. **8**: p. 217.

185. Le Guéhennec, L., et al., *In vitro and in vivo biocompatibility of calcium-phosphate scaffolds three-dimensional printed by stereolithography for bone regeneration.* Journal of biomedical materials research part A, 2020. **108**(3): p. 412-425.

186. Ren, B., et al., *Improved osseointegration of 3D printed Ti-6Al-4V implant with a hierarchical micro/nano surface topography: An in vitro and in vivo study.* Materials science and engineering: C, 2021. **118**: p. 111505.

187. Di Luca, A., et al., *Tuning cell differentiation into a 3D Scaffold presenting a pore shape gradient for osteochondral regeneration.* Advanced healthcare materials, 2016. **5**(14): p. 1753-1763.

188. Schwartz, Z., et al., *Underlying mechanisms at the bone-surface interface during regeneration.* Journal of periodontal research, 1997. **32**(1): p. 166-171.

189. Marcus, H.L., et al., *Solid freeform fabrication-powder processing.* American ceramic society bulletin, 1990. **69**(6): p. 1030-1031.

190. Sachs, E., M. Cima, and J. Cornie, *Three-Dimensional Printing: Rapid Tooling and Prototypes Directly from a CAD Model.* CIRP Annals, 1990. **39**(1): p. 201-204.

191. Lv, X., et al., *Binder jetting of ceramics: Powders, binders, printing parameters, equipment, and post-treatment.* Ceramics international, 2019. **45**(10): p. 12609-12624.

192. Chen, Z., et al., *3D printing of ceramics: A review.* Journal of the European ceramic society, 2019. **39**(4): p. 661-687.

193. Gibson, I., et al., *Additive manufacturing technologies*. Vol. 17. 2014: Springer.

194. Santoliquido, O., P. Colombo, and A. Ortona, *Additive Manufacturing of ceramic components by Digital Light Processing: A comparison between the "bottom-up" and the "top-down" approaches.* Journal of the European ceramic society, 2019. **39**(6): p. 2140-2148.

195. Kokkinis, D., M. Schaffner, and A.R. Studart, *Multimaterial magnetically assisted 3D printing of composite materials.* Nature communications, 2015. **6**(1): p. 1-10.

196. Shahzad, A. and I. Lazoglu, *Direct ink writing (DIW) of structural and functional ceramics: Recent achievements and future challenges.* Composites Part B: Engineering, 2021. **225**: p. 109249.

197. Bernasconi, R., et al., *Piezoelectric Drop-On-Demand Inkjet Printing of High-Viscosity Inks.* Advanced engineering materials, 2021. **n/a**(n/a): p. 2100733.

198. Ding, G., et al., *Dispersion and stability of SiC ceramic slurry for stereolithography.* Ceramics international, 2020. **46**(4): p. 4720-4729.

199. Liu, F.-J. and K.-S. Chou, *Determining critical ceramic powder volume concentration from viscosity measurements.* Ceramics international, 2000. **26**(2): p. 159-164.

200. Nadkarni, S.S. and J.E. Smay, *Concentrated barium titanate colloidal gels prepared by bridging flocculation for Use in solid freeform fabrication.* Journal of the American ceramic society, 2006. **89**(1): p. 96-103.

201. Kim, H., et al., *Fabrication of bulk piezoelectric and dielectric BaTiO3 ceramics using paste extrusion 3D printing technique.* Journal of the American ceramic society, 2019. **102**(6): p. 3685-3694.

202. Peng, E., D. Zhang, and J. Ding, *Ceramic Robocasting: Recent Achievements, Potential, and Future Developments.* Advanced materials, 2018. **30**(47): p. 1802404.

203. Xing, H., et al., *Effect of particle size distribution on the preparation of ZTA ceramic paste applying for stereolithography 3D printing.* Powder Technology, 2020. **359**: p. 314-322.

204. Li, X., et al., *Dispersion and properties of zirconia suspensions for stereolithography.* International Journal of Applied Ceramic Technology, 2020. **17**(1): p. 239-247.

205. Borlaf, M., et al., *Fabrication of ZrO2 and ATZ materials via UV-LCM-DLP additive manufacturing technology.* Journal of the European ceramic society, 2020. **40**(4): p. 1574-1581.

206. Stanciuc, A.-M., et al., *Robocast zirconia-toughened alumina scaffolds: Processing, structural characterisation and interaction with human primary osteoblasts.* Journal of the European ceramic society, 2018. **38**(3): p. 845-853.

207. Walton, R.L., et al., *Dispersion and rheology for direct writing lead-based piezoelectric ceramic pastes with anisotropic template particles.* Journal of the American ceramic society, 2020. **103**(11): p. 6157-6168.

208. Tang, S., et al., *Direct ink writing additive manufacturing of porous alumina-based ceramic cores modified with nanosized MgO.* Journal of the European ceramic society, 2020. **40**(15): p. 5758-5766.

209. Zhang, K., et al., *High solid loading, low viscosity photosensitive Al2O3 slurry for stereolithography based additive manufacturing.* Ceramics international, 2019. **45**(1): p. 203-208.

210. Iwata, N. and T. Mori, *Determination of optimum slurry evaluation method for the prediction of BaTiO3 green sheet density.* Journal of Asian ceramic societies, 2020. **8**(1): p. 183-192.

211. Ray, S.S., et al., *Solvent based Slurry Stereolithography 3D printed hydrophilic ceramic membrane for ultrafiltration application.* Ceramics international, 2020. **46**(8, Part B): p. 12480-12488.

212. Ding, G., et al., *Stereolithography-based additive manufacturing of gray-colored SiC ceramic green body.* Journal of the American ceramic society, 2019. **102**(12): p. 7198-7209.

213. Morita, S., et al., *3D structuring of dense alumina ceramics using fiber-based stereolithography with interparticle photo-cross-linkable slurry.* Advanced powder technology, 2021. **32**(1): p. 72-79.

214. M'Barki, A., L. Bocquet, and A. Stevenson, *Linking rheology and printability for dense and strong ceramics by direct ink writing.* Scientific reports, 2017. **7**(1): p. 6017.

215. Shirazi, S.F.S., et al., *A review on powder-based additive manufacturing for tissue engineering: selective laser sintering and inkjet 3D printing.* Science and technology of advanced materials, 2015. **16**(3): p. 033502.

216. Chen, A.-N., et al., *High-performance ceramic parts with complex shape prepared by selective laser sintering: a review.* Advances in applied ceramics, 2018. **117**(2): p. 100-117.

217. Schappo, H., et al., *Screening method for producing suitable spray-dried HA powder for SLS application.* Powder Technology, 2021. **384**: p. 62-69.

218. Anandharamakrishnan, C., *Spray drying techniques for food ingredient encapsulation*. 2015: John Wiley & Sons.

219. Pfeiffer, S., et al., *Iron oxide doped spray dried aluminum oxide granules for selective laser sintering and melting of ceramic parts.* Advanced engineering materials, 2019. **21**(6): p. 1801351.

220. McGeary, R.K., *Mechanical Packing of Spherical Particles.* Journal of the American ceramic society, 1961. **44**(10): p. 513-522.

221. Jin, L., et al., *The fabrication and mechanical properties of SiC/SiC composites prepared by SLS combined with PIP.* Ceramics international, 2018. **44**(17): p. 20992-20999.

222. Chang, S., et al., *Selective laser sintering of porous silica enabled by carbon additive.* Materials, 2017. **10**(11).

223. Ferrage, L., G. Bertrand, and P. Lenormand, *Dense yttria-stabilized zirconia obtained by direct selective laser sintering.* Additive manufacturing, 2018. **21**: p. 472-478.

224. Liu, R.-Z., et al., *Effects of B4C addition on the microstructure and properties of porous alumina ceramics fabricated by direct selective laser sintering.* Ceramics international, 2018. **44**(16): p. 19678-19685.

225. Hwa, L.C., et al., *Recent advances in 3D printing of porous ceramics: A review.* Current Opinion in Solid State and Materials Science, 2017. **21**(6): p. 323-347.

226. Carloni, D., G. Zhang, and Y. Wu, *Transparent alumina ceramics fabricated by 3D printing and vacuum sintering.* Journal of the European ceramic society, 2021. **41**(1): p. 781-791.

227. Nötzel, D., R. Eickhoff, and T. Hanemann, *Fused filament fabrication of small ceramic components.* Materials, 2018. **11**(8).

228. Westbeek, S., et al., *Multi-scale process simulation for additive manufacturing through particle filled vat photopolymerization.* Computational materials science, 2020. **180**: p. 109647.

229. Bastas, A., *Comparing the probing systems of coordinate measurement machine: Scanning probe versus touch-trigger probe.* Measurement, 2020. **156**: p. 107604.

230. Etingof, M.I., *Role of gauges in modern machine construction.* Measurement techniques, 2014. **56**(11): p. 1261-1262.

231. Usamentiaga, R., D.F. Garcia, and F.J. delaCalle, *Automated Virtual Gauges for Dimensional Quality Control.* IEEE Transactions on industry applications, 2021. **57**(3): p. 2983-2993.

232. Eren, E., S. Kurama, and I. Solodov, *Characterization of porosity and defect imaging in ceramic tile using ultrasonic inspections.* Ceramics international, 2012. **38**(3): p. 2145-2151.

233. Zhang, B., S. Liu, and Y.C. Shin, *In-Process monitoring of porosity during laser additive manufacturing process.* Additive manufacturing, 2019. **28**: p. 497-505.

234. du Plessis, A., et al., *Standard method for microCT-based additive manufacturing quality control 1: Porosity analysis.* MethodsX, 2018. **5**: p. 1102-1110.

235. du Plessis, A., et al., *Standard method for microCT-based additive manufacturing quality control 2: Density measurement.* MethodsX, 2018. **5**: p. 1117-1123.

236. Plessis, A.d., et al., *Standard method for microCT-based additive manufacturing quality control 3: Surface roughness.* MethodsX, 2018. **5**: p. 1111-1116.

237. Charalampous, P., I. Kostavelis, and D. Tzovaras, *Non-destructive quality control methods in additive manufacturing: a survey.* Rapid Prototyping Journal, 2020. **26**(4): p. 777-790.

238. Kim, H., Y. Lin, and T.-L.B. Tseng, *A review on quality control in additive manufacturing.* Rapid Prototyping Journal, 2018. **24**(3): p. 645-669.

239. Liu, C., et al., *Image analysis-based closed loop quality control for additive manufacturing with fused filament fabrication.* Journal of Manufacturing Systems, 2019. **51**: p. 75-86.

240. Liu, R., S. Liu, and X. Zhang, *A physics-informed machine learning model for porosity analysis in laser powder bed fusion additive manufacturing.* The International journal of advanced manufacturing technology, 2021. **113**(7): p. 1943-1958.

241. Westbeek, S., et al., *Multi-scale process simulation for additive manufacturing through particle filled vat photopolymerization.* Computational Materials Science, 2020. **180**: p. 109647.

242. Maurath, J. and N. Willenbacher, *3D printing of open-porous cellular ceramics with high specific strength.* Journal of the European ceramic society, 2017. **37**.

243. Whyte, D., et al., *A review on the challenges of 3D printing of organic powders.* Bioprinting, 2019. **16**: p. e00057.

244. Ngo, T.D., et al., *Additive manufacturing (3D printing): A review of materials, methods, applications and challenges.* Composites part B: engineering, 2018. **143**: p. 172-196.

245. Porter, D.L., A.G. Evans, and A.H. Heuer, *Transformation-toughening in partially-stabilized zirconia (PSZ).* Acta metallurgica, 1979. **27**(10): p. 1649-1654.

246. Schünemann, F.H., et al., *Zirconia surface modifications for implant dentistry.* Materials science and engineering: C, 2019. **98**: p. 1294-1305.

247. McGough, M.A.P., et al., *Nanocrystalline Hydroxyapatite–Poly(thioketal urethane) Nanocomposites Stimulate a Combined Intramembranous and Endochondral Ossification Response in Rabbits.* ACS biomaterials science & engineering, 2020. **6**(1): p. 564-574.

248. Yoshikawa, H. and A. Myoui, *Bone tissue engineering with porous hydroxyapatite ceramics.* Journal of artificial organs, 2005. **8**(3): p. 131-136.

249. He, X., et al., *Incorporation of microfibrillated cellulose into collagen-hydroxyapatite scaffold for bone tissue engineering.* International journal of biological macromolecules, 2018. **115**: p. 385-392.

250. Mondal, S., et al., *Hydroxyapatite nano bioceramics optimized 3D printed poly lactic acid scaffold for bone tissue engineering application.* Ceramics international, 2020. **46**(3): p. 3443-3455.

251. Baştan, F.E., et al., *Electrophoretic co-deposition of PEEK-hydroxyapatite composite coatings for biomedical applications.* Colloids and surfaces B: biointerfaces, 2018. **169**: p. 176-182.

252. Ferreira, C.R.D., et al., *Study of microstructural, mechanical, and biomedical properties of zirconia/hydroxyapatite ceramic composites.* Ceramics international, 2022.

253. Cao, Y., et al., *Fabrication and properties of zirconia/hydroxyapatite composite scaffold based on digital light processing.* Ceramics international, 2020. **46**(2): p. 2300-2308.

254. Youness, R.A., M.A. Taha, and M.A. Ibrahim, *In vitro bioactivity, molecular structure and mechanical properties of zirconia-carbonated hydroxyapatite nanobiocomposites sintered at different temperatures.* Materials chemistry and physics, 2020. **239**: p. 122011.

255. Wang, X. and P. Xiao, *Residual stresses and constrained sintering of YSZ/Al2O3 composite coatings.* Acta materialia, 2004. **52**(9): p. 2591-2603.

256. Magnani, G. and A. Brillante, *Effect of the composition and sintering process on mechanical properties and residual stresses in zirconia–alumina composites.* Journal of the European ceramic society, 2005. **25**(15): p. 3383-3392.

257. Ruiz, L. and M.J. Readey, *Effect of heat treatment on grain size, phase assemblage, and mechanical properties of 3 mol% Y-TZP.* Journal of the American ceramic society, 1996. **79**(9): p. 2331-2340.

258. Chen, I.-W. and X.-H. Wang, *Sintering dense nanocrystalline ceramics without final-stage grain growth.* Nature, 2000. **404**(6774): p. 168-171.

259. Denry, I. and J.R. Kelly, *State of the art of zirconia for dental applications.* Dental materials, 2008. **24**(3): p. 299-307.

260. Hansen, N., *Hall–Petch relation and boundary strengthening.* Scripta materialia, 2004. **51**(8): p. 801-806.

261. Guo, S.-Q., *Densification of ZrB2-based composites and their mechanical and physical properties: A review.* Journal of the European ceramic society, 2009. **29**(6): p. 995-1011.

262. Doebelin, N. and R. Kleeberg, *Profex: a graphical user interface for the Rietveld refinement program BGMN.* Journal of applied crystallography, 2015. **48**(5): p. 1573-1580.

263. ISO, *ISO 18754:2020*, in *Fine ceramics (advanced ceramics, advanced technical ceramics) — Determination of density and apparent porosity*. 2020, ISO.

264. ASTM, *Standard test methods for determining average grain size*. 2021, ASTM International: West Conshohocken, PA. p. 28.

265. Roseti, L., et al., *Scaffolds for bone tissue engineering: State of the art and new perspectives.* Materials science and engineering: C, 2017. **78**: p. 1246-1262.

266. Wang, X.-H., P.-L. Chen, and I.W. Chen, *Two-step sintering of ceramics with constant grain-size, I. Y2O3.* Journal of the American ceramic society, 2006. **89**(2): p. 431-437.

267. Dong, Y., et al., *Ultra-uniform nanocrystalline materials via two-step sintering.* Advanced functional materials, 2021. **31**(1): p. 2007750.

268. Kumar, R., et al., *Microstructure and mechanical properties of spark plasma sintered zirconia-hydroxyapatite nano-composite powders.* Acta materialia, 2005. **53**(8): p. 2327-2335.

269. Castkova, K., et al., *Synthesis of Ca,Y-zirconia/hydroxyapatite nanoparticles and composites.* Journal of the European ceramic society, 2016. **36**(12): p. 2903-2912.

270. Evis, Z., M. Usta, and I. Kutbay, *Improvement in sinterability and phase stability of hydroxyapatite and partially stabilized zirconia composites.* Journal of the European ceramic society, 2009. **29**(4): p. 621-628.

271. Gremillard, L., et al., *Elaboration of self-coating alumina-based porous ceramics.* Journal of materials science, 2006. **41**(16): p. 5200-5207.

272. Liao, C.-J., et al., *Thermal decomposition and reconstitution of hydroxyapatite in air atmosphere.* Biomaterials, 1999. **20**(19): p. 1807-1813.

273. Zhang, J., et al., *Fabrication of hydroxyapatite–zirconia composites for orthopedic applications.* Journal of the American ceramic society, 2006. **89**(11): p. 3348-3355.

274. Ji, W., et al., *Ultra-fast firing: Effect of heating rate on sintering of 3YSZ, with and without an electric field.* Journal of the European ceramic society, 2017. **37**(6): p. 2547-2551.

275. Ramachandra Rao, R. and T.S. Kannan, *Synthesis and sintering of hydroxyapatite–zirconia composites.* Materials science and engineering: C, 2002. **20**(1): p. 187-193.

276. Ling, Y., et al., *Optimisation on the stability of CaO-doped partially stabilised zirconia by microwave heating.* Ceramics international, 2021. **47**(6): p. 8067-8074.

277. Kumar, A., P. Kumar, and A.S. Dhaliwal, *Phase transformation behavior of Ca-doped zirconia sintered at different temperatures.* Journal of the Korean Ceramic Society, 2022.

278. Luo, J., S. Adak, and R. Stevens, *Microstructure evolution and grain growth in the sintering of 3Y–TZP ceramics.* Journal of materials science, 1998. **33**(22): p. 5301-5309.

279. Yashima, M. and A. Sakai, *High-temperature neutron powder diffraction study of the structural phase transition between α and α′ phases in tricalcium phosphate Ca3(PO4)2.* Chemical physics letters, 2003. **372**(5): p. 779-783.

280. Montufar, E.B., et al., *High strength, biodegradable and cytocompatible alpha tricalcium phosphate-iron composites for temporal reduction of bone fractures.* Acta biomaterialia, 2018. **70**: p. 293-303.

281. Kim, H.-W., et al., *Dissolution control and cellular responses of calcium phosphate coatings on zirconia porous scaffold.* Journal of biomedical materials research part A, 2004. **68A**(3): p. 522-530.

282. Jahn, C., et al., *Investigation of calcium zirconate formation by sintering zirconium dioxide with calcium hydroxide.* Ceramics international, 2018. **44**(10): p. 11274-11281.

283. Kumar, A., P. Kumar, and A.S. Dhaliwal, *Structural, morphological properties and phase stabilisation criteria of the calcia-zirconia system.* Advances in applied ceramics, 2021. **120**(5-8): p. 307-318.

284. Garvie, R.C., *The Cubic Field in the System CaO-ZrO2.* Journal of the American ceramic society, 1968. **51**(10): p. 553-556.

285. Zhou, G.H., et al., *The preparation and mechanical properties of the unidirectional carbon fiber reinforced zirconia composite.* Journal of the European ceramic society, 2008. **28**(4): p. 787-792.

286. Lai, J.K.L., C.H. Shek, and G.M. Lin, *Grain growth kinetics of nanocrystalline SnO2 for long-term isothermal annealing.* Scripta materialia, 2003. **49**(5): p. 441-446.

287. Fang, Z.Z. and H. Wang, *Densification and grain growth during sintering of nanosized particles.* International materials reviews, 2008. **53**(6): p. 326-352.

288. Cotič, J., et al., *Complexity of the relationships between the sintering-temperature-dependent grain size, airborne-particle abrasion, ageing and strength of 3Y-TZP ceramics.* Dental materials, 2016. **32**(4): p. 510-518.

289. Muralithran, G. and S. Ramesh, *The effects of sintering temperature on the properties of hydroxyapatite.* Ceramics international, 2000. **26**(2): p. 221-230.

290. Fan, J., et al., *Densification and grain growth in oscillatory pressure sintering of alumina toughened zirconia ceramic composites.* Journal of alloys and compounds, 2020. **845**: p. 155644.

291. Matsumoto, T.J., et al., *Zirconia–hydroxyapatite composite material with micro porous structure.* Dental materials, 2011. **27**(11): p. e205-e212.

292. Zhang, F., L.-f. Li, and E.-z. Wang, *Effect of micro-alumina content on mechanical properties of Al2O3/3Y-TZP composites.* Ceramics international, 2015. **41**(9, Part B): p. 12417-12425.

293. Turon-Vinas, M. and M. Anglada, *Strength and fracture toughness of zirconia dental ceramics.* Dental materials, 2018. **34**(3): p. 365-375.

294. Miao, X., et al., *Preparation and characterization of interpenetrating phased TCP/HA/PLGA composites.* Materials letters, 2005. **59**(29): p. 4000-4005.

295. Obada, D.O., et al., *Mechanical properties of natural hydroxyapatite using low cold compaction pressure: Effect of sintering temperature.* Materials chemistry and physics, 2020. **239**: p. 122099.

296. Li, M., et al., *An overview of graphene-based hydroxyapatite composites for orthopedic applications.* Bioactive materials, 2018. **3**(1): p. 1-18.

297. Chen, X., et al., *Mechanical properties of nanodiamond-reinforced hydroxyapatite composite coatings deposited by suspension plasma spraying.* Applied surface science, 2018. **439**: p. 60-65.

298. Curran, D.J., et al., *Mechanical properties of hydroxyapatite–zirconia compacts sintered by two different sintering methods.* Journal of Materials science: Materials in medicine, 2010. **21**(4): p. 1109-1120.

299. Erkmen, Z.E., Y. Genç, and F.N. Oktar, *Microstructural and Mechanical Properties of Hydroxyapatite–Zirconia Composites.* Journal of the American ceramic society, 2007. **90**(9): p. 2885-2892.

300. Gain, A.K., L. Zhang, and W. Liu, *Microstructure and material properties of porous hydroxyapatite-zirconia nanocomposites using polymethyl methacrylate powders.* Materials & design, 2015. **67**: p. 136-144.

301. Yang, Z., et al., *Grain size engineered lead-free ceramics with both large energy storage density and ultrahigh mechanical properties.* Nano energy, 2019. **58**: p. 768-777.

302. Kanhed, S., et al., *Porosity distribution affecting mechanical and biological behaviour of hydroxyapatite bioceramic composites.* Ceramics international, 2017. **43**(13): p. 10442-10449.

303. Kaplan, M., et al., *Production and properties of tooth-colored yttria stabilized zirconia ceramics for dental applications.* Ceramics international, 2018. **44**(2): p. 2413-2418.

304. Hannora, A.E. and S. Ataya, *Structure and compression strength of hydroxyapatite/titania nanocomposites formed by high energy ball milling.* Journal of alloys and compounds, 2016. **658**: p. 222-233.

305. Mazaheri, M., et al., *Effect of a novel sintering process on mechanical properties of hydroxyapatite ceramics.* Journal of alloys and compounds, 2009. **471**(1): p. 180-184.

306. Kothapalli, C., et al., *Influence of temperature and concentration on the sintering behavior and mechanical properties of hydroxyapatite.* Acta materialia, 2004. **52**(19): p. 5655-5663.

307. Banerjee, S.S., et al., *Understanding the influence of MgO and SrO binary doping on the mechanical and biological properties of β-TCP ceramics.* Acta biomaterialia, 2010. **6**(10): p. 4167-4174.

308. Humagain, S. *Structure and functions of bones*. 2017 [cited 2021; Available from: https://onlinesciencenotes.com/structure-functions-bones/.

309. Li, J.J., et al., *Current approaches to bone tissue engineering: The interface between biology and engineering.* Advanced healthcare materials, 2018. **7**(6): p. 1701061.

310. Koushik, T.M., C.M. Miller, and E. Antunes, *Bone tissue engineering scaffolds: Function of multi-material hierarchically structured scaffolds.* Advanced healthcare materials, 2022. **n/a**(n/a): p. 2202766.

311. Mohammadi Zerankeshi, M., S. Mofakhami, and E. Salahinejad, *3D porous HA/TCP composite scaffolds for bone tissue engineering.* Ceramics international, 2022. **48**(16): p. 22647-22663.

312. Zhang, J., et al., *Osteoimmunity-regulating biomimetically hierarchical scaffold for augmented bone regeneration.* Advanced materials, 2022. **34**(36): p. 2202044.

313. Jia, G., et al., *Exploring the interconnectivity of biomimetic hierarchical porous Mg scaffolds for bone tissue engineering: Effects of pore size distribution on mechanical properties, degradation behavior and cell migration ability.* Journal of magnesium and alloys, 2021. **9**(6): p. 1954-1966.

314. Draenert, M., A. Draenert, and K. Draenert, *Osseointegration of hydroxyapatite and remodeling-resorption of tricalciumphosphate ceramics.* Microscopy research and technique, 2013. **76**(4): p. 370-380.

315. Wu, S.-C., et al., *Preparation and characterization of four different compositions of calcium phosphate scaffolds for bone tissue engineering.* Materials characterization, 2011. **62**(5): p. 526-534.

316. Tanimoto, Y., et al., *Effect of varying HAP/TCP ratios in tape-cast biphasic calcium phosphate ceramics on response in vitro.* Journal of hard tissue biology, 2009. **18**(2): p. 71-76.

317. Yuan, H., et al., *Bone formation induced by calcium phosphate ceramics in soft tissue of dogs: a comparative study between porous α-TCP and β-TCP.* Journal of materials science: Materials in medicine, 2001. **12**(1): p. 7-13.

318. Spence, G., et al., *Carbonate substituted hydroxyapatite: Resorption by osteoclasts modifies the osteoblastic response.* Journal of biomedical materials research part A, 2009. **90A**(1): p. 217-224.

319. Pierantozzi, D., et al., *3D printed Sr-containing composite scaffolds: Effect of structural design and material formulation towards new strategies for bone tissue engineering.* Composites science and technology, 2020. **191**: p. 108069.

320. Mancuso, E., et al., *Additively manufactured BaTiO3 composite scaffolds: A novel strategy for load bearing bone tissue engineering applications.* Materials science and engineering: C, 2021. **126**: p. 112192.

321. Zadpoor, A.A., *Relationship between in vitro apatite-forming ability measured using simulated body fluid and in vivo bioactivity of biomaterials.* Materials science and engineering: C, 2014. **35**: p. 134-143.

322. Pan, H., et al., *Apatite-formation ability – Predictor of "bioactivity"?* Acta biomaterialia, 2010. **6**(11): p. 4181-4188.

323. Lu, X. and Y. Leng, *Theoretical analysis of calcium phosphate precipitation in simulated body fluid.* Biomaterials, 2005. **26**(10): p. 1097-1108.

324. Fan, X., et al., *Bone-like apatite formation on HA/316L stainless steel composite surface in simulated body fluid.* Transactions of nonferrous metals society of china, 2009. **19**(2): p. 347-352.

325. Kokubo, T. and H. Takadama, *How useful is SBF in predicting in vivo bone bioactivity?* Biomaterials, 2006. **27**(15): p. 2907-2915.

326. Kim, H.-M., et al., *Process and kinetics of bonelike apatite formation on sintered hydroxyapatite in a simulated body fluid.* Biomaterials, 2005. **26**(21): p. 4366-4373.

327. Fantini, M., M. Curto, and F. De Crescenzio, *A method to design biomimetic scaffolds for bone tissue engineering based on Voronoi lattices.* Virtual and physical prototyping, 2016. **11**(2): p. 77-90.

328. Germain, L., et al., *3D-printed biodegradable gyroid scaffolds for tissue engineering applications.* Materials & design, 2018. **151**: p. 113-122.

329. Zhang, Q., et al., *High-Strength hydroxyapatite scaffolds with minimal surface macrostructures for load-Bearing bone regeneration.* Advanced functional materials, 2022. **32**(33): p. 2204182.

330. Feng, Y., et al., *Stiffness optimization design for TPMS architected cellular materials.* Materials & design, 2022. **222**: p. 111078.

331. Maskery, I., et al., *Effective design and simulation of surface-based lattice structures featuring volume fraction and cell type grading.* Materials & design, 2018. **155**: p. 220-232.

332. Koushik, T. and E. Antunes, *9 - Ceramic three-dimensional printing*, in *Advanced flexible ceramics*, R.K. Gupta, et al., Editors. 2023, Elsevier. p. 193-214.

333. Oyane, A., et al., *Preparation and assessment of revised simulated body fluids.* Journal of biomedical materials research part A, 2003. **65A**(2): p. 188-195.

334. O'Brien, J., et al., *Investigation of the Alamar Blue (resazurin) fluorescent dye for the assessment of mammalian cell cytotoxicity.* European journal of biochemistry, 2000. **267**(17): p. 5421-5426.

335. Rampersad, S.N., *Multiple applications of Alamar Blue as an indicator of metabolic function and cellular health in cell viability bioassays.* Sensors, 2012. **12**(9): p. 12347-12360.

336. Khaleghi, S., et al., *On the directional elastic modulus of the TPMS structures and a novel hybridization method to control anisotropy.* Materials & design, 2021. **210**: p. 110074.

337. Holzer, G., et al., *Hip fractures and the contribution of cortical versus trabecular bone to femoral neck strength.* Journal of bone and mineral research, 2009. **24**(3): p. 468-474.

338. Ott, Susan M., *Cortical or Trabecular bone: What's the difference?* American journal of nephrology, 2018. **47**(6): p. 373-375.

339. Scherrer, S.S., et al., *ADM guidance—Ceramics: guidance to the use of fractography in failure analysis of brittle materials.* Dental materials, 2017. **33**(6): p. 599-620.

340. Abueidda, D.W., et al., *Mechanical properties of 3D printed polymeric Gyroid cellular structures: Experimental and finite element study.* Materials & design, 2019. **165**: p. 107597.

341. Downing, D., et al., *Increased efficiency gyroid structures by tailored material distribution.* Materials & design, 2021. **197**: p. 109096.

342. Rezapourian, M., et al., *Selective laser melted Ti6Al4V split-P TPMS lattices for bone tissue engineering.* International Journal of mechanical sciences, 2023. **251**: p. 108353.

343. Baino, F. and S. Yamaguchi, *The use of simulated body fluid (SBF) for assessing materials bioactivity in the context of tissue engineering: Review and challenges.* Biomimetics, 2020. **5**(4): p. 57.

344. Öfkeli, F., D. Demir, and N. Bölgen, *Biomimetic mineralization of chitosan/gelatin cryogels and in vivo biocompatibility assessments for bone tissue engineering.* Journal of applied polymer science, 2021. **138**(14): p. 50337.

345. Patty, D.J., et al., *Mechanical characteristics and bioactivity of nanocomposite hydroxyapatite/collagen coated titanium for bone tissue engineering.* Bioengineering, 2022. **9**(12): p. 784.

346. Vargas-Becerril, N., et al., *Structure of biomimetic apatite grown on hydroxyapatite (HA).* Ceramics international, 2020. **46**(18, Part A): p. 28806-28813.

347. Liu, L., et al., *Preparation and mechanical and biological performance of the Sr-containing microarc oxidation layer on titanium implants.* Surface and coatings technology, 2023. **463**: p. 129530.

348. Marques, P., et al., *Hydrogencarbonate as a biological buffer in simulated plasma.* Key engineering Materials, 2001: p. 27-30.

349. Arabnejad, S., et al., *High-strength porous biomaterials for bone replacement: A strategy to assess the interplay between cell morphology, mechanical properties, bone ingrowth and manufacturing constraints.* Acta biomaterialia, 2016. **30**: p. 345-356.

350. Sarkar, N. and S. Bose, *Controlled release of soy isoflavones from multifunctional 3D printed bone tissue engineering scaffolds.* Acta biomaterialia, 2020. **114**: p. 407-420.

351. Piattelli, A., et al., *Effects of alkaline phosphatase on bone healing around plasma-sprayed titanium implants: a pilot study in rabbits.* Biomaterials, 1996. **17**(14): p. 1443-1449.

352. Jaroszewicz, J., et al., *Formation of calcium phosphate coatings within polycaprolactone scaffolds by simple, alkaline phosphatase based method.* Materials science and engineering: C, 2019. **96**: p. 319-328.

353. Boonrungsiman, S., et al., *The role of intracellular calcium phosphate in osteoblast-mediated bone apatite formation.* Proceedings of the National Academy of Sciences, 2012. **109**(35): p. 14170-14175.

354. Ansari, S., K. Ito, and S. Hofmann, *Alkaline phosphatase activity of serum affects osteogenic differentiation cultures.* ACS omega, 2022. **7**(15): p. 12724-12733.

355. Yan, J., J.J. Mecholsky, and K.B. Clifton, *How tough is bone? Application of elastic–plastic fracture mechanics to bone.* Bone, 2007. **40**(2): p. 479-484.

356. Fallah, A., et al., *3D printed scaffold design for bone defects with improved mechanical and biological properties.* Journal of the mechanical behavior of biomedical materials, 2022. **134**: p. 105418.

357. Ryan, E. and S. Yin, *Compressive strength of β-TCP scaffolds fabricated via lithography-based manufacturing for bone tissue engineering.* Ceramics international, 2022. **48**(11): p. 15516-15524.

358. Rezania, N., et al., *Three-dimensional printing of polycaprolactone/hydroxyapatite bone tissue engineering scaffolds mechanical properties and biological behavior.* Journal of materials science: Materials in medicine, 2022. **33**(3): p. 31.

359. Cohen, H., et al., *The influence of impact direction and axial loading on the bone fracture pattern.* Forensic science international, 2017. **277**: p. 197-206.

360. Wedel, V.L. and A. Galloway, *Broken bones: anthropological analysis of blunt force trauma*. 2013: Charles C Thomas Publisher.

361. Kim, H.D., et al., *Biomimetic materials and fabrication approaches for bone tissue engineering.* Advanced healthcare materials, 2017. **6**(23): p. 1700612.

362. Al-Ketan, O. and R.K. Abu Al-Rub, *Multifunctional mechanical metamaterials based on triply periodic minimal surface lattices.* Advanced engineering materials, 2019. **21**(10): p. 1900524.

363. Conway, K.M., et al., *Increasing fracture toughness via architected porosity.* Materials & design, 2021. **205**: p. 109696.

364. Putra, N.E., et al., *Multi-material additive manufacturing technologies for Ti-, Mg-, and Fe-based biomaterials for bone substitution.* Acta biomaterialia, 2020. **109**: p. 1-20.

365. Feng, P., et al., *A Multimaterial Scaffold With Tunable Properties: Toward Bone Tissue Repair.* Advanced Science, 2018. **5**(6): p. 1700817.

366. Xu, X., et al., *Copper-modified Ti6Al4V alloy fabricated by selective laser melting with pro-angiogenic and anti-inflammatory properties for potential guided bone regeneration applications.* Materials science and engineering: C, 2018. **90**: p. 198-210.

367. Chen, A., et al., *Multimaterial 3D and 4D Bioprinting of Heterogenous Constructs for Tissue Engineering.* Advanced materials, 2023. **n/a**(n/a): p. 2307686.

368. Tajbakhsh, S. and F. Hajiali, *A comprehensive study on the fabrication and properties of biocomposites of poly (lactic acid)/ceramics for bone tissue engineering.* Materials science and engineering: C, 2017. **70**: p. 897-912.

369. Koushik, T.M., C.M. Miller, and E. Antunes, *Optimisation of two-step sintering parameters to produce bioactive and dense zirconia-hydroxyapatite composite ceramics.* Journal of the European ceramic society, 2023. **43**(5): p. 2222-2233.

370. Browne, D.J., et al., *An analytically and diagnostically sensitive RNA extraction and RT-qPCR protocol for peripheral blood mononuclear cells.* Frontiers in immunology, 2020. **11**: p. 402.

371. Browne, D.J., et al., *A high-throughput screening RT-qPCR assay for quantifying surrogate markers of immunity from PBMCs.* Frontiers in immunology, 2022. **13**: p. 962220.

372. Spandidos, A., et al., *PrimerBank: a resource of human and mouse PCR primer pairs for gene expression detection and quantification.* Nucleic acids research, 2010. **38**(suppl_1): p. D792-D799.

373. Bustin, S.A., et al., *The MIQE guidelines: minimum information for publication of quantitative real-time PCR experiments.* Clin Chem, 2009. **55**(4): p. 611-22.

374. Livak, K.J. and T.D. Schmittgen, *Analysis of relative gene expression data using real-time quantitative PCR and the 2− ΔΔCT method.* methods, 2001. **25**(4): p. 402-408.

375. Wulfman, C., M. Sadoun, and M. Lamy de la Chapelle, *Interest of Raman spectroscopy for the study of dental material: The zirconia material example.* IRBM, 2010. **31**(5): p. 257-262.

376. Muñoz Tabares, J.A. and M.J. Anglada, *Quantitative analysis of monoclinic phase in 3Y-TZP by Raman Spectroscopy.* Journal of the American ceramic society, 2010. **93**(6): p. 1790-1795.

377. Cuscó, R., et al., *Differentiation between hydroxyapatite and β-tricalcium phosphate by means of μ-Raman spectroscopy.* Journal of the European ceramic society, 1998. **18**(9): p. 1301-1305.

378. Loudon, R., *The Raman effect in crystals.* Advances in Physics, 1964. **13**(52): p. 423-482.

379. Deng, Z.-L., et al., *Mechanical and degradation properties of triply periodic minimal surface (TPMS) hydroxyapatite & akermanite scaffolds with functional gradient structure.* Ceramics international, 2023. **49**(12): p. 20808-20816.

380. Bouakaz, I., et al., *Hydroxyapatite 3D-printed scaffolds with Gyroid-Triply periodic minimal surface (TPMS) porous structure: Fabrication and an in vivo pilot study in sheep.* Acta biomaterialia, 2023. **170**: p. 580-595.

381. Zhang, F., et al., *3Y-TZP ceramics with improved hydrothermal degradation resistance and fracture toughness.* Journal of the European ceramic society, 2014. **34**(10): p. 2453-2463.

382. Grech, J. and E. Antunes, *Optimization of two-step sintering conditions of zirconia blanks for dental restorations.* Ceramics international, 2020. **46**(16, Part A): p. 24792-24798.

383. Maskery, I., et al., *Compressive failure modes and energy absorption in additively manufactured double gyroid lattices.* Additive manufacturing, 2017. **16**: p. 24-29.

384. Keyak, J.H., H.B. Skinner, and J.A. Fleming, *Effect of force direction on femoral fracture load for two types of loading conditions.* Journal of Orthopaedic Research, 2001. **19**(4): p. 539-544.

385. Miranda, P., et al., *Fracture modes under uniaxial compression in hydroxyapatite scaffolds fabricated by robocasting.* Journal of biomedical materials research part A, 2007. **83A**(3): p. 646-655.

386. Ćorić, D., M. Majić Renjo, and L. Ćurković, *Vickers indentation fracture toughness of Y-TZP dental ceramics.* International journal of refractory metals and hard Materials, 2017. **64**: p. 14-19.

387. Lai, T.R., C.L. Hogg, and M.V. Swain, *Evaluation of fracture toughness and R-Curve behaviour of Y-TZP Ceramics.* ISIJ international, 1989. **29**(3): p. 240-245.

388. Yazdani Sarvestani, H., et al., *Multilayered architectured ceramic panels with weak interfaces: energy absorption and multi-hit capabilities.* Materials & design, 2019. **167**: p. 107627.

389. Hong, S., et al., *Real-time analysis of cell–surface adhesive interactions using thickness shear mode resonator.* Biomaterials, 2006. **27**(34): p. 5813-5820.

390. Khalili, A.A. and M.R. Ahmad, *A Review of cell adhesion studies for biomedical and biological applications.* Int J Mol Sci, 2015. **16**(8): p. 18149-84.

391. Kozaniti, F.K., et al., *The role of substrate topography and stiffness on MSC cells functions: Key material properties for biomimetic bone tissue engineering.* Biomimetics (Basel), 2021. **7**(1).

392. Vimalraj, S., *Alkaline phosphatase: Structure, expression and its function in bone mineralization.* Gene, 2020. **754**: p. 144855.

393. Isa, Z.M., et al., *Effects of fluoride-modified titanium surfaces on osteoblast proliferation and gene expression.* International journal of oral & maxillofacial implants, 2006. **21**(2).

394. Xie, J., M.J. Baumann, and L.R. McCabe, *Osteoblasts respond to hydroxyapatite surfaces with immediate changes in gene expression.* Journal of biomedical materials research part A, 2004. **71A**(1): p. 108-117.

395. Lee, H., et al., *Intracellular Delivery of Recombinant RUNX2 Facilitated by Cell-Penetrating Protein for the Osteogenic Differentiation of hMSCs.* ACS Biomaterials Science & Engineering, 2020. **6**(9): p. 5202-5214.

396. Ledda, M., et al., *Biological response to bioinspired microporous 3D-printed scaffolds for bone tissue engineering.* International journal of molecular sciences, 2022. **23**(10): p. 5383.

397. Beck Jr, G.R., B. Zerler, and E. Moran, *Phosphate is a specific signal for induction of osteopontin gene expression.* Proceedings of the national academy of sciences, 2000. **97**(15): p. 8352-8357.

398. Liu, Q., et al., *Recent advances of osterix transcription factor in osteoblast differentiation and bone formation.* Frontiers in cell and developmental biology, 2020. **8**.

399. Chen, Y., N. Kawazoe, and G. Chen, *Preparation of dexamethasone-loaded biphasic calcium phosphate nanoparticles/collagen porous composite scaffolds for bone tissue engineering.* Acta biomaterialia, 2018. **67**: p. 341-353.

400. Wang, X., et al., *3D printing of black bioceramic scaffolds with micro/nanostructure for bone tumor-induced tissue therapy.* Advanced healthcare materials, 2021. **10**(21): p. 2101181.

401. Gatto, M.L., et al., *Biomechanical performances of PCL/HA micro-and macro-porous lattice scaffolds fabricated via laser powder bed fusion for bone tissue engineering.* Materials science and engineering: C, 2021. **128**: p. 112300.

402. Jiang, S.J., et al., *Radially porous nanocomposite scaffolds with enhanced capability for guiding bone regeneration in vivo.* Advanced functional materials, 2022. **32**(18): p. 2110931.

403. Wang, X., et al., *Bioinspired highly anisotropic, ultrastrong and stiff, and osteoconductive mineralized wood hydrogel composites for bone repair.* Advanced functional materials, 2021. **31**(20): p. 2010068.

404. Balagangadharan, K., S. Dhivya, and N. Selvamurugan, *Chitosan based nanofibers in bone tissue engineering.* International journal of biological macromolecules, 2017. **104**: p. 1372-1382.

APPENDIX

Table A1: Effect of physical and chemical attributes of BTE scaffold on their bone healing response. Structure of porosity has been classified into graded (GR) and microarchitecture (MO). Mechanical strength of the scaffolds has been classified into compression strength (Y), elastic modulus (σ_y) and fracture strength (K_{ic}).

Material	**Fabrication technique**	**Pore size (µm)**	**Porosity (%)**	**Structure of porosity**		**Mechanical strength (GPa/MPa/MPa.m$^{0.5}$)**			**Biomedical property**	**Ref.**
				MO	GR	Y	σ_y	K_{ic}		
Collagen + BCP	Sacrificial template	20 – 65 405 – 450	97		GR	25 KPa	-	-	• Interconnected porosity • Enabled controlled release of DEX • BCP/Collagen scaffolds upregulated osteogenic markers (ALP, RUNX2 and BMP-2) • Complete cell infiltration and distribution after in-vivo implantation	[399]

Ti6Al4V	LPBF (Laser powder bed fusion)		50 – 90	MO		-	42 – 240	-	• Compression strength is inversely proportion to the porosity of gyroid structure • Porosities >70% should mechanical similarity with trabecular bone • TPMS based scaffolds microarchitectures are ideal for BTE applications	[141]
Black – akermanite	FFF (Fused filament fabrication)	-	-	MO			16.36		• B-AKT scaffolds promote growth and dispersion of rBMSCs • B-AKT scaffolds could promote the expression of OCN, OPN and RUNx2 proteins • Expression of OCN was dependent on micro/nanostructure of the B-AKT scaffolds • Release of BMP-2 proteins was triggered by micro/nanostructured features	[400]
PCL + HAp	LPBF	60 – 65	6 – 12	MO		13 – 15	2 – 3.2		• Connectivity of scaffold microarchitecture enabled cell migration	[401]

		80 – 160				MPa			• Lower tortuosity of scaffold microarchitecture enables its complete colonisation • Fluid infiltration played a key role in scaffold degradation	
Chitosan + HAp	Freeze casting	84, 98	>90		GR	-	-	-	• Axially aligned pore network provides higher compression strength compared to radially aligned pore network • Orientation of pores had a limited influence on ALP activity • Bone volume/total volume(BV/TV) was higher for radially structured scaffolds • Low fibrous tissue penetration in radially structured scaffolds	[402]
Wood and hydrogels nanoHAp	Replica technique		15.4		GR	804 MPa	88.14	-	• Presence of HAp promoted cell attachment and spreading along the direction of cellulose fibrils • Upregulation of OCN, OPN, RUNX2 and ALP	[403]

									• Enables direct ingrowth of new bone into the scaffold	
HAp	SLA (3D printing)	33 - 75	300 – 900		GR	-	12 – 150	-	• Spilt P type TPMS surfaces showed a 60% increase in cell attachment compared to cross hatch type surface • Spilt P types structure showed upregulation of OCN,OPN RUNX2 and presence of type 1 collagen • Higher new bone formation observed in split-P TPMS surfaces • Split P surfaces show more osteoconductivity compared to cross-hatch type scaffolds	[379]
Silicon nanofibers + Chitosan	Freeze casting	30 – 140	-		GR	3 – 27	-	-	• Cell viability of more than 95% was observed due to porous structure • Scaffold were able to fit into the bone defects • Scaffolds produced higher bone density	[404]

									• Bone mineralisation could be tailored by adjusting silicon content • Similarity in compression modulus enabled osteogenic differentiation of hMSCs	

Table A2: Properties of 3Y-TZP and HAp materials used for the preparation of ceramic composites.

Materials	**Particle size distribution (D_{50})**	**Density (Tapped)**
TZ-3Y-E	40 nm	1.2 g/cm^3
Hydroxyapatite	4.5 μm	0.84 g/cm^3

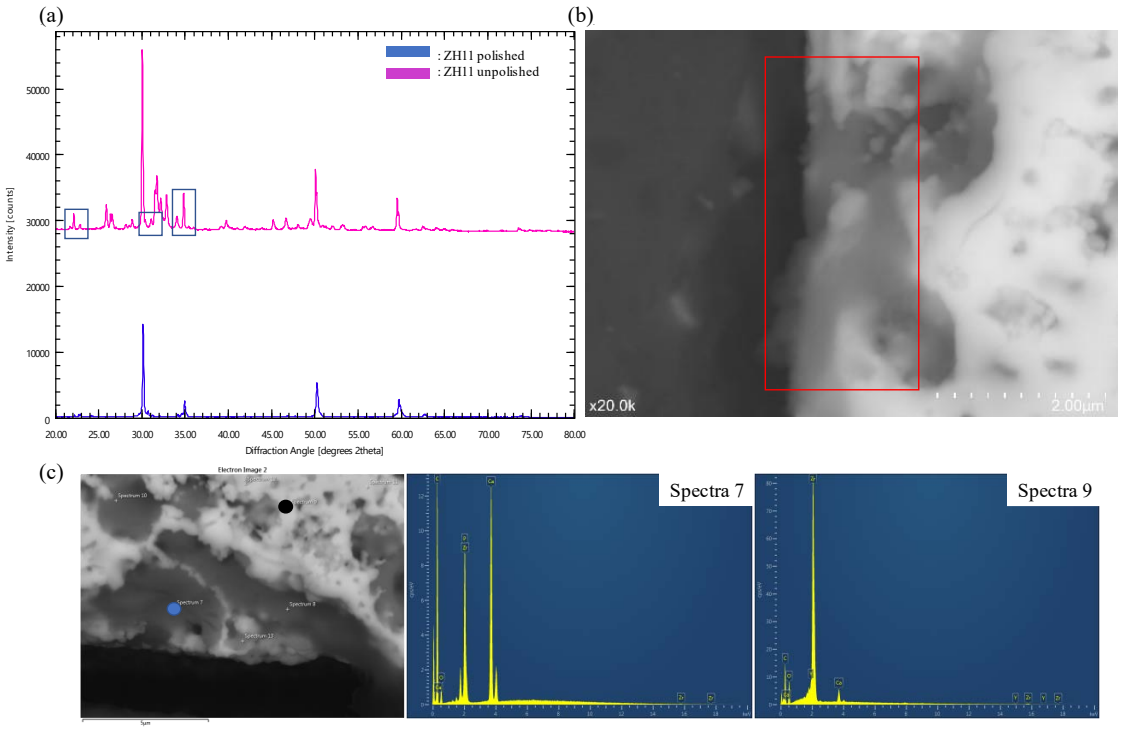

Figure A1: (a) The XRD plots of the unpolished (represented in pink) and polished surfaces (represented in blue). The marked boxes indicate the major peaks of α-TCP phases. (b) The backscatter SEM image of the ZH11 sample crossection showed the accumulation of a darker phase on the top surface of the pellet. (c) SEM-EDS of the surface showed an increase in Ca content compared to the remaining bulk as observed from spectra 7 (blue spot) and 9.(black spot).

Table A3: Rietveld refinement statistics for samples analysed for the Taguchi experiment.

Sample	Rietveld refinement information	
	Chi-square value (χ^2)	**GOF**
ZH1	1.05	1.02
ZH2	1.17	1.08
ZH3	1.14	1.07
ZH4	1.09	1.05
ZH5	1.19	1.09
ZH6	1.09	1.04
ZH7	1.42	1.19
ZH8	1.60	1.26
ZH9	1.74	1.32
ZH10	1.19	1.09
ZH11	2.95	1.72

ZH12	1.8	1.34
ZH13	1.16	1.08
ZH14	1.1	1.05
ZH15	1.59	1.26

Table A4: Rietveld refinement statistics for samples analysed for the optimisation experiment.

Sample name	Rietveld refinement	
	Chi square value	Goodness-of-fit
ZH19_1	1.68	1.30
ZH19_2	1.64	1.28
ZH19_3	1.63	1.24
ZH19_4	1.80	1.34
ZH19_5	1.42	1.19
ZH19_6	1.56	1.25
ZH19_7	1.52	1.23
ZH19_8	1.45	1.20
ZH19_9	1.95	1.40
ZH18_1	1.44	1.20
ZH18_2	1.27	1.13

ZH18_3	1.37	1.17
ZH18_4	2.17	1.47
ZH18_5	1.37	1.17
ZH18_6	1.47	1.21
ZH18_7	1.33	1.15
ZH18_8	1.27	1.13
ZH18_9	1.61	1.27
ZH17_1	1.42	1.19
ZH17_2	2.04	1.43
ZH17_3	1.49	1.22
ZH17_4	4.52	2.13
ZH17_5	2.65	1.63
ZH17_6	1.26	1.12
ZH17_7	1.43	1.20

ZH17_8	2.25	1.50
ZH17_9	1.23	1.11

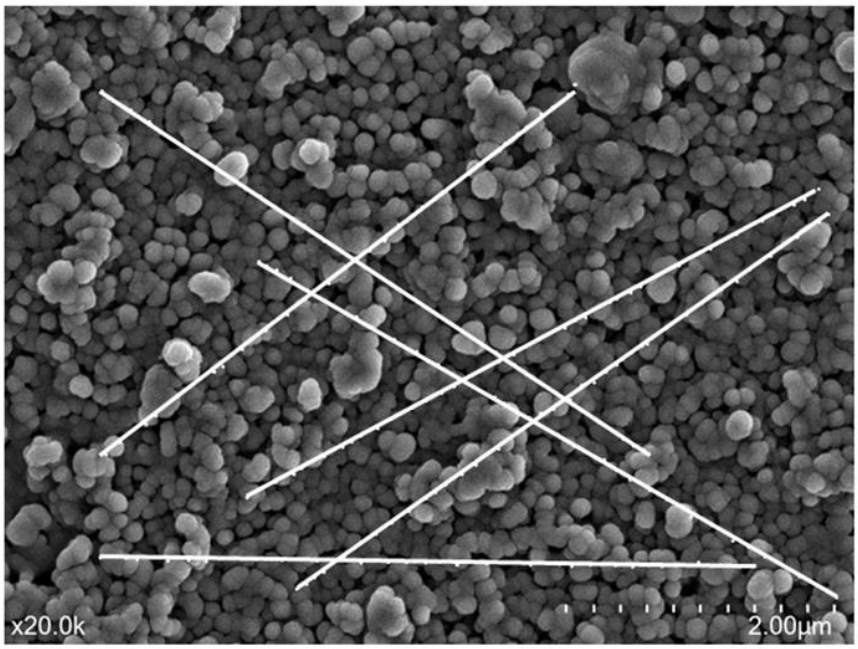

Length (mm)	Grain intersections
240	37
240	39
240	37
240	42
240	43
240	36

Intercept length : 0.00030769
Grain area :1.19629 x 10^{-7} µm^2
Grain size : 0.3458 µm

Figure A2: Example of grain size measurement according to ASTM E112.

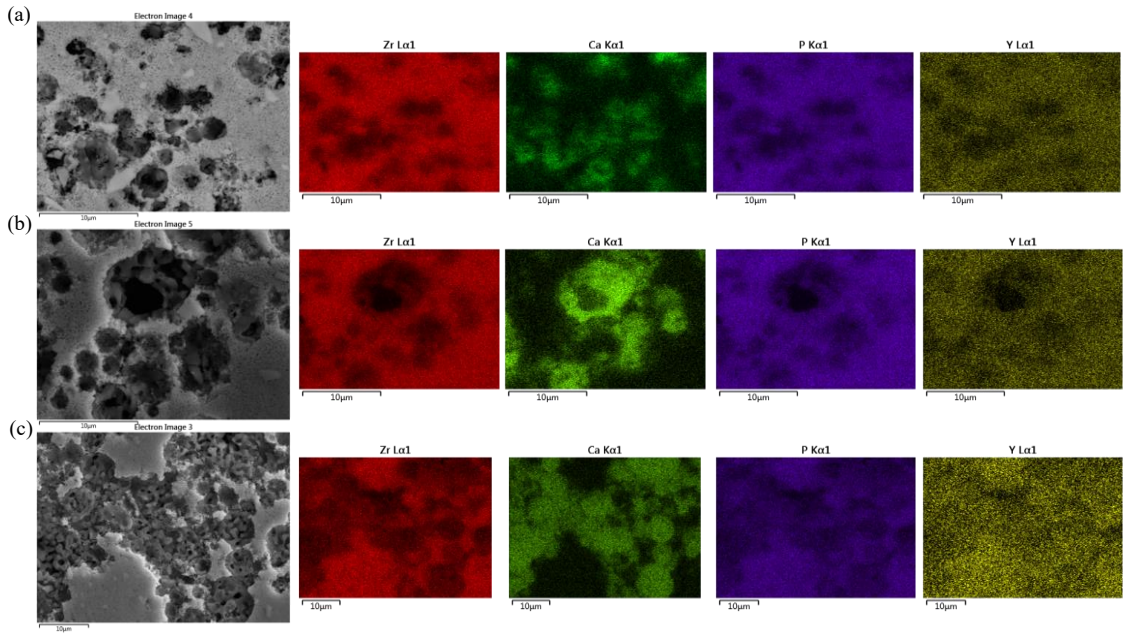

Figure A3: Distribution of elemental composition (Zr, Ca, P and Y) in sintered 3Y-TZP – HAp composites (a) ZH18_4, (b) ZH17_8 and (c) ZH19_8.

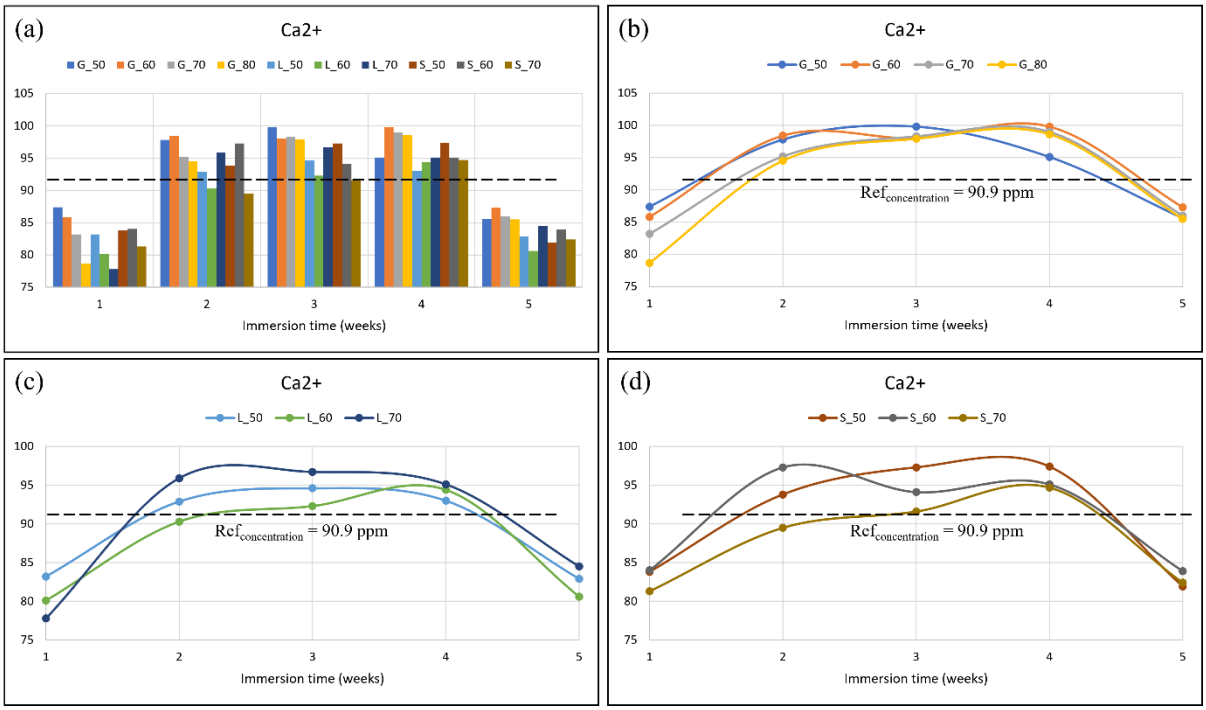

Figure A4: (a) Concentration of Ca^{2+} observed at week 1 to 5 across all TPMS structures at porosities ranging from 50% - 80%. Variation in concentration of Ca^{2+} ions in (b) gyroid, (c) lidinoid and (d) split-P based scaffolds as function of their porosity.

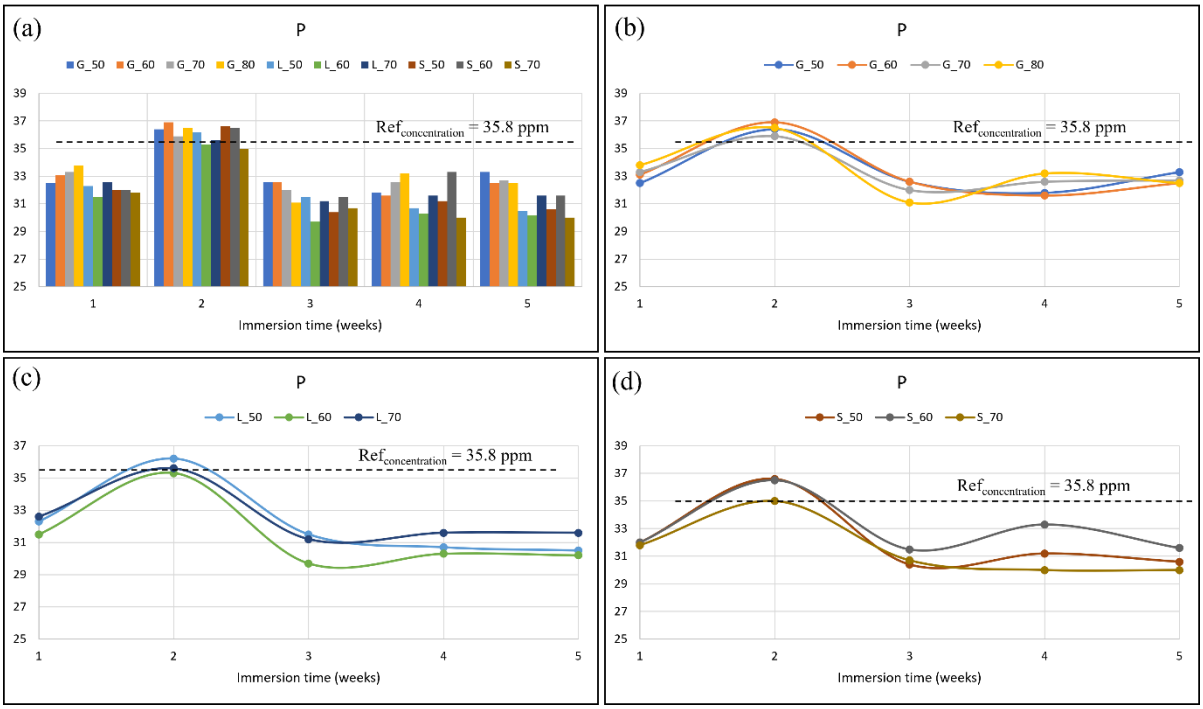

Figure A5: (a) Variation of P content observed at week1 1 to 5 across all TPMS structures at porosities ranging from 50% - 80%. Variation of P content in (b) gyroid, (c) lidinoid and (d) split-P based scaffolds as function of their porosities.

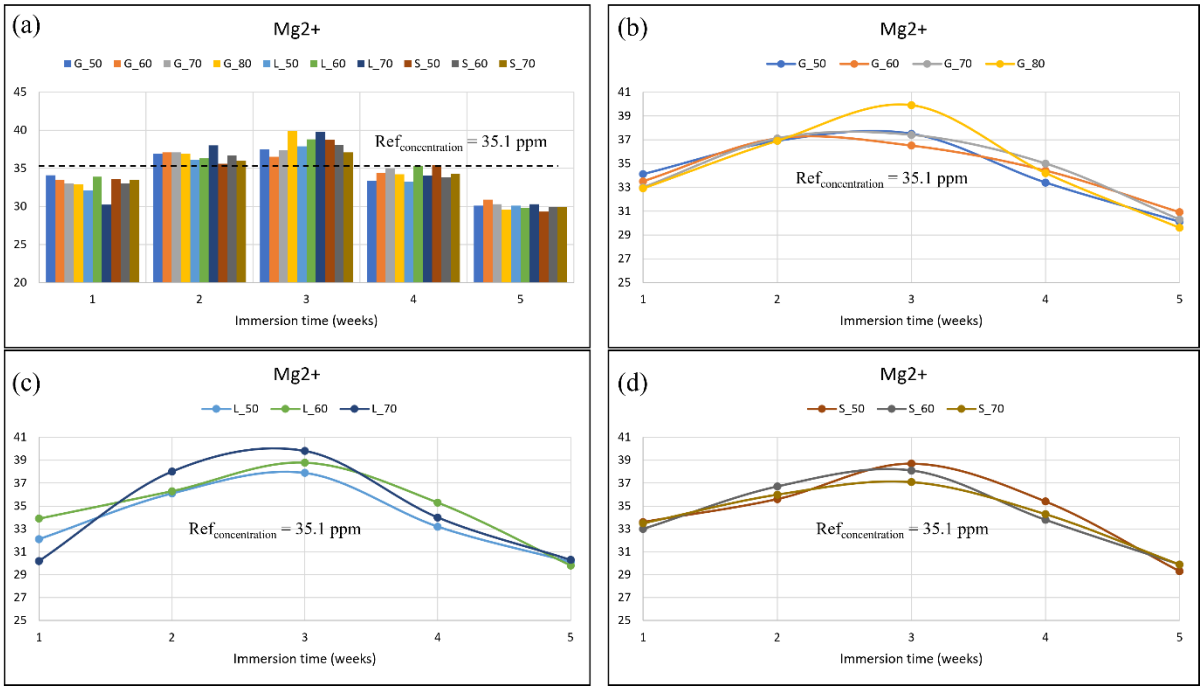

Figure A6: (a) Variation of Mg^{2+} content observed at week1 1 to 5 across all TPMS structures at porosities ranging from 50% - 80%. Variation of P content in (b) gyroid, (c) lidinoid and (d) split-p based scaffolds as function of their porosities.

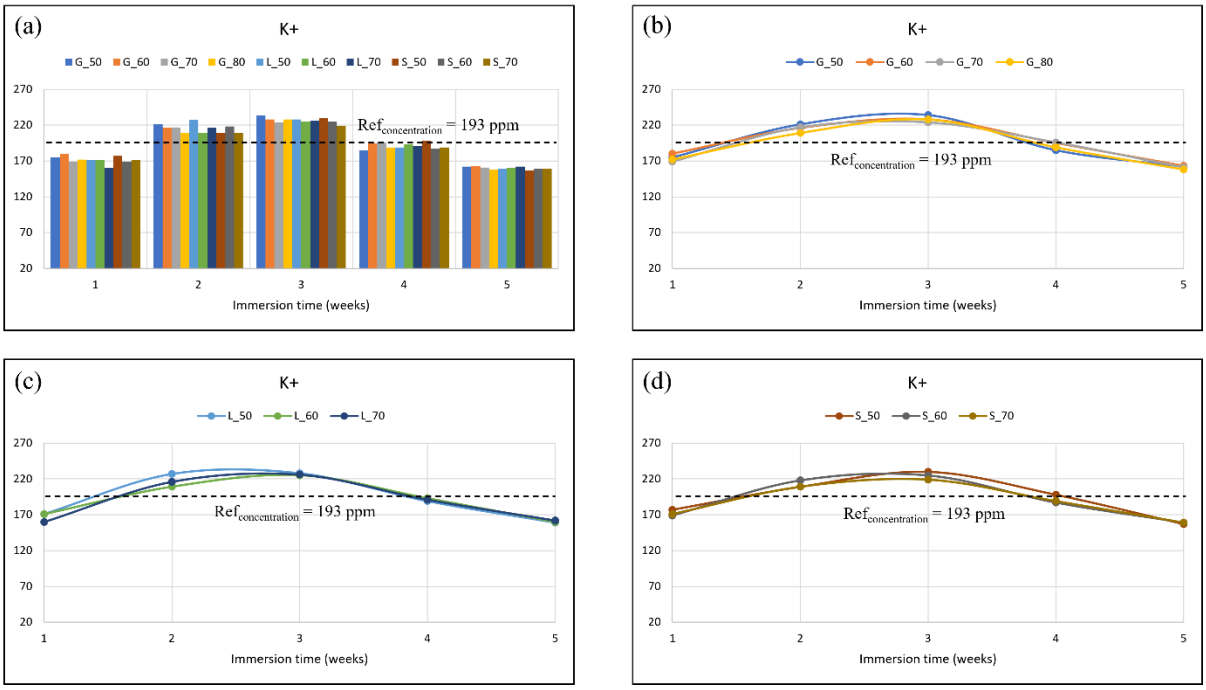

Figure A7: (a) Variation of K^+ content observed at week1 1 to 5 across all TPMS structures at porosities ranging from 50% - 80%. Variation of P content in (b) gyroid, (c) lidinoid and (d) split-P based scaffolds as function of their porosities.

Table A5: Measured change in mass of TPMS structures taken after 5 weeks of immersion in SBF solution.

TPMS structure	Sintered Mass (g) (M1)	Post-immersed mass (g) (M2)	Change in mass (g) (M2-M1)
G50	0.5993	0.6054	0.006
G60	0.5077	0.5157	0.008
G70	0.3992	0.4089	0.0097
G80	0.3029	0.3109	0.0079
L50	0.7196	0.7280	0.0084
L60	0.6129	0.6234	0.0105
L70	0.4202	0.4304	0.01027
S50	0.5911	0.5977	0.0066
S60	0.5168	0.5232	0.0065
S70	0.4693	0.4784	0.0091

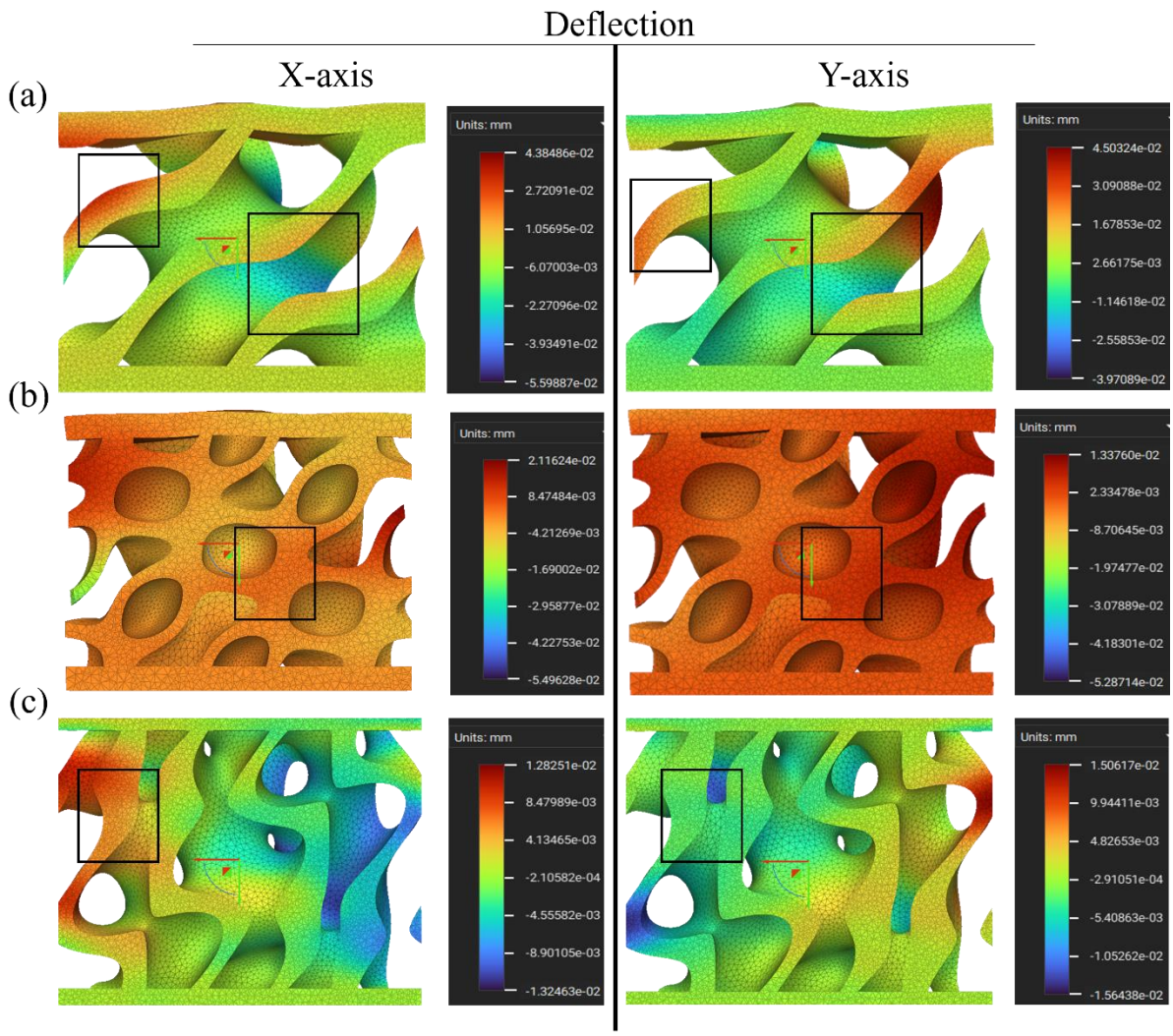

Figure A8: Deflection along x and y axis during uniaxial compression of (a) gyroid, (b) lidinoid and (c) split-P lattices. Highlighted regions indicate regions undergoing bending or stretching during deformation. Note: compression forces act along the z-direction.

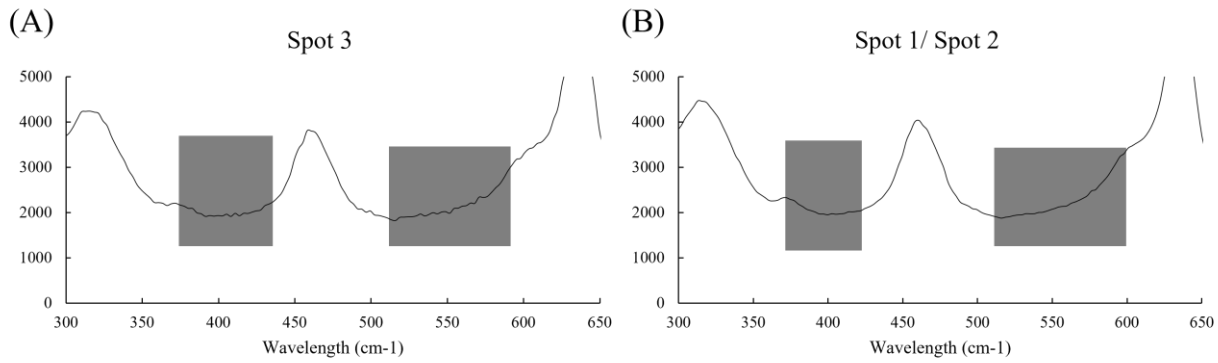

Figure A9: Raman spectra between 300 – 400 cm^{-1} and 500 – 600 cm^{-1} observed at (A) Spot 3 and (B) spot 1/spot 2.

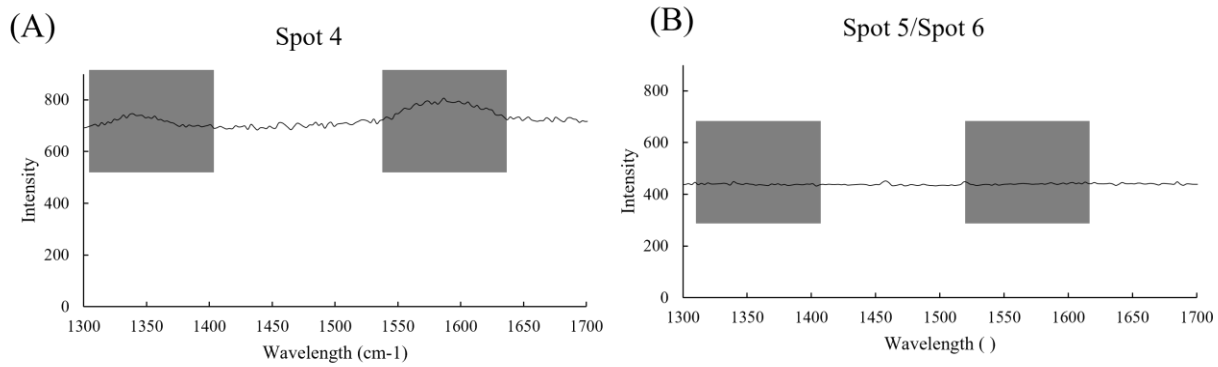

Figure A10: Raman spectra between 1300 – 1700 cm-1 observed at (A) spot 4 and (B) spot 5/6.

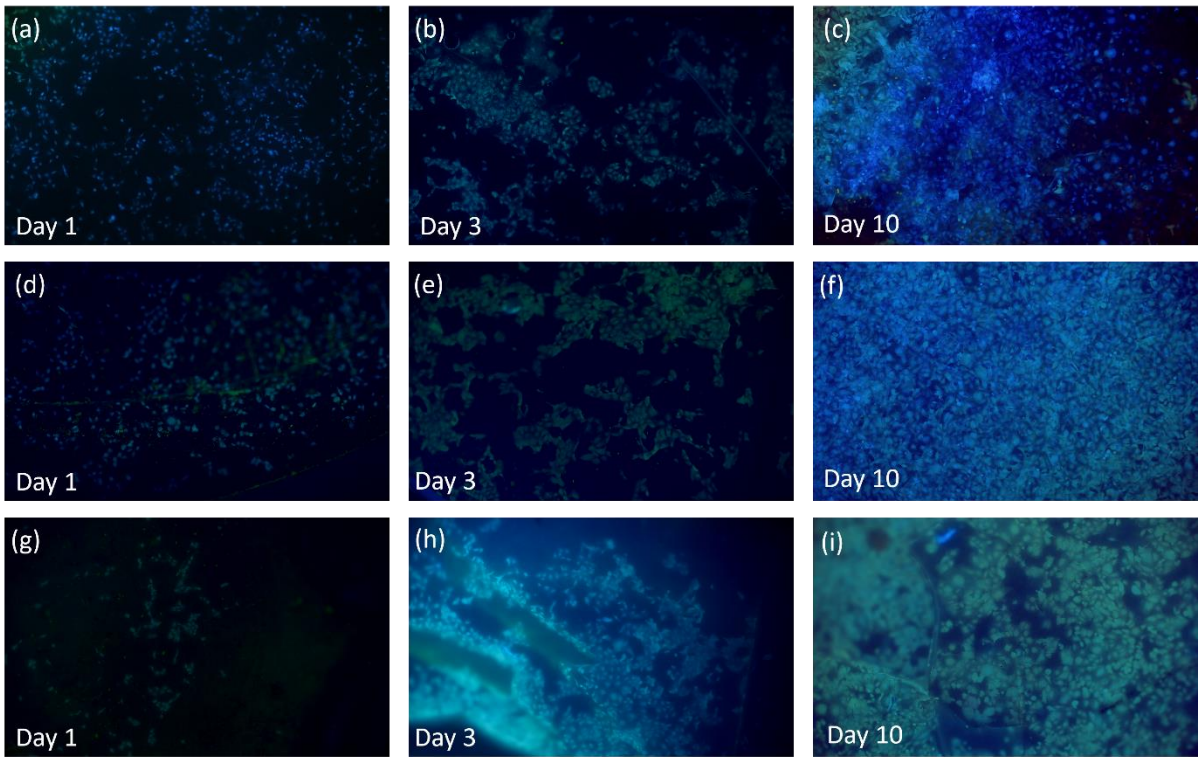

Figure A11 : Osteoblast cells observed using fluorescence microscopy at intervals of 1, 3 and 10 days on the HAp and 3Y-TZP type 1 and 3Y-TZP type 2 substrates.

RTqPCR Protocol

RTqPCR was performed as previously described [370, 371]. Briefly, RNA was isolated from osteoblasts using MagMAX™ mirVana™ Total RNA Isolation Kit (Applied Biosystems) with cells harvested at day 10 post-seed in 100uL of MagMAX™ lysis buffer (Applied Biosystems) and homogenised with pipetting. The lysate was stored at -80°C until extraction. RNA eluent was converted to cDNA using the SuperScript™ IV First-Strand Synthesis System (Invitrogen) in 10 µL total volume reactions with random hexamers and SuperScript™ reverse transcriptase at ($10U/\mu L_{RNA}$), [371]. qPCR was performed using ssoAdvanced SYBR® SuperMix (BioRad) following the manufacturer's recommendations (hot start 2 min at 95°C, followed by 40 cycles of 15 sec at 95°C and 30 sec at 60°C) [370]. Technical triplicate reactions were run at 5 µL total volume amplifying 1 µL sample, as previously described alongside no template negative controls [370, 371]. Reactions were measured by QuantStudio 5 Real-Time PCR Machine running QuantStudio Design and Analysis Software (v1.4.3, Applied Biosystems). Cycle threshold values (Ct) were determined with the threshold set in exponential phase amplification at ΔRn 0.008. All reactions were followed by a melt curve analysis ensuring primer specificity and contained desalt-grade PrimerBank™ [372] primers (Sigma-Aldrich) run at 500 nM. Reaction efficiency was calculated as previously described by Bustin et al. [373] . mRNA expression was calculated with the standard delta-delta cycle threshold ($2^{-\Delta\Delta Ct}$) method relative to Succinate dehydrogenase complex, subunit A (SDHA) expression, as previously described [374], using unseeded control cells the control group.

Table A6: Gene sequence of the primer sets used for RT-PCR.

Gene name	Forward Primer	Reverse Primer	Efficiency	Accession no
Osteocalcin Primer set 3	ATGAGAGCCCTCACACTCCTCG	3′-GTCAGCCAACTCGTCACAGTCC-5′	109.6%	NM_199173
RunX2 Primer set 2	TCAACGATCTGAGATTTGTGGG	GGGGAGGATTTGTGAAGACGG	114.3%	NM_001015051
Osteopontin Primer set 2	GAAGTTTCGCAGACCTGACAT	GTATGCACCATTCAACTCCTCG	125.7%	NM_001251830
SDHA (reference gene)	CAAACAGGAACCCGAGGTTTT	CAGCTTGGTAACACATGCTGTAT		NM_004168